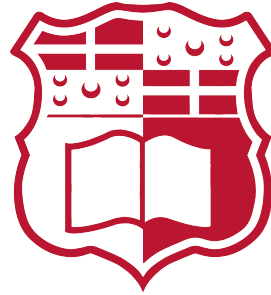


The Development and Optimisation of the B-train System for the ELENA Ring



Christian Grech

Supervisor: Dr Ing. Nicholas Sammut (UM)

Co-Supervisor: Dr Marco Buzio (CERN)

Department of Microelectronics & Nanoelectronics

University of Malta

June 2020

Submitted in partial fulfillment of the requirements for the degree of

Doctor of Philosophy

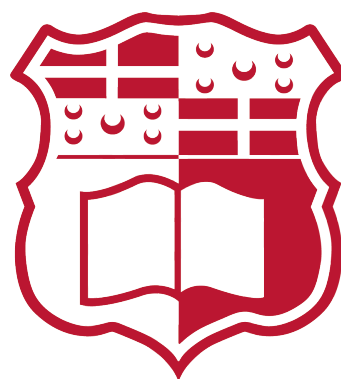
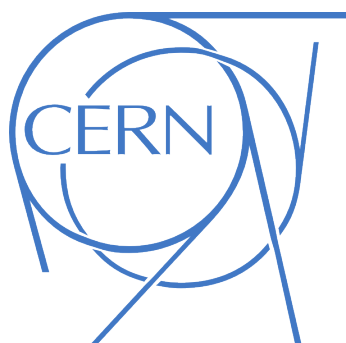


University of Malta Library – Electronic Thesis & Dissertations (ETD) Repository

The copyright of this thesis/dissertation belongs to the author. The author's rights in respect of this work are as defined by the Copyright Act (Chapter 415) of the Laws of Malta or as modified by any successive legislation.

Users may access this full-text thesis/dissertation and can make use of the information contained in accordance with the Copyright Act provided that the author must be properly acknowledged. Further distribution or reproduction in any format is prohibited without the prior permission of the copyright holder.

The research leading to the results of this thesis has received the financial support of CERN and the University of Malta.



Copyright Notice

No portion of the work referred to in the thesis has been submitted in support of an application for another degree or qualification of this or any other university or other institute of learning.

1. Copyright in text of this report rests with the Author. Copies (by any process) either in full, or of extracts, may be made only in accordance with regulation held by the Library of the University of Malta and the Library of the European Organization for Nuclear Research. Details may be obtained from the Librarians. This page must form part of any such copies made. Further copies (by any process) of copies made in accordance with such instructions may not be made without the permission (in writing) of the Author.
2. Ownership of the rights over any original intellectual property which may be contained in, or derived from, this report is vested in the University of Malta and in the European Organisation for Nuclear Research and may not be made available for use by third parties without the written permission of the University or of the Organisation, which will prescribe the terms and conditions of any such agreement.

Student Name

Signature

Acknowledgements

I would like to express my appreciation and thanks to my supervisors Dr Nicholas Sammut (University of Malta) and Dr Marco Buzio (CERN) for their guidance and patience throughout the duration of this project. I am very grateful to the various past and present colleagues in the Magnetic Measurements section at CERN, particularly to those working on the B-train project. Special thanks goes to Maria Amodeo, Anthony Beaumont, Martino Colciago, Vincenzo Di Capua, David Giloteaux, Marco Roda, Alessandro Parrella and Joseph Vella Wallbank for their help and support. Their work in the design and development of the B-train FIRESTORM prototype is acknowledged.

My thanks also goes to the Guy Deferne, Olaf Dunkel, Lucio Fiscarelli, Carlo Petrone and Stephan Russenschuck for their discussions in relation to experiments performed in the magnetic measurements laboratory. I would also like to thank all Magnetic Measurements section technical support personnel for their help in setting up the spare magnet equipment especially during the transition to the new magnetic measurements laboratory. A special thanks goes to Patrick Bestmann and Camille Vendeuvre from CERN's Alignment, Co-ordination and Engineering Group for their efforts and support when performing the laser tracker survey on the reference magnet.

I would also like to thank the whole ELENA operation crew led by Christian Carli and Tommy Eriksson, especially Lajos Bojtar, Bruno Dupuy, Pierre Freyermuth, Davide Gamba, Bertrand Lefort, Sergio Pasinelli and Laurette Ponce for their patience when asking for specific magnetic cycles in the commissioning process. I would also like to express my thanks to Maria Elena Angoletta for her support in creating an interface to acquire RF data during the commissioning period.

I would like to express my thanks to fellow students and friends Dmitry Akhmedianov, Matthias Bonora, Gianni Caiafa, Wayne Jordan Chetcuti, Raul Costa, Steffen Gutzeit, Ioannis Iakovidis, Mariano Pentella, Piotr Rogacki, Eleni Tournaki and Andreas Windischhofer for making my experience an

enjoyable one.

This PhD is the result of many years of growth and learning. I would like to express my thanks to my parents and my sisters for their relentless encouragement and support in my studies.

Abstract

In synchrotrons, the vertical magnetic field produced by dipole magnets guides charged particles along a closed horizontal orbit, determined by the equilibrium of the centripetal force and the Lorentz force. As a result, the knowledge of the magnetic field value in real-time is essential to control the trajectory of the particles. Subsequently, a direct magnetic field measurement inside a reference magnet, known as a B-train, is used to derive an estimate of the average magnetic field in the ring.

As part of a site-wide consolidation project, all the B-train systems at CERN are being replaced with upgraded electronics, software, and sensors. The Extra Low ENergy Antiproton (ELENA) ring is a new decelerator being built at CERN; hence a B-train system is required to be installed and commissioned. The ELENA ring presents challenges to magnetic field measurement systems, such as very low magnetic field and long cycle times. The aim of this thesis is to commission a measurement model for the ELENA B-train, as well as validating and optimising the instrumentation.

A measurement model is thus developed in this thesis, and applied to identify the ring and reference magnets, the sensors, as well as the electronic acquisition chain. An uncertainty estimation helps identify the biggest sources of error in the measurement, providing an insight on potential improvements in the measurement system. The ELENA B-train system is validated through a series of tests, characterising the behaviour of the sensors, the stability and the accuracy of the instrument in operating conditions, confirming a relative reproducibility and accuracy better than 2 units (10^{-4}).

A potential improvement in the measurement by changing the position of the local field sensors is investigated, and the feasibility of applying a displacement is discussed for the ELENA B-train. A magnetic field model based on the decomposition of the field into different components is finally proposed. The model is tested using the ELENA magnetic cycles, exhibiting a relative accuracy of 1 unit, giving confidence in its prediction ability in low-energy synchrotrons.

List of Publications

The following publications are the result of the work of this thesis:

Journal Papers

- **C. Grech**, R. Avramidou, A. Beaumont, M. Buzio, N. Sammut and J. Tinembart, "Metrological Characterization of Nuclear Magnetic Resonance Markers for Real-time Field Control of the CERN ELENA Ring Dipoles", *IEEE Sensors Journal*, July 2018.
- **C. Grech**, M. Buzio, N. Sammut, "A Magnetic Measurement Model for Real-Time Control of Synchrotrons", *IEEE Transactions on Instrumentation and Measurement*, July 2019.
- **C. Grech**, M. Buzio, M. Pentella, N. Sammut, "Dynamic Ferromagnetic Hysteresis Modelling using a Preisach-Recurrent Neural Network Model", *Materials*, June 2020.
- **C. Grech**, M. Amodeo, A. Beaumont, M. Buzio, V. Di Capua, D. Giloteaux, N. Sammut, J. Vella Wallbank, "Error Characterization and Calibration of Real-Time Magnetic Field Measurement Systems", *Nuclear Instruments and Methods in Physics Research Section A: Accelerators, Spectrometers, Detectors and Associated Equipment*, submitted for publication.
- **C. Grech**, M. Buzio, N. Sammut, "Prediction of Dynamic Ferromagnetic Hysteresis in Dipole Magnets using Machine Learning Techniques", submitted for publication.
- J. Vella Wallbank, M. Amodeo, A. Beaumont, M. Buzio, V. Di Capua, D. Giloteaux, **C. Grech**, N. Sammut, "The development of a real-time magnetic measurement system", in work.

Conference Papers

- **C. Grech**, A. Beaumont, M. Buzio and N. Sammut, "Performance comparison of Nuclear Magnetic Resonance and FerriMagnetic Resonance field markers for the control of low-energy Synchrotrons", *XXII IMEKO World Congress*, September 2018, Belfast, Northern Ireland.
- D. Gamba, M.E. Angoletta, P. Belochitskii, L. Bojtar, F. Butin, C. Carli, B. Dupuy, Y. Dutheil, T. Eriksson, P. Freyermuth, R. Gebel, **C. Grech**, M. Hori, J.R. Hunt, M. Jaussi, L.V. Jorgensen, B. Lefort, S. Pasinelli, L. Ponce, G. Tranquille, "ELENA Commissioning", *NAPAC*, November 2019, Michigan, USA.

Contents

Declaration of Authenticity	iii
Copyright Notice	iv
Acknowledgements	v
Abstract	vii
List of Publications	viii
Contents	x
List of Figures	xiv
List of Tables	xviii
List of Acronyms	xix
Nomenclature	xxii
1 Introduction	1
1.1 Magnets in synchrotrons	1
1.1.1 General overview	1
1.1.2 Magnetic field assessment	5
1.2 The Antimatter Factory	7
1.3 Project description and objectives	10
1.4 Structure of the thesis	13
2 Literature Review: Magnetic Field Evaluation Methods	15
2.1 Introduction	15
2.2 Magnetic field effects	16
2.2.1 Hysteresis	16
2.2.2 Eddy currents	18

2.3	Magnetic measurement techniques	19
2.3.1	Induction coils	20
2.3.2	Magnetic resonance sensors	21
2.3.3	Hall generator	23
2.3.4	Fluxgate magnetometer	25
2.4	B-train systems in other machines	26
2.4.1	CERN	26
2.4.2	Heidelberg-Ion Therapy Centre	28
2.4.3	MedAustron	29
2.4.4	Italian Centre for Oncological Hadron therapy	30
2.4.5	Alternating Gradient Synchrotron	31
2.4.6	Advanced Light Source	31
2.5	Hysteresis models	31
2.5.1	Conventional mathematical formulations	32
2.5.2	Preisach models	34
2.5.3	Physical models	38
2.5.4	Current state-of-the-art	39
2.6	The FIRESTORM project	42
2.6.1	Impact on synchrotron operation	42
2.6.2	FIRESTORM architecture	43
2.6.3	ELENA B-train specifications	48
2.6.4	Contributions to the FIRESTORM project	54
2.7	Motivation and scientific contribution	56
2.8	Conclusion	59
3	Measurement model	60
3.1	Introduction	60
3.2	Proposed model	60
3.2.1	Field integral measurement	61
3.2.2	Integration constant	62
3.2.3	Model definition	64
3.3	Parameter identification	64
3.3.1	Induction coil gain error, η	64
3.3.2	Effective coil width, \bar{w}_{eff}	66
3.3.3	Coil offset error, ϵ	68
3.3.4	Integration constant, \mathbb{I}_0	69
3.3.5	Reference-to-ring error, α	71
3.4	Uncertainty estimation	76

3.5	Conclusion	79
4	Metrological Characterisation and Calibration	81
4.1	Introduction	81
4.2	B-train characterisation	82
4.2.1	Random error sources	83
4.2.2	Systematic error sources	86
4.3	Field marker characterisation	86
4.3.1	Field uniformity	87
4.3.2	Trigger signal precision	87
4.3.3	Delay of trigger signal generation	90
4.4	Reliability Run	91
4.5	Systematic error evaluation	93
4.5.1	Procedure	93
4.5.2	Results	97
4.6	Summary	99
5	Field Marker Position Optimisation	101
5.1	Introduction	101
5.2	Optimal position search	102
5.2.1	Experimental Setup	102
5.2.2	Results and discussion	104
5.3	ELENA B-train feasibility study	107
5.3.1	Magnetic resonance sensor response	107
5.3.2	Dynamic characterisation	109
5.4	Conclusion	112
6	Dynamic Magnetic Field Hysteresis Modelling	114
6.1	Introduction	114
6.2	B-train field model	115
6.2.1	Measurements	115
6.2.2	Proposed model	116
6.2.3	Characterisation	117
6.2.4	Results	126
6.2.5	Discussion and limitations	127
6.3	Preisach-RNN model	129
6.3.1	Method	129
6.3.2	Results	133
6.4	Summary	135

7 Conclusions	137
7.1 Summary of achieved aims	137
7.2 Personal contributions	141
7.3 Future Work	142
Appendix A Performance Comparison of NMR and FMR sensors	144
References	148

List of Figures

1.1	A basic representation of a synchrotron	2
1.2	A vertical and horizontal section view of the C-shaped dipole magnet used in this work. The adopted co-ordinate convention is illustrated.	4
1.3	Functional drawing of a B-train system showing the ring magnets connected to the reference magnet housing the sensors, as well as the electronic acquisition chain.	6
1.4	Schematic diagram of the Antimatter Factory and the placement of experimental installations.	8
1.5	A schematic of the layout of the ELENA ring and its components.	9
1.6	The ELENA ring during the commissioning period.	10
2.1	Diagram showing the major and minor hysteresis loops of a ferromagnetic material.	17
2.2	An example of a degaussing cycle that is applied to a magnet to erase the residual field.	17
2.3	NMR and FMR resonant signals.	22
2.4	Hall generator principle, where a voltage proportional to the field is created across the length of a material.	24
2.5	Fluxgate magnetometer composed of a modulating coil, a bias coil and a detection coil.	25
2.6	Sensors within the LEIR magnet installed on the mid-plane of the gap just outside the vacuum chamber.	28
2.7	Sensors installed within the HIT bending dipole magnet	29
2.8	CNAO B-train system block diagram, including the power supply, magnet and acquisition control loop.	30
2.9	Block representation of the classical Preisach model, where the model is approximated by a finite superposition of various rectangular operators.	35

2.10	Three types of operators used to represent hysteresis in Preisach models: the Preisach (rectangular) operator, PI operator and KP operator.	37
2.11	A graphical representation of the model defined in Equation 2.15, which is composed of the magnetisation, eddy current and residual field contributions.	40
2.12	Simplified circuit of a C-shaped dipole magnet	41
2.13	Timeline of the FIRESTORM project milestones.	43
2.14	Schematic of the FIRESTORM B-train architecture	44
2.15	The SPEC board and FMC module.	45
2.16	B-train White Rabbit Ethernet frame.	47
2.17	ELENA injection and extraction lines. The ion source can partially be seen at the bottom left corner.	50
2.18	Magnetic cycles used in the ELENA ring during commissioning. . . .	51
2.19	ELENA B-train reference magnet sensor setup.	52
2.20	ELENA FIRESTORM acquisition chains	53
2.21	Overview of the accuracy and range characteristic of different measurement techniques, highlighting the possible options that can meet the requirements for the ELENA B-train.	54
2.22	ELENA reference magnet	55
3.1	Hard edge model used to define ℓ_m along the length of a magnet. . .	63
3.2	Measured magnetic length at ± 200 A/s. The values up to 0.98 were measured during ramp-up whilst values higher than 0.98 were measured during ramp-down.	63
3.3	Equivalent model of the coil and acquisition chain.	65
3.4	Measurement of the ambient temperature during the machine's commissioning period.	66
3.5	Relative cross-calibration coil placement. A reference coil and the coil that is going to be calibrated are subjected to the same field, whilst the resulting flux is measured.	67
3.6	ELENA coil cross-calibration measurement	68
3.7	Laser tracker survey measurements performed on the ELENA reference magnet.	69
3.8	Main cycles used in the ELENA ring.	70
3.9	Residual field measurement after degaussing. Multiple sensors are used, and an average is calculated along the magnet's longitudinal plane.	72

3.10	The reference and ring magnets' acceptance cycle transfer function at 200 A/s.	73
3.11	Acceptance and operational transfer functions for the spare magnet. The marked plateaus refer to the two ramp-down plateaus in the antiproton deceleration mode of operation.	74
3.12	Operational cycle transfer function for the spare magnet extrapolated during ramp-down.	75
3.13	Reference-to-ring scaling factor. The hysteresis cycle's ramp-up represents acceleration of H^- ions, while the ramp-down represents antiproton deceleration.	76
4.1	Reference magnet and electronic experimental setup to determine the precision of NMR field markers for the ELENA B-train.	88
4.2	The different B and B/\dot{B} combinations investigated and the operating points.	88
4.3	NMR signals at 46.5 mT and 58 mT/s.	89
4.4	NMR signal output and the generated trigger signal by the Peak Detector SPEC card.	91
4.5	Drift on the deceleration cycle's intermediate plateau. t_p and $t_p + \Delta t$ indicate the points considered for calculating the drift.	93
4.6	Random error measurement at injection and extraction	94
4.7	Simplified schematic diagram of the LLRF system	94
4.8	The revolution frequency (black) and the reciprocal of its first derivative (red) as a function of the ELENA magnetic field.	96
4.9	The points in the deceleration cycle where RF is on and measurements were acquired.	97
4.10	$B(t)$ vs. $\delta B(t)$ before and after the ELENA B-train's calibration.	98
5.1	In order to characterise the magnetic length, the excitation current is ramped up from 0 A to 275 A and then ramped down to 0 A at 200 A/s.103	
5.2	Measured magnetic length at $y = 5$ mm, $x = 0$ mm.	105
5.3	Measured magnetic length at $y = 16$ mm, $x = 0$ mm.	106
5.4	Measured magnetic length at $y = 25$ mm, $x = 0$ mm.	106
5.5	Measured magnetic length at $y = 5$ mm, $x = 50$ mm.	107
5.6	Magnetic length variation when changing x , y and s	108
5.7	Measured NMR voltage signal amplitude at 45 mT and 340 mT.	110
5.8	Horizontal section view of the ELENA B-train sensor setup.	111

5.9	Determination of Γ , as a function of integral field variation. It is concluded that for high field markers, feasibility of displacement occurs at $v > 0.09$ Tm/s, whilst for low field markers, this happens at $v > 0.21$ Tm/s.	112
5.10	Trigger time data acquisition when the acceleration and deceleration cycles are interleaved.	113
6.1	An example of the integral field measurement, indicating which parts of the measurement are used to determine the model components. . .	115
6.2	Measured transfer functions at different ramp rates.	116
6.3	Residual field characterisation	118
6.4	Hysteresis component curve fit	119
6.5	Dynamic characterisation	120
6.6	General structure of the ANN	120
6.7	Flowchart illustrating the model's training and validation method . .	123
6.8	Performance of ten different neural network structures	124
6.9	Measured and modelled transients at 500 A/s	125
6.10	Neural network architecture used to identify the transient component coefficients	126
6.11	Residual distribution of the fitted model, with respect to current and time.	128
6.12	Actual and estimated non-linear ELENA field. The estimation using the model by Caspers <i>et al.</i> is also depicted.	129
6.13	Schematic representation of the proposed Preisach-RNN model. . . .	131
6.14	The magnetic field signal and its derivative that form the training, validation and testing datasets.	132
6.15	The magnetic field signal and its derivative applied for the model's evaluation.	132
6.16	Major loop predictions and training data.	134
6.17	Minor loop predictions at random ramp-rates.	134
6.18	The outcome of the sensitivity analysis for each individual input. . .	135
A.1	Reference magnet and electronic experimental setup to compare the precision of two magnetic resonance field markers for the ELENA B-train.	145
A.2	Cycles applied and corresponding field levels (shown as dotted lines). .	146
A.3	Generated NMR and FMR signals at 200 mT and 368 mT/s, along with the corresponding trigger signals.	147

List of Tables

1.1	Summary of the state-of-the-art and motivation behind this work . . .	13
2.1	SPEC board technical specification	45
2.2	Control frame breakdown	47
2.3	ELENA dipole magnet specifications	49
2.4	Cycle properties and timings for the two ELENA B-train chains . . .	52
3.1	Sources of uncertainty in the ELENA measurement model	78
3.2	Individual uncertainty contributors of the ELENA measurement model in deceleration mode at injection level	79
4.1	Trigger signal precision for different combinations of B and \dot{B}	90
4.2	ELENA B-train reliability run results for both acceleration and deceleration cycles.	92
4.3	ELENA B-train beam measurements	98
5.1	Magnetic length variation, when changing y	104
5.2	Magnetic length variation, when changing x	105
6.1	Hysteresis component parameters	119
6.2	ANN parameter list	127
6.3	Recurrent neural network parameters list	133
A.1	Measured trigger signal repeatability for NMR and FMR sensors . . .	147

List of Acronyms

AD Antiproton Decelerator	7
ADC Analogue-to-Digital Converter	45
AEGIS Antihydrogen Experiment: Gravity, Interferometry, Spectroscopy	7
ALPHA Antihydrogen Laser PHysics Apparatus	7
ALS Advanced Light Source	31
ANN Artificial Neural Network	33
ASACUSA Atomic Spectroscopy And Collisions Using Slow Antiprotons	7
ATRAP Antihydrogen Trap	7
BASE Baryon Antibaryon Symmetry Experiment	7
C1 Chain 1	43
C2 Chain 2	43
CERN European Organisation for Nuclear Research	7
CNAO Italian Centre for Oncological Hadron therapy	30
ELENA Extra Low ENergy Antiproton	7
ESR Electron Spin Resonance	22
FESA Front End Software Architecture	11
FIRESTORM Field In REal-time Streaming from Online Reference Magnets	10

FMC FPGA Mezzanine Card	11
FMR FerriMagnetic Resonance	22
FPGA Field Programmable Gate Array	30
GBAR Gravitational Behaviour of Antihydrogen at Rest	7
HIT Heidelberg-Ion Therapy Centre	28
LEIR Low Energy Ion Ring	10
LEP Large Electron-Positron Collider	6
LHC Large Hadron Collider	1
LLRF Low-Level Radio Frequency	93
MLP Multilayer Perceptron	33
NARX Non-linear AutoRegressive with eXogenous inputs	34
NMR Nuclear Magnetic Resonance	11
NRMSE Normalised Root Mean Square Error	42
KP Krasnosel'skiĭ Pokrovskiĭ	36
PCIe Peripheral Component Interconnect express	44
PI Prandtl-Ishlinskiĭ	36
PS Proton Synchrotron	8
PSB Proton Synchrotron Booster	10
RF Radio Frequency	2
RMS Root Mean Square	84
RNN Recurrent Neural Network	58

SPEC Simple Peripheral Component Interconnect Express FPGA Mezzanine Card carrier	44
SPS Super Proton Synchrotron	10
TPU Transverse Pick-up Unit	95
YIG Yttrium Iron Garnet	22

Nomenclature

Term	Unit	Description
A_c	m^2	effective coil area
α	-	reference-to-ring magnet error
b	-	bias
B	T	average magnetic field
\bar{B}	T	average estimated synchrotron magnetic field
\dot{B}	T/s	rate of change of magnetic field with respect to time
\dot{B}_d	T/s	drift rate
β	-	sensor displacement advantage
c	m/s	speed of light in vacuum
C	F	capacitance
γ	Hz/T	gyromagnetic ratio
$\gamma_{\alpha\beta}$	-	elementary hysteresis operator
Γ	-	ratio of magnetic length variation at two points
d	m	thickness
δV	V	voltage offset
δB	T	measured field error
ΔB	T	field offset
ΔB_{NMR}	T	delay between NMR and trigger signal field equivalent
Δt	s	time difference
Δt_{NMR}	s	delay between NMR and trigger signal
$\Delta t_{\text{NMR-FMR}}$	s	delay between NMR and FMR trigger signals
$\Delta \Phi$	Wb	magnetic flux change
Δx	m	lateral position offset

ϵ	-	coil gain error
f	Hz	frequency
f_{loops}	Hz	feedback loops frequency
f_{off}	Hz	offset frequency
f_{prg}	Hz	programmed revolution frequency
f_{rad}	Hz	radial loop frequency
f_{rev}	Hz	revolution frequency
F	N	force
g	-	gain parameter
\mathcal{G}	T	integrated field gradient
h	-	hidden layer nodes
H_c	A/m	coercive force
ζ	-	learning rate
η	-	coil offset factor
θ	°	beam deflection angle
I	A	magnetisation current
\dot{I}	A/s	rate of change of current
I_p	A	peak current
\mathbb{I}	Tm	integral magnetic field
\mathbb{I}_0	Tm	integration constant
\mathbb{I}_D	Tm	dynamic integral field component
\mathbb{I}_L	Tm	linear integral field component
\mathbb{I}_R	Tm	residual field component
\mathbb{I}_{res}	Tm	residual integral field
\mathbb{I}_T	Tm	transient field component
J	A/m ²	current density
k_{int}	-	integrator gain error
K	-	model constant
ℓ_m	m	effective magnetic length
l^*	m	nominal magnetic length

L	H	inductance
λ	-	gain error
m_0	kg	particle rest mass
M	A/m	magnetisation
μ	H/m	permeability
n	-	number of cycles
N_B	-	number of bending dipole magnets in a synchrotron
N_T	-	number of coil winding turns
p	eV/c	momentum
p_i	-	uncertainty parameter
q	eV	particle charge
r	m	radius
R_c	Ω	coil resistance
R_g	H^{-1}	magnetic reluctance
R_H	Ω	Hall coefficient
R_{in}	Ω	input resistance
ρ	Ωm	resistivity
s	m	beam path
s^*	m	optimal field marker position
S	m^2	surface
σ	-	standard deviation
σ_d	T	drift random error contribution
σ_m	T	field marker random error contribution
σ_n	T	noise random error contribution
t	s	time
t_{ex}	s	extraction time
t_{inj}	s	injection time
t_k	s	field marker trigger time
\mathcal{T}	Tm/A	integral transfer function
\mathcal{T}_{ref}	Tm/A	reference magnet's integral transfer function

$\mathcal{T}_{\text{ring}}$	Tm/A	ring's integral transfer function
$\mathcal{T}_{\text{spare}}$	Tm/A	spare magnet's integral transfer function
u_c	-	combined standard uncertainty
v	m/s	velocity
V_0	V	voltage offset
V_c	V	induced coil voltage
V_H	V	Hall voltage
\bar{V}	V	reference voltage
w	m	coil winding width
\bar{w}_{eff}	m	effective width
Φ	Wb	magnetic flux
x	m	lateral position
χ	T	transfer function scaling factor
y	m	vertical position
\dot{v}	Tm/s	variation of the rate of change of integral field
z	-	model output

The code developed in this thesis can be found online at <https://github.com/cgre23/ELENA-B-train-Commissioning>

Chapter 1

Introduction

1.1 | Magnets in synchrotrons

1.1.1 | General overview

Over the past century, researchers have explored and built a detailed description of Nature in terms of elementary building blocks of matter interacting via fundamental forces. This knowledge was attained through large-scale, but ultra-precise experiments using machines that accelerate and collide particles at very high energies [1]. A particular type of these machines, synchrotrons, make use of electromagnetic fields to bend and accelerate charged particles to close to the speed of light. One such machine is the Large Hadron Collider (LHC) [2], which smashes particles against each other. As fundamental particles are created in these collisions, these particles are studied so that we understand more about the origins of the Universe.

Synchrotrons represent some of the most elaborate and challenging technological efforts accomplished. Hence, unsurprisingly, their development has generated advances for society that span far beyond their scientific aims. The knowledge on these machines has been crucial to the development of other technologies such as medical imaging scanners in hospitals [3] and nuclear power stations for example. Medium-sized synchrotrons also allow scientists

to produce particle beams that can be used to investigate the structure of materials [4]. The most common type of synchrotrons, however, are the small industrial and medical accelerators found all around the world. These are used for treating cancer, preventing terrorist attacks at ports and airports [1] and sterilising equipment [5].

Figure 1.1 presents a basic layout of a synchrotron. The particles are injected in the machine and travel through a vacuum chamber, where the amount of gas is minimised. Radio Frequency (RF) cavities provide the electric field, controlling the speed of the particles in the machine. The electric field is synchronised with the magnetic field so that the beam of particles maintains its orbit around the ring. As the particles pass through the electric field, energy is transferred from the radio wave to the particles.

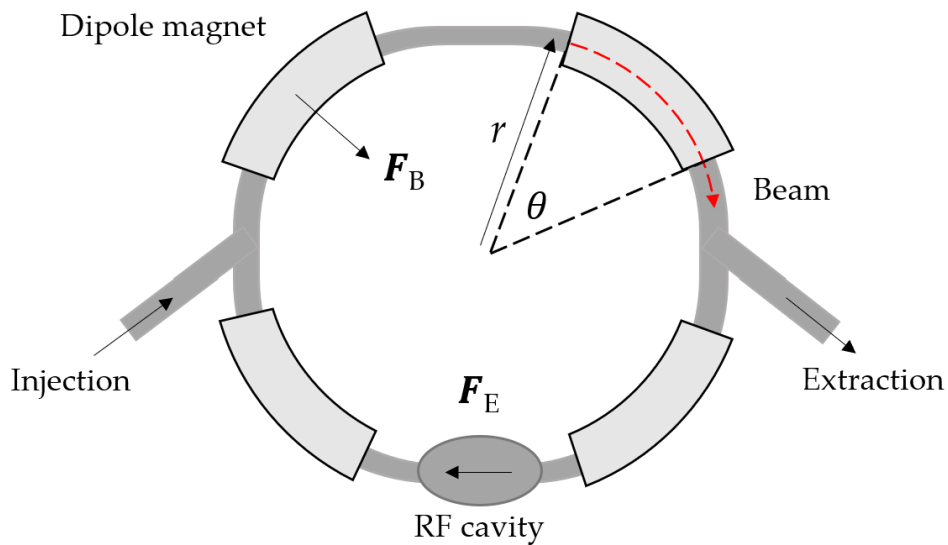


Figure 1.1: A simple representation of a synchrotron, showing the path that the beam of particles follows, along with related parameters.

Dipole magnets, on the other hand, are used to steer the particles around the machine. These magnets are also known as bending magnets, as they bend the beam with an angle θ and radius r . Other magnet types of higher order in synchrotrons are used to correct the magnetic field. In particular, quadrupole magnets produce a force that points towards the centre in one plane and away from it in the other plane. This results in a focusing or defocusing effect on the beam, depending on the position of the magnet [6]. Subsequently, once the desired energy has been reached, the beam is extracted towards the experiment.

The properties of a particle with charge q inside a synchrotron are controlled by the Lorentz force, F_L , which is defined as the sum of the electric force F_E , and magnetic force F_B , as follows:

$$F_L = q(E + \mathbf{v} \times \mathbf{B}) = qE + q(\mathbf{v} \times \mathbf{B}) = F_E + F_B, \quad (1.1)$$

where E is the electric field vector, acting along the particle's direction of motion, B is the magnetic field vector, acting perpendicular to the particle's direction of motion, and v is the particle's velocity [6].

The determination of the deflection of a particle by a magnetic or electric field is important in the control of charged particle beams. Since in high energy beams the speed is a large value, this presents a considerable amplification factor whenever a magnetic field is applied. Hence it is more convenient to use magnetic fields for bending the beam, rather than electric fields. Neglecting the electric field component, the Lorentz force, and the centripetal force F_C , on the particle are:

$$F_L = qvB, \quad (1.2)$$

$$F_C = \frac{pv}{r}, \quad (1.3)$$

where p is the momentum of the particles [7]. Assuming an ideal spatially uniform dipole magnet along the beam path, having pure vertical field lines, the condition for a perfect circular path can be described as the equality between these two forces, resulting in the following condition:

$$\frac{p}{q} = Br. \quad (1.4)$$

This condition relates the so-called beam rigidity Br to the momentum of the particle, defining, in the end, the machine's size for a given magnetic field of the dipole magnets.

Synchrotrons come in various sizes, depending on their application. By having a circular machine, the same equipment can be used for each turn that the particles make. Having a closed loop, the full bending angle is exactly 2π . Referring to Figure 1.1, considering the beam path as s , and the beam deflection as θ :

$$\theta = \frac{ds}{r} = \frac{B ds}{Br}. \quad (1.5)$$

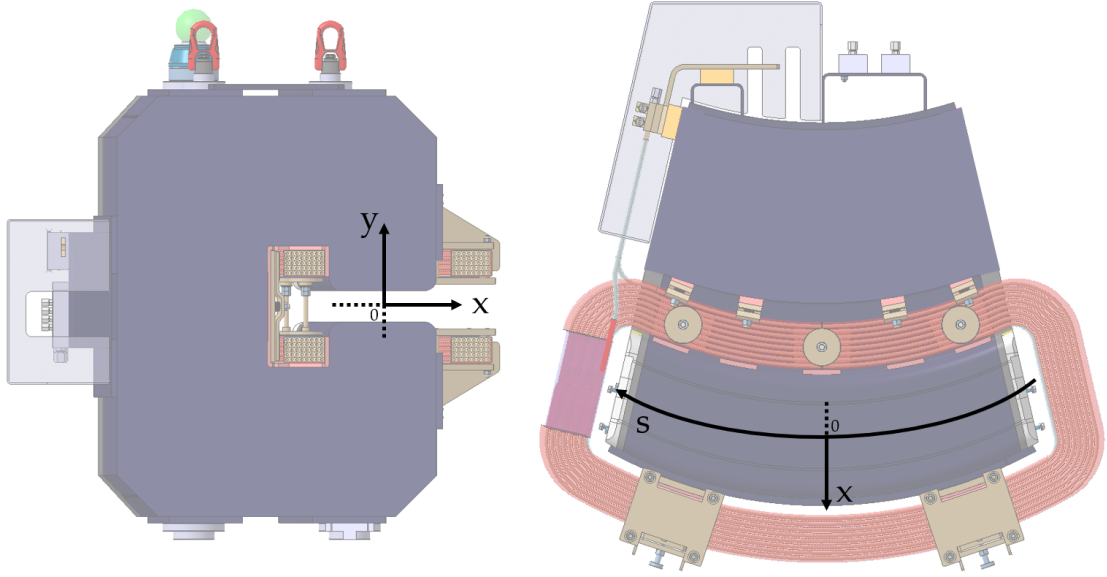


Figure 1.2: A vertical section view (left) and a horizontal section view (right) of the C-shaped dipole magnet used in this work. The adopted co-ordinate convention is illustrated.

This leads to the following condition for a closed orbit [8]:

$$2\pi = \frac{\int B ds}{Br}. \quad (1.6)$$

This equation can subsequently be used to determine the magnetic field required in a synchrotron of a particular radius r .

This thesis is focused on normal-conducting magnets, consisting of a ferromagnetic yoke that guides and concentrates the magnetic flux in the gap. The magnetic field is generated by an excitation current, I in coils surrounding the magnet poles. Figure 1.2 shows a vertical section view (left) and a horizontal section view (right) of the C-shaped dipole magnet used in this work. The position of a point in the gap of the magnet is defined using co-ordinates x , y and s . The x -axis is lateral and lies in the plane of symmetry of the poles, whilst the y -axis is the vertical axis. The s -axis is longitudinal and spans along the central line between the pole edges. The origin for the x , y coordinates lies on the s -axis, at which point $s = 0$.

1.1.2 | Magnetic field assessment

Precise knowledge of the magnetic field in synchrotrons is crucial for RF cavity control, beam diagnostics and qualitative feedback to operators. In particular, magnetic field reproducibility and stability play an important role to maintain the beam on the desired central trajectory [9]. This refers to the consistency of the field assessment conducted over repetitions of various cycles. As a result, correct observation of the instantaneous field must be guaranteed for machine operation. Moreover, care is taken to keep track of the powering history due to the hysteretic behaviour of the yoke's magnetisation. For this reason, magnet pre-cycling and thorough cycle configurations are tested and set in place during a synchrotron's commissioning. Accurate magnetic field assessment in a synchrotron can be obtained using either an on-line or off-line approach [9]. In this thesis, two common on-line approaches are considered for deriving the magnetic field in the bending dipole magnets of a synchrotron: real-time magnetic measurement systems and magnetic field models.

A B-train is a real-time magnetic field measurement system, aptly named as in the past it distributed the field as a train of pulses on a dual digital serial channel, where one pulse represented a certain increment or decrement. The instrument consists of multiple sensors installed within a dedicated reference magnet (where possible). This magnet is identical to those in the ring, physically isolated to be easily accessible, and electrically connected in series with them to generate the same field at any given time. An acquisition chain contains the electronics required to process the sensor data and transmit it to the users. A functional layout of a B-train system is depicted in Figure 1.3. A fixed induction coil provides a voltage, V_c proportional to the field rate of change, which is integrated to obtain the field. The constant of the integration is provided by an additional local sensor (field marker), which provides a trigger signal, t_k when a preset magnetic field value B_m is reached. The B-train is designed to provide the average field $\bar{B}(t)$ over all the bending magnets in the ring:

$$\bar{B}(t) = B_m - \frac{1}{A_c} \int_{t_k}^t V_c(\tau) d\tau, \quad (1.7)$$

where $k = 1, 2, \dots, n$ refers to multiple field markers and A_c is the effective area of the induction coil.

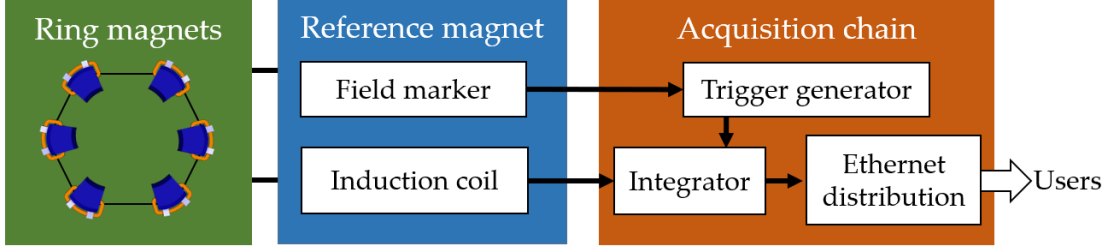


Figure 1.3: Functional drawing of a B-train system showing the ring magnets connected to the reference magnet housing the sensors, as well as the electronic acquisition chain.

On the other hand, magnetic field models obtained from simulations or previous magnetic measurements present a substitute for the magnetic field assessment in synchrotrons. Such models are used in synchrotrons where a reference magnet is not available for real-time measurement. A magnetic field model can also run in parallel with a real-time B-train system, where it can help calibrate the system or else act as a backup. Alternatively, at the Large Electron-Positron Collider (LEP) [10] and the LHC, an off-line approach is implemented [9]. Look-up tables are pre-generated in these cases and used to derive the excitation current required to power the magnets. In particular, a semi-empirical model based on a large database of test results was developed for the LHC [11], which generates the look-up tables as well as a description of the dynamic behaviour of multipole field errors.

The estimated field obtained by either of the forementioned methods is fed back to the RF system, where it is used to compute the revolution frequency f according to the following relation [12]:

$$f = \frac{c}{2\pi r} \frac{1}{\sqrt{1 + \left(\frac{m_0 c}{Brq}\right)^2}} \quad (1.8)$$

where c is the speed of light, r is the average nominal beam radius and m_0 is the rest mass of the particle in the synchrotron.

1.2 | The Antimatter Factory

The Antimatter Factory located at the European Organisation for Nuclear Research (CERN) is the primary factory for creating the most expensive atoms, by weight, worldwide. In fact, it is one of the few places in the world where antiatoms are created daily. Antiatoms are notably difficult test subjects. Having the same mass but opposite charge to ordinary atoms, they annihilate in a flash of energy when combining with normal matter, which makes up everything around us [13]. Hence, antiatoms must be carefully manufactured and trapped for each test. Moving and trapping antiprotons or positrons (antielectrons) is easy because they are charged particles. But the most common element used in antimatter experiments is neutral antihydrogen, produced by combining the two. It is far more difficult to capture, so a specific trap which considers that the element is slightly magnetic is used. Another difficulty in making antimatter is that the particles can only exist for a short amount of time before disappearing. Despite the challenges, the scientific output from these experiments is anticipated to be cutting-edge. Ordinary matter and antimatter are predicted to behave identically, responding identically to gravity, for example. However, in the universe around us, it can be noted that more matter exists than antimatter [14], which contradicts what we know so far about antimatter. Any asymmetry noted between the two types of matter could be an indicator of new unknown forces, beyond those defined by the standard model and Einstein's general relativity [15].

The Antimatter Factory produces low-energy antiprotons for antimatter studies by slowing down these particles using two decelerators: the Antiproton Decelerator (AD) [16] and the Extra Low ENergy Antiproton (ELENA) ring [17]. This complex supplies antiprotons to six different experiments. In particular, the Antihydrogen Laser PHysics Apparatus (ALPHA) [18], Atomic Spectroscopy And Collisions Using Slow Antiprotons (ASACUSA) [19], Baryon Antibaryon Symmetry Experiment (BASE) [20] and Antihydrogen Trap (ATRAP) [21] experiments use different techniques to study antihydrogen atoms and their properties. The two other experiments, Antihydrogen Experiment: Gravity, Interferometry, Spectroscopy (AEGIS) [22] and Gravitational Behaviour of Antihydrogen at Rest (GBAR) [23] investigate the behaviour of antihydrogen atoms under the effect of gravity.

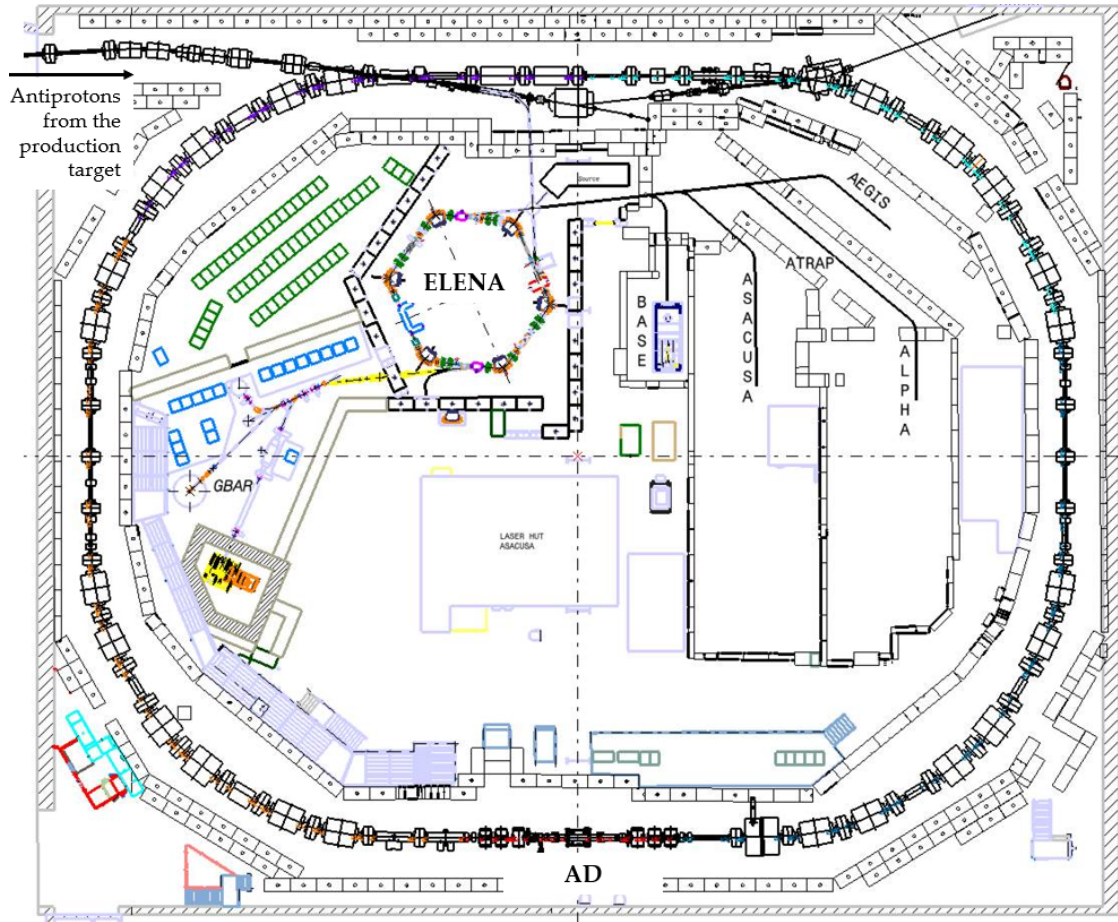


Figure 1.4: Schematic diagram of the Antimatter Factory and the placement of experimental installations [24]. Antiprotons from the production target are injected into the AD, decelerated and slowed down further in the ELENA ring before being transported by magnetic beamlines to the six experiments.

A schematic diagram of the Antimatter Factory complex is illustrated in Figure 1.4. Antiprotons are created from a proton beam coming from the Proton Synchrotron (PS) that is fired into a block of iridium. At this stage, the antiprotons produced have too much energy to be used to make antiatoms, and they are moving randomly in all directions. The first decelerator, the AD, slows down these particles to an energy of 5.3 MeV¹. A technique known as electron cooling is used to reduce the spread of energy of the antiprotons and their deviation from the central path.

Once the antiprotons are slowed down, they are ready to be ejected into the second decelerator. The ELENA ring is a new deceleration ring being commissioned at CERN's Antimatter Factory. The small 30.4 m circumference synchrotron further slows down antiprotons from the AD from 5.3 MeV down

¹In particle physics, the energy is expressed in eV (electron-volts) where 1 eV is the energy gained, or lost, by an electron when traversing across an electric potential of 1 V.

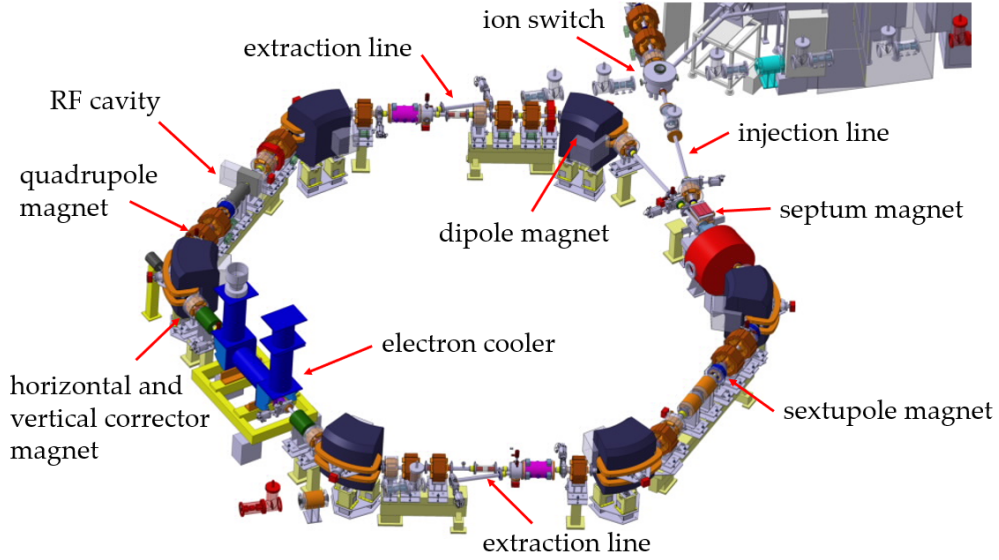


Figure 1.5: A schematic of the layout of the ELENA ring and its components [24].

to 100 keV. Decreasing the energies to this level, and making use of an electron cooler to reduce beam emittance, is expected to allow the existing ATRAP, ALPHA, and AEGIS experiments to capture around 100 times more particles in traps, compared to directly using the 5.3 MeV AD beam. Considerable improvements in the atomic spectroscopy and collision experiments of ASACUSA are expected as well [25]. A new beamline was constructed for GBAR, the newest collaboration in the complex to receive antiprotons directly from the ELENA ring.

The ELENA machine uses an RF cavity to decelerate the antiprotons, providing an RF voltage over a frequency range between 144 kHz and 2 MHz [26]. Since antiprotons present several challenges to produce and they need to be distributed amongst six experiments, progress in the commissioning of the ELENA ring is also made using H^- ions and protons coming from a local source. Moreover, ELENA includes a system dealing with cycle generation, timing and synchronisation that allows interleaved machine cycles, permitting simultaneous machine studies [27]. A schematic of the layout of the machine is shown in Figure 1.5. The ring includes six C-shaped dipole magnets, with a bending angle θ , of 60° , and a bending radius r of 0.927 m [17]. An additional magnet is used as a reference for the B-train system, whilst a spare magnet is used for tests in a measurement laboratory.

Commissioning of the ELENA ring started in November 2016 and culminated in August 2017 with the first antiproton beam circulating in the ring. Figure 1.6

shows the mechanically finished ring with the majority of its main components at the start of first beam. Commissioning of the ring continued until the end of 2018, and is expected to restart after CERN's long shutdown in 2021. GBAR was the first experiment to receive antiprotons from the ELENA.

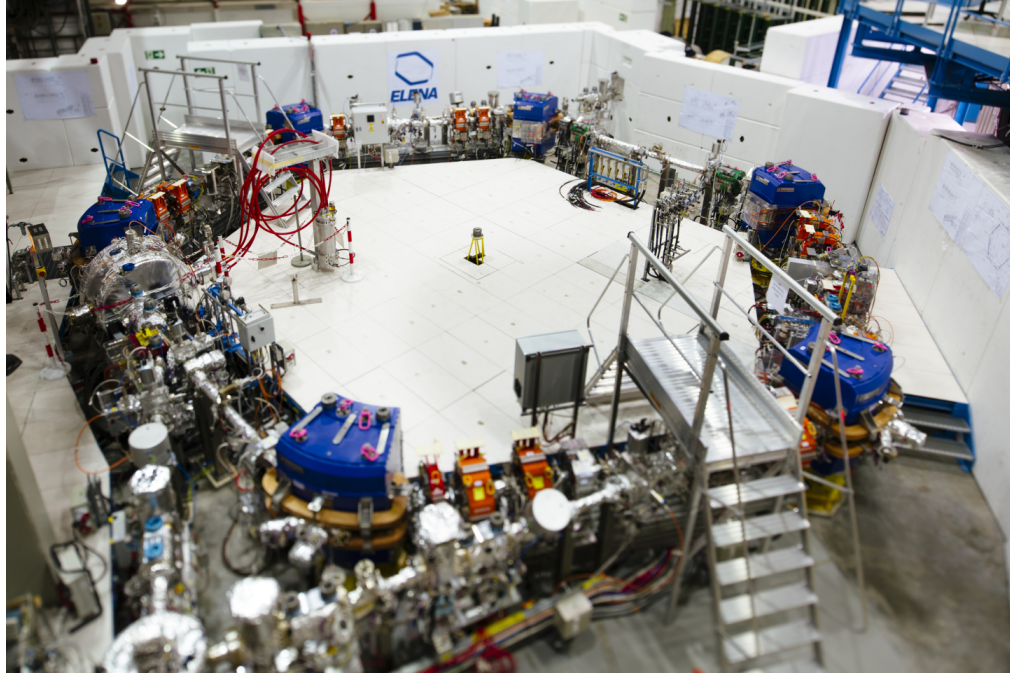


Figure 1.6: The ELENA ring during the commissioning period [28].

1.3 | Project description and objectives

The Field In REal-time Streaming from Online Reference Magnets (FIRESTORM) project is a CERN-wide consolidation project of the B-train systems for the PS, Proton Synchrotron Booster (PSB), Super Proton Synchrotron (SPS), Low Energy Ion Ring (LEIR) and AD, as well as the installation of a new B-train for the ELENA ring. Each system includes a field simulation facility, which can be used to tune the instrument after each restart and, under certain circumstances, to replace the B-train measurement.

The main reason for changing the previous systems is due to ageing electronic components, with spare components becoming limited or obsolete. Also, the failure to meet the required precision under certain conditions motivates the need for improved measurement techniques [29]. As a result, a common and renovated B-train system was proposed to be deployed progressively across the six machines. In particular, the main design features include:

- Uniform electronics across all machines, which results in improved maintainability. This also includes improved remote diagnostics capabilities.
- Using CERN-standard components such as Linux Front Ends, Front End Software Architecture (FESA) C++ software, FPGA Mezzanine Cards (FMCs) and White Rabbit serial distribution [30].
- Serial distribution over optical fibre (White Rabbit) with a bandwidth up to 1 MHz and a maximum latency up to 20 μ s.
- Using magnetic field sensors found industrially such as Nuclear Magnetic Resonance (NMR) probes and signal processing units.

This consolidation project is expected to reach its peak in 2021, when the synchrotrons at CERN will restart after upgrades. In the machines where a B-train already exists, the setup and configuration of the instrument is expected to transition from the older (legacy) system by having the two systems running in parallel over a trial period. However, in the case of the ELENA, both the magnets and measurement system are yet to be characterised, as this is the ring's first magnetic field measurement system. Even though a uniform system exists for all machines, each machine requires a different sensor configuration, calibration methods, performance evaluation techniques and simulation facility based on the synchrotron's beam characteristics.

The aim of this thesis is to develop and optimise the B-train system for the ELENA ring, contributing to both the measured and simulation facilities that it offers. To achieve this goal, the following specific objectives have been set:

- **To characterise the B-train system and formulate a magnetic measurement model.** The model infers the average field in the ring magnets based on the measurement of the reference magnet. This involves understanding the behaviour of the ring and reference magnets, electronics, and sensors within the reference magnet. An upgraded measurement model to Equation 1.7 is proposed, as well as a rigorous uncertainty analysis that sheds light on potential improvements to the B-train.

- **To validate the performance of the ELENA B-train in operation and confirm a measurement reproducibility and accuracy target of 2 units².** The behaviour of the measurement system is investigated in different operating conditions. This involves the characterisation of random errors created by the measurement, as well as systematic errors and their calibration with beam measurements.
- **To optimise the position of the field marker sensors.** An experimental search for the optimal position within the ELENA dipole magnet is carried out. A performance comparison analysis between the original and proposed sensor setup is performed to investigate the feasibility of implementing this idea in the ELENA B-train system.
- **To develop a model for magnetic field prediction in the ELENA ring.** Following dynamic measurements of the magnet, an analytical model is proposed which can perform within the 2 units accuracy target.

In this work, two types of measurements are performed in different environments:

- Off-line measurements performed on a spare magnet test bench in a measurements laboratory. In this case, measurements are acquired using a data acquisition box and the data is processed at a later stage.
- On-line measurements are B-train measurements obtained during the commissioning and operation of the instrument.

The project's motivations with respect to the current state-of-the-art are summarised in Table 1.1. The novelty developed in this work lies in the development and application of a rigorous measurement model, including a new field marker calibration method and validation technique. Another novelty in this work is the investigation of the field marker sensor position within the magnet, proving potential improvements in the magnetic field measurement accuracy. Finally, a magnetic field model is presented, which improves on the current state-of-the-art facilities for dynamic hysteresis prediction in synchrotrons.

²The unit used for relative measurement accuracy or reproducibility in this thesis is 1 unit = 1×10^{-4} = 100 parts per million (ppm).

Table 1.1: Summary of the state-of-the-art and motivation behind this work

Current state-of-the-art	Motivation and research gap
-Synchrotron field measurement systems are used in high-energy accelerators with very short cycle times.	-The commissioning of a field measurement system operating in very low fields and long cycle times.
-B-train measurement models require careful trial-and-error systematic error compensation using a beam calibration method.	-Upgrading the measurement model with a focus on providing an absolute measurement without the requirement for a beam calibration method.
-Field markers are historically positioned in the centre of the reference magnet gap wherever possible.	-Finding an optimal field marker position which provides a more reproducible performance.
-Real-time magnetic field measurement is preferred over the use of models due to hysteresis and dynamic effects.	-Development of a hysteresis model operating as a backup to the measurement that can model high-hysteresis, low-saturation and strong eddy current effects.

1.4 | Structure of the thesis

This work is divided into the following chapters in order to help the reader understand the work done, and how this contributes to the operation of the ELENA B-train.

An overview of synchrotrons and the role of magnets in these machines is provided in Chapter 1. The two different approaches to assess the magnetic field in synchrotrons are discussed, where B-train systems are introduced as an efficient mechanism for estimating the magnetic field in real-time, thus ensuring the proper functionality of synchrotrons. The ELENA ring is introduced as a new decelerator at CERN and its basic components are briefly described. The goal of this project is to commission and validate a B-train system for the ELENA ring as part of CERN's FIRESTORM project. This project is defined together with the expected project objectives.

The techniques used in evaluating the magnetic field in a synchrotron are reviewed in detail in Chapter 2. Different measurement techniques used in B-train systems are discussed, as well as the application of these systems in various synchrotrons. The challenges in magnetic field evaluation are highlighted, and the state-of-the-art hysteresis modelling techniques that have been applied to synchrotrons over the years are compared. A description of the FIRESTORM architecture is then provided, including detail on each

module making up an acquisition chain. This is followed by more details on the operating conditions and the performance specifications for the ELENA B-train. Following a literature review and identification of the research gap, the motivation behind this work is presented.

Subsequently, Chapter 3 presents a magnetic measurement model for B-train systems, including the characterisation procedures undergone in the case of the ELENA ring. Measurements performed during the ELENA commissioning period are described and discussed. This chapter also presents an uncertainty estimation, highlighting the main error sources in the measurement procedure.

The performance of the characterised system is evaluated in Chapter 4. This consists of three performance-related exercises carried out throughout the commissioning stage of the ELENA. The metrological performance of NMR field markers for the ELENA is evaluated, followed by a reliability run of the instrument, as well as a beam calibration which determines the accuracy of the commissioned instrument.

Chapter 5 presents innovative measurements performed in an experimental search for an optimal position for field markers within the magnet gap. Measurements at different dynamic conditions are also presented and discussed. Finally, the feasibility of changing the position of the field marker sensors for the ELENA B-train is investigated.

This is followed by Chapter 6, which presents two magnetic field models. The first model is based on off-line measurements of the ELENA dipole magnet, focusing on the decomposition of the field in the gap of the magnet using polynomial equations and machine learning methods. The second hysteresis model is a Preisach-Recurrent Neural Network, which can model both major and minor loop hysteresis for material science applications.

Finally, Chapter 7 summarises the achievements of this work, providing some concluding remarks and suggestions for possible future work. An appendix is included as an addendum to this study. This delves deeper into the comparison of the performance of two possible sensors that could be used as part of the ELENA B-train setup.

Chapter 2

Literature Review: Magnetic Field Evaluation Methods

2.1 | Introduction

Chapter 1 defined two different on-line methods used to evaluate the magnetic field in synchrotrons: B-train systems and magnetic field models. This chapter gives more details on the magnetic field behaviour in synchrotrons, as well as a review of the two field evaluation methods. A short background and literature review of different measurement techniques used in off-line and on-line measurements of dipole magnets is presented. This is followed by a review of the setup and commissioning procedure of B-train systems in different machines, as well as a review of different hysteresis modelling techniques. The FIRESTORM project is subsequently introduced, as well as the proposed B-train architecture for the ELENA ring. In conclusion, the motivations behind this thesis are presented, in relation to the development of the research field.

2.2 | Magnetic field effects

A magnet's yoke guides and concentrates the magnetic flux in the gap of the magnet. The ferromagnetic properties of materials used in the cores of synchrotron magnets are dependent on a number of factors such as composition, thermal and mechanical history, and dynamic effects. This section discusses the two main effects that characterise synchrotron magnets when a beam of particles is circulated in the vacuum chamber.

2.2.1 | Hysteresis

Ferromagnetic materials consist of many small regions called domains, in which all the magnetic dipoles are aligned in a parallel manner. When the material is in a demagnetised state, the directions in which the domains are magnetised are either randomly distributed, or in a way such that the resultant magnetisation of the specimen is zero [31]. When an external magnetic field is applied to the material, the domains are forced to orient in the same direction. The energy lost during the transition of domains between magnetic states leads to the effect of hysteresis.

Figure 2.1 shows the $B - H$ relationship of basic types of hysteresis curves, with H_{\max} and B_{\max} referring to the maximum applied field intensity and flux density respectively. Magnetising a ferromagnetic material, first with a monotonous increasing field, and after an arrival to the saturation state with a monotonous decreasing field, the magnetisation does not come back along the original curve. The first increase in field intensity results in the initial magnetisation curve, and going back to a current of zero, the residual amount of magnetic flux density B_{res} is termed as the residual flux.

In order to erase this residual flux, a current in the opposite polarity is applied until the coercive magnetising force, H_c is reached. This process in ferromagnetic magnets is called *degaussing* [32] and is carried out by applying a series of triangular waves with the amplitude decreasing by a fraction at every maximum point, as demonstrated in Figure 2.2. The maximum value of this signal should at least be higher than any current applied to the material [33]. Due to the fact that most synchrotrons operate using a unipolar power supply, such a procedure may not be possible everywhere, leading to alternative solutions such as avoiding ramping down to zero current but to a

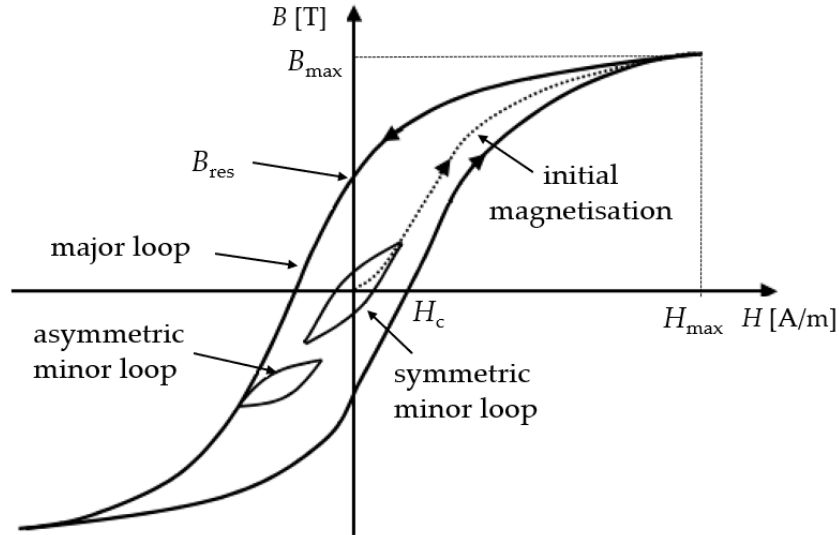


Figure 2.1: Diagram showing the major and minor hysteresis loops of a ferromagnetic material.

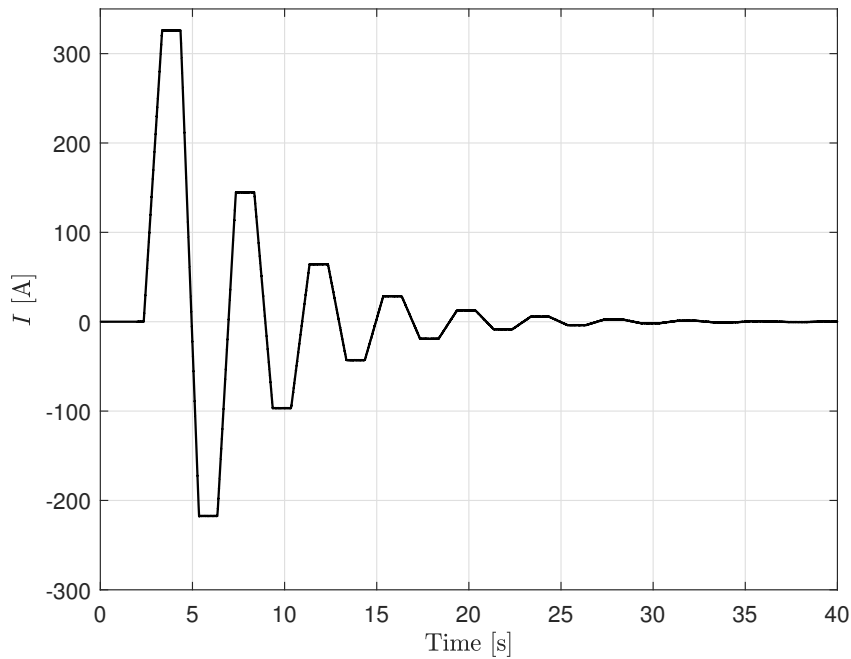


Figure 2.2: An example of a degaussing cycle that is applied to a magnet to erase the residual field.

low current value [34]. The conventional hysteresis loop is a major loop, where the saturation magnetisation of the material is reached. In most applications, however, saturation is never reached. After the material is demagnetised, when cycling symmetrically between $\pm H_{\max}$, the flux density exhibited is categorised as a symmetric minor loop.

In synchrotrons, the dipole magnetic field is produced using either iron-dominated magnets or superconducting magnets, the latter in the case fields beyond 2 T are desired [6]. A dipole field is generated in the gap of the magnet by an electric current I in current carrying coils surrounding the magnet poles. A ferromagnetic yoke surrounds the coils, providing a return path for the magnetic flux. In a typical synchrotron operational cycle, the current increases monotonously up to a pre-defined maximum value with a possible pause on the ramp-up or ramp-down, and then goes back down to the minimum value. Hence, the excitation current keeps the same sign, in the first quadrant of the hysteresis loop, and saturation is rarely reached. This is referred to as an asymmetric minor loop.

Starting the magnetisation process from a demagnetised state, during the first few cycles the hysteresis loop will not be closed. This shows the presence of a transient state between the initial magnetisation curve and a stable state when applying the same excitation cycle repeatedly. This stage of stabilisation of minor loops is called *accommodation* [35, 36], and the cycles performed in this transient period are referred to in the synchrotron context as *pre-cycles*. The number of these pre-cycles is usually determined by experimental measurement of the field reproducibility at a specific point in the cycle. Minimum pre-cycle time is important as pre-cycles which are too long reduce the time available for beam experiments. Bottura *et al.* [37] propose four pre-cycles to stabilise the magnetic field in resistive magnets.

2.2.2 | Eddy currents

In synchrotrons, magnetic cycles consist of dynamic changes, with the current changing linearly with time to ramp-up to a magnetic field level, and then ramping down again to the original field level. Faraday's law states that a voltage is induced in a conductor loop, if it is subjected to a magnetic flux which varies with time. According to the law:

$$\nabla \times \mathbf{E} = -\frac{\partial \mathbf{B}}{\partial t}, \quad (2.1)$$

where an electric field \mathbf{E} is generated, which in conductive materials is related proportionally to the current density \mathbf{J} :

$$\mathbf{J} = \sigma \mathbf{E}, \quad (2.2)$$

with σ representing the material's conductivity [38]. The induced current forms around the magnetic field lines in a circular manner and stands perpendicular to them. Eddy currents are induced in the laminations, magnet coil and in the vacuum chamber of a synchrotron magnet [39]. They reduce the magnetic field by inducing themselves a magnetic field in the opposite direction according to Lenz's law.

Problems with measuring dynamic magnetic fields come about due to eddy currents. One of the effects of the magnetic field created by eddy currents includes the impairment of the field quality in the magnet's good field region. Another effect is that it delays the achievement of the nominal DC field, where one must wait for the eddy current to decay before one can reach a stable situation for injecting or extracting the particles. In the cases of fast changing magnetic fields, the resulting Lorentz force must be kept in mind as it might lead to stresses in the material [40].

In order to minimise these effects, measures are taken during a magnet's design stage by using insulated lamination sheets. Eddy current effects depend on multiple factors such as the magnetic properties of the iron yoke, temperature and mechanical tolerances that lead to undesired air gaps in the magnetic circuit [41]. Hence, these effects are hard to predict and experimental measurements need to be performed to characterise this behaviour [42]. This effect is measured by evaluating the time constants of the different eddy current circuits that are expected in the magnet. These include the pole eddy currents, end plate eddy currents as well as eddy currents in individual laminations [43].

2.3 | Magnetic measurement techniques

Numerous proven measurement techniques and equipment are readily available for measurement tasks related to normal-conducting magnets. It is hence prudent to investigate existing possibilities carefully before considering the development of a more unfamiliar measurement method. This section will review the most common techniques used in the measurement of synchrotron magnets, both in off-line environments, as well as in real-time B-train measurements.

2.3.1 | Induction coils

Induction coils are a collection of sensors composed of a number of loops of conducting wire, subjected to a magnetic field B , generating a voltage V_c , as described by Faraday's law of induction in Equation 2.3. The coil voltage is given by the rate of change of the magnetic flux Φ , where the negative sign indicates that the induced voltage generates a current that leads to a field which opposes the flux variation with time [44]. For a loop with a surface S :

$$V_c = -\frac{d\Phi}{dt} = -\frac{d}{dt} \int_S \mathbf{B} \cdot d\mathbf{S}, \quad (2.3)$$

where $d\mathbf{S}$ is the normal to the surface. A voltage can be induced in the coil either by varying the magnetic field, or by changing the orientation of the coil. In the case of a constant magnetic field, the coil's orientation or position is changed [45]. In a dynamic magnetic field, such as in B-train systems, the coil is kept static, and the coil provides a measurement of the flux change ($\Delta\Phi$) between two time markers (t_{start} and t_{end}). The average value of the field over the coil's area can be calculated from either the instantaneous or voltage integral with time:

$$\Delta\Phi = \Phi_{end} - \Phi_{start} = -\int_{t_{start}}^{t_{end}} V_c d\tau. \quad (2.4)$$

Performing integrals on measurements brings the advantage that unwanted high-frequency noise components are filtered [44]. Another benefit of this method is the flexibility in the design of the instrument so that it fits the requirements of a measurement. It can be made small for point measurements, or very long in the beam path direction so that the integral field along the gap can be measured. An induction coil is a linear device and its sensitivity can be designed according to the field to be measured. In practice, the application of the induction method is restricted to field levels above $0.1 \mu\text{T}$, with no specific limitation at the upper end.

The main limitation in fixed coil measurements is the small voltage offset generated by parasitic currents in the electronics or thermal voltages. An input voltage offset results in a visible field drift when integrated, that often cannot be distinguished from the physical field change [46]. When the measurement is longer than a few seconds, this phenomenon becomes significant, and hence

the voltage offset must be removed before the integration occurs.

The quantity of interest in magnetic field measurements for synchrotrons is the integral field $\mathbb{I}(t)$, which can be defined as:

$$\mathbb{I}(t) = \int_{-\infty}^{\infty} B(t, s) ds, \quad (2.5)$$

where $B(t, s)$ is the magnet's field profile as a function of time and s is the longitudinal co-ordinate. The magnetic flux linked through an induction coil within the magnet's gap is used to derive $\mathbb{I}(t)$. Considering that the field variation in the direction transverse to each coil is negligible, the flux at any given time for N_T winding turns is [44]:

$$\Phi(t) = N_T \int_{-\infty}^{\infty} w(s) B(t, s) ds = w_{\text{eff}}(t) \int_{-\infty}^{\infty} B(t, s) ds, \quad (2.6)$$

where $w(s)$ is the winding width, which varies along the coil because of manufacturing tolerances, and w_{eff} is the effective width, represented by:

$$w_{\text{eff}}(t) = \frac{\Phi(t)}{\mathbb{I}(t)} = \frac{N_T \int_{-\infty}^{\infty} w(s) B(t, s) ds}{\int_{-\infty}^{\infty} B(t, s) ds}. \quad (2.7)$$

The effective width expresses the average geometric coil width, weighted by the field profile. Hence it is dependent upon the specific magnet being measured, where the same $B(s)$ is expected for both calibration and normal measurements. This parameter is crucial in B-train measurements as it defines the relationship between the measured flux and the desired integral field measurement.

2.3.2 | Magnetic resonance sensors

The magnetic resonance phenomenon is based on the change of the spin state of the nuclei or electrons in the presence of an external field B_0 . The resonance, i.e., the jump between the two spin states, happens when an excitation RF signal with frequency f_0 , having a magnetic component perpendicular to B_0 corresponding to the difference between the energy of the two states is fed to the sample:

$$f_0 = \frac{\gamma}{2\pi} B_0, \quad (2.8)$$

where γ is referred to as the gyromagnetic ratio. Nuclear Magnetic Resonance (NMR) is a standard for field sensors, providing the best accuracy for a vast magnetic field range [47], with $\gamma/2\pi = 42.576$ MHz/T [48]. The

commercial NMR equipment is designed to operate by sweeping the frequency and locking when a resonance curve occurs. In the application of these sensors in marker mode, the NMR probe is excited at a predefined frequency by an RF signal generator. The NMR signal in Figure 2.3 is produced, where the minimum peak indicates the presence of the applied resonant frequency. The main constraint of NMR field markers is that they cannot be used for fields lower than 43 mT, as the field needs to be strong for the spin-flip energy gap to rise well above the thermal noise [49]. Hence at lower fields, the signal-to-noise ratio and the width of the resonance signal are diminished. The performance deteriorates as well in inhomogeneous fields since the spin in different probe regions resonates at varying times. In the event of high space gradients, the system cannot lock the resonant frequency and a compensation coil has to be added [50].

In circumstances where a field lower than 43 mT is needed, Electron Spin Resonance (ESR) sensors can be used. The FerriMagnetic Resonance (FMR) sensor makes use of the ESR phenomenon, based on the difference between the energy emitted and absorbed by electrons switching between opposite spin states. A FerriMagnetic Resonance (FMR) sensor composed of a band-pass Yttrium Iron Garnet (YIG) filter operates with $\gamma/2\pi = 28.02$ GHz/T [51], generating a resonant signal as shown in Figure 2.3. Due to small probe sizes and comparatively low Q-values, considerable field gradients can be

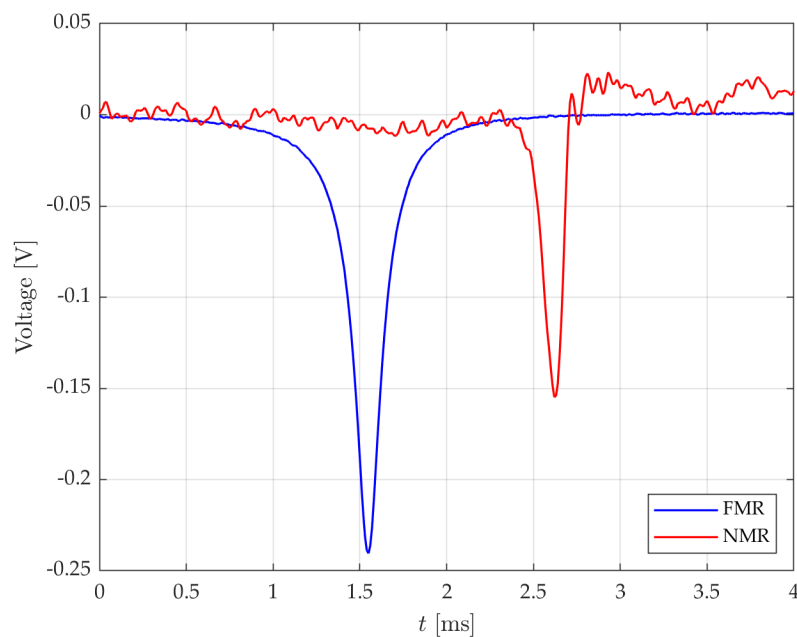


Figure 2.3: NMR and FMR resonant signals at 0.2 T.

tolerated [52]. In addition, FMR markers are compatible with commercially available NMR teslameters and hence FMR probes can be interchanged with NMR probes quite easily. On the contrary, an FMR resonant signal has a broad resonance peak (making it more difficult to detect the peak), and is temperature-dependent as it has to be optimised for each specific application.

Several studies [51–55] investigate the application of magnetic resonance probes as field markers for synchrotrons. NMR field markers applied in combination with an induction coil measurement have already been applied to the high precision field measurement of the SPS, operating a cycle with plateaus at 60 mT and 2 T, but these are not used anymore [47]. However, NMR field markers are still operational in the PSB. Beaumont [53] investigates the performance of both NMR and FMR field markers implemented in the PS ring, where a reproducibility of 5 μT and 12 μT respectively is reported when a combined-function magnet is operated at different field levels. It also confirms that in the case of NMR sensors, as the ramping rate is decreased, the reproducibility improves, with the best performance observed at 25.6 mT/s. In the case of FMR sensors, the effect of the ramp rate, gradient and temperature has been found to match the specifications for their application as field markers, with the biggest limitation being a stable support [54]. This demonstrates that in contrary to NMR sensors, FMR sensors perform well in high field gradients, and in fact, they are used in the LEIR where the magnets exhibit relatively high field gradients [56].

2.3.3 | Hall generator

The Hall generator provides an instant point measurement of the field, using simple equipment and a compact probe. Considering a block such as in Figure 2.4, a voltage V_H is developed when a current passes through the conducting material located in a magnetic field:

$$V_H = \frac{IBR_H}{d} \quad (2.9)$$

where d is the block's thickness and R_H is the Hall coefficient of the material used. When a magnetic field is present, charge carriers experience the Lorentz force, accumulating on one face of the material, leaving an opposite charge on the other face. This results in a voltage proportional to the field. Since Hall generators are sensitive only to the magnetic field component perpendicular to

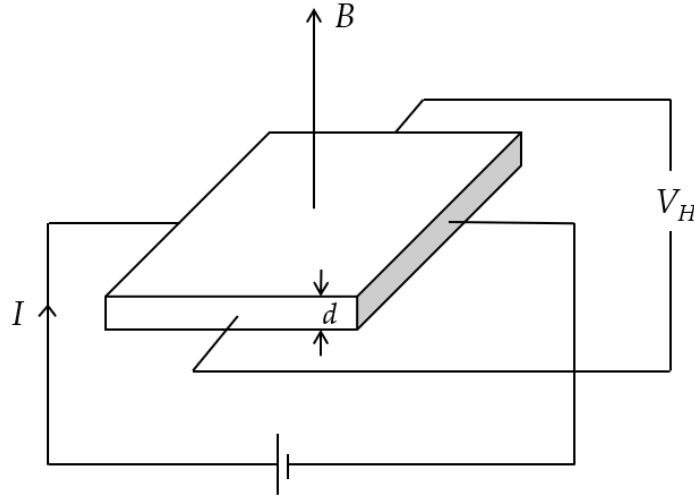


Figure 2.4: Hall generator principle, where a voltage proportional to the field is created across the length of a material.

its plane, they can additionally be used to determine the flux density direction.

Hall generators are normally mounted on a probe and referred to as Hall probes. There are two main types of Hall probes used in magnetic measurement applications. Uni-planar Hall probes are able to measure fields in one direction: transversal or axial. These sensors are sensitive to the field component perpendicular to the device surface. The second type of Hall probes are made of two or three-axis devices, consisting of plates that are oriented in different directions.

The benefit of this sensor is that it is possible to make a cheap instrument with the mT range to a few Ts with an accuracy of 1000 ppm, which can be improved at the expense of the measurement speed [57]. Using precision voltmeters, accurate voltage measurements are possible in the μV range, providing a resolution better than $0.1 \mu\text{T}$. The most significant factor which affects the instrument's accuracy is the variation of temperature. R_H has a temperature dependency that can be of the order of 100 to 1000 ppm/ $^{\circ}\text{C}$. Magnetic field gradients can also have an effect on the Hall voltage due to the finite size of the probe, and hence this limits the measurement of inhomogeneous fields [58].

2.3.4 | Fluxgate magnetometer

A fluxgate magnetometer consists of three coils wound around a thin and linear ferromagnetic core as shown in Figure 2.5. The sinusoidal current in the modulating coil produces a magnetic field beyond the saturation field of the material, whilst the detection coil picks up the voltage and generates an error signal proportional to the field. The bias coil maintains zero field in the material, improving the linearity of the instrument. This is done based on the error signal from the detection coil. Once the error signal is zero, the measured field is equal and opposite to the field generated by the bias coil. Commercially, fluxgate magnetometers can be found with an upper limit of the order of a few tens of mT and a resolution of 1 nT [57]. With the ability to measure at such low ranges, this makes fluxgate magnetometers popular in the measurement of fringe and background magnetic fields.

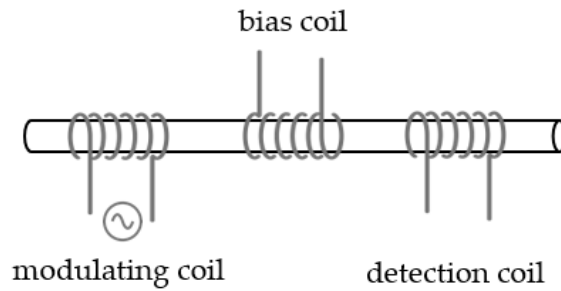


Figure 2.5: Fluxgate magnetometer composed of a modulating coil, a bias coil and a detection coil.

A basic version of the fluxgate concept is known as *peaking strip* [51], adapted to generate trigger signals when the external field exceeds a threshold value, hence causing the magnetisation to flip. The biggest advantage of applying this sensor is the compatibility with field gradients, improved as its size is reduced. Nonetheless, the dissipated heat in the bias coil makes it unsuitable for operation above a few mT [59]. It can provide a point measurement of magnetic fields with an accuracy of 100 ppm or better, limited by the error in the value attributed to the bias coil [58]. Both inhomogeneous and uniform fields can be measured with fine peaking strips. These sensors have been used as field markers in the PS since its commissioning, but were eventually replaced, as they require very specialised manual labour to build, as they need to be encased in a blow glass capsule to preserve the state of mechanical strain in the magnetic element.

In conclusion, this section has provided a quick overview of some of the most common measurement methods used in the synchrotron environment. The techniques described are complementary, and a well-chosen combination of multiple of these methods can definitely meet most requirements.

2.4 | B-train systems in other machines

B-train systems use a combination of integral and local magnetic field measurement techniques to estimate the dipole field, as shown in Equation 1.7. Induction coils are the primary sensors used for the integral field measurement. Any sensor capable of measuring absolute field values could be considered, in principle, to take the role of a field marker. Hall-effect sensors, peaking strips and magnetic resonance based sensors have been used successfully in the past. This section will review the sensor setups in machines other than the ELENA ring, measurement models and performance of several B-train systems implemented in particle physics research centres and hadron therapy centres.

2.4.1 | CERN

At CERN, five machines make use of B-train systems: the LEIR, the PSB, the PS [60], the Super Proton Synchrotron (SPS) and the AD, where in particular, the PSB, LEIR, SPS and PS form part of the LHC injector chain. These instruments have been in operation for several decades, however, despite their good track record, certain improvements such as an increase in resolution are necessary for long-term reliability.

The PS ring is composed of 100 combined-function magnets, having hyperbolically-shaped poles that include a quadrupole field component to the dipole component. The magnets consist of two halves where the slope of the poles is inverted, such that the quadrupole is focusing in one half and defocusing in the other half. An additional reference magnet is set aside to be used for the B-train system. The induction coils are placed in the centre of two blocks on the focusing side and on the defocusing side. The setup includes one FMR field marker at 48.5 mT on the focusing side and another FMR marker at 49.5 mT on the defocusing side, just below the injection field level. The minor difference between the two field marker levels is due to the different field configurations in the two halves of the magnet and is aimed at having the two digital triggers generated approximately at the same time. The two halves of

the magnet function as two independent magnets and the generated signals are fed in parallel to a single B-train acquisition chain, where the field values are averaged.

The PSB consists of four superimposed rings and an induction coil with an equivalent surface of 1.6 m^2 is placed in the centre of the third ring of a separate reference magnet. Metrolab's PT2025 teslameter [48] and NMR probes are used as part of the field marker setup. This B-train system consists of one field marker per unit, marking at a field level of 110.8 mT, i.e., slightly lower than the injection level. To date, the PSB B-train is using a prototype of the FIRESTORM system, and the new instrument will become operational as of 2021. In the SPS ring, an induction coil and NMR setup can be found in two reference magnets [61]. Field markers have not been used in the SPS since the 90's, but are set to be re-introduced [62].

In the LEIR, no separate reference magnet is available as the accelerator is composed of only four 90° bending dipoles. As a result, the induction coils and FMR markers are installed in the non-uniform, fringe-field region of an operational ring dipole magnet as shown in Figure 2.6. This means that maintenance or replacement of these sensors is extremely impractical. The LEIR B-train includes one field marker for each unit, set at a field level of 251.2 mT, and a short 0.6 m^2 induction coil. Similarly, the B-train system implemented in the AD uses a magnet from the ring, and the field marker is a NMR sensor, set at 330.7 mT. In this case, a field model is preferred over the measured B-train for RF stability due to field fluctuations on long plateaus [63].

In these cases, the instruments are characterised using a more detailed version of the measurement model in Equation 1.7:

$$\bar{B}(t) = \frac{g_1}{l^*} \left(B_m \ell_m + B_{\text{off}} - \frac{g_2}{w_{\text{eff}}} \int_{t_k}^t V_c(\tau) d\tau \right), \quad (2.10)$$

where g_1 and g_2 are scale parameters, B_{off} represent an offset error and

$$l^* = \frac{2\pi r}{N_B} \quad (2.11)$$

is the fraction of the circumference corresponding to each dipole magnet, where r is the ring's nominal bending radius and N_B is the number of dipole magnets [65]. The magnetic length parameter, ℓ_m is the ratio between integral

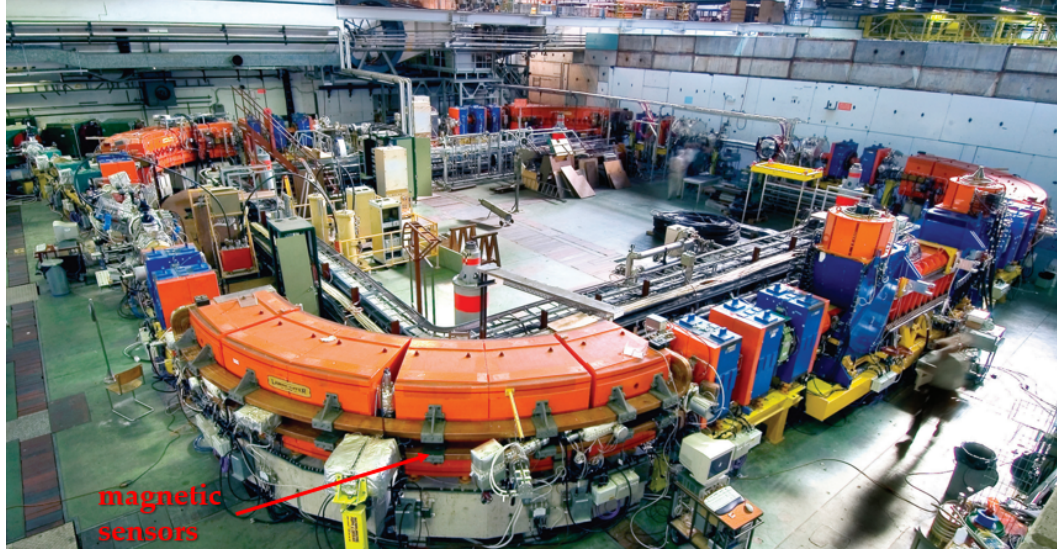


Figure 2.6: Sensors within the LEIR magnet installed on the mid-plane of the gap just outside the vacuum chamber [64].

and local field, and is used to infer the integral field based on the field marker point measurement. Parameters are initially set to their nominal value, with the calibration parameters g_1 and g_2 set to 1, and B_{off} set to zero. Once the beam in the machine is available, an *in-situ* calibration takes place, where the calibration parameters are calculated to correct any mismatches between the nominally calculated parameters and the actual parameters with the beam in place.

2.4.2 | Heidelberg-Ion Therapy Centre

The Heidelberg-Ion Therapy Centre (HIT) in Germany is a particle therapy centre with a synchrotron that accelerates proton and carbon ions to treat localised tumours in cancer patients. Knowledge of the magnetic field is crucial in this case as it is used to control the power supplies using a feedback approach. In this way, field errors caused by hysteresis and eddy current effects can be compensated. A B-train system with an induction coil and Hall probe is implemented on a ring magnet as shown in Figure 2.7. NMR probes could not be used as the field is inhomogeneous, and hence a Hall probe was optimised to work in the 50 - 200 mT range [66].

For optimal performance, a beam radial deviation within 1 mm is expected, which requires an accuracy of 2 units in the field measurement [67]. The field is measured in only one ring magnet, as it is shown that the difference between them is negligible. A precise integrator that compensates for drift and calibrates during the measurement is also applied [68]. The system is characterised by a

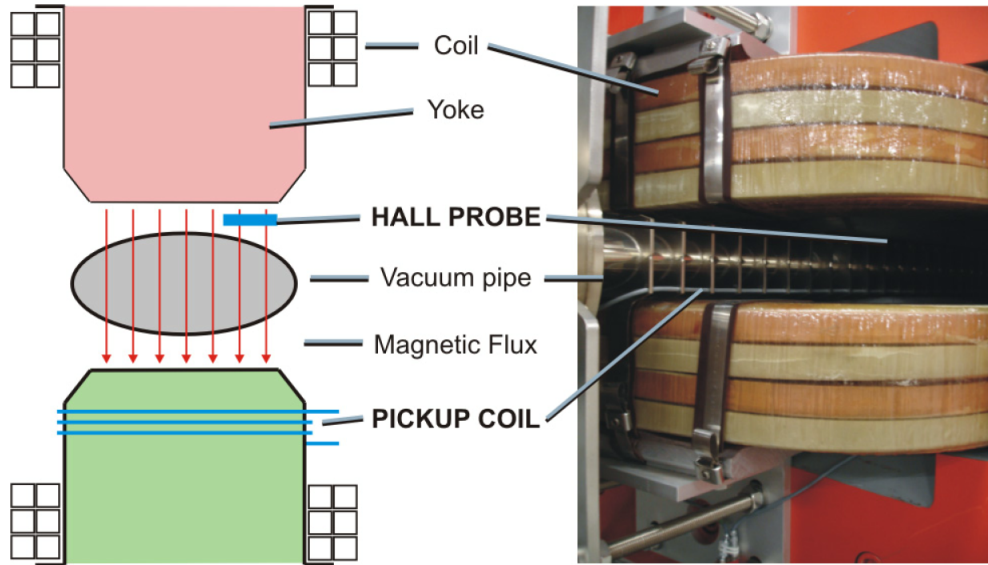


Figure 2.7: Sensors installed within the HIT bending dipole magnet [67].

measurement model that is similar to Equation 2.10, but applied for the integral magnetic field [67]:

$$\mathbb{I}(t) = g_1(V_H(t_k) - V_0) - g_2 \int_{t_k}^t V_c(\tau) d\tau \quad (2.12)$$

where $V_H(t_0) - V_0$ is the Hall voltage, corrected for offset errors, whilst g_1 and g_2 are scale factors associated with the two sensors. An *in-situ* calibration takes place when the beam is available to correct for errors resulting from fringing fields and non-linearities of the integrator. The advantage of an *in-situ* calibration is that it includes all effects caused by cables, power supplies, sensors and electronics [69].

2.4.3 | MedAustron

MedAustron, an Austrian centre focusing on ion therapy and research is based on a synchrotron composed of 16 dipole magnets generating fields from 90 mT to 1.5 T [70]. A separate dipole magnet placed outside the synchrotron is used as a reference magnet, enabling the precise measurement of the field without the disturbance of the particle beam [71].

The sensor setup consists of a curved printed circuit board coil array [70] as well as a NMR probe per unit with a PT2025 teslameter. The system allows distribution of the field at 300 kHz and is used for RF and power converter control. A simulated facility is also available, that can be used in parallel or

as a replacement [72]. The B-train system was developed in collaboration with CERN and hence benefits from a similar architecture and measurement model as described in Section 2.4.1.

2.4.4 | Italian Centre for Oncological Hadron therapy

The Italian Centre for Oncological Hadron therapy (CNAO) in Italy is a hadron therapy facility based on a synchrotron that can accelerate both protons and carbon ions. The field is measured in a separate dipole magnet connected in series with the 16 ring magnets and is then fed back to the power supply. It is also used to control the frequency of the RF cavity. A diagram of the control system is shown in Figure 2.8. A Field Programmable Gate Array (FPGA) generates control signals for the power supply and treats the digitised measured signals. The readings are translated into two digital bit signals B_{up} and B_{down} , corresponding to an increment and decrement of the field, respectively. This is fed to the power supply which calculates the output current to be sent to the magnets [73].

The field is obtained by integrating the induced voltage in a coil in the reference magnet. Both NMR and Hall probes were tested as field markers to obtain the absolute value of the field at the beginning of each cycle and during the highest plateau [73, 74]. However, the cycle-to-cycle stability of the system was not sufficient to reach the desired precision of $10 \mu\text{T}$, with oscillations up to 0.13 mT [75]. Hence, a method referred to as RF-master was adopted

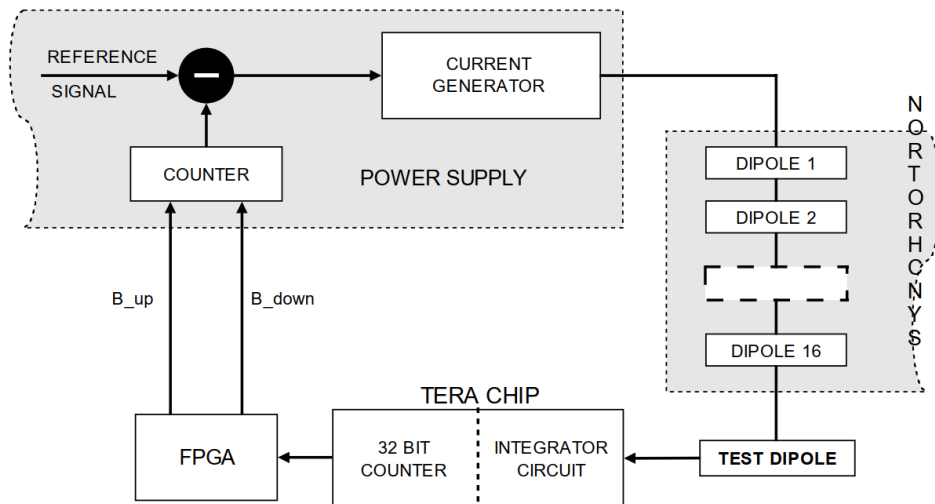


Figure 2.8: CNAO B-train system block diagram, including the power supply, magnet and acquisition control loop [73].

in 2018 that uses the RF cavity to calculate the absolute field level, based on the measurement of the beam position. This method works only when the beam is injected, and hence for initial operation, suitable parameters have to be adopted that are not too far off [76]. This method brings the advantage of reducing hardware, at the expense of additional functionality in the firmware.

2.4.5 | Alternating Gradient Synchrotron

Another magnetic field measurement system used in synchrotrons is found in Brookhaven National Laboratory's Alternating Gradient Synchrotron. A 'Gauss Clock' electronic system integrates the voltage from a coil within a reference magnet and outputs a pulse each time the integral field increases to a certain value. In this case no field marker is implemented, and the measurement is calibrated by measuring the momentum of the accelerating particles along with the clock pulses. The momentum is calculated based on measured values for the radius and frequency of the beam particles [77].

2.4.6 | Advanced Light Source

The Advanced Light Source (ALS) is an electron accelerator/storage ring situated at the Lawrence Berkeley Laboratory in the United States of America. In this case as well, real-time magnetic field tracking is provided using a Gauss Clock system. The sensor system consists of a peaking strip sensor set at 10 mT, as well as a coil that is wound around the pole of one of the 24-series connected dipole magnets [78]. The Gauss clock is used to trigger RF ramping and beam position monitors, and is calibrated based on the measured momentum of the beam.

2.5 | Hysteresis models

Besides the use of real-time magnetic field measurements for synchrotron field control, magnetic field models capable of characterising hysteresis, can also be implemented. In literature, there are numerous modelling techniques used to characterise hysteretic behaviour. This section reviews the most important models from a historical and practical point of view, with the focus being the dynamic property, as it is a crucial requirement for synchrotron field control. The different models considered in this work are classified in three main

categories: conventional mathematical formulations, Preisach models based on the use of operators to characterise hysteresis and physical models based on a mathematical representation of the material's behaviour. In the end, the current state-of-the-art in the synchrotron magnet spectrum is presented.

2.5.1 | Conventional mathematical formulations

The detailed modelling of hysteresis systems using the laws of physics has often resulted in models that are sometimes too complex to be used in practical applications involving system characterisation, identification, or control. For this reason, alternative models of these complex systems have been proposed that make use of conventional identification methods, that normally have no physical meaning. Hence, such models are mostly empirical, based on previously acquired experimental data. As a result, this makes them popular in practical applications such as circuit simulation.

2.5.1.1 | Differential models

Hysteresis models based on differential equations combine some physical understanding of the hysteresis system along with black-box modelling. Consequently, some researchers have termed these models *semi-physical* [79]. These models focus on the fact that the output varies its properties as the direction of the input is varied. The most popular differential-based model is the Duhem model [80]. Applications of this model range from control [81–84] to electron microscopy [85] and it was also extended to model rate-dependent hysteresis [85–87].

This model has been applied in various contexts under different names. One of the most popular variations is the one proposed by Coleman and Hodgdon [88], used mostly in describing piezo-electric actuator hysteresis [89–92], and extended to model dynamic effects [93, 94]. Another variation was proposed initially by Bouc early in 1971 [95] and subsequently generalised by Wen [96]. In the meantime, this model has become known as the Bouc-Wen model and has been applied in the current literature to represent mathematical components with hysteretic behaviours [97].

By choosing a set of parameters appropriately, it is possible to adapt the response of this model to various hysteresis loops [97–99]. To convert the Bouc-Wen model to be rate-dependent, this model characterises the static and

dynamic components separately, where the latter component is modelled using a linear Hammerstein model and is capable of modelling the rate-dependent hysteresis in a particularly low range frequency from 1 Hz to 100 Hz [100]. A survey by Hassani *et al.* [101] gives more details on the Duhem and Bouc-Wen models for the control of hysteresis in smart materials.

Another differential model that is able to model minor loops and rate-dependent behaviour is the Chua model [102]. The key concept of the Chua model is that the trajectory of flux density against the magnetic field is uniquely determined by the last point at which the time derivative of the flux density changes sign [103]. Other specialised variations of the Duhem model include the Madelung model [104], the Dahl friction model [105], the LuGre friction model [106], and the presliding friction model [107]. All the models highlighted are rate-independent and would require additional mechanisms to model dynamic effects.

2.5.1.2 | Non-linear system identification methods

This section considers the application of other common non-linear system identification methods for hysteresis modelling. Such techniques were not developed specifically for modelling hysteresis but have been applied to this domain by numerous researchers.

Artificial Neural Networks (ANNs) are models of computation, that are inspired from biological behaviours. An ANN consists of a series of nodes or units, and a set of connections associated with them, representing synapses in a biological neural network. Each neuron is associated with an activation function, which determines the output of that node by calculating a weighted sum of its input and adds a bias. The activation function does the non-linear transformation of the input, making it capable to learn and perform complex tasks. In general, an ANN consists of three different kinds of nodes, specifically the input, hidden and output nodes, organised in three separate layers. The connections between the nodes in each layer are referred to as weights. Traditionally, ANNs are widely applied to static problems, such as the classification and pattern recognition. Some examples are Multilayer Perceptrons (MLPs), radial basis function networks and convolutional neural networks. However, ANNs in a traditional approach, such as these three networks are not capable of representing temporal and dynamic situations [108]. Therefore, either

modifying the network or using several ANNs becomes the most natural choice. In fact, in [109], Hwang *et al.* employed two ANNs to describe the ascending and descending hysteresis loops, and Wu [110] *et al.* used multiple hidden layers when implementing a backpropagation neural network to describe rate-independent hysteresis. It can be noted though that these works are limited to simpler applications, such as single loop or first-order reverse curves.

Other types of neural networks use some form of memory to model hysteresis. This can be introduced in the neural network by means of time delays and/or through feedback [111]. Examples are the time delay neural network [108], which delays the input signal by a specified period, and the Elman network [112, 113] which consists of an additional context layer, which receives input from, and returns values to, the hidden layer. Another technique called Non-linear AutoRegressive with eXogenous inputs (NARX) uses both time delays and feedback units, and is hence capable of accommodating the dynamic, complex and non-linear nature of time series prediction problems [114]. Applications of this modelling technique are various and range in application. In [115], this model is used in the identification of robotic hysteresis, where the authors attribute the success of this model in its application to the use of previous output values. On the other hand, in [108], several variations of NARX models are proposed for monitoring hysteretic structural behaviour. Cheng *et al.* [101] employ two such sub-models, one to model hysteresis and another to model dynamic effects.

Considering other conventional system identification methods, Wei and Sun propose a model combining three major blocks: a gradient investigator which checks the polarity of the rate of change of the input, an extreme-value template, which is a shift register recording extreme inputs and corresponding outputs, and an output function determining an active polynomial function once an extreme input value is reached [116]. Other non-linear identification methods used in hysteresis modelling include finite impulse response (FIR) filters [117] and support vector regression [118].

2.5.2 | Preisach models

Amongst the variety of hysteresis models found in literature, the Preisach-type models prove to have great potential to explain various magnetisation processes,

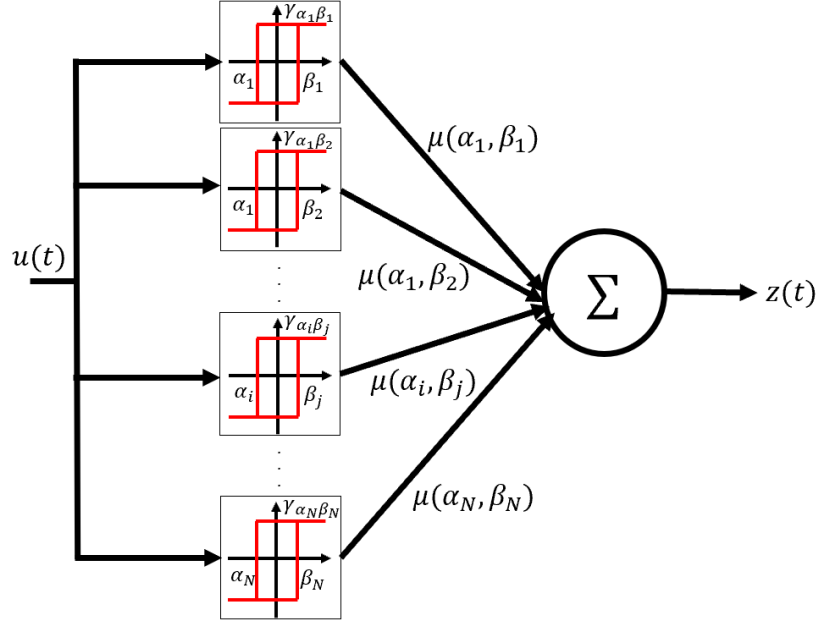


Figure 2.9: Block representation of the classical Preisach model, where the model is approximated by a finite superposition of various rectangular operators.

and is one of the most common models used to represent the hysteresis behaviour in non-linear systems. Principally, the Preisach model is defined using a double integrator as:

$$z(t) = \int \int_{\alpha \geq \beta} \mu(\alpha, \beta) \gamma_{\alpha\beta} u(t) d\alpha d\beta, \quad (2.13)$$

where $z(t)$ is the model's output at time t , $u(t)$ is the model input at time t , and $\gamma_{\alpha\beta}$ represents rectangular hysteresis operators, where α and β are the up and down switching values, respectively[119]. As shown in Figure 2.10(a) these operators can only assume a value of $+1$ or -1 . The function $\mu(\alpha, \beta)$, known as the density function, represents the only model unknown that is obtained from experimental data. The model can be visualised as a continuous system of parallel-connected two-position relays, where each relay is activated with input $u(t)$. The individual outputs are multiplied by the density function and then integrated over all the specified values of α and β to obtain output $z(t)$ [120]. The model can be reasonably approximated by a finite superposition of numerous rectangular operators [121] as represented in Figure 2.9.

The classical Preisach model is rate-independent. Subsequently, to implement the rate-dependent Preisach model, researchers propose several modifications such as fractional derivation [122], modified hysterons [123] and Hammerstein

structures [124]. On the other hand, Mayergoyz [125] introduces the weight function's dependence on the speed of output variations; comparably, Mrad and Hu [126] propose an input-rates dependence of the weight function. Both approaches assume the weight function is the appropriate component to represent dynamic behaviour [127, 128]. Alternatively, in [129] a linear dynamic model is included prior to the Preisach operator and the dynamic characteristics are represented by the linear dynamic part. This class of cascade arrangement is known as 'external dynamic hysteresis model' and found in several works [130–133].

The identification of the Preisach density function is one of the most complex steps in implementing the model. In most circumstances, this function can be identified using measurements and the application of a numerical method, which can be a specific formulation [134, 135] or using conventional methods such as an Everett integral [136] or Gaussian/Lorentzian functions [137]. The function can then be applied in software using a look-up table of values. Other black-box identification techniques for the density function include genetic algorithms [138], fuzzy models [139] and ANNs [121, 140–144].

There are two main variations of the Preisach model in literature: the Prandtl-Ishlinskii (PI) model and the Krasnosel'skiĭ Pokrovskiĭ (KP) model. The PI model combines the linearly weighted superposition of a number of operators with varying threshold values and weights. Figure 2.10(b) shows this operator's characteristic, denoted by $P_r[u](t)$. As an attempt to model rate-dependent hysteresis, several works propose variations to the play operator by including the dependence of an envelope function of the input's rate of change [145–147] or by modification of the threshold function [148] or weights [149]. Other works [150–153] cascade a separate model with the static model to exhibit the dynamic effects. In a similar case to Preisach models, Wang *et al.* [154] use neural networks for the identification of the unknown function. In the mentioned work, the function is expressed using an internal time-delay recurrent neural network, which can map dynamic characteristics by saving its internal state. One limitation of the classical PI model is that it cannot exhibit either asymmetric hysteresis loop or saturated hysteresis loops [149, 155]. However in [150] Jiang *et al.* propose modifying the model to combine two asymmetric operators which can independently simulate the ascending and

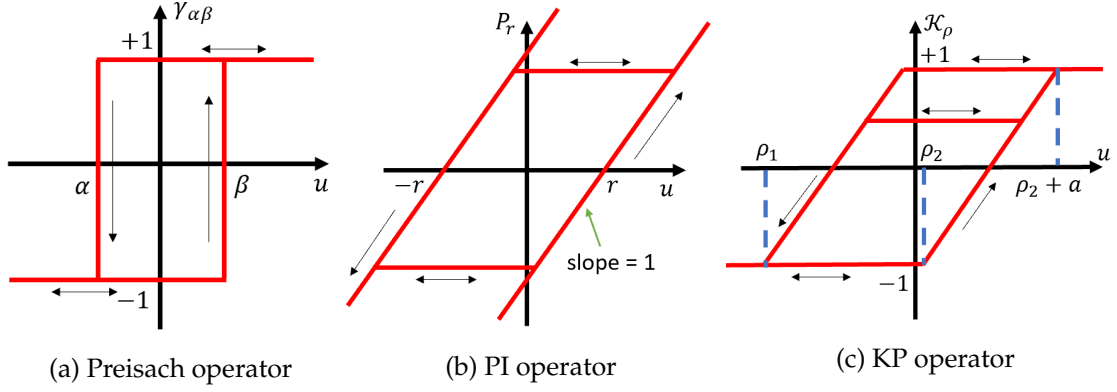


Figure 2.10: Three types of operators used to represent hysteresis in Preisach models: the Preisach (rectangular) operator, PI operator and KP operator.

descending branches of hysteresis.

Another variation of the Preisach model, the KP model, was implemented by Banks, Kurdila and Webb [156] using an operator developed to represent hysteresis as a cumulative effect [157]. Figure 2.10(c) shows this operator's input-output behaviour, denoted by \mathcal{K}_ρ . Applying an input signal, the output response of the KP kernel shows either a horizontal line between two ridge functions or a track along one of the curves of the ridge function.

In contrary to the Preisach model, the PI and KP models present continuity of the mapping in the parameter space, which is important for model identification when having a significant number of operators [158]. As an example, in [159] to represent a specific hysteresis loop, the Preisach model, which makes use of a discontinuous operator where the output is either -1 or $+1$, the model requires around 20,000 relay operators, which results in a long time to perform the model identification process. For the PI and KP models, where both consist of continuous operators, and the output is any value between -1 and $+1$, it requires less kernels to model a specific hysteresis loop, which can significantly reduce the computational burden.

Other variations of the Preisach model exist for several applications, such as an operator derived from the Stoner-Wohlfarth model to simulate Goss-textured magnetic materials [160]. In other cases [161–163], to overcome the multi-valued mapping problem another dimension is added, which includes the elementary hysteresis characteristic to convert the problem to a single-valued mapping.

Consequently, the model will be able to approximate the hysteresis system.

2.5.3 | Physical models

Physical models attempt to represent the behaviour of a phenomenon by simulating basic processes that the materials experience. The most popular physical hysteresis model is the Jiles-Atherton model. This model divides the hysteresis process into the reversible and the irreversible magnetisations [164]. The magnetisation is the lumped change in magnetic state by applying an external magnetic field to the magnetic material and producing a corresponding magnetic flux. The model describes the behaviour of distinct magnetic particles and domains and how these can be evaluated as bulk material using a lumped expression:

$$M_{\text{total}} = M_{\text{irreversible}} + M_{\text{reversible}}. \quad (2.14)$$

A difficulty with the Jiles-Atherton model is extracting the parameters [165]. Jiles *et al.* [166] propose a method for obtaining the parameters through a set of experimental data. On the other hand, Lewis *et al.* [167] propose an improved numerical approach for calculating the magnetic parameters. The model is able to aptly represent major loops that have a sigmoid shape. The influence of several excitation signals and the different parameters on the model was studied in [168].

The original model lacks rate dependence, which is essential to accurately apply the model to synchrotron field control. It is also unable to precisely model minor loops. Carpenter [169] presented a modification to solve this issue, based on the loops' turning points, whilst Jiles [166] used a comparable technique. Approaches implemented to optimise the model parameters to fit major and minor loops have focused mostly only on the major loop, either using direct numeric methods as described by Lewis *et al.* [167] or through least squares approaches to fit the experimental data and model such as carried out by Schmidt and Guldner [170] or Lederer *et al.* [171]. A dynamic model is proposed by Cao *et al.* [172], with a cascaded linear structure which exhibits the dynamics, where a hybrid genetic algorithm is used to obtain the unknown parameters. Hamada *et al.* [173] propose another modified dynamic Jiles-Atherton model which couples a diffusion equation for mean frequency with the static model.

The main strengths of this model are that it is widely used with plenty of available support for circuit simulators, it has reasonable convergence and is appropriately accurate across various operating conditions [174]. It is also widely used in inverse compensation of hysteresis [175]. Another model, the energetic model proposed by Hauser [176] varies from the Jiles-Atherthon model as it is not based on the concept of displacement from the anhysteretic magnetisation state, but based on energy balance. The model calculates the magnetic energy of a material by decomposing the total energy density in four components [177].

2.5.4 | Current state-of-the-art

Reviewing the types of models used in predicting the magnetic field in synchrotron magnets, in light of the three categories of hysteresis models defined in this chapter, it is very clear that the majority of the models implemented in an on-line setting are mathematical-based analytical formulations with a physical description of the different elements making up the phenomenon. In the case of iron-dominated magnets, the current state-of-the-art magnetic field model at CERN is a differential model based on a simple evaluation of the three contributing components [178]. Caspers *et al.* propose a first order differential equation which can represent the different dynamic effects in magnetic materials:

$$B(t) = K_1 I - K_2 L \frac{dI}{dt} + B_{\text{res}}. \quad (2.15)$$

The model consists of three terms: K_1 , K_2 and B_{res} , representing the magnetisation, eddy current and residual field contributions, respectively and L is the inductance. Fig. 2.11 shows a simplified representation of the model. K_1 and K_2 are determined as described in Equation 2.16 and Equation 2.17 respectively, where I is the magnetisation current, R_g is the magnetic reluctance, R_c is the magnetic reluctance of the core, μ_0 is the relative permeability, N is the number of turns and g is the gap length:

$$K_1 = \frac{\mu_0 N}{g} \left(\frac{R_g}{R_g + R_c} \right) \quad (2.16)$$

$$K_2 = \frac{\Delta B_{\text{max}}}{V_{\text{max}}}, \quad (2.17)$$

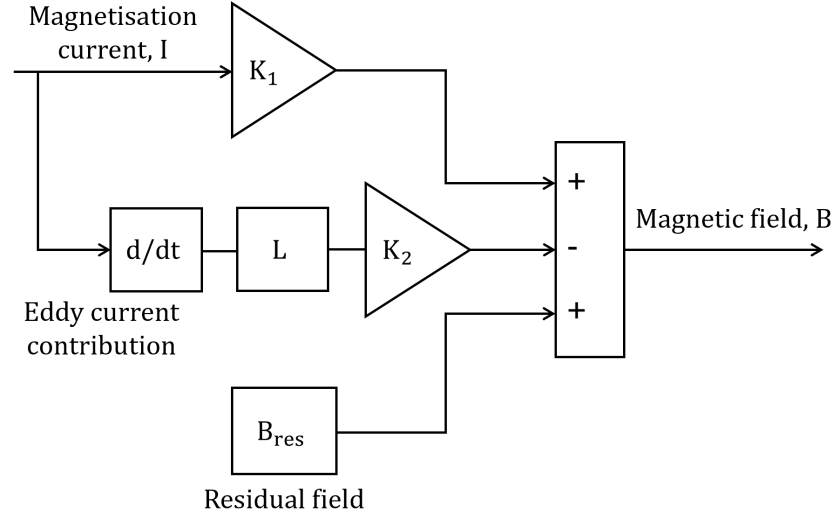


Figure 2.11: A graphical representation of the model defined in Equation 2.15 [178], which is composed of the magnetisation, eddy current and residual field contributions.

where ΔB_{\max} represents the maximum reduction in the magnetic field due to eddy currents, for a maximum voltage V_{\max} .

This model has been implemented at CERN for the PSB and the AD [63]. Whilst the model is simple and efficient for real-time operation, its disadvantage is that it only represents eddy current contributions for infinitely long ramp rates, ignoring decay effects when the ramp rate is zero. This becomes problematic especially in cases where magnetic cycles have very long plateaus.

Other works describe models designed using analytical formulation of magnetic behaviour. In [179], Bozoki defines a relationship between the excitation current and the magnetic field of dipole magnets, fitted using a polynomial model by taking into account previous magnetic measurements. The model is then corrected in real-time using beam measurements. The benefit is that this compensates for any inaccuracies in the magnet measurements, however it does not consider the fact that some beam measurements' significance differs under different operational conditions (such as increased beam intensity). Another analytical model based on contributions of the magnet strength (M) of iron-dominated magnets is proposed by Brown [180], where he proposes the decomposition of the magnet strength into four terms: a linear (L), residual (R), hysteretic (H) and interjacent (J) term:

$$M(I, I_{re}, I_{pre}, D) = L(I) + R(I_{pre}, D) + H(I, D) + J(I, I_{re}, I_{pre}, D), \quad (2.18)$$

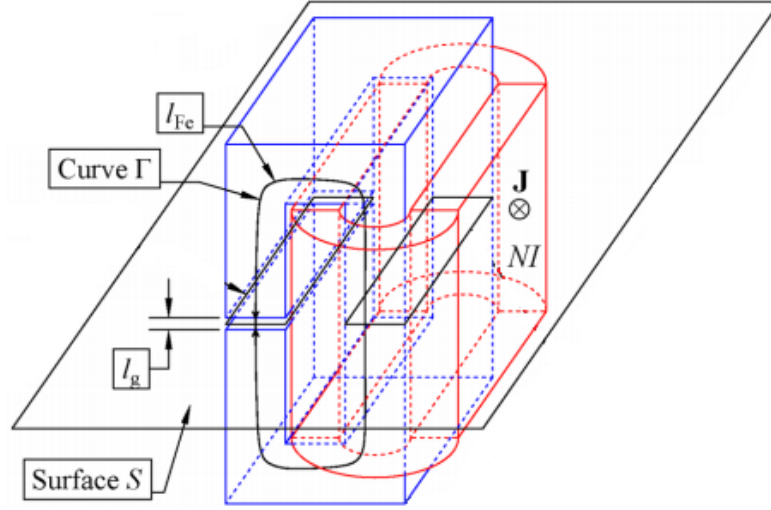


Figure 2.12: Simplified circuit of a C-shaped dipole magnet, adapted from [182].

where I_{re} is the reset current (current at the beginning of a ramp), I_{pre} is the preset current (reset current of previous ramp) and D is the ramp direction (+1 or -1). These four terms are expressed in polynomial form, fitted according to previous magnetic measurements. The model exhibits a relative residual magnitude better than 3 units for all currents tested. However, this model has been validated with excitation currents of only one polarity and it does not account for dynamic hysteresis.

A physical model representing the behaviour of C-shaped dipole magnets presented by Feynman [181] has been applied to an accelerator dipole magnet [182]. Figure 2.12 shows the simplified diagram, with the yoke in blue and the powering coil in red. Surface S is a sphere of infinite radius whose shell intersects the horizontal symmetry plane of the magnet; Γ is a closed curve representing the average path of the magnetic field strength in the circuit; l_{Fe} is the length of curve Γ in the yoke; l_g is the length of curve Γ in the gap of the magnet; J is the current density which is given by the magnetomotive force NI .

Starting from Ampere's law along Γ :

$$H_{Fe}l_{Fe} + H_g l_g = NI, \quad (2.19)$$

where H_{Fe} is the magnitude of the magnetic field strength in the core and H_g is the magnitude of the magnetic field strength in the gap. Considering the assumption that the magnetic flux closes through a surface of constant area, the operating point of the dipole magnet is given by the simultaneous solution of

the two equations:

$$\begin{cases} M_{\text{Fe}} l_g + H_{\text{Fe}}(l_g + l_{\text{Fe}}) = NI \\ M_{\text{Fe}} = f(H_{\text{Fe}}) \end{cases} \quad (2.20)$$

where $M_{\text{Fe}} = f(H_{\text{Fe}})$ is the iron's magnetisation functional relation.

In Pricop's work [182], the hysteresis modelling of the gap induction of a PS magnet was performed by finding the functional relation using measurements of material samples obtained from the magnet's lamination. The performance of the model was then compared to experimental measurements on the magnet, with ten magnetic field ramp-up and ramp-down variations, with a maximum of 45 A/s. Calculating the Normalised Root Mean Square Error (NRMSE) based on the reported results, a value of 1.7 units was deduced on the performance of the model with respect to the measurements.

2.6 | The FIRESTORM project

The FIRESTORM project is being carried out with the aim of upgrading all B-train systems at CERN before the LHC restart in 2021. Since the B-train instruments started operating in the 1950s, most of the measurement technology became obsolete, and critical electronic components that were unique and unrepairable started ageing. Besides this, due to the upgrade of synchrotrons along the years, the requirements for the B-train became more and more stringent. The modernised B-train system addresses the shortcomings of the current B-train systems and consolidates the existing B-train systems under common hardware/software platforms. This section presents the architecture of the new FIRESTORM B-train system, as well as the ELENA B-train specifications that are relevant for the commissioning of the instrument. Work which was performed as a team effort by various people on the electronic and software design of this system is not the scope of this thesis, and hence a top-level description of each unit making up the acquisition chain is provided.

2.6.1 | Impact on synchrotron operation

The FIRESTORM project is a consolidation project consisting of several design, testing and implementation phases taking place over fourteen years. The main milestones of the project are illustrated in Figure 2.13. The proposed FIRESTORM system is expected to have a major positive effect on the

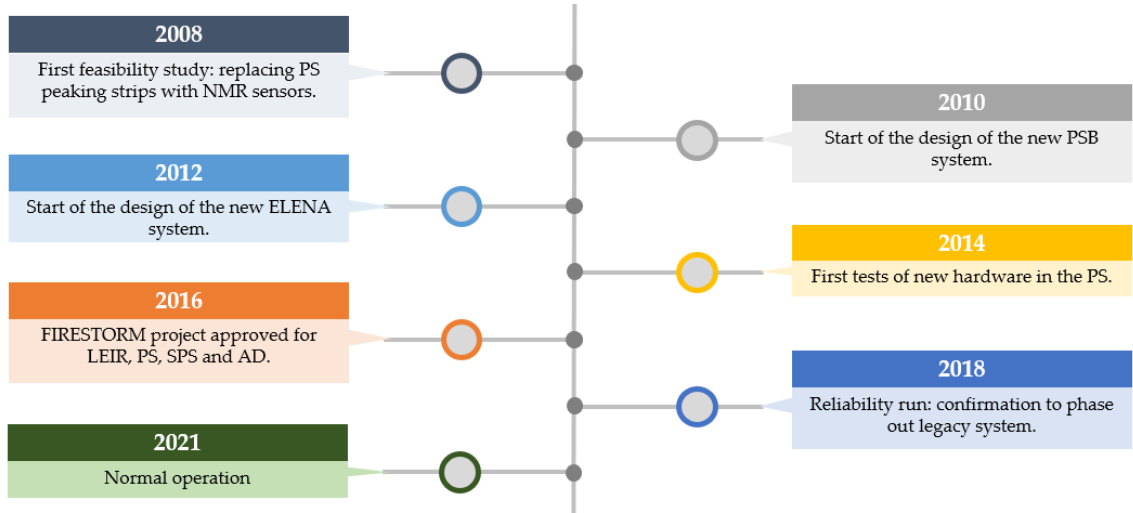


Figure 2.13: Timeline of the FIRESTORM project milestones.

performance of synchrotrons at CERN. The following are three examples of accelerator operations that are affected:

- Improved operational flexibility such that various supercycle compositions are supported, including software to automatise adjustments that in the past were performed manually to compensate for hysteresis effects.
- Improved accuracy of the measured field through upgraded sensors and integrators, which leads to better radial beam control and lower losses.
- Upgraded diagnostics and remote configuration, as well as the removal of several manual interventions to perform integrator calibrations, switching between the two chains and switching between the measured and simulated facilities.

Moreover, the proposed project allows for the measurement to be transmitted to the machine operation teams, such that high level applications can be created and integrated within the existing control software.

2.6.2 | FIRESTORM architecture

The B-train setup consists of two separate acquisition chains operating simultaneously: Chain 1 (C1) and Chain 2 (C2), where C1 is the operational chain and C2 is the spare chain. The architecture of a B-train chain is illustrated in Figure 2.14. The induction coil provides a voltage V_c , proportional to the rate of change of the field, that is integrated to obtain the field. Adding the contribution of the field marker at t_k , an absolute measurement can be

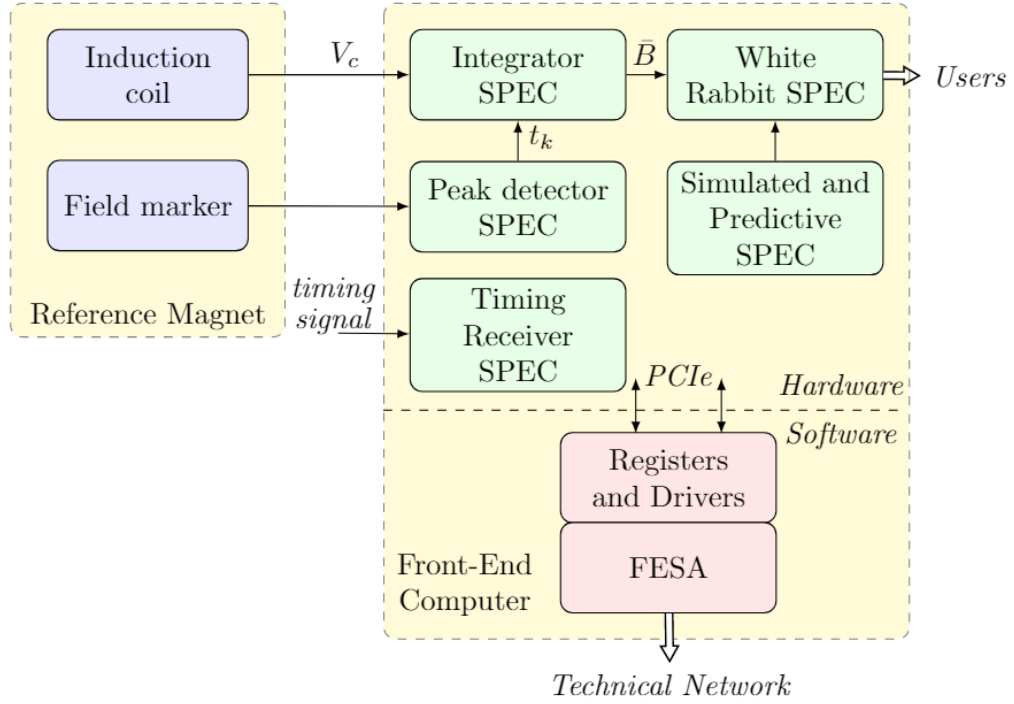


Figure 2.14: Schematic of the FIRESTORM B-train architecture.

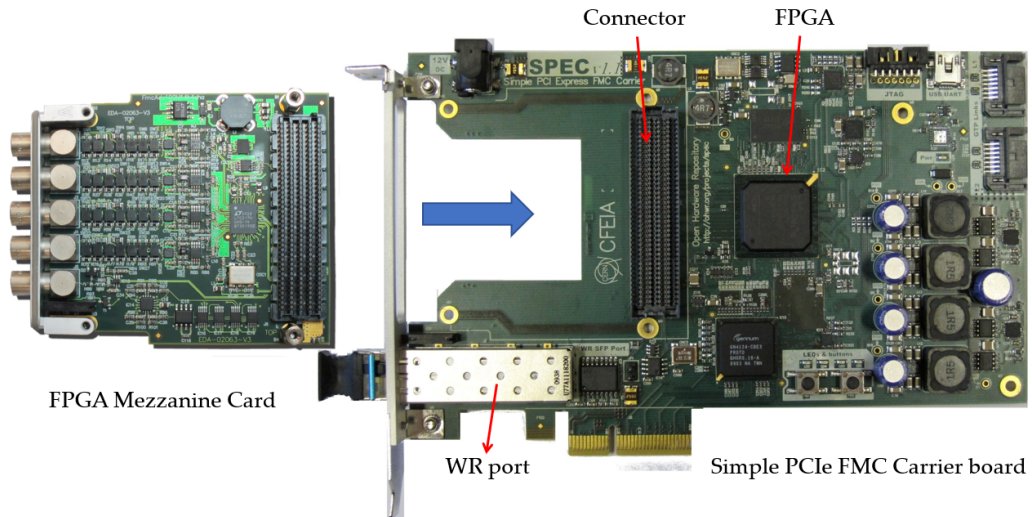
determined and transmitted. The core of the acquisition chain consists of a front-end computer which houses the electronics and software components of one chain.

The front-end computer comprises five types of Simple Peripheral Component Interconnect Express FPGA Mezzanine Card carrier (SPEC) boards [183] that take care of the measurement signal processing, as well as the distribution of the magnetic field to the users. The SPEC board was developed at CERN with the technical specifications listed in Table 2.1. The board is equipped with a network distribution unit, Xilinx Spartan-6 FPGA [184] and FPGA Mezzanine Card (FMC) slot [185], as shown in Figure 2.15. Five different FMC modules are custom-designed, four of which specifically for this project, whilst the Central Timing Receiver module is deployed in all front-end computers at CERN. These cards are incorporated within a modular structure, and they interface with each other using the Peripheral Component Interconnect express (PCIe) standard.

The Central Timing Receiver SPEC card [186] receives events through the General Machine Timing link, which is a differential RS-485 network driven by master modules and distributed around the synchrotron complex [187]. This scheme allows beam negotiation and synchronisation between the accelerators. A start-cycle trigger (C0) acts as a reference for the start of a cycle, and is useful

Table 2.1: SPEC board technical specification [183]

Resource		Details
FPGA	Type	Xilinx Spartan-6 (XC6SLX-45T/100T)
	Slices (bRAM)	6822 (401Kb) / 15822 (976Kb)
	Memory	2 Gb DDR3, 32 Mb Flash PROM
Clocking resources	XO	Crystal oscillator (10-280 MHz)
	TCXO	Temperature compensated crystal oscillator (25 MHz)
	VCXO	Voltage controlled crystal oscillator (20 MHz)
	Synthesizer	Low-jitter frequency synthesizer
Front panel	FMC	Connection to FMC slot with low pin count (LPC) connector
	SFP	Small Formfactor Pluggable (SFP) cage for fibre-optic transceiver
Stand-alone features	Power supply	External 12 V DC
	Ports	USB Mini-B connector, 4 LEDs, 2 buttons

**Figure 2.15:** The SPEC board and FMC module (adapted from [183]).

for aligning the measurement data and the events mentioned in Table 2.4 for the ELENA. Another trigger called the zero-cycle trigger, signals the start of a zero cycle, which is a cycle in which no beam is being circulated in the machine, and the magnetic field in the dipole magnets is kept constant. It is used to fill timing slots that are not needed in synchrotron operation. The FIRESTORM B-train system uses the zero trigger to start an integrator calibration.

The Peak detector SPEC cards detect the peak of the field marker resonance signal and generate a trigger signal. Each card can host two field markers simultaneously [188]. A signal conditioner removes the signal's DC offset, followed by a low-pass filter and an Analogue-to-Digital Converter (ADC).

Depending on the field marker type, filters are added to remove random peaks in the signal. The FPGA is used to detect the peak of the resonant signal. As shown in Figure 2.3, the resonant signal dips when the pre-configured magnetic field value is reached. A threshold is set such that when it is exceeded, the signal is differentiated using a seven-point finite difference approximation [189]. A zero crossing eventually signals the presence of the peak in the resonant signal, and a digital trigger is generated at time t_k . Another precaution is taken to avoid unwanted triggers, whereby the peak detection only occurs during a specified marker time window, which is different for every field marker and cycle type in a synchrotron.

Each chain contains an Integrator SPEC card, which determines the measured \bar{B} signal by integrating the coil voltage [190]. The coil signal is conditioned by an anti-aliasing filter with a cut-off set at 100 kHz acquired by an 18-bit, 2 MHz ADC and then integrated numerically. The integration is initiated upon reception of the digital trigger at t_k from the Peak detector SPEC card. Besides integrating the signal, this SPEC card also corrects for the drift accumulated by the signal. The correction scheme is described in detail in [189], and consists of two mechanisms. The first one is controlled via a potentiometer, which is limited in the reduction of the offset voltage. The second mechanism corrects for finer offsets in the order of tens of microvolts. The voltage offset removal occurs periodically, typically once every five minutes upon the reception of the zero-trigger signal.

The Simulated and Predictive SPEC card [191] is available to transmit the value of the magnetic field based on a look-up table or field model respectively. Whilst in normal circumstances the measured B-train is used, the simulated/predictive B-train can be used for off-line tests when the power converter is not available, or when there is an issue with the measured B-train. The simulated B-train fetches vectors from the LHC Software Architecture database in the technical network [192] depending on the cycle being operated. The SPEC card then implements Bresenham's line algorithm to determine the field value at a specific time value [189]. The predictive B-train on the other hand uses the power converter current value to determine the magnetic field based on a pre-defined model. A switching chassis installed in the acquisition chain allows users to switch between the different field sources.

Table 2.2: Control frame breakdown

Bit number	Details
0-7	source type (e.g. 0x42 ASCII code for field measurement)
8	Simulation indicator: '0' if B is measured, '1' if simulated
9	Unused
10	C0
11	Zero cycle pulse
12	Focusing low marker flag (used in the PS)
13	Defocusing low marker flag (used in the PS)
14-15	Version ID

The White Rabbit SPEC card is responsible for distributing the magnetic field values to the users [191]. This card makes use of the CERN-developed White Rabbit network, which is an IEEE-1588 Ethernet-based network for data transfer and synchronisation [193]. The system distributes digitally absolute values of \bar{B} and its derivative in Ethernet frames at 250 kHz [30]. This technology offers several benefits. In particular, it allows for precise time-tagging of events and data collection from several distant locations, providing sub-nanosecond accuracy and picosecond synchronisation precision of all nodes [17]. The White Rabbit network allows for deterministic and bidirectional data transmission, as well as the use of optical fibre technology, which means that induced noise, typically found in electrical transmissions is avoided. A White Rabbit switch port is installed within the B-train acquisition chain to connect the card to the White Rabbit network. The transmitted Ethernet frame consists of 224 bits as can be seen in Figure 2.16, with a control slot (CTRL) to control the active field, B and \dot{B} slots with the default field and field derivative, one slot reserved for the legacy measurement (where available), a slot for the FIRESTORM measurement, a slot for the simulated field and another for the predicted field. A 16-bit cyclic redundancy check (CRC) at the end of the frame tests data for correctness during transmission. The composition of the 16-bit control frame is listed in Table 2.2 below.

CTRL	\bar{B}	\dot{B}	Legacy B	Measured B	Simulated B	Predicted B	CRC
16 bits	32 bits (signed)	32 bits (signed)	32 bits (signed)	32 bits (signed)	32 bits (signed)	32 bits (signed)	16 bits

Figure 2.16: B-train White Rabbit Ethernet frame.

The control software deployed in the front end computer, which allows users to interface with the instrument is called the Front End Software Architecture (FESA). FESA provides a graphical interface as well as a C++ environment for developing code to interact with the SPEC cards. This software receives the timing signal from the Central Timing Receiver SPEC card, resulting in pulse-to-pulse modulated capabilities. This allows the instrument to optimise settings for different cycling conditions, as well as make gain and offset corrections to the B-train measurement. The FESA interface can be accessed through CERN's technical network, which offers connectivity for the machine control devices and industrial systems.

The B-train FESA class architecture consists of four C++ classes interfacing with the measurement hardware for configuration and diagnostics:

1. FSBT_BTG class: interfaces with Simulated/Predictive FMC module;
2. B_train class:
 - interfaces with Integrator and Peak detector FMC modules;
 - sets calibration constants of the measurement model;
 - gets measured \vec{B} and \dot{B} ;
 - interfaces with NMR/FMR field markers;
 - sets RF frequency generator parameters;
 - communicates with NMR teslameters;
3. COMET_EVM class: interfaces with environmental monitor which measures temperature;
4. Cosmos_WRS class: general White Rabbit diagnostics.

Each acquisition chain contains around 250 parameters, with most of these available in pulse-to-pulse mode.

2.6.3 | ELENA B-train specifications

Whilst the FIRESTORM B-train system is designed to be as uniform as possible across synchrotrons, the ELENA ring, being a decelerator, presents additional challenges to the setup and operation of the real-time magnetic field measurement.

The ELENA dipole magnets are normal-conducting, iron-dominated electromagnets. These magnets produce a dipole field of 0.36 T at injection and 0.05 T at extraction. The latter low field presents a challenge due to enhanced dependence upon background field perturbations and hysteresis effects. Another challenge is presented due to the foreseen long duration of plateaus. The required relative field quality of 2 units ($\times 10^{-4}$) is expected, as the mean field variation must be lower than 10 μ T [26]. A full list of properties for the dipole magnet is given in Table 2.3.

Table 2.3: ELENA dipole magnet specifications

Parameter	Value
Nominal magnetic field	0.36 T
Nominal bending angle	60 °
Pole iron gap	76 mm
Bending radius	927 mm
Nominal current	275 A
Resistance at 20 °C	46 m Ω
Inductance at 100 Hz	28 mH
Yoke length	950 mm
Magnet mass	4370 kg

Before the installation of the ELENA ring at CERN, the antimatter experiments forming part of CERN’s Antimatter Factory received antiproton beams at 5.3 MeV from the AD decelerator. With the installation of ELENA, antiprotons can be slowed down further to 100 keV, which is a major improvement in the antimatter research field, as this allows at least one order of magnitude more antiprotons to be trapped and studied [194]. The ELENA machine features electron cooling to control emittance during the deceleration of antiprotons, preserving beam intensity as they are extracted towards the experiments.

During the commissioning period of the machine, a standalone ion source installed next to the ring delivers H^- ions and protons at 100 keV. This is implemented for testing in case antiprotons from the PS are not available or during periods of no beam in the long AD supercycle. Figure 2.17 shows the injection and extraction lines, as well as the ion source in the bottom left corner. Antiprotons are injected into the ELENA solely from the AD, where the dipole

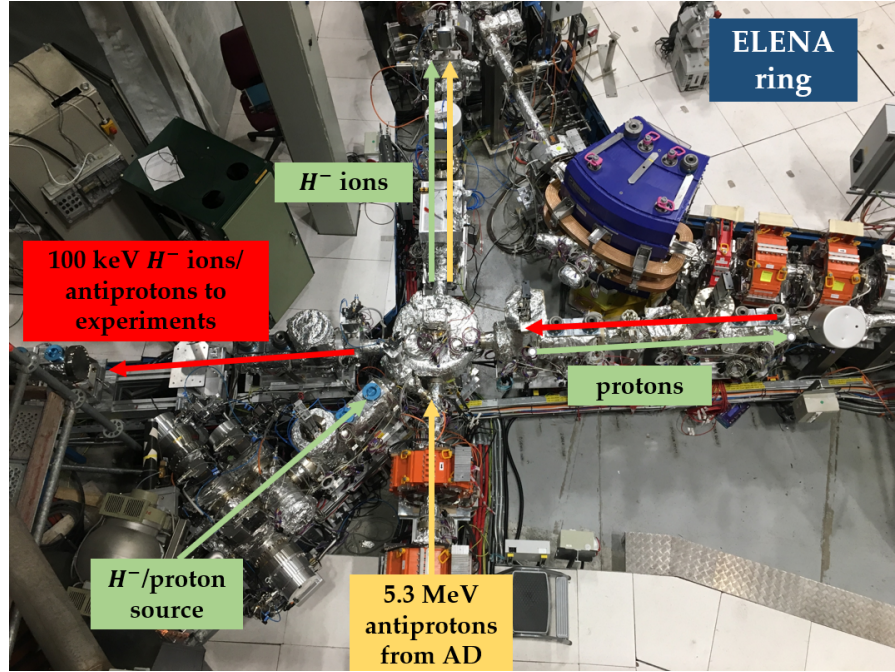
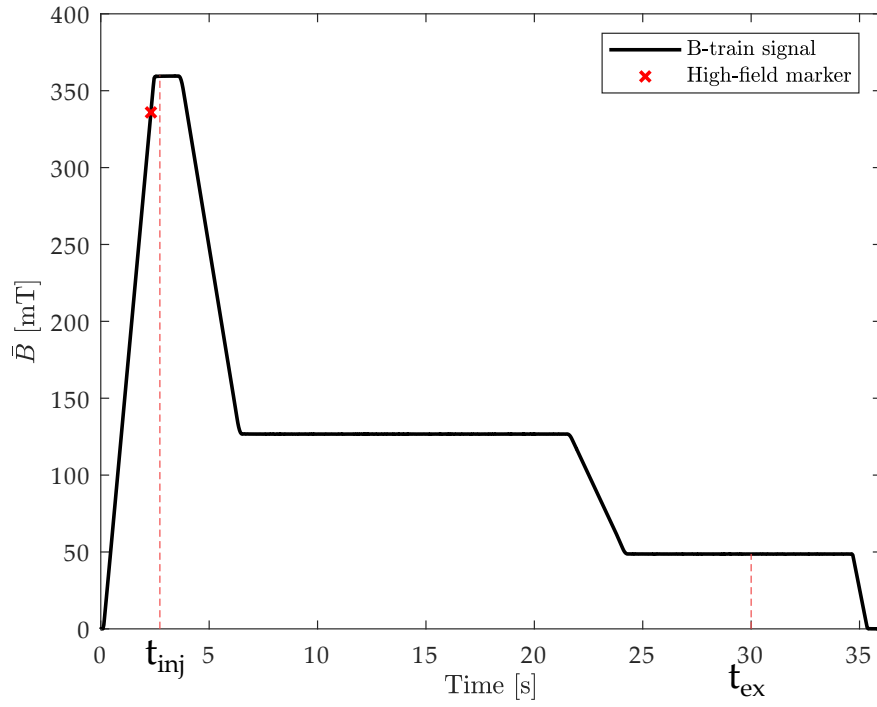


Figure 2.17: ELNA injection and extraction lines. The ion source can partially be seen at the bottom left corner. [194]

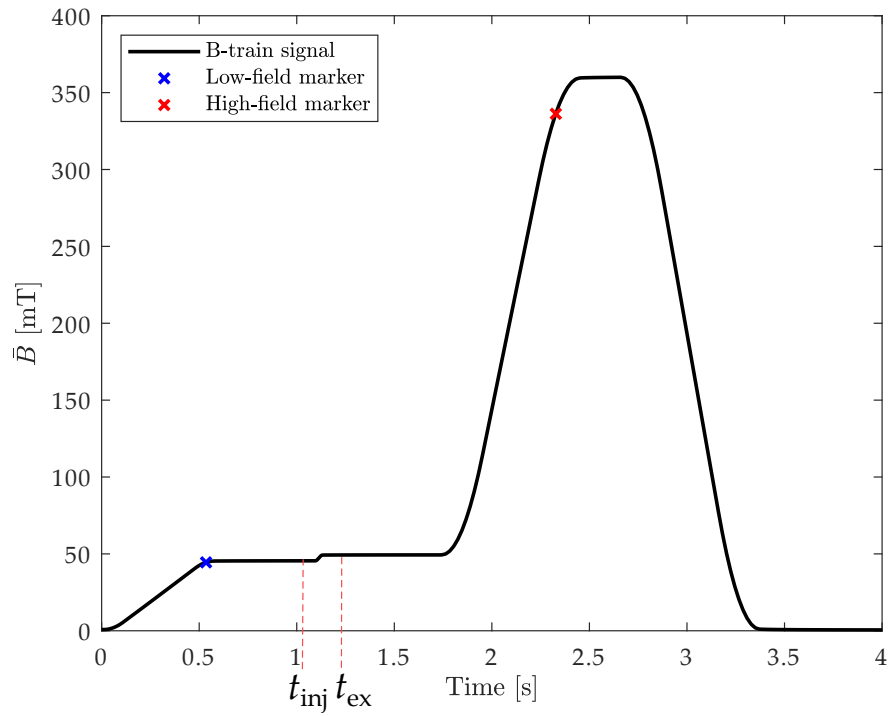
magnets are first ramped up to a momentum level of 100 MeV/c to match the energy of the beam incoming from the AD, and then the beam is slowed, first to a level of 35 MeV/c and then to 13.7 MeV/c using the electron cooling process. The magnetic cycle in this case is shown in Figure 2.18(a) .

H^- ions are injected with nominal polarity, which is important for the commissioning of systems such as the electron cooler. As shown in Figure 2.18(b) H^- particles are injected at 13.7 MeV/c and extracted at a slightly higher level. Another possibility is the injection of protons with a reverse polarity, where the current to the bending dipole magnets is reversed, resulting in an opposite field value. This can be useful for commissioning magnetic systems and to measure beam optics [17]. Table 2.4 gives the properties related to the two cycles for both B-train chains.

The ELNA B-train system includes two chains with identical electronics, but independent sensors. The full sensor setup used for the ELNA B-train can be seen in Figure 2.19, whilst the acquisition chains are shown in Figure 2.20. The choice of sensors implemented in the ELNA is carried out according to the field range and accuracy required by the application. Figure 2.21 shows an order-of-magnitude summary of the characteristics of several measurement techniques, in terms of accuracy and range [46], highlighting the three methods



(a) Deceleration cycle: antiprotons are injected at $t = 2.7$ s and extracted at $t = 30$ s.



(b) Acceleration cycle: H^- ions are injected at $t = 1$ s and extracted at $t = 1.2$ s.

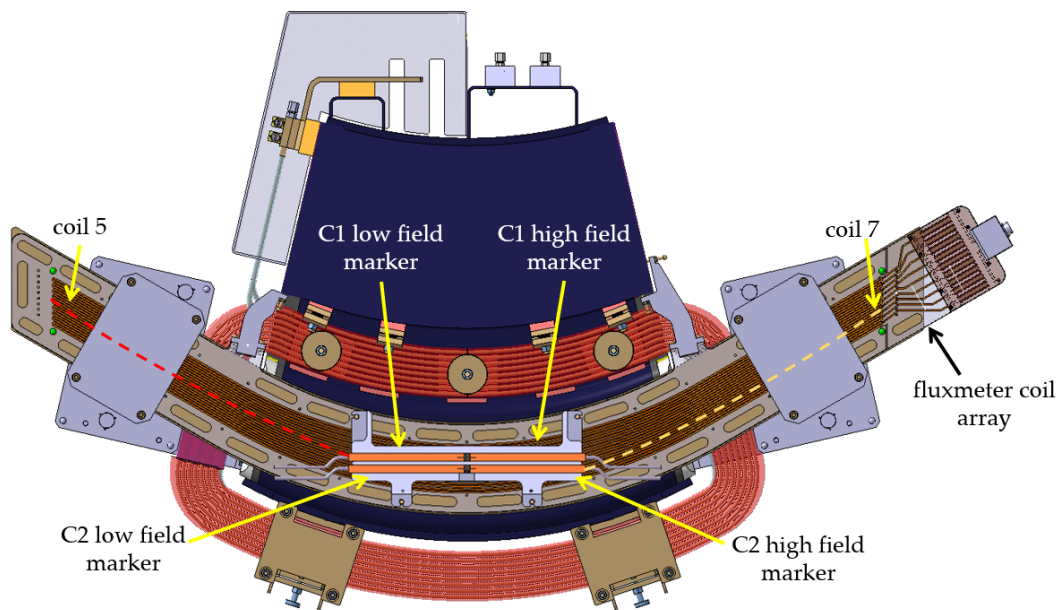
Figure 2.18: Magnetic cycles used in the ELENA ring during commissioning.

Table 2.4: Cycle properties and timings for the two ELENA B-train chains.

Parameter	Symbol	Unit	Deceleration		Acceleration	
			C1	C2	C1	C2
Injection time	t_{inj}	ms	2727		1029	
Extraction time	t_{ex}	ms	30000		1229	
B-train output at t_{inj}	$\bar{B}(t_{\text{inj}})$	mT	359.3		45.46	
B-train output at t_{ex}	$\bar{B}(t_{\text{ex}})$	mT	49.30		49.27	
Current at t_{inj}	$I(t_{\text{inj}})$	A	276		34.8	
Current at t_{ex}	$I(t_{\text{ex}})$	A	38		37.8	
Field marker trigger time	t_k	ms	2315.0	2314.4	535.2/2328	535.0/2327
Field marker value	$\bar{B}(t_k)$	mT	340		45/340	45/340
Ramp rate at t_k	$\dot{B}(t_k)$	mT/s	160		100/650	100/650
Nominal current-to-field ratio	\bar{B}/I	mT/A	1.3			

(induction coils, ESR and NMR) that meet the 2-unit mark accuracy and 10^{-3} T to 1 T range requirements desired. In the end, a combination of induction coils and NMR field markers is implemented for operation.

In the majority of cases in accelerator magnets, a rectangular long induction coil is used for measuring the field change, which helps achieve a precise geometry and simplifies the calculation of calibration coefficients [44]. Since the ELENA dipole magnets are curved, a static coil is designed with the same shape to follow the nominal beam orbit. Each chain is based on a custom-made 594-turn

**Figure 2.19:** ELENA B-train reference magnet sensor setup.

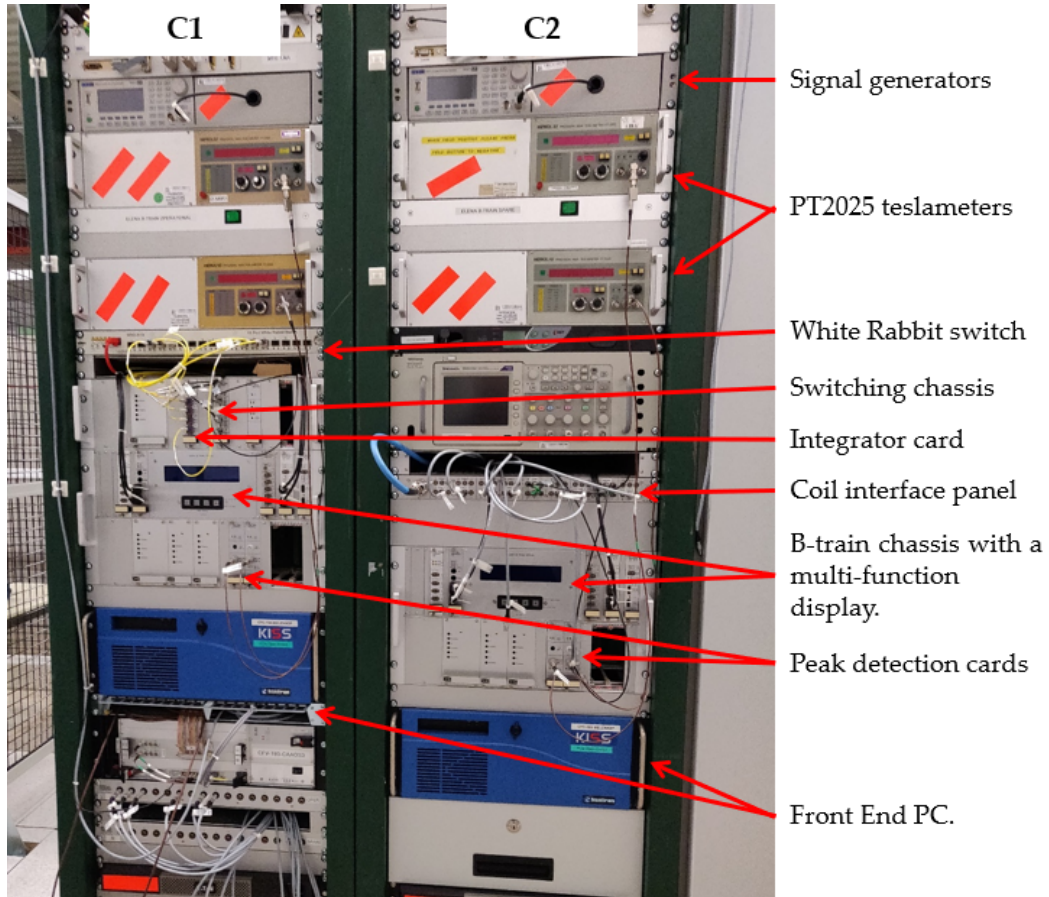


Figure 2.20: ELENA FIRESTORM acquisition chains.

litz-wire induction coil that is 1650 mm long and 9 mm wide. The kind of cable used consists of thousands of fine insulated filaments. The subdivision of the conductor substantially reduces the AC losses due to the skin effect [44]. Nine coils attached to a fiberglass support make up the fluxmeter coil array, which is rigidly fixed to the magnet's yoke [195]. Chain 1 makes use of the central coil (coil 5) whilst Chain 2 measures the induced voltage in coil 7. The main advantage of this coil is that it detects the full vertical field. The measurement of the full dipole integral is not done in any other synchrotron at CERN, hence the implementation of a coil which spans the entire length of the magnet gap in the ELENA guarantees a higher level of accuracy [17].

Each ELENA B-train chain includes two Metrolab NMR probes [48] as field markers, connected to a fiberglass support at the magnet's centre and set at low (45 mT) and high (340 mT), as required for acceleration of hydrogen negative ions during machine commissioning and antiproton deceleration during normal operation respectively. Reaching the main requirement in terms of the field reproducibility in the ELENA is a challenging target [17]. This is due to the

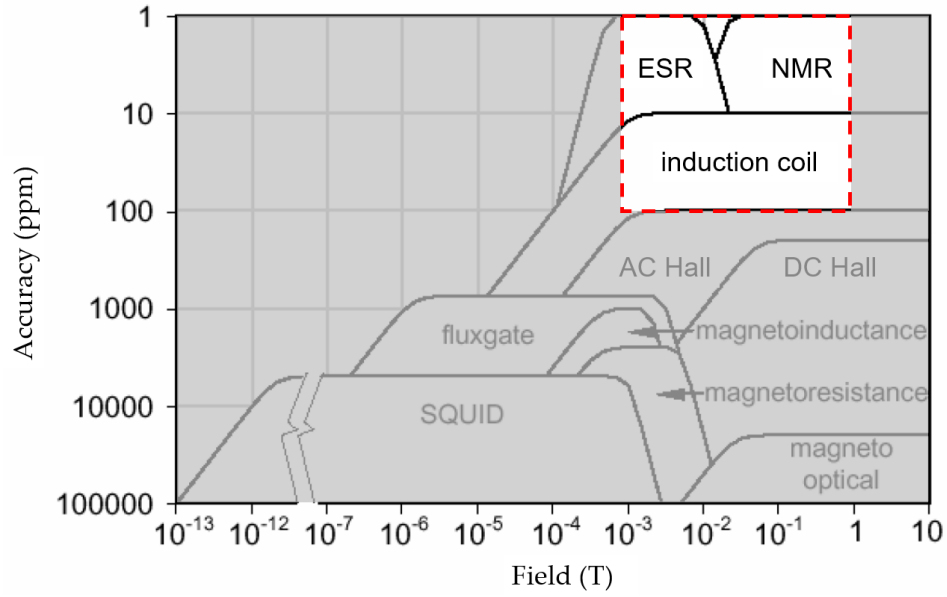


Figure 2.21: Overview of the accuracy and range characteristic of different measurement techniques, highlighting the possible options that can meet the requirements for the ELENA field measurement (adapted from [46]).

impact of long cycle times on integrator drift. As explained in Section 2.6.2, an offset voltage in the coil measurement can produce errors which increase with time. The FIRESTORM system compensates for this error at the beginning of a cycle, however having a cycle thirty seconds long may cause errors which build-up to an unacceptable level in the deceleration cycle's extraction point.

All the sensors are installed within the reference magnet that is devoid of a vacuum chamber. This magnet is electrically connected in series with the ring magnets and is installed further than 50 m from them, which makes stray fields negligible. However, one must keep in mind that if the ring magnets are affected by cross-talk, this will not be picked up by the reference magnet. Figure 2.22 shows the reference magnet situated in the ELENA powerhouse. Another major source of perturbation is the vertical component of the geomagnetic field, which however equally affects both the reference and ring magnets. The building where the magnets are placed is also temperature controlled, which ensures a stable temperature throughout the year.

2.6.4 | Contributions to the FIRESTORM project

Whilst the design and construction of the first FIRESTORM prototype took place before the commissioning of the ELENA ring started, the ELENA B-train is still one of the first machine to test this architecture under machine operation



Figure 2.22: ELENA reference magnet

conditions. In particular, throughout the commissioning of the ELENA B-train, the following contributions were made to the FIRESTORM architecture:

- Bipolar field operation: as the ELENA ring is expected to operate using either protons and antiprotons (or hydrogen ions) flowing in opposite polarities, the magnetic field exhibited by the dipole magnets is bipolar. Whilst no changes are needed to be made to the induction coil signal and ensuing settings, the field marker level is negated in cases where protons are being circulated in the ring. This added functionality was developed and tested during the ELENA commissioning stage.
- Operation of field markers below 50 mT: whilst operating in the lower-limit capability of the field marker sensors, this was still a unique and challenging operational condition, especially to reach the expected reproducibility target.
- Multiple field markers: due to long machine cycles, multiple field markers were introduced in the ELENA, which involved additional software components to be tested.
- Characterisation of the integrator: the integrator was tested with an accurate voltage source in order to note any errors at the receiving end of the FESA diagnostic software. As a result, a 2.3% gain error was discovered due to a software bug and was corrected for all prototypes.

2.7 | Motivation and scientific contribution

In light of the commissioning of the new ELENA ring, a B-train system is required for the operation of the RF cavity. The architecture of a new measurement system has been developed over several years, with the plan to consolidate all the LHC injector chain B-train systems by 2021. In the case of the ELENA ring, a complete set of acceptance measurements for each individual ring magnet is available, as well as unrestrained access to the sensors and the reference magnet. This brings about the opportunity to characterise the behaviour of the untested measurement system, as well as all the ring magnets in relation to the reference magnet by formulating a measurement model.

While calibration of the sensors individually is relatively unambiguous, characterisation of the system as a whole presents several challenges. First, the field marker is usually a sensor with dimensions in the millimetre range, such as a Hall probe, from which an average over a path up to a few metres long must be inferred. Secondly, the coil can be offset from the expected central position in the magnet gap, because of space constraints or alignment tolerances. Finally, material and geometric uncertainties inherent in the fabrication process which cannot be avoided, may lead to variations between the field in the reference magnet and the average magnetic field experienced by the beam in the ring, which need to be accounted for.

As was shown in Section 2.4, several *ad-hoc* factors are usually used to compensate the forementioned error sources, to ensure the experimental match between the beam's bending radius, momentum and magnetic field. However, such a shortcut is not entirely suitable. In the framework of a synchrotron chain, absolute magnetic field knowledge is preferred to ensure energy matching and seamless particle transfer between machines. In itself, the use of measurement models in the area of magnetic sensors is a vast topic [196–198]. In the context of Tokamak magnets, a similar problem arises when inferring the magnetic field in the inaccessible interior of the vacuum vessel from flux loops placed on its surface, to allow vertical plasma control [199]. Measurement models have likewise been implemented for space applications to predict low-frequency fields radiated by components all around a satellite. In such cases, parameters can be determined from a distinct set of measurements done at different positions in the far field [200, 201]. In the research stage of this project, however,

no comparable models have been noted in the context of synchrotron magnets.

The scientific contribution of such a measurement model lies in two aspects:

- focus on the absolute measurement characterisation, in contrast to the mere reproducibility required from previous systems, which culminated in careful trial-and-error systematic error compensation during the machine’s commissioning phase;
- a detailed uncertainty evaluation, that gives confidence to machine operators trying to detect the source of any noted beam instability.

In the B-train commissioning process, three types of tests are performed to validate the performance of the instrument. As part of the decision to choose the appropriate field marker sensor, the precision and characteristics of the sensor in the expected operating conditions are tested. This test also provides insights on the optimal cycle configuration that can be implemented by machine operators. The performance of the B-train instrument is evaluated by devising appropriate metrics that cover all the possible error sources in the measurement. Following the implementation of the measurement model parameters, the ELENA B-train precision is characterised by performing a reliability run, in order to confirm a relative reproducible performance better than 2 units. This work characterises the source of the different random errors separately, identifying the main error source and providing suggestions to reduce this error in the ELENA. The third test is carried out when the beam is present in the ring, where a novel method to confirm the accuracy of the instrument based on the position of the beam is proposed.

This thesis explores the possibility of improving the performance of a B-train system by changing the position of the field marker sensor within the gap of the magnet. Currently, in B-train systems where a separate reference magnet is available, the field marker sensors are always placed in the centre of the magnet at $s = 0$, which presents several advantages such as good field uniformity (a requirement for magnetic resonance sensors). However, the variation of the ℓ_m with respect to I can introduce additional uncertainties in the B-train measurement, which needs to operate strictly with errors in the order of 10^{-4} . This work considers the displacement of sensors in the ELENA B-train system to reduce this error.

The commissioning of the ELENA B-train system also requires a hysteresis model to predict the magnetic field, that can work in parallel with the measurement or act as a backup. The requirements for such a model are:

- Focus on minor loop modelling, with an expected accuracy within 2 units.
- Modelling minor loop accommodation is not essential.
- Rate-dependent behaviour is important.
- Reasonable parameter identification procedure.
- Practical implementation for real-time operation.

Even though physical models seem more reasonable, most of them demand considerable physics knowledge and are unique based on the geometry and material of the magnet. On the contrary, models based on analytical mathematical formulations do not provide understanding of the material's behaviour, therefore they cannot be used to obtain new physical insight. However, they are application-independent and can correctly predict the behaviour of a consistent and well-controlled material without needing too much background in material science. As a result, these models are extensively used in modelling and hysteretic system control in the particle accelerator world. However, further analysis needs to take place to confirm that such models can address all cyclic conditions during operation. These are also the easiest models to implement in real-time. On the other hand, operator-based models such as the Preisach model suffer from the difficulty of implementation, where static models are typically used with high computation times.

This project aims to build on the work carried out by Caspers *et al.* [178] and Brown [180]. A model based on the decomposition of the integral field is proposed, able to account for dynamic effects and in particular for the eddy current decay at the initial stage of a plateau. An improved accuracy better than 2 units is expected for the model's implementation in the ELENA, as well as the use of formulations that are not computationally intensive for real-time operation. As a result of this literature review, a Preisach model based on a Recurrent Neural Network (RNN) is also proposed for modelling dynamic ferromagnetic hysteresis for material science applications where computation times can be higher. The model is able to model both major and minor loops.

2.8 | Conclusion

The overview of the different methods for magnetic field evaluation serves as a useful introduction to better understand the approaches adopted in this study to commission the ELENA B-train. This chapter presented an introduction to the main magnetic field effects exhibited in synchrotron magnets, which need to be addressed in such a task. Moreover, the different measurement techniques used in this field have been described as well as studies detailing various B-train systems implemented in research and hadron therapy centres. The second approach for evaluating the magnetic field, hysteresis models, has also been reviewed highlighting cases in literature and more specifically, cases where these have been applied in synchrotrons. This chapter also provided a general overview of the work carried out before and during this thesis on the development of a new FIRESTORM B-train system. The hardware and software components that make up this instrument have been described. Furthermore, the specific properties and challenges related to the operation of the ELENA B-train, as well as the proposed sensor setup have been discussed.

Additionally, based on the reviewed studies, the motivation behind this thesis has been presented, noting the resulting scientific contributions. It has been shown that this work will advance the knowledge on the behaviour of B-train systems and their performance in synchrotrons, as well as the development of a new hysteresis modelling techniques to predict magnetic field behaviour in synchrotrons.

Chapter 3

Measurement model

3.1 | Introduction

This chapter presents a model that estimates the average magnetic field of a synchrotron based on real-time sensor measurements of a reference magnet connected in series with the ring magnets. The proposed model links measurement theory to empirical observations and aims to provide a method for commissioning a B-train system without the presence of the beam. The theoretical concepts behind the model are first discussed, followed by the measurements carried out to acquire the model parameters for the ELENA B-train. Finally, an uncertainty estimation is performed to identify the combined standard uncertainty of the B-train measurement, as well as the individual contribution of each error source.

3.2 | Proposed model

The B-train system distributes to its users the average field $\bar{B}(t)$ of every bending dipole in the ring, assumed to be identical to each other:

$$\bar{B}(t) = \frac{\mathbb{I}(t)}{l^*}, \quad (3.1)$$

where l^* is calculated according to Equation 2.11. For the ELENA ring $r = 0.927$ m and $N_B = 6$ is the number of dipole magnets. In the formulation of the model, the time t and the excitation current $I = I(t)$ are used interchangeably as independent variables, assuming that only one cyclic waveform is used and that the inverse relationship $t(I)$ is uniquely defined on the hysteresis loop branches.

3.2.1 | Field integral measurement

In Equation 2.7, it was shown that the integral field, $\mathbb{I}(t)$, is obtained from the combination of a field marker output and the magnetic flux linked through the coil. The integration limits are extended for simplicity to infinity. For the ELENA B-train, this is justified, as the length of the coil stretches beyond the magnet's poles and allows to acquire the whole magnetic field produced within the requested tolerance.

The relationship between the measured flux and the integral field can be described by the effective width parameter. However, if the iron yoke enters the saturation stage as the field increases, the field profile flattens, potentially influencing this parameter. In the case of the ELENA bending magnets, an average effective width can be assumed, as saturation is negligible. This parameter is practically a constant and can be expressed as:

$$\bar{w}_{\text{eff}} = \frac{\Phi(\bar{t})}{\mathbb{I}(\bar{t})} \quad (3.2)$$

where \bar{t} is the time when the magnet's nominal excitation current is reached, after eddy current effects have decayed.

The value of the absolute integral field within the gap of the magnet is found by combining the output of the coil measurement and the field marker integration constant. The coil measurement on its own cannot provide an absolute measurement of the integral field, and hence the field marker is necessary for contributing an absolute reference point. The combination of the two sensor outputs occurs by splitting the time axis into a sequence of integration intervals $t_k \leq t < t_k + 1$, with $k = 1, 2, \dots$ where each t_k represents the time instant when a field marker trigger is received. The integral field is calculated during each interval in this manner:

$$\mathbb{I}(t) = \Delta\mathbb{I} + \mathbb{I}(t_k) = \frac{\Delta\Phi(t)}{\bar{w}_{\text{eff}}} + \mathbb{I}_0, \quad (3.3)$$

where $\Delta\mathbb{I}$ represents the coil measurement and \mathbb{I}_0 represents the integration constant at the preset field marker level. The flux measurement is considered as:

$$\Delta\Phi(t) = - \int_{t_k}^t (V_c(\tau) - \delta V) d\tau, \quad (3.4)$$

where δV represents the unavoidable voltage offset, which leads to a field drift. As the offset is noted to vary randomly over time scales of seconds and longer, an effective systematic correction is not possible. Several methods to calculate and correct the field drift are reviewed in [202]. In all B-train systems at CERN, the drift correction method consists of resetting the integration at every t_k , as well as including one or more field markers per cycle in case of long cycles. Once a digital trigger is received from the field marker, the B-train output is smoothed over a period of 20 ms, to avoid discontinuities which can destabilise the beam. As a result, the field marker is contributing to the measurement in two ways: the coil integration constant as a reference measurement point, as well as drift correction.

3.2.2 | Integration constant

Since the integration constant is an integral field parameter in T_m , it cannot be measured directly, as the field marker contributes a magnetic field local value $B(t_k, 0)$ in T. However, it is a highly accurate and reproducible measurement. Consequently, an additional parameter to translate the measurement in T to T_m is required. The ratio between the desired integral field constant and the measured local field is represented by the magnetic length parameter, normally defined as a function of the excitation current:

$$\ell_m(t(I)) = \frac{\mathbb{I}(t(I))}{B(t(I), 0)}, \quad (3.5)$$

such that $\mathbb{I}(t_k) = \ell_m(I(t_k))B(t_k, 0)$. This definition is based on a hard edge approximation of the true field shape of the profile along the magnet's longitudinal dimension, as can be seen in Figure 3.1 [203].

An example of the ELENA dipole magnetic length at the centre of the magnet, measured at 200 A/s is illustrated in Figure 3.2. In all legacy B-train systems at CERN, a fixed value of ℓ_m for each field marker is considered, obtained from off-line measurements. This is then adjusted by trial and error when the beam is present in the machine. A novel calibration method for this parameter is

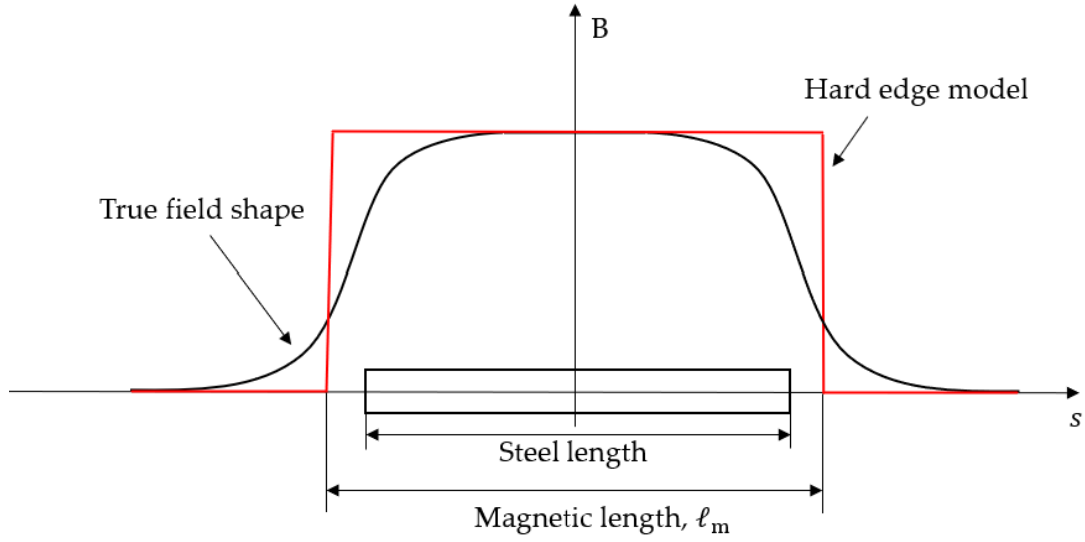


Figure 3.1: Hard edge model used to define ℓ_m along the length of a magnet [203].

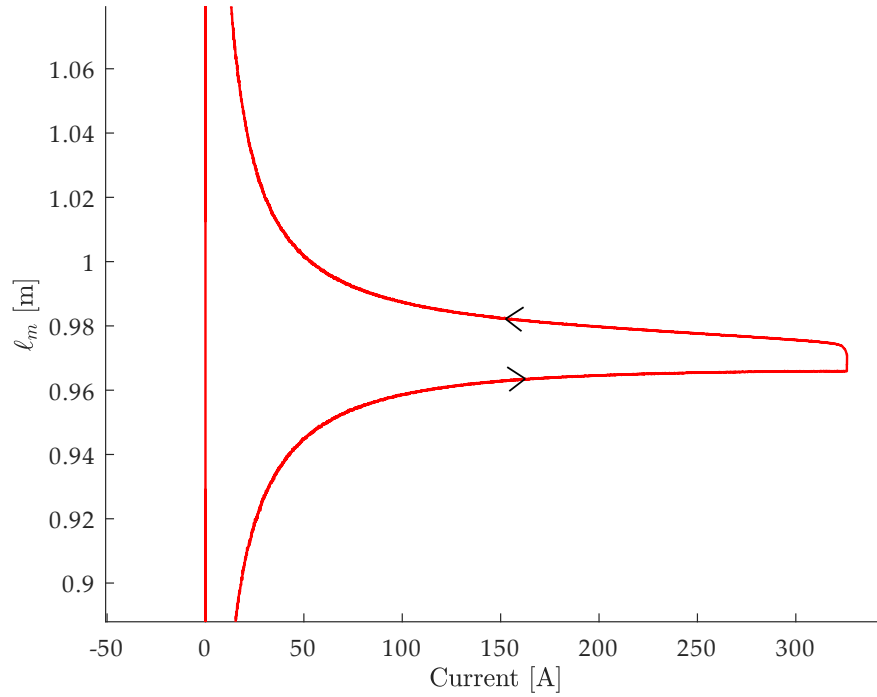


Figure 3.2: Measured magnetic length at ± 200 A/s. The values up to 0.98 were measured during ramp-up whilst values higher than 0.98 were measured during ramp-down.

proposed in Section 3.3.4, where the value is obtained directly from an *in-situ* measurement.

3.2.3 | Model definition

The measurement model can be defined by combining Equation 3.1 and Equation 3.3. In addition, three further parameters are added to represent non-ideal effects:

$$\bar{B}(t) = \frac{(1 + \alpha)(1 + \epsilon)}{l^*} \left[(1 + \eta) \frac{\Delta\Phi(t)}{\bar{w}_{\text{eff}}} + \mathbb{I}_0 \right]. \quad (3.6)$$

The field integral, obtained by the combination of the induction coil and the field marker is defined within the square brackets. The integrated flux is compensated by the parameter $1+\eta$, which corrects for the gain error in the coil acquisition chain (including the pre-amplifier, filter, ADC and effective width). Compensation for the potential coil offset with respect to the central beam trajectory is accounted for by the coefficient $1+\epsilon$. Since the field is not uniform in the transverse direction, an offset in the coil's placement may cause a systematic error. The remaining coefficient $1+\alpha$ is included to consider any difference between the reference and ring magnets. The three correction terms η , ϵ and α are non-dimensional and expected to be much smaller than one.

3.3 | Parameter identification

This section describes in detail each model parameter, as well as the respective identification procedure implemented for the ELENA B-train commissioning. The measurements of the reference magnet and acquisition chain presented in this section were carried out during the commissioning stage of the B-train. The measurements of the individual ring magnets, on the other hand, were performed by CERN's magnetic measurement team as part of the acceptance test campaign of the ELENA dipole magnets in 2015.

3.3.1 | Induction coil gain error, η

The induction coil gain factor $1+\eta$ is introduced to account for scale errors by the electronic coil acquisition chain. This configuration is modelled using the equivalent circuit in Figure 3.3. The induced voltage is represented by V_c and the coil effects are modelled by R_c , L_c and C , which represent the resistance, self-inductance of the coil, and the sum of distributed capacitance between the turns of the coil and the shielded cable respectively. This factor is included as part of the model to compensate for two error sources: the gain error k_{int} of the input stage of the integrator, which includes the ADC and filter, and the

loading effect as a result of the finite input resistance of the integrator, R_{in} . Since the useful frequency content of the measured magnetic field is normally below 100 Hz, the low-frequency approximation is applied. As a result, the induction coil gain factor that needs to compensate for the attenuation due to the circuit's input impedance and ADC gains is defined in Equation 3.7 as:

$$1 + \eta = \left(1 + \frac{R_c}{R_{\text{in}}}\right) (1 + k_{\text{int}}). \quad (3.7)$$

The values of R_c and R_{in} were obtained using an Agilent 34401A multimeter [204]. In the case of the ELENA B-train, $R_c \simeq 5 \text{ k}\Omega$ and $R_{\text{in}} \simeq 2 \text{ M}\Omega$. The nominal uncertainty of the resistance measurements in the range considered is 1.5 units, which is negligible when compared to the standard deviation of the ambient temperature of the room housing the reference magnet. The deviation in temperature has been calculated to be around $0.7 \text{ }^\circ\text{C}$, based on around 178,000 data points taken over a year of machine operation. Figure 3.4 shows the data points, where the gaps represent breaks in machine operation. Considering the temperature coefficient of the resistivity of copper of $0.004 \text{ }^\circ\text{C}^{-1}$, the individual uncertainty R_c is still around 30% that of R_{in} .

The integrator gain, k_{int} , can be measured by feeding a reference voltage source \bar{V} to the integrator input for a precisely known time interval Δt . The product of these two parameters is then compared to the measured flux $\Delta\Phi$ as follows:

$$k_{\text{int}} = 1 - \frac{\Delta\Phi}{\bar{V}\Delta t}. \quad (3.8)$$

The uncertainties of both reference voltage and integration time are in the order of a few ppm and can be neglected. The repeatability of the flux measurement,

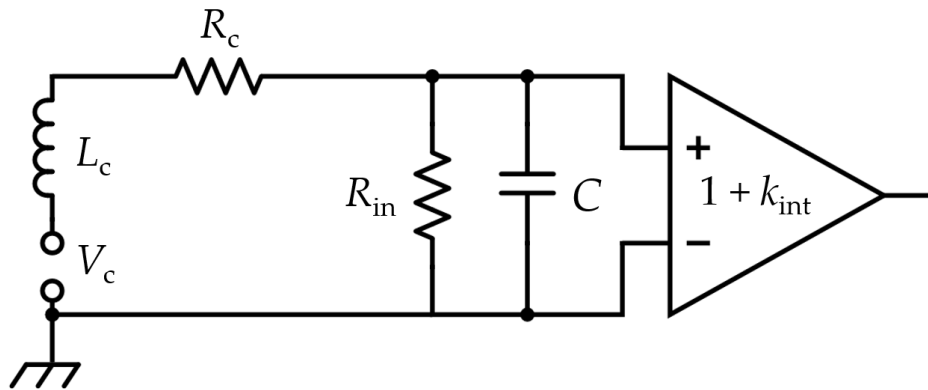


Figure 3.3: Equivalent model of the coil and acquisition chain.

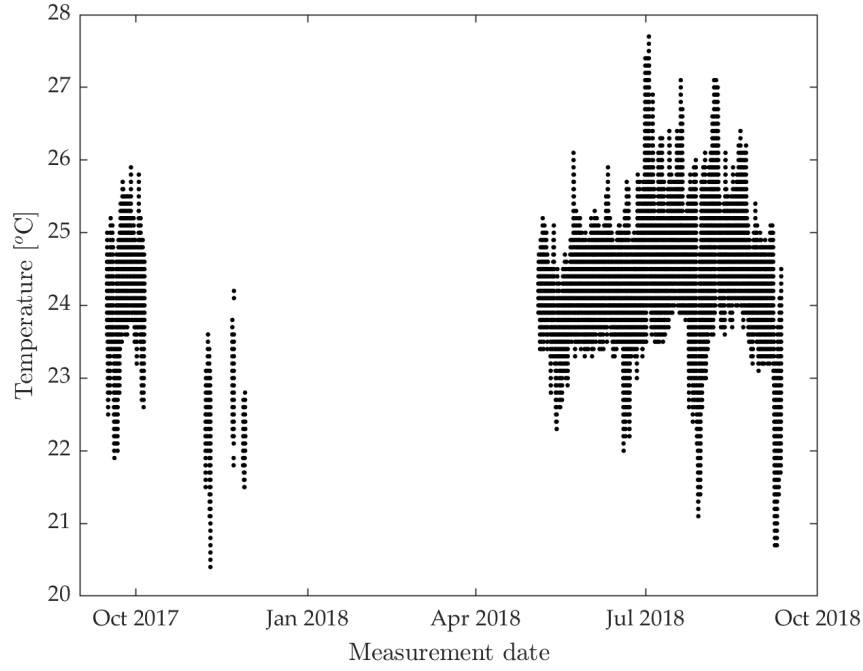


Figure 3.4: Measurement of the ambient temperature during the machine’s commissioning period.

on the other hand is the remaining major source of uncertainty, which is affected by integrator drift and is normally about 0.3 units.

3.3.2 | Effective coil width, \bar{w}_{eff}

In Equation 2.7, the effective width of a coil has been defined as an average width weighted by the field and number of turns. Despite the fact that a lot of effort goes in the winding process of the coils, the total surface of the coils can vary from each other by a few 10^{-3} [44]. Hence, each coil needs to be calibrated separately before it is used. The coil’s effective width parameter cannot be measured geometrically to an accurate degree; however it can be determined by performing either one of two different off-line measurements:

- using Equation 3.2, knowing the integral field $\Delta\mathbb{I}(\bar{t})$ from an independent measurement, this can be compared to the acquired flux change at this point. Such a measurement of the integral field can be obtained, in curved magnets such as the ELENA bending magnets, with a finely-spaced Hall probe map. This measurement is, however, very time consuming and expects the Hall probe map to be cross-calibrated against a more precise absolute reference, such as NMR or stretched-wire measurements.

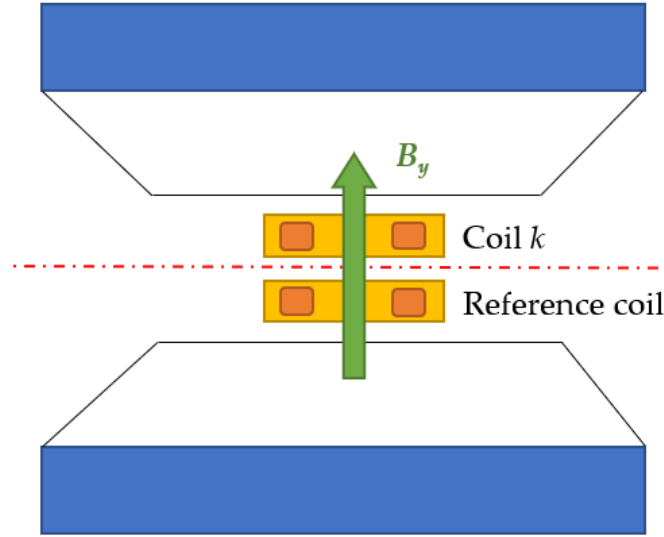


Figure 3.5: Relative cross-calibration coil placement. A reference coil and the coil that is going to be calibrated are subjected to the same field, whilst the resulting flux is measured.

- performing a relative cross-calibration by comparing the k -th coil in an array against a reference coil, placed on top of it symmetrically across the magnet mid-plane as shown in Figure 3.5, so that it is exposed to the same field inside the magnet gap. The ratio of the measured flux differences provides the effective width:

$$\bar{w}_{\text{eff}}^k = \bar{w}_{\text{eff}}^{\text{ref}} \frac{\Delta\Phi^k}{\Delta\Phi^{\text{ref}}}. \quad (3.9)$$

When calibrating a significant number of coils, this method is effective, as long as the absolute calibration of the reference coil is known.

For the ELENA B-train fluxmeter coil array, the former method is used to determine the effective width for one coil, whilst the latter calibration procedure is carried out to calibrate the rest of the fluxmeter coil array used in the reference magnet. For the relative cross-calibration, the magnet is first pre-cycled to allow transient phenomena to die out, and subsequently the magnet is excited with a current cycle ranging from 0 to 275 A. Figure 3.6 shows the setup implemented, where eight consecutive measurements are taken. Applying Equation 3.9, an estimate of $\bar{w}_{\text{eff}} = 2.84146$ m is obtained over eight trials. Consequently, an uncertainty of $80 \mu\text{m}$ (0.28 units^1) is calculated.

¹Normalisation for measurements related to the ELENA ring is done with respect to the nominal field level of 0.36 T.



Figure 3.6: ELENA coil cross-calibration measurement

3.3.3 | Coil offset error, ϵ

The coil offset factor, $1 + \epsilon$, is included in the measurement model to account for the transversal difference in position between the coil and the nominal beam path, denoted as Δx . The ELENA B-train system makes use of two coils, one at the centre and another at $x = 22$ mm. The biggest contribution to the non-uniformity is given by the in-built integrated field gradient:

$$\mathcal{G}(t) = \int_{-\infty}^{+\infty} \frac{dB(t,s)}{dx} ds \approx 0.208 \text{ Tm/m}, \quad (3.10)$$

This gradient is a result of the sector shape of the poles and plays a crucial role in keeping the beam focused. The corresponding field error for the central coil, relative to the integrated field is represented as:

$$\epsilon(t) = \frac{\mathcal{G}(t)}{\mathbb{I}(t)} \Delta x. \quad (3.11)$$

The uncertainty of ϵ is dominated by the uncertainty of the transversal offset, which for the ELENA is obtained by measuring the position of the induction coil relative to the magnet with a 3D laser tracker. This instrument produces a laser beam sent via a two-axis servo-controlled mirror at a suitably placed reflecting target. The target returns the laser beam back along the same optical path [205]. The system measures the 3D coordinates in a polar coordinate system, and having an accurate drawing of the measured object, one can deduce the absolute position of any other point on the fixed object.

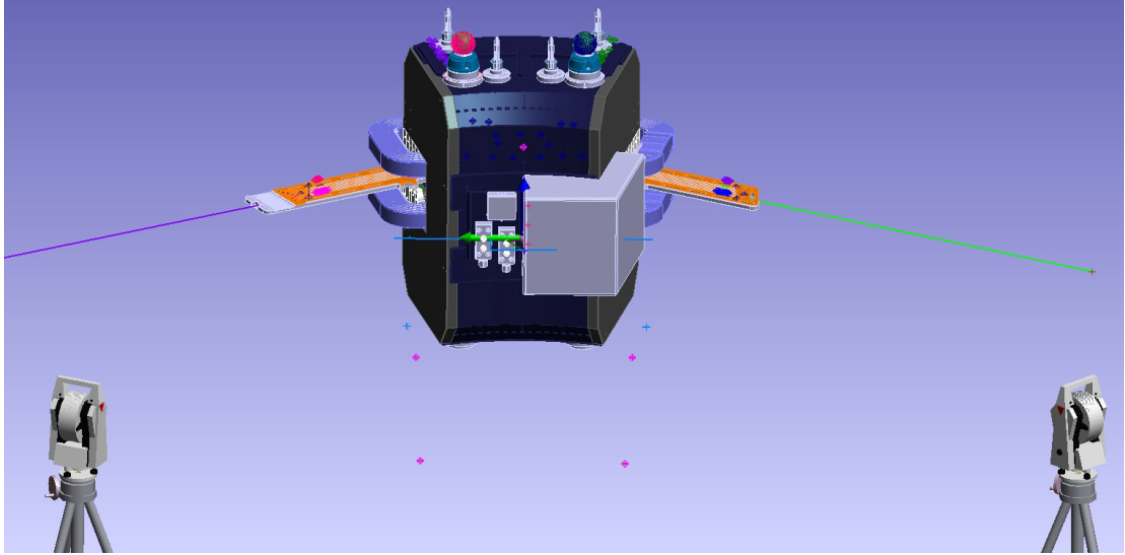


Figure 3.7: Laser tracker survey measurements performed on the ELENA reference magnet.

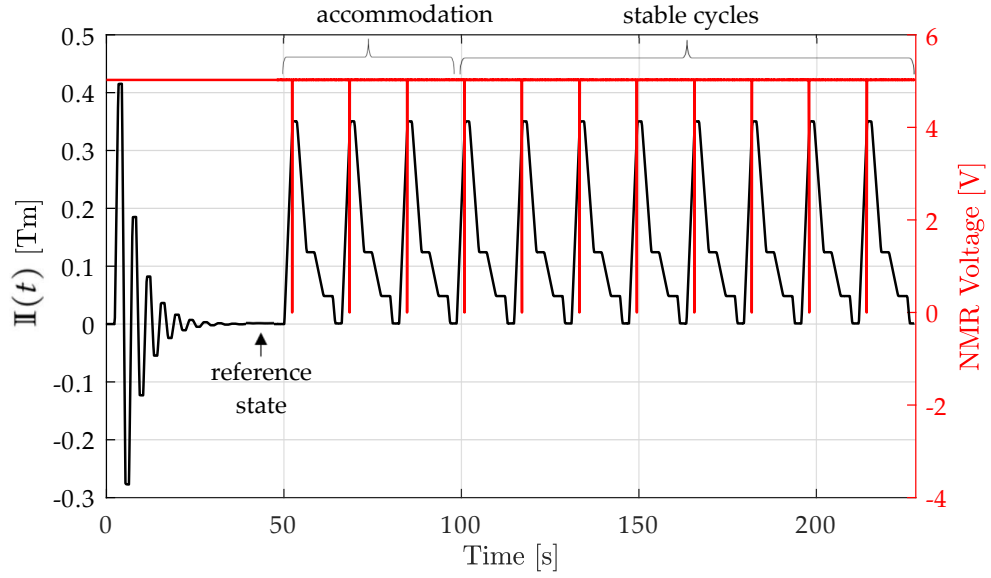
This measurement was performed by CERN’s survey team, purposefully when the synchrotron was turned off to avoid any water pump-induced vibrations on the walls and floor, which would perturb the measurement. The instrument used in this case was Hexagon Metrology’s Leica AT402 [206]. Figure 3.7 shows the measurements obtained superimposed by the magnet and fluxmeter array’s 3D diagrams. The value of Δx was subsequently quantified to about 0.2 mm, resulting in $\epsilon \approx -6 \times 10^{-5}$.

3.3.4 | Integration constant, \mathbb{I}_0

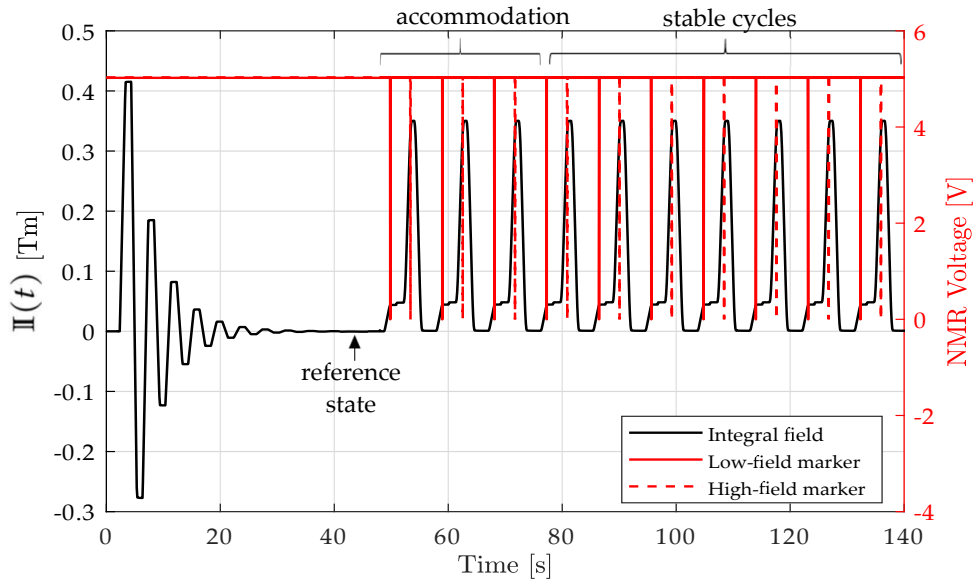
The integration constant provides an absolute reference point to the relative coil measurement. The identification procedure for this parameter requires a bipolar power supply and involves the *in-situ* measurement of the coil voltage and field marker trigger signals. Figures 3.8(a) and 3.8(b) show the measurement data for the ELENA deceleration and acceleration cycles respectively, where the magnets are first degaussed to reach a demagnetised reference state. Then, the excitation current is cycled, and the flux change measured by the coil is integrated according to:

$$\mathbb{I}(t) = \mathbb{I}_{\text{res}} + \frac{\Delta\Phi(t)}{\overline{w}_{\text{eff}}}. \quad (3.12)$$

Following the degaussing cycle, the magnet settles on a stable hysteresis loop after an initial transient of three cycles pertaining to the magnet’s accommodation process. At this point, the field integral is reproducible from cycle to cycle. The integrator drift is corrected on the stable cycles by assuming



(a) Deceleration cycle: measurements of the integral field and the NMR voltage at 340 mT.



(b) Acceleration cycle: measurements of the integral field and the NMR voltage at 45 mT and 340 mT.

Figure 3.8: Absolute *in-situ* calibration measurements.

loop closure, an assumption validated by independent NMR measurements. The integration constant is derived for every field marker by averaging the integral field at the respective trigger time over $n \geq 7$ stable cycles:

$$I_0 = \frac{1}{n} \sum_{j=3}^{3+n} I(t_j). \quad (3.13)$$

For the ELENA B-train, this calibration procedure has been performed repeatedly at two different field levels for both the acceleration and deceleration cycles. The resulting coefficients for the deceleration cycle are noted below, and the result's uncertainty has been estimated from the standard deviation of the results:

- $\mathbb{I}_0 = 326.836 \text{ mTm}$ at 340 mT, $u(\mathbb{I}_0) = 13 \text{ } \mu\text{Tm}$
- $\mathbb{I}_0 = 43.125 \text{ mTm}$ at 45 mT, $u(\mathbb{I}_0) = 12 \text{ } \mu\text{Tm}$

This process must be repeated for every magnetic cycle and field marker. The effect of doing so on operation is minimal as the time taken, including setting up, post-processing and uploading results is only a few hours.

The reference state chosen for this measurement is the residual magnetisation, \mathbb{I}_{res} , after degaussing the magnet. This is measured with a Projekt Elektronik Teslameter FM 3002 Hall probe [207], cross-calibrated with two fluxgate magnetometers (Bartington Mag-03MS70 and Mag-03MS1000 [208]) in the range below 1 mT. The residual field is measured along the central induction coil inside the reference magnet, which is aligned along the beam trajectory, and then integrated with respect to the distance from the centre of the magnet. Figure 3.9 shows the measured field along the beam trajectory. Two peaks in the field at -400 mm and 400 mm are noted, which correspond to the end-plates of the magnet, made of ARMCO pure iron in place of the laminations in the rest of the magnet. The considered field values are an average of the measured data points. Subsequently, the standard deviation at each point is calculated and integrated, in order to estimate the error in measurement. The integral residual field after degaussing is calculated to be $0.0303 \pm 0.0054 \text{ mTm}$ (0.8 units of the nominal field).

3.3.5 | Reference-to-ring error, α

The measurement model includes a parameter to account for differences between each individual magnet in the ring and the reference magnet. The magnets can differ minimally due to assembly tolerance, or errors in the number of laminations in the yoke. Regarding the ELENA bending magnets, for contingent reasons, the reference magnet's yoke was produced using a different steel type than the other seven magnets (the six magnets in the ring, plus a spare magnet), making them substantially different. This makes the introduction of this parameter in the ELENA B-train measurement especially important.

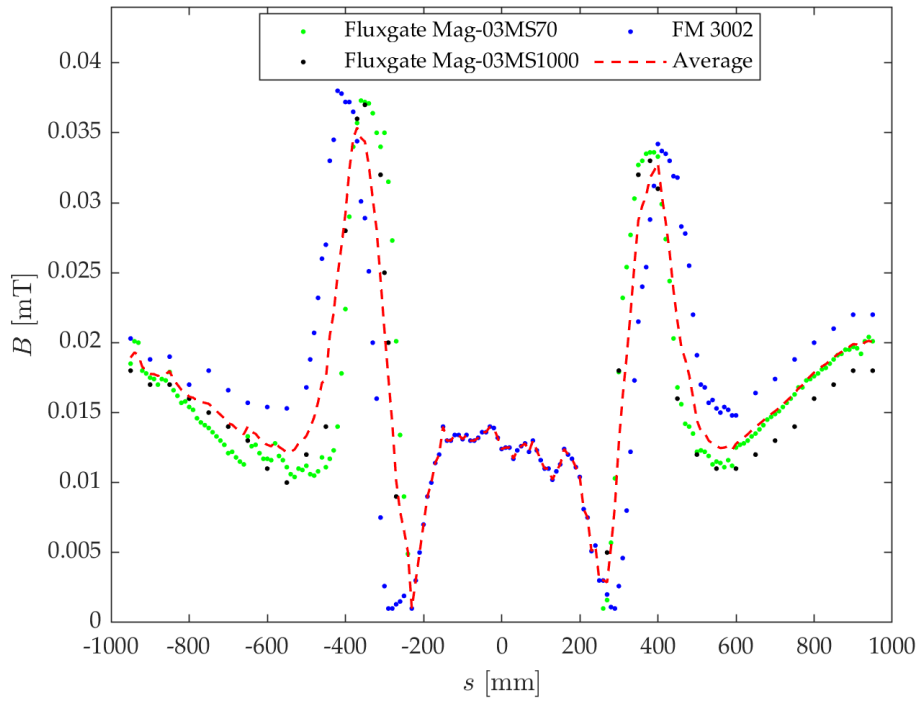


Figure 3.9: Residual field measurement after degaussing. Multiple sensors are used, and an average is calculated along the magnet's longitudinal plane.

The measurement of each individual magnet is typically done before these are assembled in the ring. The following measurement campaigns were carried out:

- acceptance cycles up to 326 A at 200 A/s: all magnets [43];
- operational cycles up to 276 A at 115 A/s: reference and spare magnet only.

As can be noted, the operational magnetic cycles implemented during commissioning were optimised at a lower maximum current level than the cycles applied during the acceptance tests, which were intended to cover the full design range. Since measurement of the individual ring magnets is not possible after they are installed, observations have to be made by adapting these acceptance measurements.

The relationship between magnets is represented as a function of the excitation current by the integral transfer function (shown in Figure 3.10):

$$\mathcal{T}(I, \dot{I}) = \frac{\mathbb{I}(t(I))}{I}, \quad (3.14)$$

which is the ratio of the field to the excitation current for a cycle with a given ramp rate \dot{I} . This expression and the following ones have two solutions, one

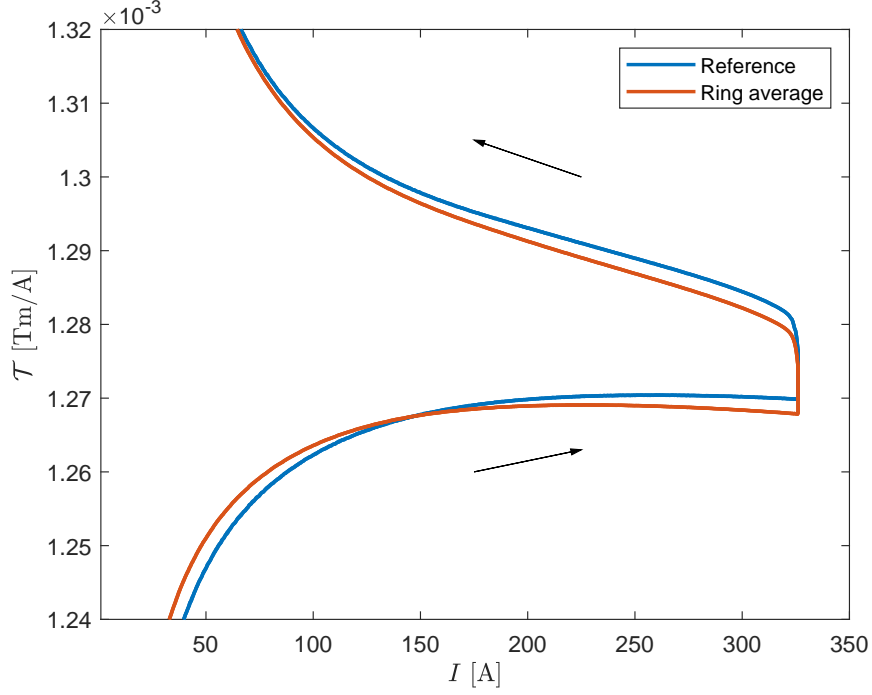


Figure 3.10: The reference and ring magnets' acceptance cycle transfer function at 200 A/s.

for each hysteresis loop branch. As can be observed in Figure 3.10, the magnet does not reach saturation, however the width of the hysteresis is around 2%, which is large when compared to other synchrotrons (e.g. 0.5% in the PSB). This is significant for the ELENA as it is the only synchrotron expected to both accelerate and decelerate particles, as this is necessary for commissioning the electron cooler. In order to consider the effect of eddy current losses on the hysteresis loop width, parametrisation in terms of \dot{I} is needed, as clearly visible in Figure 3.11. The reference-to-ring scaling factor is hence expressed as a function of the current I :

$$1 + \alpha(I, \dot{I}) = \frac{\mathcal{T}_{\text{ring}}(I, \dot{I})}{\mathcal{T}_{\text{ref}}(I, \dot{I})}, \quad (3.15)$$

where the subscripts ref and ring represent the reference magnet and the average of the magnets in the ring respectively.

An intermediate scaling factor between the two ramp rates, 115 and 200 A/s, has been derived from measurements of the spare magnet, assuming that the effect of a ramp rate change is approximately equal for all the magnets. The two hysteresis loops are illustrated in Figure 3.11 and the scaling factor can be

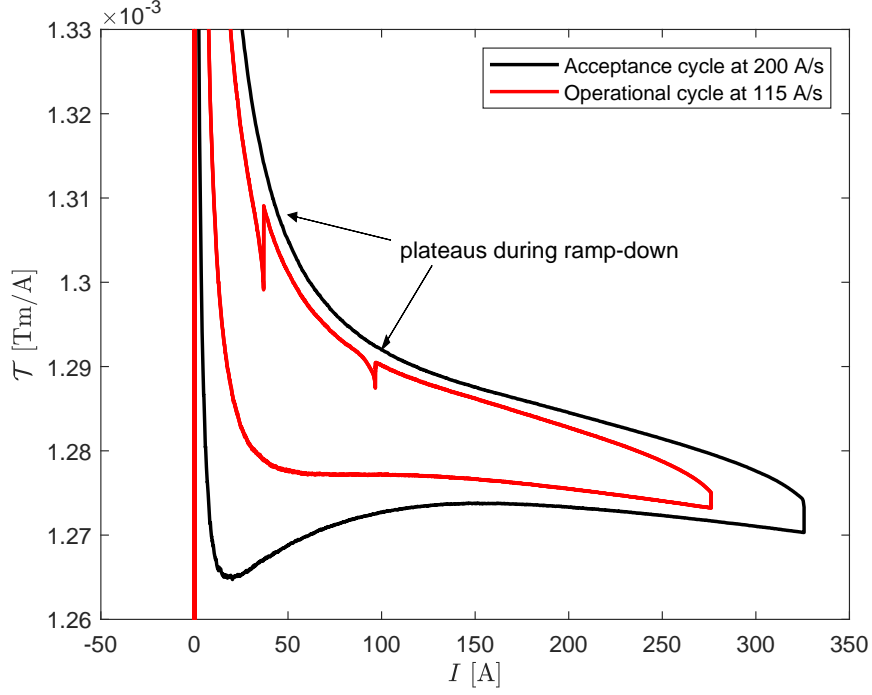


Figure 3.11: Acceptance and operational transfer functions for the spare magnet. The marked plateaus refer to the two ramp-down plateaus in the antiproton deceleration mode of operation.

defined as:

$$\chi(I, 115) = \frac{\mathcal{T}_{\text{spare}}(I, 115)}{\mathcal{T}_{\text{spare}}(I, 200)}. \quad (3.16)$$

Operation cycles include several plateaus, during which the field varies while the current is constant and eddy currents are dying out. Hence, by using a double exponential curve as a scaling factor, the curves have been smoothed to avoid discontinuities. At this point, the behaviour of each magnet measured in the acceptance campaign can be extrapolated to the required operational conditions. An example is shown for ramp-down in Figure 3.12 and is represented as:

$$\mathcal{T}_{\text{ring}}(I, 115) = \chi(I, 115) \mathcal{T}_{\text{ring}}(I, 200), \quad (3.17)$$

$$\mathcal{T}_{\text{ref}}(I, 115) = \chi(I, 115) \mathcal{T}_{\text{ref}}(I, 200). \quad (3.18)$$

In the end, the reference-to-ring scaling factor under operational conditions is illustrated in Figure 3.13 and is defined as:

$$1 + \alpha(I, 115) = \frac{\mathcal{T}_{\text{ring}}(I, 200)}{\mathcal{T}_{\text{ref}}(I, 115)} \frac{\mathcal{T}_{\text{spare}}(I, 115)}{\mathcal{T}_{\text{spare}}(I, 200)}. \quad (3.19)$$

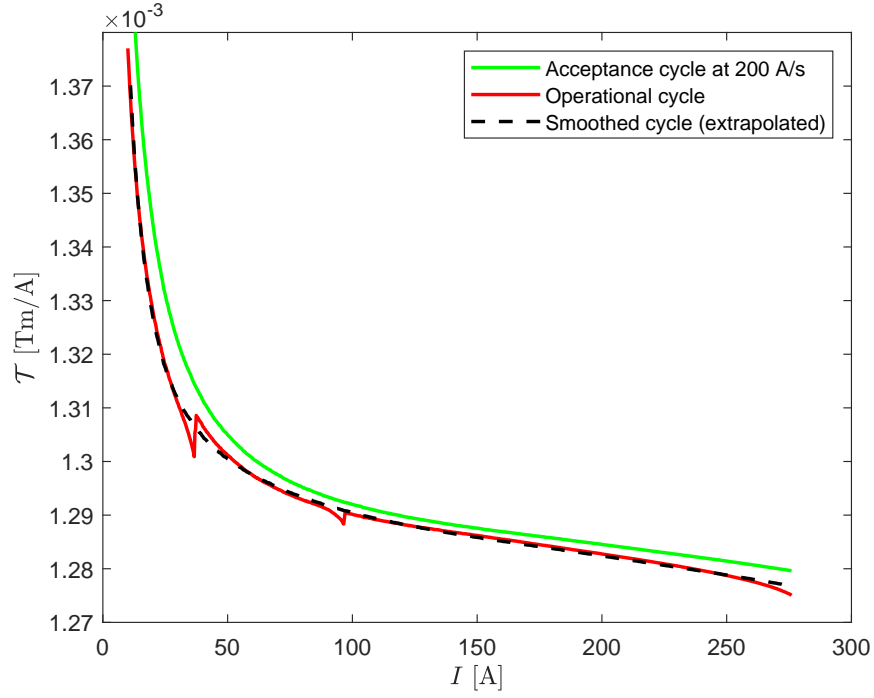


Figure 3.12: Operational cycle transfer function for the spare magnet extrapolated during ramp-down.

It can be noted that the calculated parameter is fairly stable on the ramp-down of the deceleration cycle, which is the most important criterion for the ELENA. Up until the commissioning of the ELENA ring, the FIRESTORM hardware could not handle coefficients which vary in real-time. Therefore, an average value has been implemented for operation, whilst the standard deviation of the residual is considered to estimate the associated uncertainty:

$$\bar{\alpha} = \frac{1}{I_{\max} - I_{\min}} \int_{I_{\min}}^{I_{\max}} \alpha(I, 115) dI \approx 0.999, \quad (3.20)$$

$$u(\alpha)^2 = \frac{1}{I_{\max} - I_{\min}} \int_{I_{\min}}^{I_{\max}} (\alpha(I, 115) - \bar{\alpha})^2 dI \quad (3.21)$$

$$\Rightarrow u(\alpha) \approx 3.2 \times 10^{-4}.$$

Considering the scaling factor of the ramp-up of the accelerating cycle, the variation is much larger, around 0.5%, which leads to a bigger uncertainty of 1.45×10^{-3} . The different residual field level in the reference and ring magnets may be attributed to this result, as this value impacts the up-branch of the hysteresis loop of the transfer function, as this approaches the mid-range linear region.

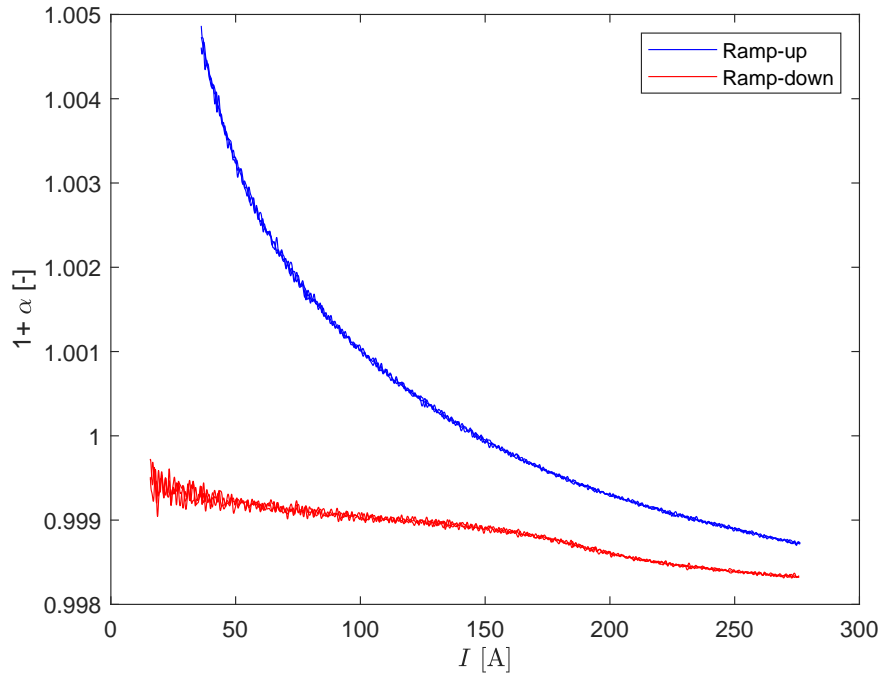


Figure 3.13: Reference-to-ring scaling factor. The hysteresis cycle's ramp-up represents acceleration of H^- ions, while the ramp-down represents antiproton deceleration.

3.4 | Uncertainty estimation

The development of a measurement model permits the opportunity of obtaining a detailed quantitative estimate of the measurement uncertainty. This is necessary both for the instrument developers to identify improvements in the individual components of the acquisition chain, as well as for the machine operators and end users of the B-train system. Understanding the source of the measurement uncertainty can lead to a better understanding of the system and can allow planning for future optimisations of the software.

Expressing the systematic and random errors related to the measurement is one approach used for describing the measurement. The 'Guide to the expression of uncertainty in measurement' [209] provides a different method to perceive the quality of the measurement output, by grouping all sources of errors in one uncertainty value. The guide identifies two methods for expressing the uncertainty of a measurement:

- Type A uncertainties obtained from observed repetitions of the measurement.
- Type B uncertainties evaluated using available knowledge.

Defining the output quantity as z , and the input parameters $p_1, p_2, p_3, \dots, p_N$, then a relationship between the two quantities is [209]:

$$z = f(p_1, p_2, p_3, \dots, p_N). \quad (3.22)$$

An estimate of the output quantity is hence defined as:

$$\bar{z} = f(\bar{p}_1, \bar{p}_2, \bar{p}_3, \dots, \bar{p}_N). \quad (3.23)$$

In order to estimate the uncertainty of \bar{z} using information on $\bar{p}_1, \bar{p}_2, \bar{p}_3, \dots, \bar{p}_N$, the measured quantities are assumed to have normal distributions, and the function f and its derivative are assumed to be continuous within the range of \bar{z} . A Taylor series limited to the first order gives:

$$z - \bar{z} = \sum_{i=1}^N \left(\frac{\partial f}{\partial p_i} \right) (p_i - \bar{p}_i), \quad (3.24)$$

where $(p_i - \bar{p}_i)$ are small differences. Applying the square of Equation 3.24:

$$(z - \bar{z})^2 = \sum_{i=1}^N \left(\frac{\partial f}{\partial p_i} \right)^2 (p_i - \bar{p}_i)^2 + 2 \sum_{i=1}^{N-1} \sum_{j=i+1}^N \frac{\partial f}{\partial p_i} \frac{\partial f}{\partial p_j} (p_i - \bar{p}_i)(p_j - \bar{p}_j). \quad (3.25)$$

Considering the differences in Equation 3.25 as experimental measurements, the variance of the output quantity can be expressed as the combination of the variances $u^2(\bar{p}_i)$ and of the covariances $u(\bar{p}_i, \bar{p}_j)$ of the input parameters estimates [210]. The law of forward uncertainty propagation is derived for the combined variance $u_c^2(\bar{z})$:

$$u_c^2(\bar{z}) = \sum_{i=1}^N \left(\frac{\partial f}{\partial p_i} \right)^2 u^2(\bar{p}_i) + 2 \sum_{i=1}^{N-1} \sum_{j=i+1}^N \frac{\partial f}{\partial p_i} \frac{\partial f}{\partial p_j} u(\bar{p}_i, \bar{p}_j). \quad (3.26)$$

The partial derivatives in Equation 3.26 are also referred to as sensitivity coefficients. If the input quantities are not correlated or have a low degree of correlation such that the covariance $u(\bar{p}_i, \bar{p}_j)$, the combined uncertainty is expressed as:

$$u_c(\bar{z}) = \sqrt{\sum_{i=1}^N \left(\frac{\partial f}{\partial p_i} \right)^2 u^2(p_i)}. \quad (3.27)$$

Table 3.1: Sources of uncertainty in the ELENA measurement model

Parameter, p_i	Source of uncertainty	Type of uncertainty
α	Assumption that this factor is a constant	Type A
ϵ	Uncertainty on the transversal coil position measurement	Type B
\mathbb{I}_0	Repeatability of high field marker integration constant	Type A
η	Effect of temperature fluctuations on coil resistance	Type B
\bar{w}_{eff}	Repeatability of the coil width calibration	Type A
$\Phi(t)$	Repeatability of flux measurement	Type A

In the case of B-train systems, applying this law, the partial derivatives of the average field are computed with respect to each one of the six arguments p_i displayed in Equation 3.6, which includes five parameters, plus the measured flux:

$$\frac{\partial \bar{B}}{\partial \alpha} = \frac{(1 + \epsilon)}{l^*} \left[(1 + \eta) \frac{\Delta \Phi(t)}{\bar{w}_{\text{eff}}} + \mathbb{I}_0 \right], \quad (3.28)$$

$$\frac{\partial \bar{B}}{\partial \epsilon} = \frac{(1 + \alpha)[(1 + \eta)\Delta \Phi(t) + \mathbb{I}_0 \bar{w}_{\text{eff}}]}{l^* \bar{w}_{\text{eff}}}, \quad (3.29)$$

$$\frac{\partial \bar{B}}{\partial \eta} = \frac{(1 + \alpha)(1 + \epsilon)\Delta \Phi(t)}{l^* \bar{w}_{\text{eff}}}, \quad (3.30)$$

$$\frac{\partial \bar{B}}{\partial \bar{w}_{\text{eff}}} = -\frac{(1 + \alpha)(1 + \epsilon)(1 + \eta)\Delta \Phi(t)}{l^* \bar{w}_{\text{eff}}^2}, \quad (3.31)$$

$$\frac{\partial \bar{B}}{\partial \Delta \Phi(t)} = \frac{(1 + \alpha)(1 + \epsilon)(1 + \eta)}{l^* \bar{w}_{\text{eff}}}, \quad (3.32)$$

$$\frac{\partial \bar{B}}{\partial \mathbb{I}_0} = \frac{(1 + \alpha)(1 + \epsilon)}{l^*}. \quad (3.33)$$

The combined standard uncertainty of the average field measurement, $u_c(\bar{B})$, is then derived as:

$$u_c(\bar{B}) = \sqrt{\sum_{i=1}^N \left(\frac{\partial \bar{B}}{\partial p_i} \right)^2 u^2(p_i)}, \quad (3.34)$$

where all the variables are assumed to be normally distributed and independent from each other. Table 3.1 shows the individual uncertainty sources and the uncertainty type. The individual contribution of each term for the ELENA

Table 3.2: Individual uncertainty contributors of the ELENA measurement model in deceleration mode at injection level

Parameter, p_i	Value	$u(p_i)$	$\left(\frac{\partial \bar{B}}{\partial p_i}\right) u(p_i) [\mu\text{T}]$
α	0.0012	3×10^{-4}	221
ϵ	-6×10^{-5}	1.05×10^{-4}	73
\mathbb{I}_0	326.836 mTm	13 μTm	13
η	0.002475	3×10^{-5}	11
\bar{w}_{eff}	2.84146 m	80 μm	10
$\Phi(t)$	0.99411 Tm ²	30 μTm^2	10

measurement of the deceleration cycle, particularly at injection, is shown in Table 3.2. The subsequent combined uncertainty at injection is:

- Ramp-down: $u_c(\bar{B}) = 2.3 \times 10^{-4}$ T (6.4 units),
- Ramp-up: $u_c(\bar{B}) = 5.6 \times 10^{-4}$ T (15.6 units)

The outcome of the uncertainty estimation exercise is that in the case of the ELENA, the implementation of the measurement model on its own is not able to assure an uncertainty value lower than 2 units. It is noted that the measurement is dominated by the errors inherent in the extrapolation to the ring (due to the different composition of the reference magnet and the ring magnets) and the position of the coil. These values are specific to ELENA, hence significantly better performance is anticipated for the other similar systems currently being commissioned. Regarding the ELENA field measurement, the measurement model has to be coupled with a beam calibration method to ensure that the desired performance target is achieved.

3.5 | Conclusion

An upgraded measurement model, that can be used in the commissioning of B-train systems has been presented in this chapter. The model combines measurement theory with empirical observations to infer the absolute average field of the ring based on the measurement of a reference magnet. The most important advantage of such a model is that the B-train system can be commissioned even when the beam is not present. The parameter identification method for every model term has been described as carried out for the ELENA

B-train. An uncertainty estimation exercise has been performed to shed light on the biggest sources of error in the measurement. In the case of the ELENA, the measurement model is not enough to ascertain a reproducibility better than 2 units and hence it has to be accompanied by a beam calibration method to ensure that the target performance is reached.

Chapter 4

Metrological Characterisation and Calibration

4.1 | Introduction

Throughout the commissioning of the ELENA ring, several tests have been carried out to validate the performance of the B-train system, and to understand the sources of error in the measurement. In this chapter, different error sources in the measurement are described and highlighted in the form of a linear model. In addition, three tests characterising the behaviour of the ELENA B-train are described:

- Field marker characterisation tests: taking place at the initial stages of the commissioning period;
- Reliability run: performed when the B-train is setup according to the measurement model;
- Beam calibration: carried out when the beam is available in the ring.

The first test has been performed to validate the field marker sensor for operation. Besides making sure that the sensor is repeatable within the desired target, the field uniformity of the magnet is checked to be within the acceptable

limits of the sensor, and appropriate ramp rate values for the operation of the ring are proposed. Secondly, the reliability run measurements are aimed to confirm the instrument's performance on a statistical basis. Finally, the beam calibration procedure is described, which corrects the systematic errors within the instrument, as well as the results obtained for the ELENA B-train.

4.2 | B-train characterisation

The metrological performance of an instrument can be identified by characterising the different measurement error sources. These errors can be classified in two categories: random errors associated with the fact that when repeating a measurement, a different measured quantity from the previous value is obtained; as well as systematic errors resulting in an offset between the measured and reference values [209]. A simple model to represent these errors in the measurement is a linear, additive model [211]:

$$\bar{B}(t) = (1 + \lambda)B(t) + \Delta B + \sigma_r(t), \quad (4.1)$$

where $\bar{B}(t)$ refers to the measured and transmitted B-train output whilst $B(t)$ is the actual magnetic field value seen by the beam. The remaining three terms represent three types of errors. The parameter $(1 + \lambda)$, represents a gain error, where normally $|\lambda| \ll 1$. The term ΔB , represents the offset error. These two terms jointly represent the systematic error. The last term, σ_r indicates the random error, typically assumed as identically distributed. This parameter is a function of time that can be represented by the sum of three uncorrelated contributions, which therefore add quadratically:

$$\sigma_r(t) \approx \sqrt{\sigma_d^2(t) + \sigma_n^2 + \sigma_m^2}, \quad (4.2)$$

where σ_d is the uncertainty in the field measurement due to integrator drift as a function of time, σ_n represents the uncertainty due to random noise and σ_m is the uncertainty associated to the repeatability of the field marker. These contributions are described individually in the upcoming section, including the method by which they have been evaluated from experimental data.

4.2.1 | Random error sources

Random errors are caused by fluctuations in the instrument reading, resulting in an unpredictable interpretation of the measurand. The three random error sources in the B-train measurement are the integrator drift fluctuations, noise resulting from the coil measurement and the field marker trigger generation time.

4.2.1.1 | Integrator drift contribution, σ_d

The integrator drift error is the most significant error in inductive field measurements. Parasitic voltages in the electronics and thermoelectric effects cause a small offset voltage, leading to a drifting output when integrated. Several in-built strategies are implemented in the B-train's integrator, including a voltage source in series with the input, that is set manually via a potentiometer to eliminate the offset voltage. As the voltage offset varies with time, the periodic integrator reset using field markers is crucial to prevent integrator drift from accumulating indefinitely. This would result in unacceptable deviations from the actual field, as the total integration time can be of the order of months. Nonetheless, the drift accumulated within one cycle can still present a problem, especially for the ELENA, which operates using long cycles. This validates the decision to set the field marker to trigger just before the beam's injection, when the accuracy required by the measurement is most critical.

In order to evaluate the drift, the most practical method is to identify a time interval $(t_p, t_p + \Delta t)$ during which the magnetic field is known beforehand to be stable, due to the magnet excitation current $I(t)$ being kept constant. Such field plateaus are common in all synchrotrons, where they are used for beam injection, extraction or in the case of the ELENA for electron cooling. One must keep in mind to adjust the time interval to avoid possible transients due to power converter instability or eddy current decay. The drift rate \dot{B}_d , in T/s, for a given cycle where a plateau has been identified, is evaluated in the first approximation in Equation 4.3:

$$\dot{B}_d = \frac{\bar{B}(t_p + \Delta t) - \bar{B}(t_p)}{\Delta t} - \left. \frac{B}{I} \right|_I \dot{I}, \quad (4.3)$$

where an appropriate correction is affected for the excitation current drift, \dot{I} , scaled by the field-to-current ratio of the magnet evaluated at the appropriate

current level. Another representation can be achieved by considering the presence of noise, by computing a least-squares linear regression model according to Equation 4.4:

$$\tilde{B}(t) = \tilde{B}_0 + \left(\dot{B}_d - \frac{B}{I} \bigg|_I \dot{I} \right) (t - t_p). \quad (4.4)$$

The voltage offset which causes the observed field drift is given by:

$$V_0 = \dot{B}_d A_c, \quad (4.5)$$

where A_c is the coil area. On any particular cycle, this offset can be considered with good approximation to be constant, nevertheless considerable variations of the order of several seconds can be observed, that are essentially random. This confirms the fact that the measurement errors throughout a cycle are strongly correlated, due to the temporarily systematic character of the offset, while the overall error considered at an arbitrary time has a random character. Equation 4.6 shows a quantitative representation of this behaviour, where the Root Mean Square (RMS) average is evaluated over a set of N cycles:

$$\sigma(\dot{B}_d) = \sqrt{\frac{1}{N} \sum_{k=1}^N \dot{B}_{d,k}^2}, \quad (4.6)$$

and then the expected value of the field error is expressed as a function of time during a cycle as:

$$\sigma_d(t) = \sigma(\dot{B}_d) (t - t_k). \quad (4.7)$$

4.2.1.2 | Random noise, σ_n

The random noise measured with respect to the average represents the lowest-level error, i.e., the measurement resolution. The standard deviation of the $\bar{B}(t)$ over a specific period, Δt gives a complete description. The noise contribution, represented by σ_n , can be obtained according to Equation 4.8, evaluated on a plateau, as the RMS value of the residual of the linear regression equation in Equation 4.4:

$$\sigma_n = \sqrt{\frac{1}{\Delta t} \int_{t_p}^{t_p + \Delta t} (\bar{B}(\tau) - \tilde{B}(\tau))^2 d\tau}. \quad (4.8)$$

4.2.1.3 | Field marker contribution, σ_m

The final random error source contributed by the field marker, introduces an error due to the uncertainty presented by the sensor. Temperature, as well as electrical and mechanical noise have an impact on the differentiating algorithm used to find the resonance peak in the sensor's output signal. The error associated to the field marker can be characterised in terms of the delay between the time t_k when the field reaches the preset threshold value, i.e., $B(t_k) = B_m$, and the time \tilde{t}_k when the digital trigger is actually received by the integrator:

$$\Delta t_k = \tilde{t}_k - t_k > 0. \quad (4.9)$$

The delay Δt_k includes a dominant contribution from the systematic latency associated to the detection of the resonance and the generation of the trigger pulse, plus a random component. The latency is accounted for by the systematic offset term ΔB in Equation 4.1. The contribution associated to the frequency stability of the RF signal source is typically of the order of one ppm or better, which can be safely neglected. The resulting field error is proportional to the delay:

$$B(t_k + \Delta t_k) - B(t_k) \approx \frac{dB}{dt} \Delta t_k. \quad (4.10)$$

As was discussed in the case of integrator drift, this error has a systematic character for any given magnetic cycle, but on a cycle-to-cycle basis it is considered as a random variable that can be interpreted as the jitter of the field marker. Experimentally, the delay Δt_k is not directly accessible since the actual field B is unknown. However, an estimate can be obtained under reproducibility conditions from the standard deviation of the trigger times measured over a sequence of N identical cycles:

$$\sigma(\Delta t_k)^2 \leq \sigma(t_k)^2 = \frac{1}{N} \sum_{k=1}^N t_k^2 - \left(\frac{1}{N} \sum_{k=1}^N t_k \right)^2. \quad (4.11)$$

The inequality in Equation 4.11 takes into account that any ripple in the excitation current can result in a slightly different field at the same time during a magnetic cycle, even when the cycles are nominally the same. As a result, the upper bound is taken as a conservative error estimate:

$$\sigma_m = \frac{dB}{dt} \sigma(t_k). \quad (4.12)$$

4.2.2 | Systematic error sources

The offset and gain errors of a measurement system contribute towards a systematic error, which affects the accuracy of the measurement. These errors are normally constant or proportional to the actual value. The systematic error sources in B-train systems are an imperfect calibration of the instrument, measurement drift and field marker trigger generation delay.

In the case where the measurement system is not ideally setup due to human errors, defective equipment and non-linearities in the electronics not considered during the commissioning of the instrument, systematic errors may arise. In general, systematic errors can be estimated by comparing the output of an instrument with a metrologically certified source of the measurand, or with the results obtained with another instrument known to be more accurate. In case of the real-time field measurement there are no metrological standards, other than the kind of inductive setup that is being presented. As a result, an indirect calibration is proposed, possible only in the domain of synchrotrons, based upon measurements done on the circulating beam and the RF subsystem. This procedure is discussed in detail in Section 4.5.

4.3 | Field marker characterisation

This section describes tests performed to evaluate the behaviour of NMR sensors as field markers using Metrolab's PT2025 teslameter [48]. A study on the amplitude and width characteristics of the resonant signal for the application of these sensors in the ELENA B-train has already been carried out [212]. The following tests were performed when the commissioning started in November 2016, in order to validate the sensor choice prior to machine's operation and to propose suitable ramp rate values for the machine's magnetic cycles. The performance target is having a measurement reproducibility within the 2-unit ($\times 10^{-4}$) mark, which is crucial especially at the low field limit of the NMR marker (which is around half of the tested level). This is investigated in different field and ramp rate conditions to allow operation teams flexibility when choosing the cycle specifications.

4.3.1 | Field uniformity

The choice of NMR sensors as field markers is made keeping in mind the field precision needs, as well as the uniformity of the field in the ELENA dipole. When the field is not homogeneous, one side of the sample resonates at a different frequency from the other side. With an increasing field gradient, the sensor's resonance peak broadens and flattens, leading to inconsistent behaviour. Hence, the ELENA dipole's uniformity is compared to the Metrolab PT2025 teslameter specifications. The manufacturer's recommended limits are 600 ppm/cm at low field and 1400 ppm/cm at high field. The field uniformity was measured to be 130 ppm/cm at 100 A and 400 A during the series acceptance campaign [43], which is well within the accepted limit in both cases.

4.3.2 | Trigger signal precision

A trigger signal is generated by the peak detector circuit when a minimum peak in the resonant signal occurs. The uncertainty presented by the field marker (σ_m) under different field and ramp rate conditions is investigated to ensure performance within the 2-unit mark.

The test is performed using the ELENA reference dipole magnet, PT2025 teslameter by Metrolab [48] and a National Instruments data acquisition card NI-USB 6366 [213], with an acquisition rate of 1 MHz. Probe 1 (field range of 43 mT to 130 mT) is used for the low field measurements while Probe 3 (field range of 170 mT to 520 mT) is used at the high field mark. Four identical teslameters are compared for both chains. A separate Peak detector SPEC card is used for each sensor in order to generate four trigger signals. Figure 4.1 shows the complete setup.

Following the outcomes of the initial study [212] and more insight from operators of the machine, twelve (B, \dot{B}) are chosen, with more options at low field due to the bigger challenges presented in these conditions. Figure 4.2 shows the different combinations of B and B/\dot{B} that are investigated, as well as the eventual operating conditions for the low field marker (acceleration) and high field marker (acceleration and deceleration).

The Peak detector SPEC card generates a trigger signal at t_k at the minimum peak of the resonant signal. The trigger signal corresponds approximately to the moment when $B(t)$ matches the preset NMR field level, but includes the

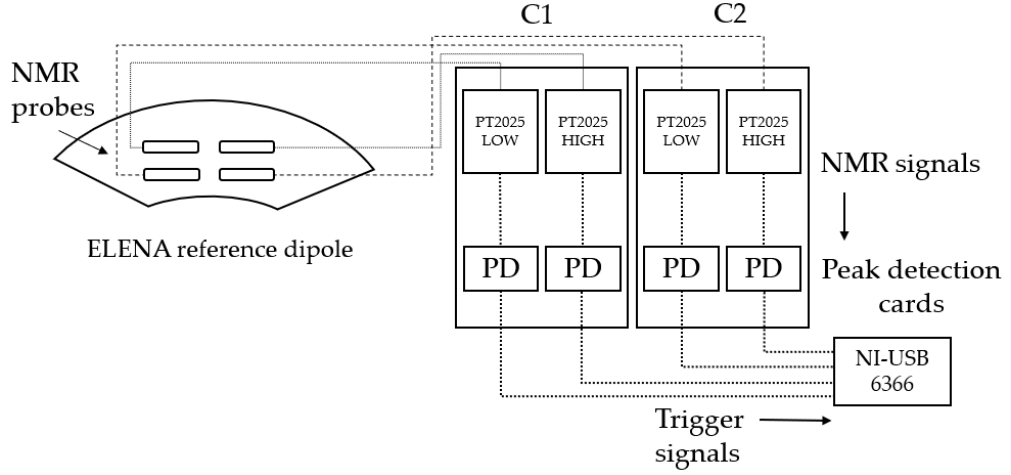


Figure 4.1: Reference magnet and electronic experimental setup to determine the precision of NMR field markers for the ELENA B-train.

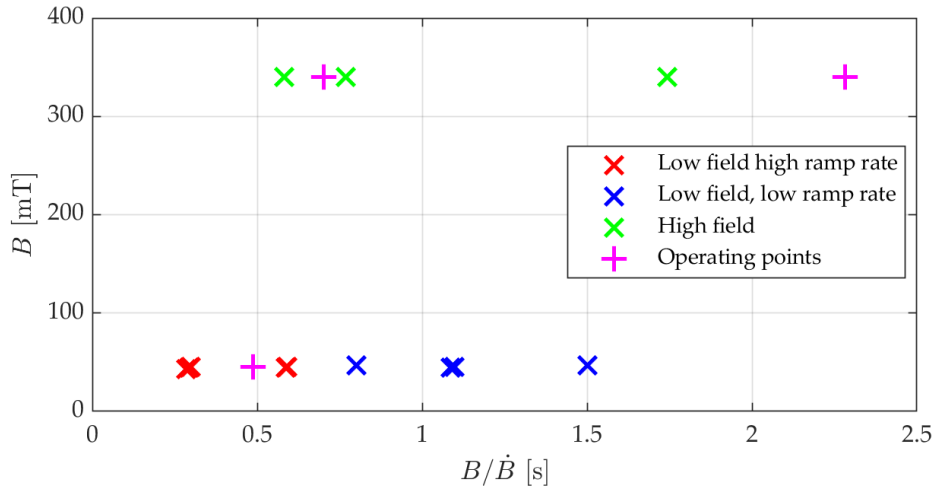


Figure 4.2: The different B and B/\dot{B} combinations investigated and the operating points.

effect of the filters as well as the electronics, both the RF demodulator in the teslameter and the FPGA peak detector. The chosen probes have an in-built bandpass filter from 100 Hz to 2 kHz, which however is unable to guarantee the signal quality due to the high electrical noise levels due to nearby power supplies. To avoid spurious peaks, a low-pass filter with a cut-off frequency of 2.3 kHz is applied before the Peak detector SPEC card. The effect of this filter on the peak time is measured to be around $62 \mu\text{s}$. Considering the effect of both filters at operational field ramp rates, the total delay does not exceed $80 \mu\text{s}$. The effect of these systematic differences is explored in Section 4.3.3.

Figure 4.3 shows 100 examples of the NMR signal recorded from the C1 unit at 46.5 mT and 58 mT/s. The comparison of the hundred cycles assumes that the magnetic history is repeatable as a function of time after ignoring the

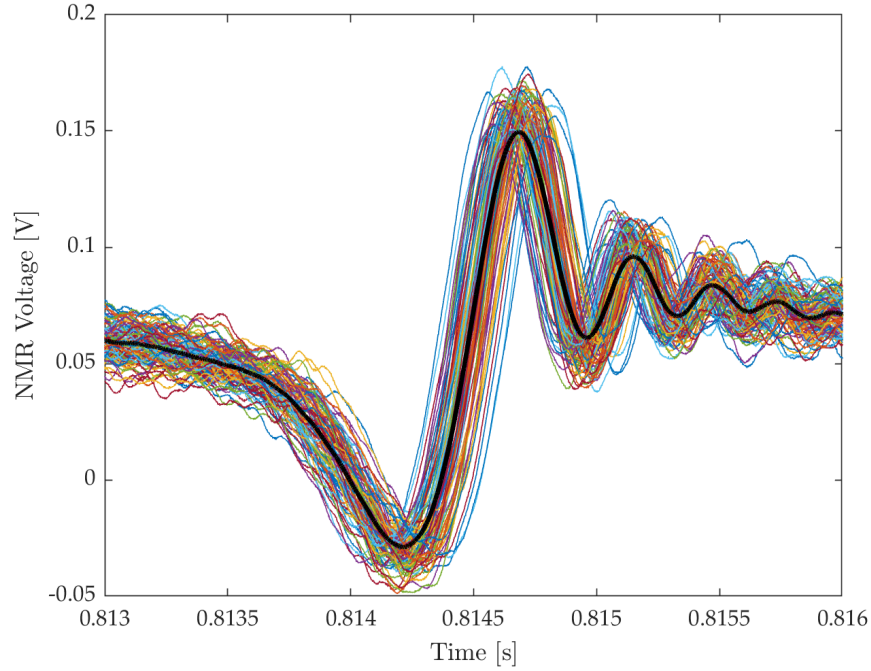


Figure 4.3: NMR signals at 46.5 mT and 58 mT/s, with the average signal shown in black.

first three magnetic cycles. An equivalent value to the standard deviation of the trigger time is calculated in Tesla, σ_m , as shown in Equation 4.12. The relative standard deviation σ_m/B is used to compare the performance amongst difference conditions to the desired target value.

Table 4.1 shows the results, grouped in three categories: low field, high ramp rate (in red); low field, low ramp rate (in blue) and high field (in green). Lower standard deviation values are noted for slow ramp rates at low field. The repeatability of the trigger signal for $B/\dot{B} > 0.8$ s is better than $4.5 \mu\text{T}$ (1 unit), while for faster ramp rates it is better than $9 \mu\text{T}$ (2 units). At high field a repeatability better than $3 \mu\text{T}$ (0.09 units) is noted. All cases are better than the target set for the ELENA ring operation.

In another test performed in this series, the precision of the trigger signal is compared for NMR and FMR sensors installed in the magnet gap. An independent t-test finds no statistically significant difference between the performance of the two sensors, leading to the decision to remain using the NMR sensors due to the commercial availability of these sensors. A complete description of this test is documented in Appendix A.

Table 4.1: Trigger signal precision for different combinations of B and \dot{B}

B [mT]	\dot{B} [mT/s]	B/\dot{B} [s]	$\sigma(t_k)$ [ms]		σ_m [μ T]		σ_m/B [10^{-4}]	
			C1	C2	C1	C2	C1	C2
43.0	151	0.284	0.037	0.036	5.6	5.5	1.30	1.28
44.5	151	0.294	0.047	0.047	7.1	7.1	1.60	1.60
45.0	151	0.297	0.054	0.059	8.2	9.0	1.82	2.00
44.5	76	0.588	0.063	0.062	4.8	4.7	1.08	1.06
45.0	76	0.594	0.075	0.075	5.7	5.7	1.27	1.27
46.5	58	0.800	0.057	0.055	3.3	3.2	0.71	0.69
44.5	41	1.077	0.067	0.065	2.8	2.7	0.63	0.61
45.0	41	1.090	0.104	0.109	4.3	4.5	0.96	1.00
46.5	31	1.490	0.108	0.099	3.4	3.1	0.73	0.67
340	584	0.582	0.0039	0.0044	2.3	2.6	0.07	0.08
340	443	0.767	0.0056	0.0067	2.5	3.0	0.07	0.09
340	195	1.744	0.0138	0.0137	2.7	2.7	0.08	0.08

4.3.3 | Delay of trigger signal generation

Figure 4.4 shows the resonant signal as well as the generated trigger signal. A time delay Δt_{NMR} between the minimum peak of the NMR signal and the falling edge of the trigger signal (active low) can cause a systematic error in the measurement if it is not corrected. Hence, this delay is measured and converted to an equivalent field value ΔB_{NMR} by multiplying with the ramp rate value. For the three categories:

- Low field, high ramp rate: $10 \mu\text{T} < \Delta B_{\text{NMR}} < 23 \mu\text{T}$;
- Low field, low ramp rate: $4 \mu\text{T} < \Delta B_{\text{NMR}} < 8 \mu\text{T}$;
- High field: $2 \mu\text{T} < \Delta B_{\text{NMR}} < 6 \mu\text{T}$.

These measurements confirm the preference for low ramp rates at low fields. The amplitude is in fact found to be within the uncertainty value and in the end, is accounted for in the novel field marker calibration method described in Section 3.3.4.

In conclusion, the fore-mentioned tests have validated the choice of Metrolab's PT2025 teslameter and NMR probes in accordance with the FIRESTORM system

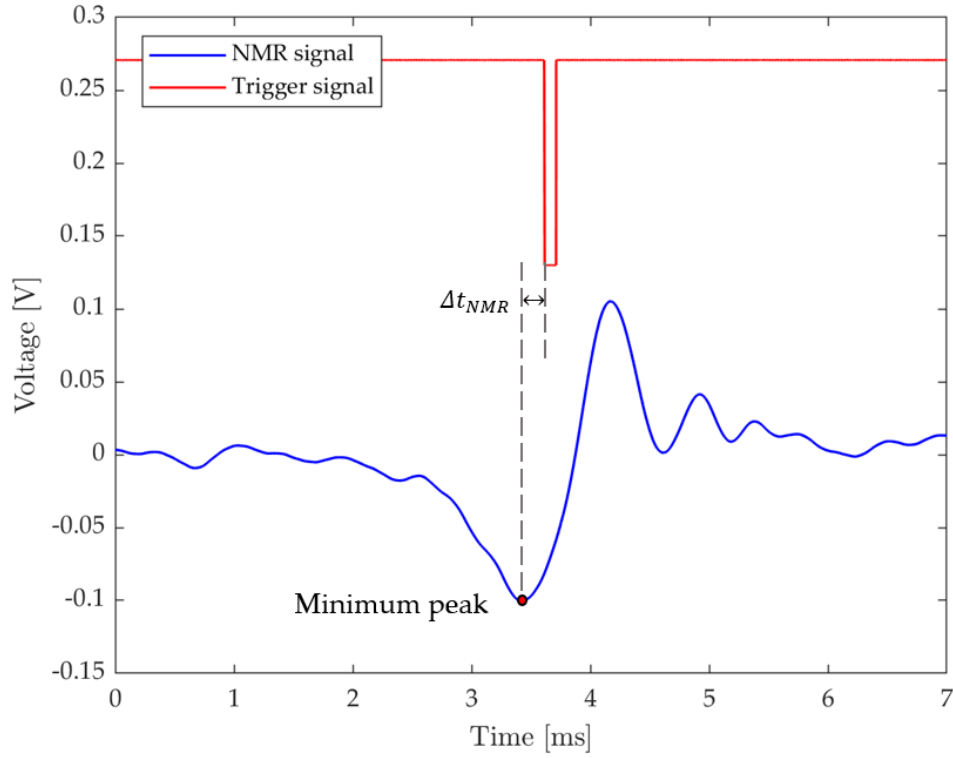


Figure 4.4: NMR signal output and the generated trigger signal by the Peak Detector SPEC card.

for the operation of the ELENA ring. These results were instrumental in choosing the \dot{B} parameter (as shown in Figure 4.2) for each magnetic cycle.

4.4 | Reliability Run

A reliability run consisting of the measurement of 3,000 cycles was performed in November 2018, in order to validate the performance of the sensors, electronics, controls and transmission of the ELENA B-train on a statistical basis. This was done prior to the presence of the beam in the ring, and hence systematic errors could not be identified in this case. Both the acceleration and deceleration cycles were implemented and measurements presented here are from the C1 chain. Measurements were acquired using the FESA interface at a sample rate of 10 kHz.

Table 4.2 shows the results obtained for the operational chain. The overall stability of the B-train system throughout the run was satisfactory. Figure 4.5 shows the drift in the measurement of the deceleration cycle's intermediate plateau. The drift error contribution, is notably at its highest at the extraction point of the deceleration cycle. Figure 4.6 shows the distribution of the field

Table 4.2: ELENA B-train reliability run results for both acceleration and deceleration cycles.

Parameter	Unit	Acceleration		Deceleration
Average drift rate, \dot{B}_d	$\mu\text{T/s}$	1.0 ± 1.5		1.0 ± 1.5
Random error due to drift at injection, $\sigma_d(t_{\text{inj}})$	μT	0.74		0.62
Random error due to drift at extraction, $\sigma_d(t_{\text{ex}})$	μT	1.0		42
Random error due to noise, σ_n	μT	2.9 ± 0.1		
Peak-to-peak noise	μT	13.8 ± 0.5		
Marker jitter, $\sigma(t_k)$	μs	60.1	9.7	21.5
Field marker uncertainty, σ_m	μT	5.9	6.5	3.4
Relative field marker uncertainty, $\sigma_m/B(t_k)$	$\times 10^{-4}$	1.3	0.19	0.10
Measured repeatability at injection, $\sigma(\bar{B}(t_{\text{inj}}))$	μT	3.9		4.1
Measured repeatability at extraction, $\sigma(\bar{B}(t_{\text{ex}}))$	μT	4.1		37
Total random error at injection, $\sigma_r(t_{\text{inj}})$	μT	6.6		4.5
Total random error at extraction, $\sigma_r(t_{\text{ex}})$	μT	6.6		42

measured at injection and extraction over 3,000 consecutive cycles, normalised with respect to the respective average. The standard deviation, σ_d , at extraction is about six times higher than at injection, which is however still within tolerance. The shape of the distributions is approximately gaussian, which confirms the essentially random nature of the voltage offset fluctuations over time.

The measured noise level is comparable to the drift contribution at injection. On the other hand, the relative repeatability of the field marker trigger signal is calculated to be 1.3 units at 45 mT, while at 340 mT, it is better than 0.2 units, both of which are below the targeted 2 units level. The sub-optimal performance at low field is expected, due to the high signal-to-noise ratio of the resonant signal at this range.

The total random error evaluated according to the model of Equation 4.2 is given in Table 4.2, both at injection and at extraction. At injection, the dominant contribution is the noise σ_n . At extraction, the dominant contribution is the drift σ_d , where the relative error is about 1 unit, which is acceptable for operation. These results should be compared to the actual reproducibility of the measured magnetic field \bar{B} , also given in Table 4.2. The difference between the measured

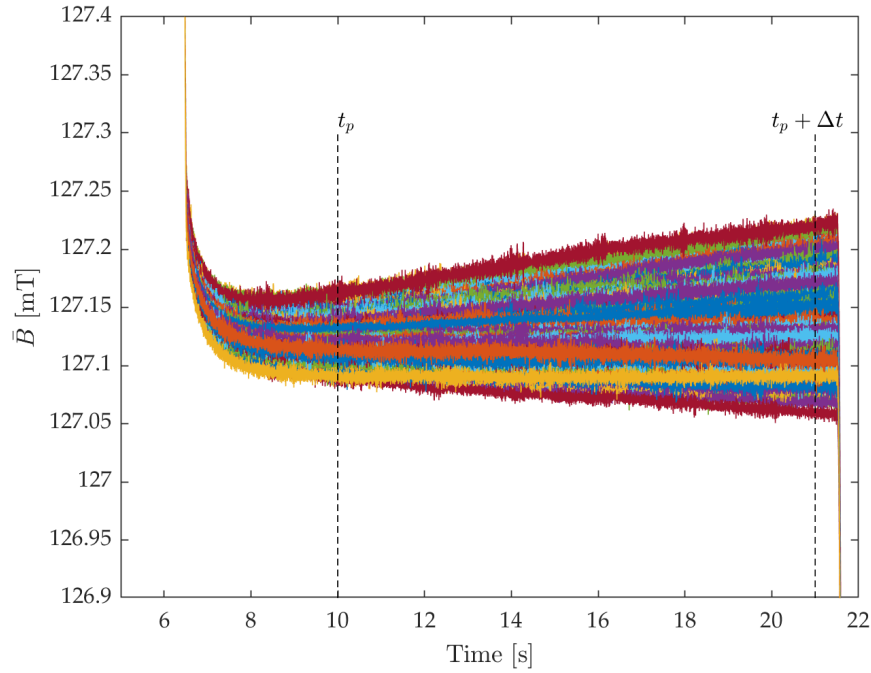


Figure 4.5: Drift on the deceleration cycle's intermediate plateau. t_p and $t_p + \Delta t$ indicate the points considered for calculating the drift.

repeatability and the estimated total random error is as low as $5 \mu\text{T}$. This essentially validates the assumptions on which the model of Equation 4.2 is based.

4.5 | Systematic error evaluation

Whilst most FIRESTORM B-train systems will be commissioned using the calibrated legacy B-train as a metrological standard, in the case of the ELENA ring, this is not possible, as the FIRESTORM B-train is the first magnetic field measurement system to be installed in this machine. As the proposed measurement model was not able to ensure a performance level within 2 units, another method is carried out to evaluate and eliminate systematic errors, where the RF parameters are measured and the magnetic field error as a function of time is derived.

4.5.1 | Procedure

In a synchrotron, the electric field provided by the RF cavity must be synchronised with the bending magnetic field. The ELENA ring is equipped with an in-house developed Low-Level Radio Frequency (LLRF) system, which is already deployed in the LEIR, PSB and MedAustron [214]. The LLRF

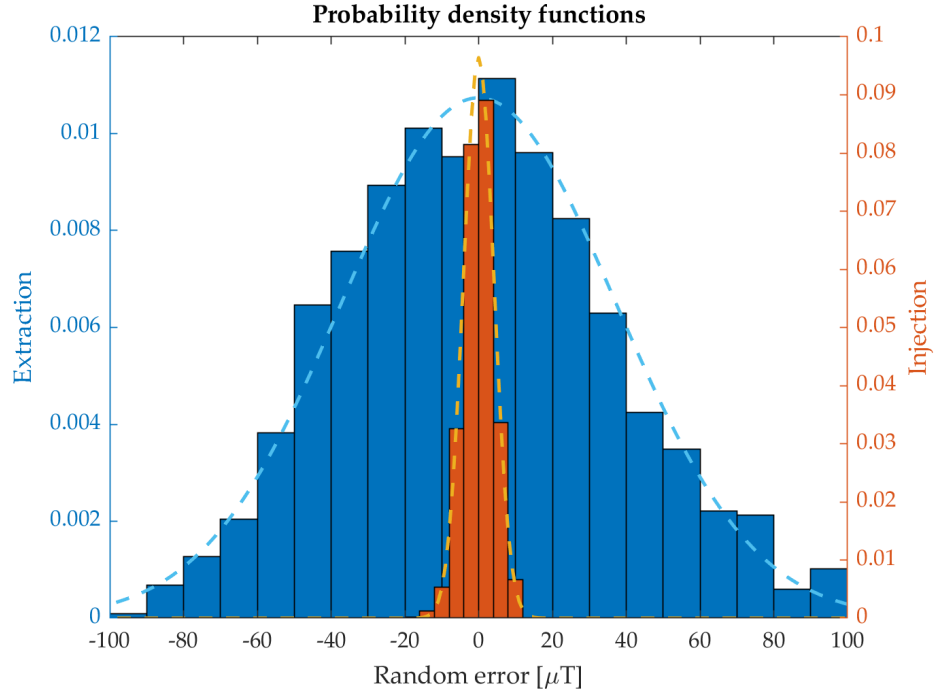


Figure 4.6: Random error measurement at injection and extraction

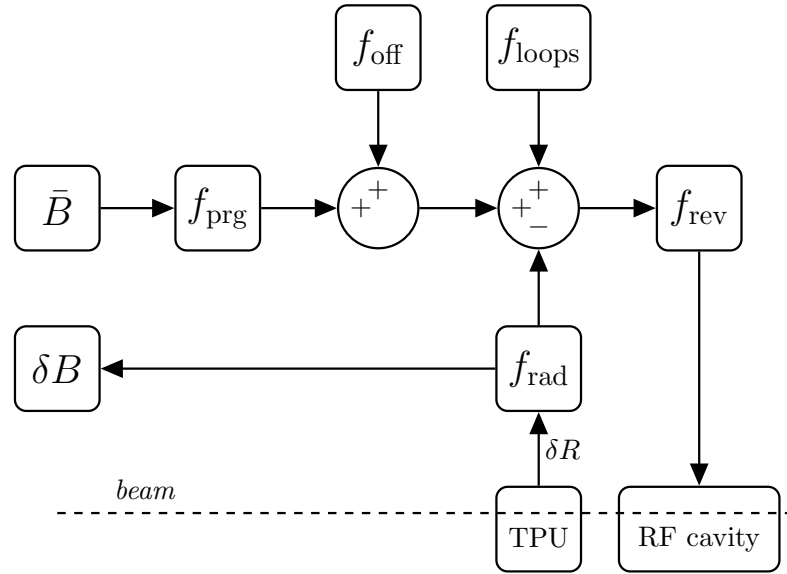


Figure 4.7: Simplified schematic diagram of the LLRF system

receives the B-train measured field, $\bar{B}(t)$ via an optical fiber, and calculates the programmed revolution frequency f_{prg} according to Equation 1.8.

Figure 4.7 shows a simplified schematic of the LLRF, illustrating the procedure for obtaining the revolution frequency applied to the cavity, $f_{\text{rev}}(t)$. The revolution frequency applied to the cavity is obtained according to:

$$f_{\text{rev}} = (f_{\text{prg}} + f_{\text{off}}) + f_{\text{loops}} - f_{\text{rad}}, \quad (4.13)$$

where:

- f_{off} is an optional frequency offset that may be added to f_{prg} when carrying out special tests, or to correct the B-train input in those occasions when it may be suspected or known to be wrong; for the present tests, f_{off} was set to zero.
- f_{loops} includes the contributions of three independent feedback loops: the longitudinal phase loop, which keeps the particles bunched together, and the injection and extraction loops, that synchronise the particle bunches in and out of the ring by measuring the phase of the beam and comparing it with a reference generator.
- f_{rad} is the radial loop contribution that keeps the beam in the centre of the vacuum chamber. This loop is based on feedback from the mean radial position error δR , obtained by averaging the measurements of several Transverse Pick-up Units (TPUs) placed along the ring [215]. The minus sign in Equation 4.13 is in accord with a polarity convention that associates a positive correction, $f_{\text{rad}} > 0$, with a decrease in revolution frequency, as needed to push the beam radially outwards according to Equation 1.8.

Ignoring the contribution of f_{loops} and hence considering only the elements contributing to radial equilibrium, in presence of a field measurement error δB , such that:

$$B = \bar{B} + \delta B, \quad (4.14)$$

this leads to:

$$f_{\text{rev}}(\bar{B} + \delta B) = f_{\text{prg}} - f_{\text{rad}}, \quad (4.15)$$

which means that, in the first approximation, the field error is proportional to the radial loop contribution f_{rad} :

$$\delta B = \bar{B} - B \approx \frac{f_{\text{rad}}}{\frac{\partial f_{\text{prg}}}{\partial B}}. \quad (4.16)$$

Attributing this field error entirely to the field measurement is a conservative assumption. In practice, the centring action of f_{rad} compensates other sources, such as environmental and stray magnetic fields, imperfect knowledge of the machine radius and measurement errors of the beam radial position or the RF. The term $(\partial f / \partial B)^{-1}$ in Equation 4.16, expressed in $\mu\text{T/Hz}$, represents

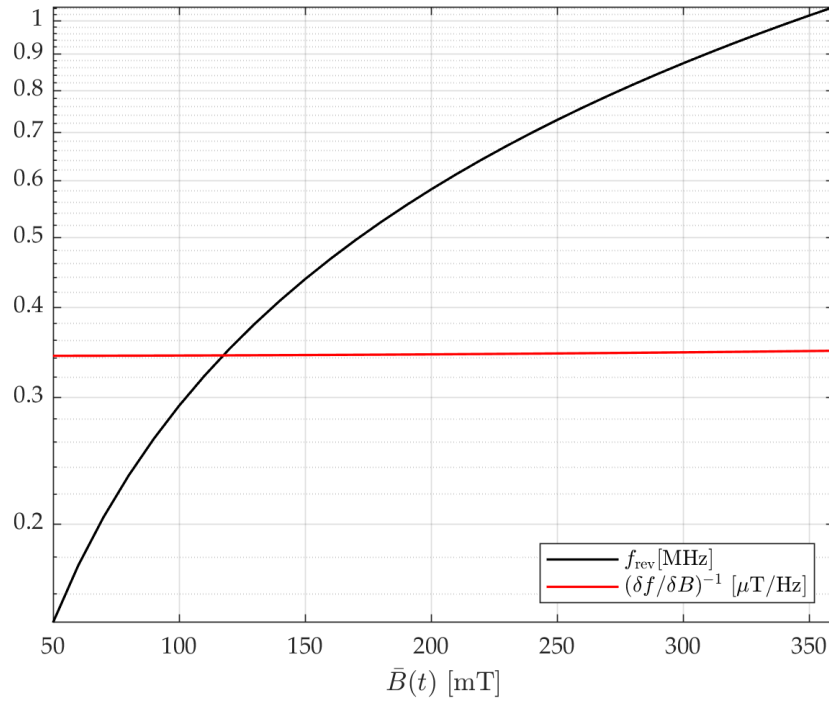


Figure 4.8: The revolution frequency (black) and the reciprocal of its first derivative (red) as a function of the ELENA magnetic field.

the uncertainty of the estimated field error per unit of uncertainty of the revolution frequency, and is also plotted in Figure 4.8. In these circumstances, the uncertainty of the frequency is 1 Hz or less. In general, the uncertainty ratio increases with the field, which means that field error estimates are generally more precise at extraction than injection for the ELENA. The increase is limited to about one order of magnitude in the ELENA (which is similar to the PSB and LEIR).

The field error in Equation 4.16 can be evaluated at several different field levels over a set of repeated cycles, to obtain a set of data points $(\bar{B}, \delta B)_{i=1..n}$. The systematic error parameters λ and ΔB defined in Equation 4.1 can be estimated by least-square fitting the data points with the linear model:

$$\delta B = \lambda \bar{B} + \Delta B, \quad (4.17)$$

obtained by substituting Equation 4.16 in Equation 4.1, neglecting the random error term and taking into account that both parameters are small.

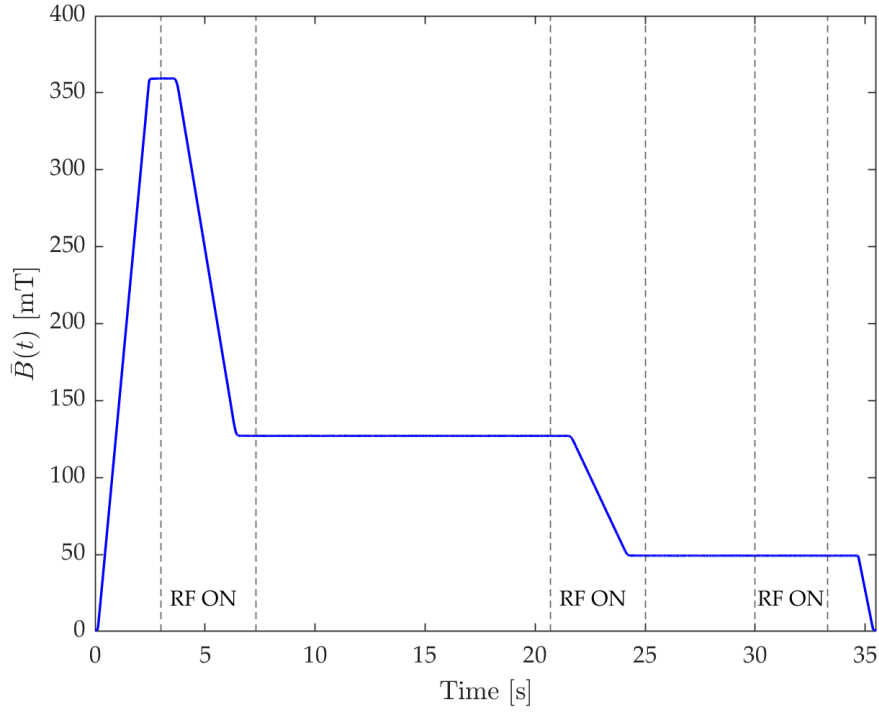


Figure 4.9: The points in the deceleration cycle where RF is on and measurements were acquired.

4.5.2 | Results

The results of the beam-based calibration carried out for ELENA are listed in Table 4.3. Measurements are acquired repeatedly in periods when the RF is on as shown in Figure 4.9. Figure 4.10 shows the measurements of $\delta B(t)$ obtained for the deceleration mode during the ELENA ring's commissioning, before and after the calibration procedure. A first-order polynomial is fitted over the former set of measurements, resulting in $\lambda = -2.6 \times 10^{-3}$ and $\Delta B = 0.77$ mT. This is equivalent to an error of 0.16 mT at injection, which is well within the uncertainty estimation derived in Section 3.4. This may be attributed to the difference between the magnets in the ring and the reference magnet, which is a prototype made with a different grade of magnetic steel.

When the two error parameters were compensated, the measurement was repeated, resulting in a gain error $\lambda = 6.3 \times 10^{-6}$ and an offset $\Delta B = -1.3 \mu\text{T}$. The calibration procedure is noted to reduce both gain and offset errors by more than two orders of magnitude, down to the level of just a few ppm, well below random errors. The validity of this procedure was further confirmed by showing that, even with the radial RF loop switched off, the beam could be still

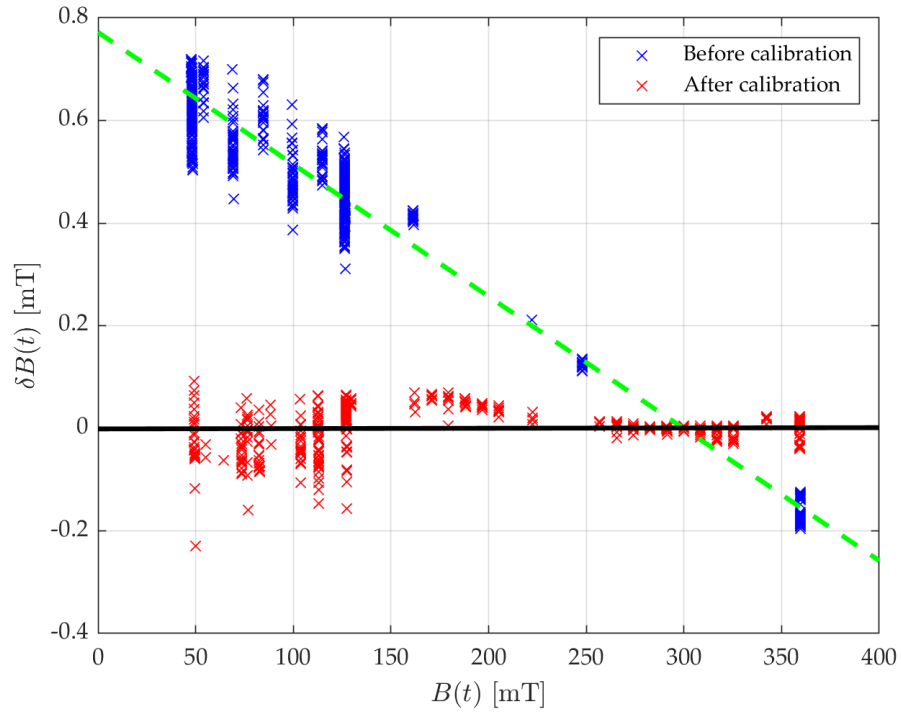


Figure 4.10: $B(t)$ vs. $\delta B(t)$ before and after the ELENA B-train's calibration.

Table 4.3: ELENA B-train beam measurements

Parameter	Unit	Injection	Intermediate	Extraction
Revolution frequency, $f_{\text{rev}}(t)$	kHz	1043.4 ± 0.063	371.2 ± 0.008	144.0 ± 0.107
Mean radial position, $\bar{r}(t_{\text{inj}})$	mm	-0.353 ± 0.008	-0.430 ± 0.017	1.596 ± 0.110
Radial loop frequency, $f_{\text{rad}}(t)$	Hz	34.4 ± 55	-95 ± 48	116 ± 153

injected and extracted with minimal losses.

Table 4.3 demonstrates that the largest frequency correction is in the order of 100 Hz, resulting in a radial position error of less than 2 mm. Based on these measurements, the systematic B-train error is noted to be $0.97 \mu\text{T}$ (0.027 units) at injection and $-0.99 \mu\text{T}$ (0.2 units) at extraction. In the ELENA ring, the reported errors are acceptable for keeping the beam on the closed orbit, as they are well within the target error tolerance of 2 units, confirming the functionality of the B-train and RF system.

4.6 | Summary

This chapter has given an overview of the experiments performed to validate the performance of the ELENA B-train. During an extensive series of preliminary tests, the instrument allowed smooth and reliable beam operation, thus proving its viability for the commissioning of the machine. First, a linear model is presented which characterises the two types of errors present in the measurement: random and systematic errors. Three experiments are described to identify the characteristics of the system. The first test characterised the behaviour of NMR sensors as field markers for the ELENA B-train, as well as the determination of the optimal ramp rate parameters. The main outcome of this campaign is that the most critical conditions are at low field, where the ramp rate should be kept as low as possible. At field levels lower than 47 mT, a repeatability better than $4.5 \mu\text{T}$ is noted using slow ramp rates ($B/\dot{B} > 0.8 \text{ s}$), whilst for faster ramp rates, it is better than $9 \mu\text{T}$. At high fields using a high ramp rate, the repeatability is found to be better than $3 \mu\text{T}$. The homogeneity of the ELENA reference dipole magnet at the nominal low and high field values satisfies the maximum field gradient acceptable for the two PT2025 teslameter probes (Probe 1 and Probe 3).

The second test, the reliability run performed during the commissioning period investigated the stability of the ELENA B-train, with a repeatability of $4.1 \mu\text{T}$ at injection and $37 \mu\text{T}$ at extraction. It is demonstrated that the larger error at extraction is due to the drift in the measurement. In general, the total random errors, are at the level of 0.1 units at injection, and in the worst-case, at extraction, random errors are at the level of 1 unit, which is within the specification of the machine. The third experiment described a novel procedure to calibrate systematic measurement errors using beam-based measurements. This experiment related beam feedback measurements with the B-train measurement, to derive the systematic error in the instrument. An initial measurement concluded that the instrument's systematic error is within the target error tolerance of 2 units. Following the calibration, the systematic error was reduced by two orders of magnitude. This experiment proves the potential of the measurement model to setup B-train systems when no beam is available.

Possible future improvements to the B-train's performance are being considered such as an adapted field marker for drift correction on long plateaus [202], and direct use of the measured radial beam position to estimate magnetic field

measurement errors. The calibration method will also be used in the upcoming three-year operation phase of CERN's synchrotrons, where the acquisition of δB and f_{rad} data is expected to provide a foundation for high-precision statistical estimation of the instruments' parameters and their stability.

Chapter 5

Field Marker Position Optimisation

5.1 | Introduction

In the measurement of curved dipole magnets, fixed integral coils are used as part of the sensor setup. However, these are only able to detect field changes. As a result, an integration constant is obtained separately by a local field sensor placed in the centre of the magnet. In such cases, the magnetic length is introduced to derive the integral field value from the measured local field.

In all the B-train systems at CERN, the magnetic length ℓ_m is assumed to be constant, ignoring the dependence upon the current, I . This is justified when the magnets are cycled using one cycle type, however when introducing multiple cycles with different operating conditions such as the rate of change in current, \dot{I} , errors are introduced. The field marker sensors in B-trains at CERN are always placed in the centre of the magnet at $s = 0$, which presents several advantages such as good field uniformity (a requirement for magnetic resonance sensors). However, this is not always possible in cases where a reference magnet is not available, and sensors have to be installed next to the vacuum chamber within an operational magnet.

The main motivation behind these measurements is the fact that the variation of the ℓ_m with respect to I was found to introduce additional uncertainties in the B-train measurement, which needs to operate strictly with errors in the order of 10^{-4} . In this chapter, an optimal position for the placement of field markers in the ELENA magnet is found, and the feasibility of displacing the sensors in the B-train system is investigated. In particular, the variation of the magnetic length is explored as a function of the excitation current I along the s , x and y axes. Furthermore, the feasibility of displacing the field markers from the centre of the ELENA magnet is investigated by comparing the performance of two setups installed within the magnet during commissioning of the ring.

5.2 | Optimal position search

5.2.1 | Experimental Setup

The following measurements are executed using the spare ELENA bending dipole in CERN's magnetic measurement laboratory. Figure 3.6 shows the magnet, which in this case is equipped with a spare curved fluxmeter array, three Projekt Elektronik AS-NTM-2 Hall probes [216] and a National Instruments NI-USB 6366 data acquisition system [213]. The magnet is initially degaussed using a bipolar power converter, and then cycled repeatedly from 0 A to 275 A at a ramp rate of 200 A/s. Figure 5.1 shows the applied excitation current signal.

To ensure a stable and reproducible measurement, three pre-cycles are performed before the measurement is initiated. The coil integral field and local field measurements are acquired simultaneously along the following space: between $0 \leq s \leq 470$ mm, $0 \leq x \leq 80$ mm and $5 \leq y \leq 25$ mm (refer to Figure 1.2). It has to be noted that the magnet pole is at $s = 430$ mm. Whilst the coil is kept in a fixed position throughout the measurement, the three Hall probes are placed on top of each other, and are displaced along the s and x axes. Three consecutive cycles are recorded at every position, and subsequently the calculated magnetic length values are averaged. In the post-processing stage, a moving average with a 20 kHz cut-off is implemented due to the noisy Hall probe and current signals. The integrator drift is corrected by finding the induced voltage on the plateau before the ramp-up of each measured cycle, and then subtracting this voltage from the measured coil voltage.

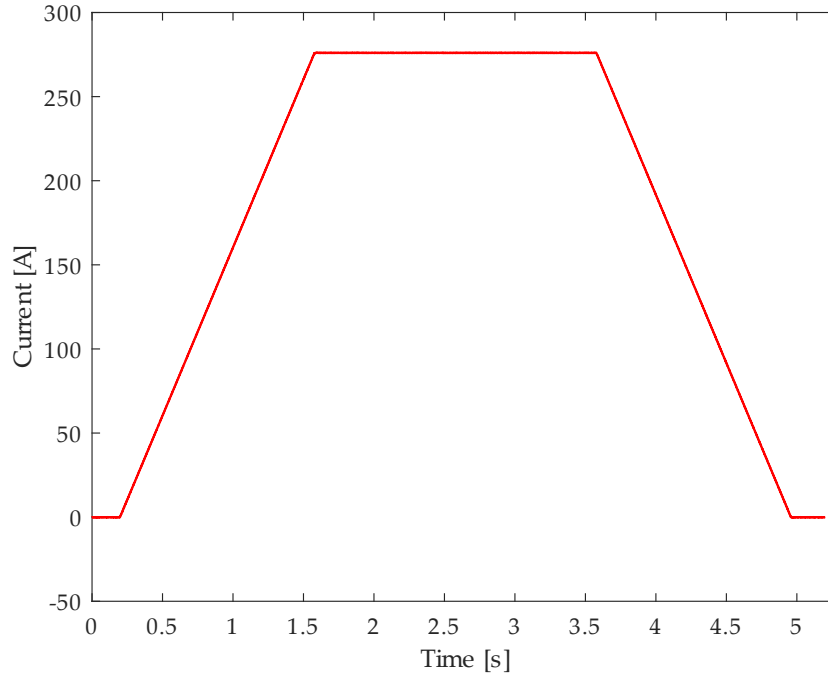


Figure 5.1: In order to characterise the magnetic length, the excitation current is ramped up from 0 A to 275 A and then ramped down to 0 A at 200 A/s.

For a magnet cycled dynamically at a ramp rate $\dot{I} = 200$ A/s, the best stability of the magnetic length is found in the current range $[I_1, I_2]$ of interest. The position along the beam path (s plane) where this occurs is referred to as the optimal position, s^* . The stability is hence evaluated by means of the relative variation of the magnetic length:

$$\frac{\Delta \ell_m(s)}{\bar{\ell}_m(s)} = \max_{I_1 \leq I \leq I_2} \frac{\ell_m(s, I)}{\bar{\ell}_m(s)} - \min_{I_1 \leq I \leq I_2} \frac{\ell_m(s, I)}{\bar{\ell}_m(s)}, \quad (5.1)$$

where $\bar{\ell}_m(s)$ is the average magnetic length defined by:

$$\bar{\ell}_m(s) = \frac{1}{I_2 - I_1} \int_{I_1}^{I_2} \ell_m(s, \mathcal{I}) d\mathcal{I}. \quad (5.2)$$

This parameter indicates the maximum relative error that is expected on the field integral $\mathbb{I}(t)$ when assuming a constant magnetic length value. The metric used in this experiment to describe the advantage of moving the local field sensor is the ratio of the relative magnetic length variation at $s = 0$ mm to the relative magnetic length variation at s^* :

$$\beta = \frac{\Delta \ell_m(0)}{\bar{\ell}_m(0)} \frac{\bar{\ell}_m(s^*)}{\Delta \ell_m(s^*)}. \quad (5.3)$$

Values of $\beta > 1$ indicate an advantage of displacing the sensor at s^* rather than $s = 0$.

5.2.2 | Results and discussion

Figures 5.2 to 5.5 show the measured magnetic length values along s at four discrete currents on the ramp-up and ramp-down curves. The four graphs represent four different x and y positions that have been considered. The curves are obtained by linearly interpolating the field profiles along the nine different positions along the s axis. To investigate the variations of the magnetic length along the x and y axes, three different positions are considered in each axis. The measurement uncertainty is approximately 0.4 mm, which encompasses the magnetic field repeatability and the Hall probe positioning error.

Figure 5.2, Figure 5.3 and Figure 5.4 show the magnetic length profiles at increasing y values and $x = 0$, where it can be seen that the magnetic length values converge towards a position at around $s = 340$ mm where the variation in the parameter is minimal. As the value of y increases, it is noted that the optimal position becomes increasingly smeared. This is seen better in Figure 5.6(a) whereas y increases, the relative variation in $\ell_m(s^*)$ increases proportionally, with minimal variance in the value of s^* . These results are listed in Table 5.1, which also highlights the calculated β parameters.

When the vertical position is kept fixed at $y = 5$ mm and the Hall probe is moved outside of the magnet by increasing x , ℓ_m remains mostly unchanged, except that s^* shifts closer to $s = 0$. This can be observed in Figure 5.2 and Figure 5.5. In Figure 5.6(b) the relative magnetic length variation is plotted, and Table 5.2 lists the corresponding numerical data. The β parameter remains

Table 5.1: Magnetic length when changing y , at $x = 0$ mm and $0 \leq s \leq 470$ mm.

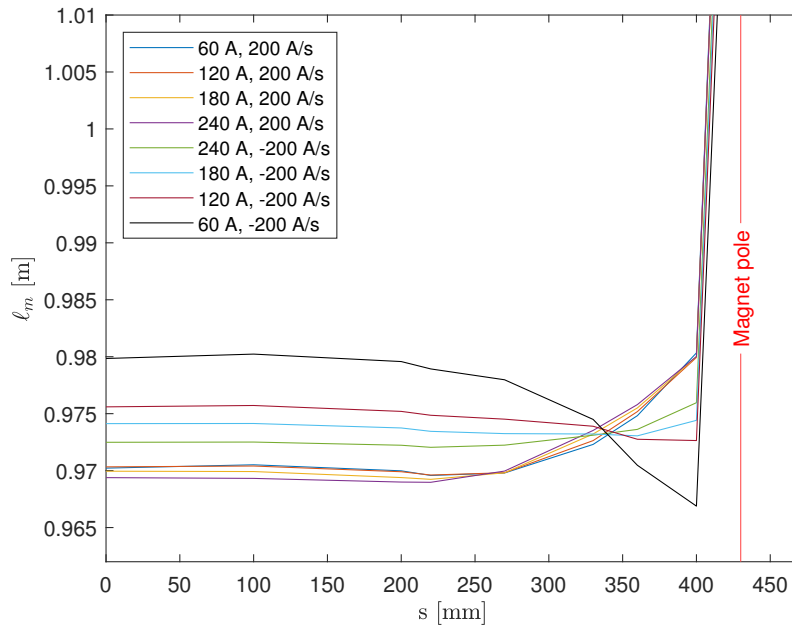
y (mm)	s^* (mm)	$\bar{\ell}_m(s^*)$ (mm)	$\Delta\ell_m(s^*)$ (mm)	$\frac{\Delta\ell_m(s^*)}{\ell_m(s^*)}$ ($\times 10^{-4}$)	$\frac{\Delta\ell_m(0)}{\ell_m(0)}$ ($\times 10^{-4}$)	β (-)
5	340.1	973.6	1.28	13.2	114.8	8.67
16	342.4	974.1	1.63	16.7	112.0	6.71
25	348.0	975.2	2.97	30.4	103.4	3.40

Table 5.2: Magnetic length variation, when changing x , at $y = 5$ mm and $0 \leq s \leq 470$ mm.

x (mm)	s^* (mm)	$\bar{\ell}_m(s^*)$ (mm)	$\Delta\ell_m(s^*)$ (mm)	$\frac{\Delta\ell_m(s^*)}{\bar{\ell}_m(s^*)}$ ($\times 10^{-4}$)	$\frac{\Delta\ell_m(0)}{\bar{\ell}_m(0)}$ ($\times 10^{-4}$)	β (-)
0	340.1	973.6	1.28	13.2	114.8	8.67
50	321.9	973.0	1.41	14.5	118.6	8.21
80	308.2	979.3	1.25	12.7	119.7	9.39

practically unchanged as the probe is moved out of the magnet. The relative variation of the magnetic length is minimal in the range $300 \leq s \leq 350$ mm. This trend was also observed at $y = 16$ mm and $y = 25$ mm.

This experiment concludes that there is an optimal position located towards the edge of the poles, where $\Delta\ell_m(s)/\bar{\ell}_m(s)$ with respect to the excitation current is minimal. This phenomenon arises from the increase in the local field close to the end-plate as it consists of a different material than the yoke. Placing the local field sensor closer to the $y = 0$ presents a greater advantage than placing the sensor at a higher vertical offset. On the other hand, moving the sensor from the central path in the x direction, the optimal position s^* is noted to shift

**Figure 5.2:** Measured magnetic length at $y = 5$ mm, $x = 0$ mm.

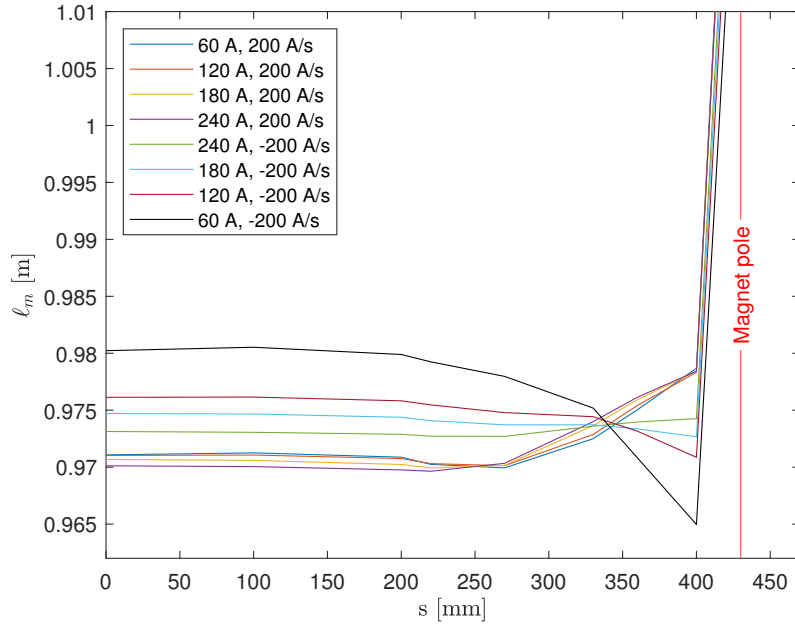


Figure 5.3: Measured magnetic length at $y = 16$ mm, $x = 0$ mm.

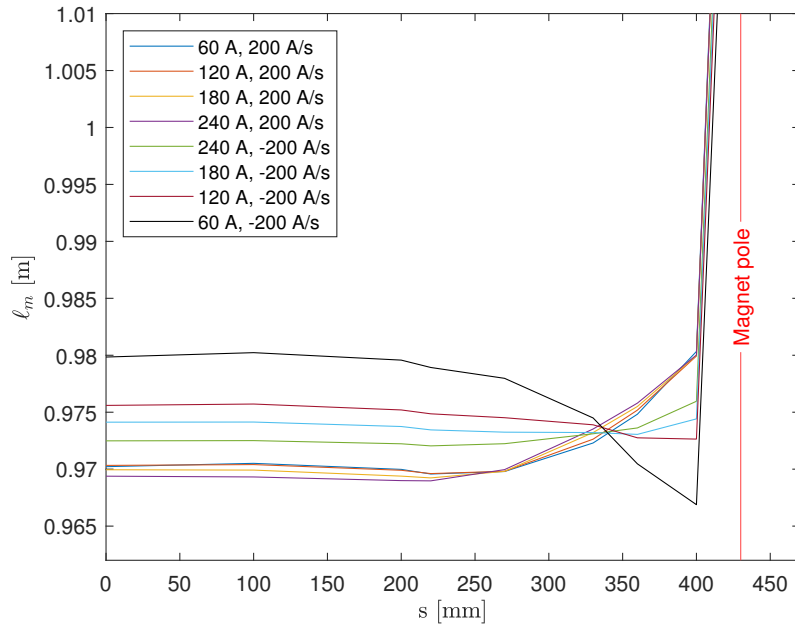


Figure 5.4: Measured magnetic length at $y = 25$ mm, $x = 0$ mm.

proportionally closer to $s = 0$. Installing the sensor at s^* can possibly reduce the uncertainty in the magnetic length parameter, in applications such as B-train systems, where this parameter is assumed to be constant.

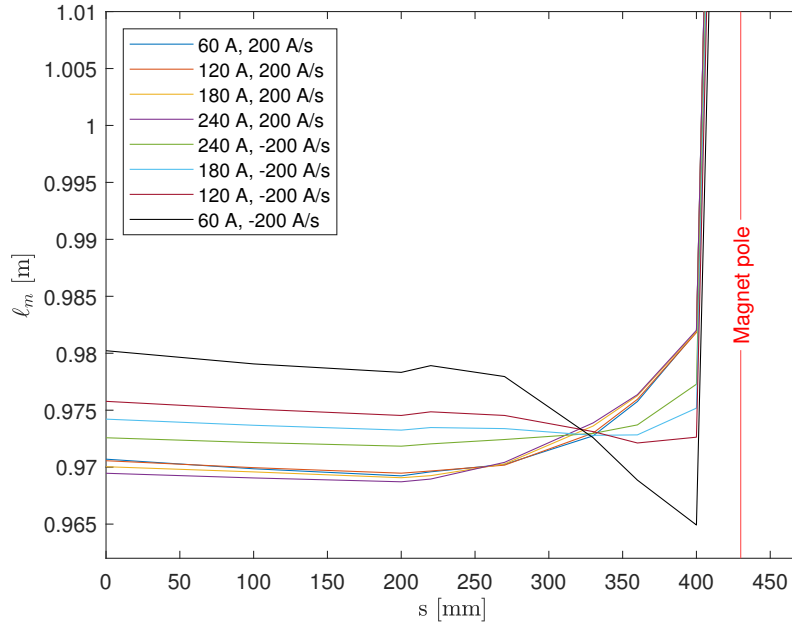


Figure 5.5: Measured magnetic length at $y = 5$ mm, $x = 50$ mm.

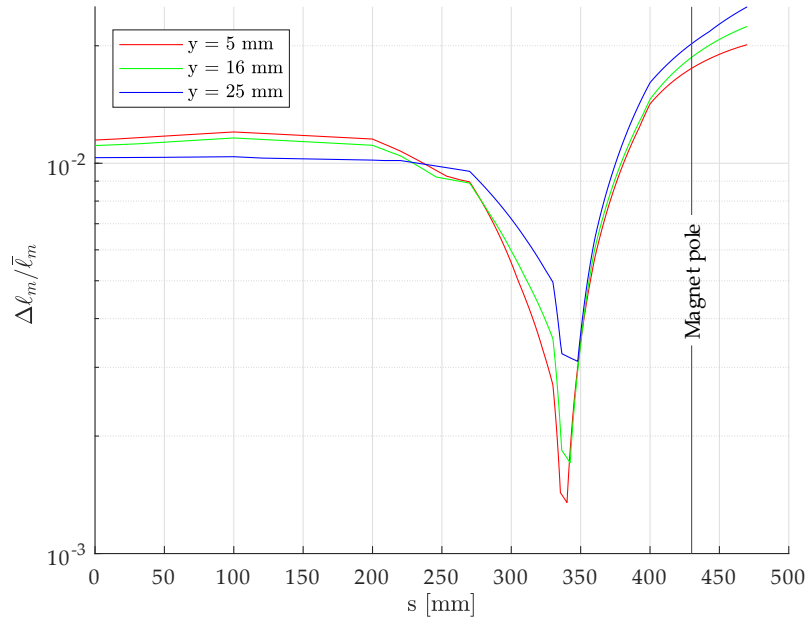
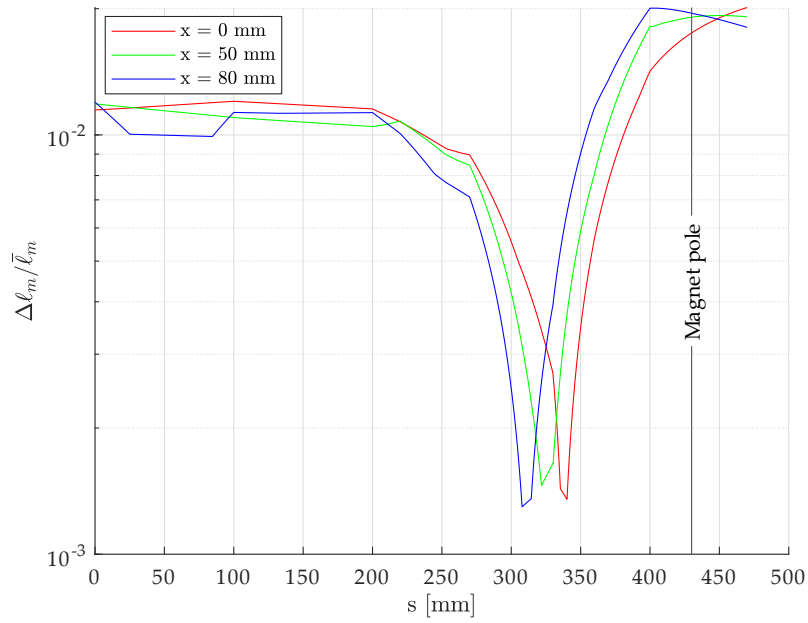
5.3 | ELENA B-train feasibility study

Following the determination of an optimal position for local sensors in the ELENA dipole magnet, this section assesses the feasibility of displacing the field marker sensors in the ELENA B-train system when operated using both the acceleration and deceleration cycles. In particular, the response of magnetic resonance sensors will be investigated along the magnet gap, as well as the effect of differing ramp rate conditions.

5.3.1 | Magnetic resonance sensor response

As the field level within the magnet gap becomes lower at the pole edge, the amplitude of a magnetic resonance sensor's response is expected to decrease. Determining the boundary of the magnet where the sensor signal response is above the noise level is essential when considering displacing the sensors towards the pole edge.

An experiment is carried out on the spare ELENA dipole magnet, where two NMR probes are preset at 45 mT and 340 mT, and fixed to a fiberglass support. The support is consequently moved along the s and x axes, where the resonance signals are recorded using the NI-USB 6366 data acquisition system [213]. The magnet is operated with a cycle similar to the acceleration cycle, ramping up at 70 A/s up to 46 mT and then ramping up to 360 mT

(a) Relative magnetic length change when varying y (b) Relative magnetic length change when varying x **Figure 5.6:** Magnetic length variation when changing x , y and s .

at 115 A/s. Measurements are repeated three times at each position and the peak-to-peak voltage is derived.

Figure 5.7 shows a map of the interpolated voltage amplitudes for the low-field and high-field probes. The measurements are shown in black, whilst the

repeatability of the measurement is illustrated in red. Results indicate that even though the sensors' response falls steadily, the voltage level remains well above noise levels up to $s = 400$ mm and $x = 40$ mm. The low sensor response beyond this point can be explained by the lower magnetic field due to the fringe field. This observation allows the possibility of moving the ELENA field marker sensors towards the optimal position at $s = 340$ mm. When repeated for two FMR sensors, similar results were observed.

5.3.2 | Dynamic characterisation

In Section 5.2, the magnetic length was characterised as a function of the excitation current and position, keeping the ramp rate fixed at 200 A/s. This section investigates the effect of dynamic properties of the magnet on ℓ_m . In B-train systems, field marker sensors are set at one field value in a ramping field and can be exposed to various cycle types and ramp rates. A measurement is proposed, where three field markers set at 45 mT, 200 mT and 340 mT are subjected to different ramp rate conditions.

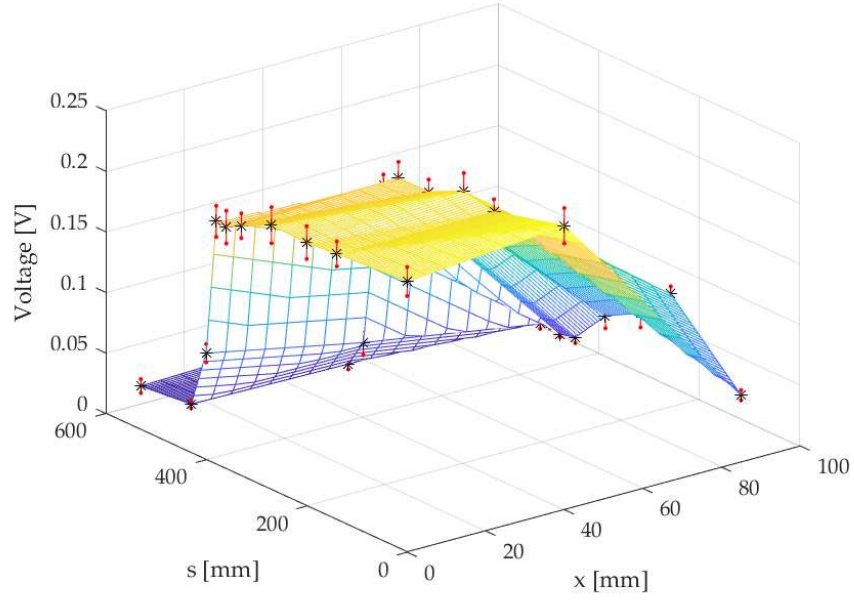
5.3.2.1 | Method

Two identical setups are assembled within the ELENA spare magnet, each setup making use of two FMR and one NMR sensor. Figure 5.8 shows the two setups: one fixed at $s = 0$ mm and another at $s = 340$ mm. The coil voltage and the six resonant signals are measured simultaneously at eight ramp rate values ($200 \leq \dot{I} \leq 900$ A/s) and repeated three times. The dynamic conditions are represented by the variation of the rate of change of the integral field, defined by v :

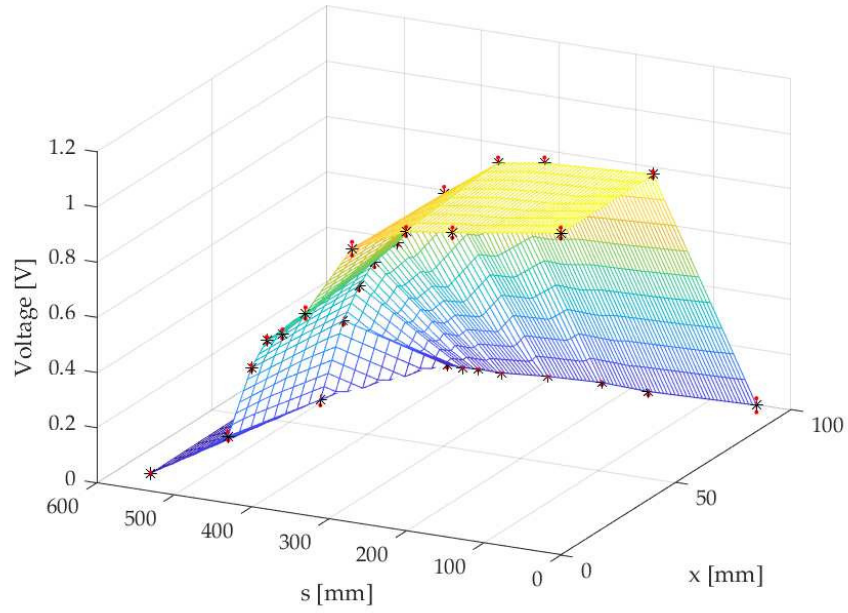
$$v = \sigma \left(\frac{d\mathbb{I}}{dt} \right), \quad (5.4)$$

where σ is the standard deviation of the values of rate of change of the integral field. This quantity is derived with an increasing number of signals n , where $6 \leq n \leq 24$ for eight repetitions. Since each measurement occurs at a single current value, a new metric is defined for the magnetic length behaviour. The ratio of the variation of the magnetic length at s_0 to the variation of the magnetic length at s_1 is defined as:

$$\Gamma = \frac{\max \ell_m(s_0) - \min \ell_m(s_0)}{\max \ell_m(s_1) - \min \ell_m(s_1)}, \quad (5.5)$$



(a) 45 mT



(b) 340 mT

Figure 5.7: Measured NMR voltage signal amplitude at 45 mT and 340 mT.

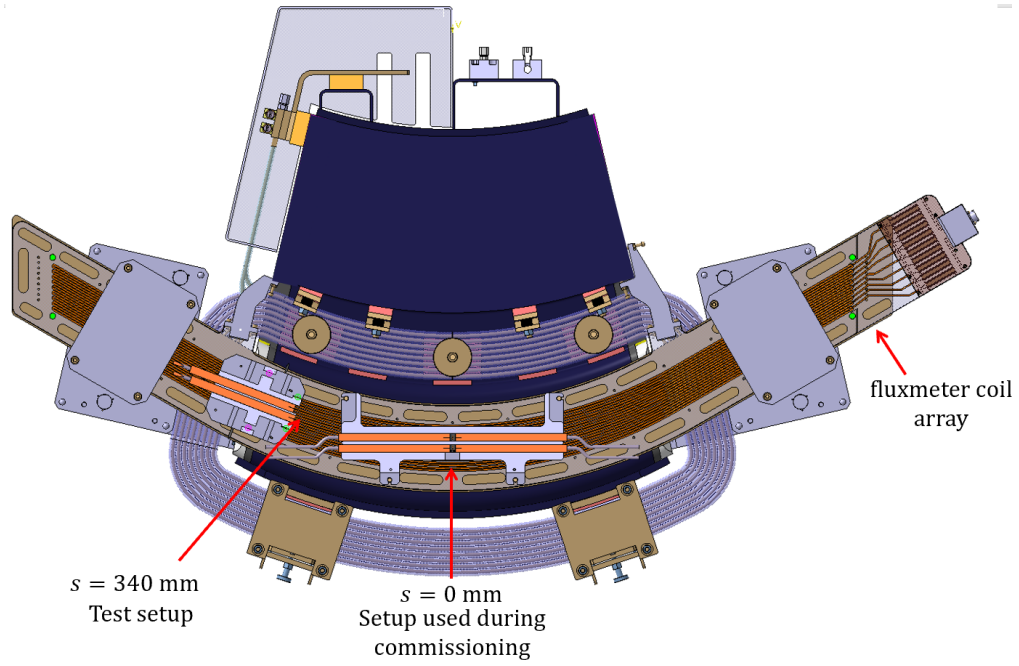


Figure 5.8: Horizontal section view of the ELENA B-train sensor setup.

where in this case, $s_0 = 0$ mm and $s_1 = 340$ mm.

5.3.2.2 | Results

Figure 5.9 shows the variation of Γ with different dynamic field conditions. A horizontal line at $\Gamma = 1$ depicts the point from where the variation of the magnetic length at s_1 becomes lower than that at s_0 . Results indicate that the sensor setup at $s = 340$ mm becomes feasible for $v > 0.21$ Tm/s at 45 mT, and $v > 0.09$ Tm/s at 200 mT and 340 mT. The lower v values for the low-field sensor can be attributed to the lower field levels at the pole edge and external perturbations, which are exacerbated at this low field level.

In the ELENA B-train, the low-field marker is only implemented in the acceleration cycle, whilst the high-field marker is implemented in both operation modes. Hence, at the commissioning stage, there is no valid reason for displacing the low-field marker. On the other hand, the high-field marker is exposed to an integral field change of 0.49 Tm/s and 0.15 Tm/s on the acceleration and deceleration cycles, respectively.

This has been observed by installing the proposed setup within the ELENA reference magnet and cycling the magnet with both the acceleration and deceleration cycles in an interleaved manner. Measurements of the

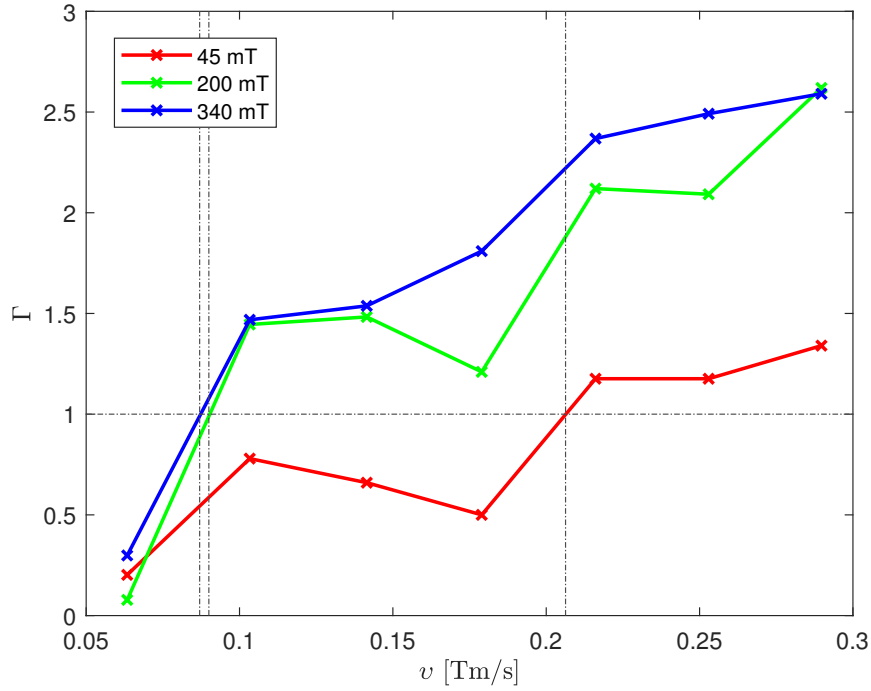


Figure 5.9: Determination of Γ , as a function of integral field variation. It is concluded that for high field markers, feasibility of displacement occurs at $v > 0.09$ Tm/s, whilst for low field markers, this happens at $v > 0.21$ Tm/s.

reproducibility of the trigger time (t_k) have been captured for both setups simultaneously over 24,000 cycles as can be seen in Figure 5.10. Two different trigger times are noted for each sensor setup, one for each mode of operation, however one can note the reduced range in the trigger time measurements for the proposed setup. In fact, for a v value of 0.168 Tm/s, the range of t_k is calculated to be 13.6 ms at $s = 0$ mm and 7.5 ms at $s = 340$ mm. This presents a relative improvement in the field marker uncertainty component of 45% between the two setups.

5.4 | Conclusion

This chapter investigated the positioning of local field sensors installed in the gap of dipole magnets, which are used to infer the integral field. The magnetic length defines the ratio between the integral and local field, and is dependent on the sensor's position, excitation current and rate of change of current. Whilst in B-train systems, such sensors are typically placed in the centre of the magnet, this work has shown that there is a position towards the edge of the poles where the relative change of the magnetic length with respect to the excitation current is minimal. Measurements have been carried out in three axes along the

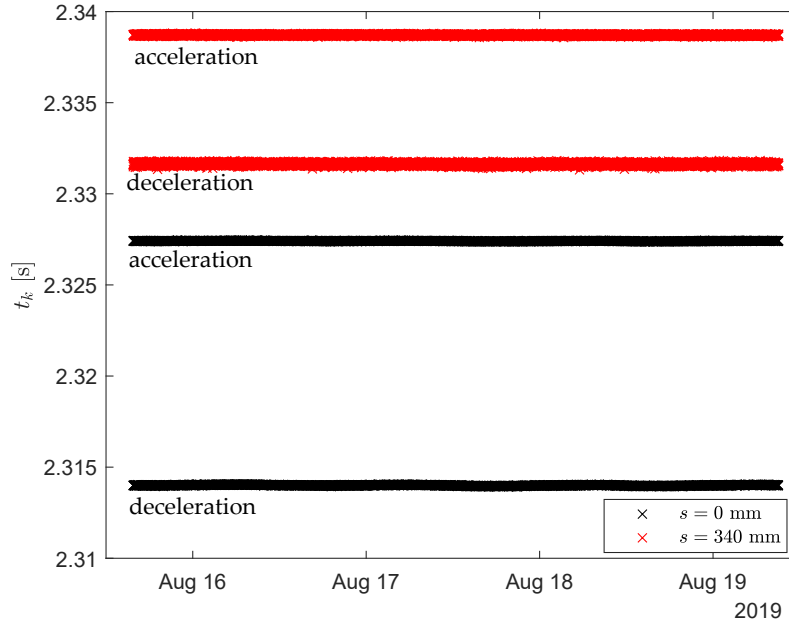


Figure 5.10: Trigger time data acquisition when the acceleration and deceleration cycles are interleaved. Measurements are presented for a sensor setup in the central position $s = 0$ mm and the proposed position $s = 340$ mm.

magnet gap, where moving the local field sensor horizontally in the x direction, the optimal position is noted to shift closer to $s = 0$, whilst offsetting the sensor upwards in the y direction, the variation of the magnetic length increases proportionally. As a result, an optimal position of $s = 340$ mm, $y = 5$ mm and $x = 0$ mm is deduced for the ELENA bending dipole magnet.

Another two tests have been performed with regards to the feasibility of displacing the sensors for the ELENA B-train. Firstly, the operability of magnetic resonance sensors at the proposed position within the magnet gap has been confirmed. Secondly, two field marker setups have been fixed in the dipole magnet, one at the original position and another at the proposed position. A range of dynamic operating conditions was executed, and the magnetic length variation was noted. Results showed that a sensor setup at $s = 340$ mm is feasible for $v > 0.21$ Tm/s at 45 mT, and $v > 0.09$ Tm/s at 200 mT and 340 mT. Finally, a scenario in the ELENA B-train was highlighted where it is advantageous to displace the local field sensors towards the pole edge. In this case, a reduction in the variation of the trigger time results in a potential improvement in the measurement's uncertainty, which helps improve beam performance in machine operation.

Chapter 6

Dynamic Magnetic Field Hysteresis Modelling

6.1 | Introduction

This chapter proposes two dynamic hysteresis models: a field model is required for the ELENA B-train, which can be used for off-line tests when the power converter is not available, or when there is an issue with the real-time measurement, whilst a second model is presented for material science applications. A mathematical model is presented for the former case, based on the decomposition of the integral field effects, where these effects are represented using several curve fitting techniques. The characterisation of each individual model term is provided, with examples from the ELENA dataset, followed by the results obtained for the two ELENA modes of operation. The second dynamic hysteresis model consists of a Preisach and RNN model, able to model both major and minor hysteresis loops at different ramp rates. The results of the model are presented, including a sensitivity analysis to ensure that the neural network is appropriately trained.

6.2 | B-train field model

6.2.1 | Measurements

The measurements which are the basis of the proposed model come from one measurement campaign taking place in CERN's magnetic measurement laboratory. The ELENA spare bending magnet is used, equipped with a spare curved-coil fluxmeter and a National Instruments NI-USB 6366 [213] acquisition system (see Figure 3.6). A bipolar power converter is used to power the magnet, which is first degaussed, then cycled from 0 to the nominal peak current level, I_p , and various current ramp rates \dot{I} . Three pre-cycles are executed prior to the measurements to ensure stability and reproducibility of the field better than 100 ppm. Subsequently, three stable cycles are measured at 20 kHz, as shown in Figure 6.1. The integration constant to be added to fluxmeter measurements is obtained from the measurement described in Section 3.3.4.

In this campaign, measurements of the integral field, \mathbb{I} are carried out at eight different \dot{I} values (50, 100, 200, 300, 400, 500, 600, 900 A/s) and seven different I_p values (40, 50, 100, 150, 200, 250, 276 A). Both the coil output as well as the current signals are acquired simultaneously at a sample rate of 200 kHz. Figure 6.2 shows the measured transfer functions at the different ramp rates and a peak current of 276 A. It can be observed that the saturation effects in the ELENA bending magnets are minimal [17], as well as the asymmetric behaviour at ramp-up and ramp-down.

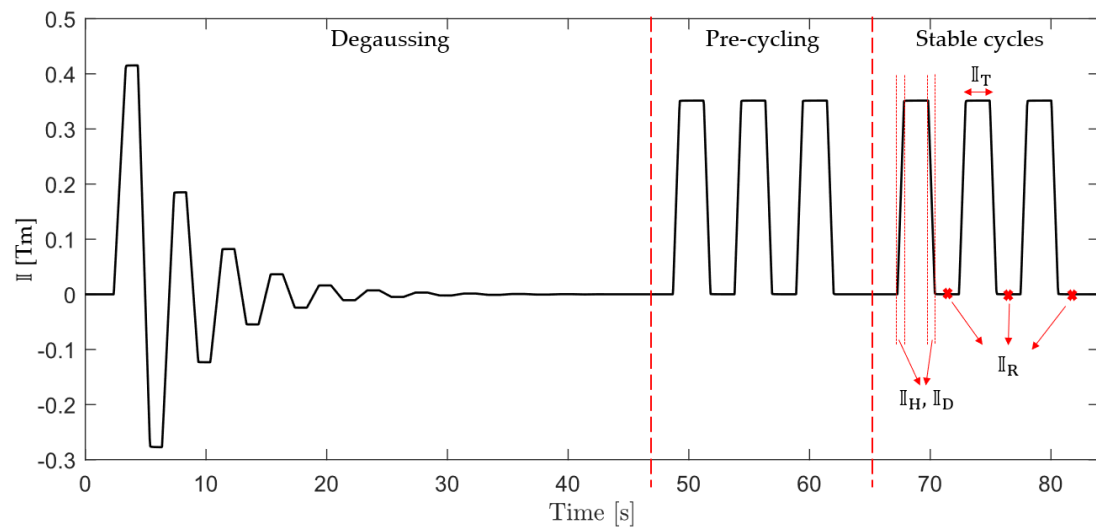


Figure 6.1: An example of the integral field measurement, indicating which parts of the measurement are used to determine the model components.

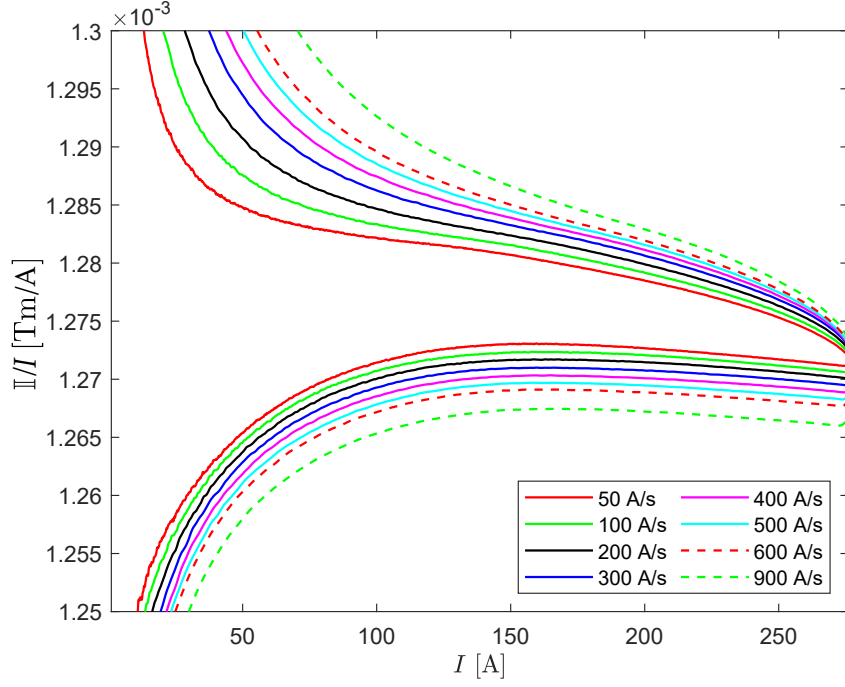


Figure 6.2: Measured transfer functions at different ramp rates.

6.2.2 | Proposed model

To describe the dipole magnet's behaviour, the integral magnetic field $\mathbb{I}(t)$ is selected as the modelled quantity. The model aims to build on the field decomposition model proposed by Caspers *et al.* [178]. The proposed model is comprised of five terms: a linear term \mathbb{I}_L , a residual field term \mathbb{I}_R , a hysteresis term \mathbb{I}_H , a dynamic term \mathbb{I}_D , and a transient term \mathbb{I}_T . The integral field is expressed as:

$$\mathbb{I} = \mathbb{I}_L \left(\frac{I}{I^*} \right) + \mathbb{I}_R \left(\frac{I_p}{I^*} \right) + \mathbb{I}_H \left(\frac{I}{I^*}, \text{sgn}(\dot{I}) \right) + \mathbb{I}_D \left(\frac{I}{I^*}, \frac{\dot{I}}{\dot{I}^*} \right) + \mathbb{I}_T \left(\frac{\Delta I}{I^*}, \frac{\dot{I}_r}{\dot{I}^*}, t_0 \right), \quad (6.1)$$

where I^* is the maximum magnet current, \dot{I}^* is the maximum current ramp rate and $\text{sgn}(\dot{I})$ is the ramp direction, with +1 indicating a ramp-up and -1 indicating a ramp-down. The transient term represents the integral field behaviour during plateaus, and is a function of ΔI , the change in current from the previous to the current plateau, and \dot{I}_r , which is the ramp rate preceding the plateau, and t_0 is the time from the start of a plateau. The components are expressed with normalised input variables to provide consistency of representation among magnets. In the next section, each parameter is characterised for the ELENA magnet measurements in different dynamic conditions.

This work assumes that the magnets are operated in a repeatable environment, ignoring the accommodation effect, which is typically three to five cycles. Keeping the composition of the model as simple as possible for potential real-time implementation, the integral field is modelled using parameters which can be provided to B-train systems as inputs to the Predictive SPEC card. For a field model in operation in synchrotrons, an accuracy target of 2 units is expected, especially at injection and extraction levels. The aim of this work is to reach the forementioned accuracy target, and also improve the modelling accuracy of the simple model used at the PSB and AD [178], described in Section 2.5.4.

6.2.3 | Characterisation

As can be observed in Figure 6.2, the degree of non-linearity in the ELENA magnetic field behaviour is minimal, accounting to less than 10% of the measurement. The characterisation procedure involves the identification of the linear, residual and hysteresis components, and then subtracting these components from the integral field to identify the dynamic and transient properties of \mathbb{I} .

6.2.3.1 | Linear component, \mathbb{I}_L

The linear component \mathbb{I}_L , is obtained by fitting a first-order polynomial equation to the $I - \mathbb{I}$ measurements. This results in:

$$\mathbb{I}_L = c_1 \frac{I}{I_*}, \quad (6.2)$$

where c_1 is the coefficient. This term removes the linear trend in the measurement which accounts for the majority of weighting in the ELENA dipole integral field. Note that \mathbb{I}_L is defined to have a value of 0 at $I = 0$. In the case of the ELENA, $c_1 = 0.3512 \text{ Tm}$.

6.2.3.2 | Residual field component, \mathbb{I}_R

The residual field before and after each measured cycle at the different ramp rates is noted by considering the average of 10,000 samples. The chosen area is noted to be at the point where the eddy currents have completely decayed, around two seconds following a ramp-up/down. Figure 6.3 shows the measured residual field values at different current peaks I_p and ramp rates \dot{I} , including the standard deviation. A first-order polynomial equation is fitted to

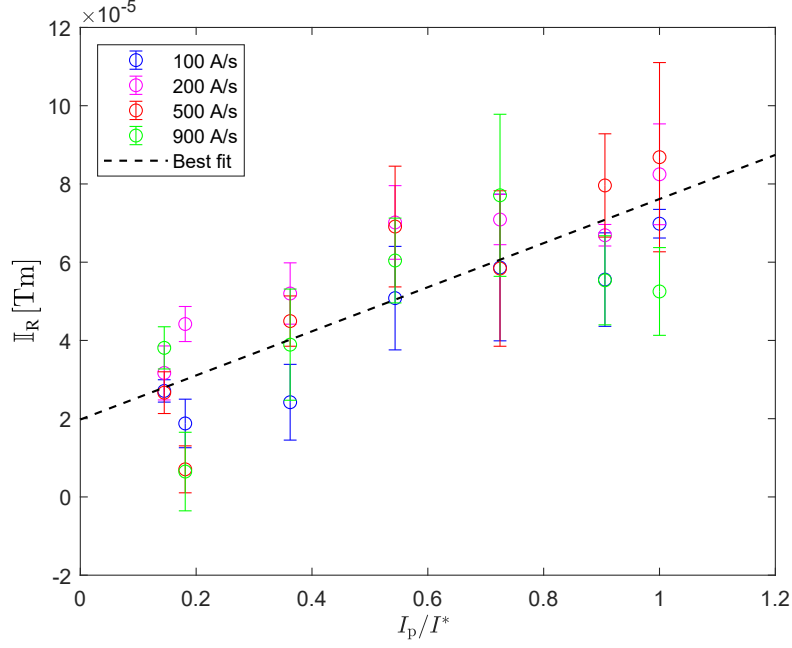


Figure 6.3: Residual field characterisation

these points:

$$\mathbb{I}_R = c_2 \frac{I_p}{I^*} + c_3, \quad (6.3)$$

where $c_2 = 5.6 \times 10^{-5}$ Tm/A and $c_3 = 2 \times 10^{-5}$ Tm.

6.2.3.3 | Hysteresis component, \mathbb{I}_H

As ELENA is one of the few synchrotrons at CERN expected to both accelerate and decelerate particles, the accurate modelling of both the ramp-up and ramp-down behaviour is essential. Modelling the static hysteresis curve is difficult, as measurements of this curve are not available. In this case, this component is modelled by fitting one hysteresis curve at a very low ramp rate. The measured current and magnetic field are first interpolated separately for ramp-up and ramp-down at intervals of 0.1 A over the range of the measured current. A fourth-order polynomial function is used to model the ramp-up and ramp-down signals as follows:

$$\mathbb{I}_H = c_{4j} \left(\frac{I}{I^*} \right)^4 + c_{5j} \left(\frac{I}{I^*} \right)^3 + c_{6j} \left(\frac{I}{I^*} \right)^2 + c_{7j} \left(\frac{I}{I^*} \right) + c_{8j}, \quad (6.4)$$

where c_{4j} to c_{8j} are coefficients obtained for each signal. Each coefficient is distinct for ramp-up ($\text{sgn}(\dot{I}) = +1$) or ramp-down ($\text{sgn}(\dot{I}) = -1$). Table 6.1 shows the value of the parameters obtained for the ELENA. The fit between the measurements and the curves is noted to have a R^2 better than 0.99 and a sum of

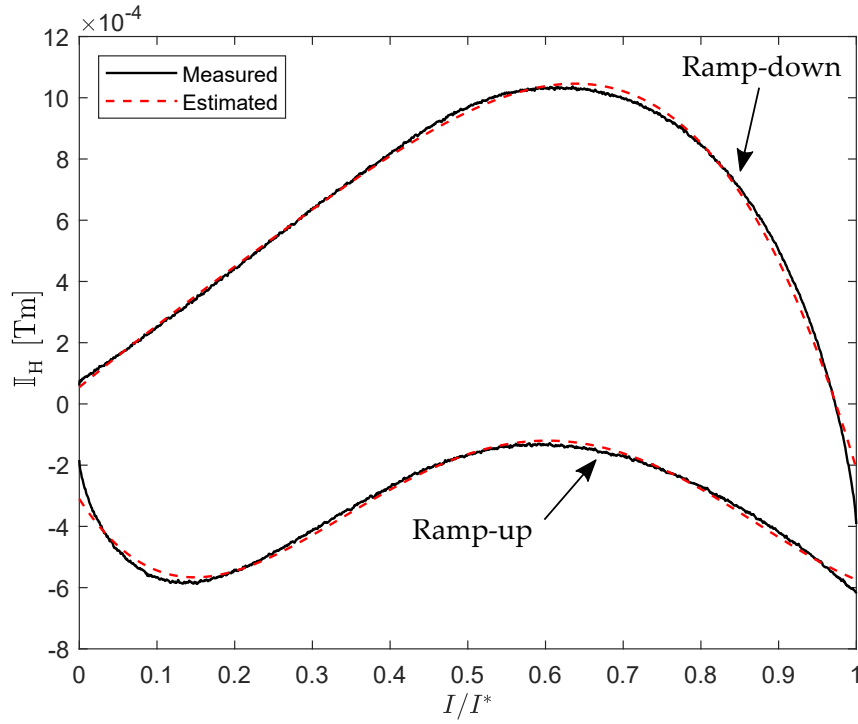


Figure 6.4: Hysteresis component curve fit

squared errors better than 9×10^{-7} . The measured and fitted curves are shown in Figure 6.4.

6.2.3.4 | Dynamic component, I_D

The dynamic component accounts for the eddy current effects in the magnet in pulsing fields. This component is modelled by subtracting the forementioned contributions of the measured field, as shown in Figure 6.5. This component is represented as a function of the normalised current and ramp rate values:

$$I_D = g\left(\frac{I}{I^*}, \frac{\dot{I}}{\dot{I}^*}\right). \quad (6.5)$$

The function g is modelled using an Artificial Neural Network (ANN). In this work, neural networks are used to represent complex terms which are dependent on more than one parameter, taking advantage of the ANN's ability

Table 6.1: Hysteresis component parameters

$\text{sgn}(\dot{I})$	c_{4j}	c_{5j}	c_{6j}	c_{7j}	c_{8j}
+1	0.01022	0.02487	0.01831	0.003920	-3.1142×10^{-4}
-1	0.004741	0.003621	0.001263	0.002117	5.4373×10^{-5}

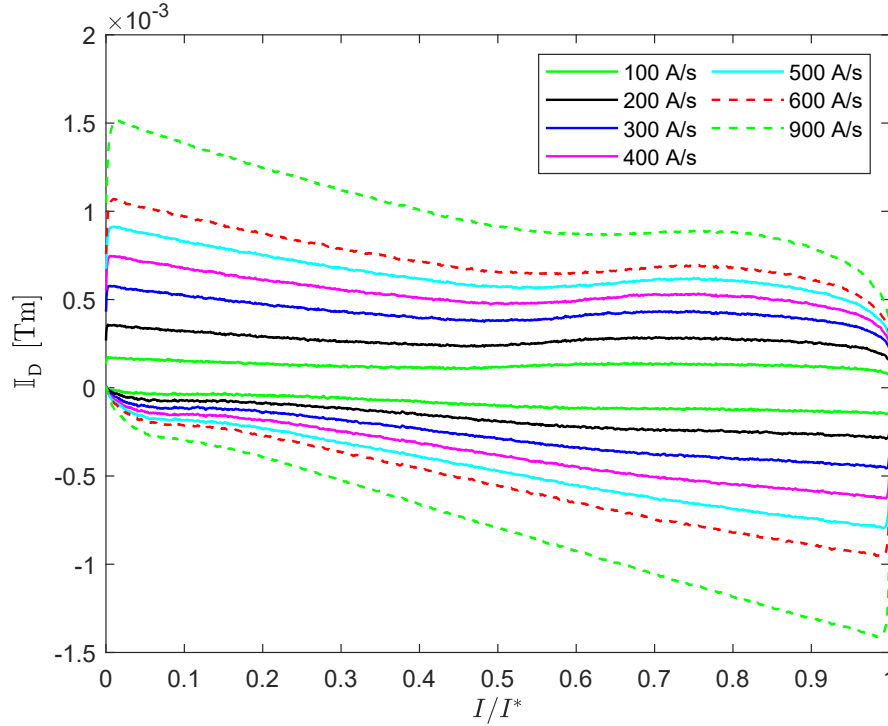


Figure 6.5: Dynamic characterisation

to explore relationships among data which may be difficult to arrive at using traditional methods [217]. These structures are preferred over RNNs, as due to the recurrent nature of RNNs, the computation is slow. Figure 6.6 shows the general structure of this model, as implemented in this case for estimating \mathbb{I}_D .

At each time step, the input vector $\mathbf{v}(t)$, which in this case includes the normalised current and ramp rate values, is processed at the input layer. Each instant $\mathbf{v}(t)$ is added with the bias vector ${}^1\mathbf{b}$ and multiplied by the input

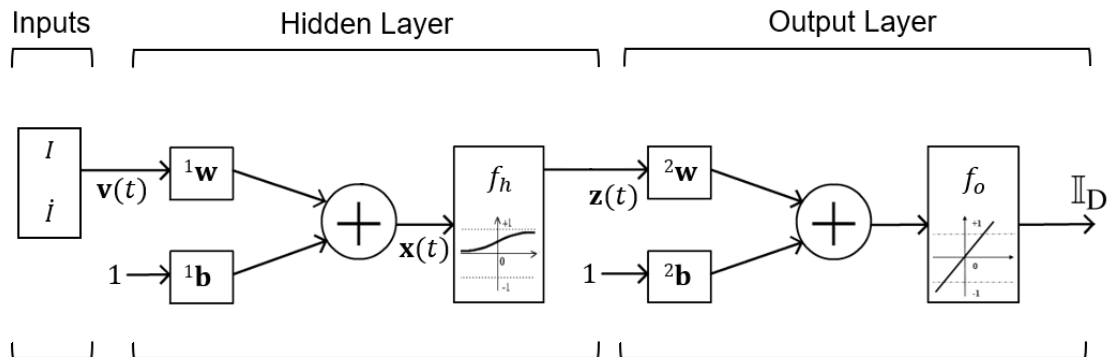


Figure 6.6: General structure of the ANN

weight matrix ${}^1\mathbf{w}$. The internal state $\mathbf{z}(t)$, is obtained after the application of the activation function $f_h(x)$ on the input as follows:

$$\mathbf{z}(t) = f_h[{}^1\mathbf{w}(\mathbf{v}(t) + {}^1\mathbf{b})]. \quad (6.6)$$

The activation function, which in this case is a sigmoid function, is defined as:

$$f_h(x) = \frac{1}{1 + e^{-x}}. \quad (6.7)$$

The internal state $\mathbf{z}(t)$ is then summed with bias ${}^2\mathbf{b}$, multiplied by the weights ${}^2\mathbf{w}$, and the result passes through a linear activation function $f_o(x)$ as:

$$\mathbb{I}_D = f_o[{}^2\mathbf{w}(\mathbf{z}(t) + {}^2\mathbf{b})], \quad (6.8)$$

where \mathbb{I}_D is the estimated output.

In this work, the network's weights are calculated using the *feedforwardnet* command from the Deep Learning Toolbox by MATLAB [218]. The training algorithm is the Levenberg-Marquadt algorithm [219], which is a non-linear least squares optimisation algorithm incorporated into the backpropagation algorithm for training neural networks. This algorithm is a combination of the Gradient Descent and Gauss-Newton methods, and hence merges the advantages of these methods [220]. The Levenberg-Marquadt algorithm aims to optimise the weights according to the following objective function:

$$V(t) = \frac{1}{2}(\tilde{\mathbb{I}}_D(t) - \mathbb{I}_D(t))^T(\tilde{\mathbb{I}}_D(t) - \mathbb{I}_D(t)), \quad (6.9)$$

where $\tilde{\mathbb{I}}_D$ represents the measured dynamic integral field component. As a result, the weights are updated using the following equation:

$${}^i\mathbf{w}(t+1) = {}^i\mathbf{w}(t) + \zeta \left(-\frac{\partial V}{\partial t} \right), \quad (6.10)$$

where ζ is a positive number expressing the learning rate of the weights. This parameter controls the change in the weights for every iteration, so that the model can be fine-tuned with small updates. This process is repeated for all the training data. One iteration for updating the entire dataset is called an epoch. Once the model is trained, it can be used to make predictions using a different dataset. At this stage, only the final set of weights and new inputs are needed to

provide future predictions.

The dataset is divided into three sets: a training set (70% of data), a validation set (15% of data) and a testing set (15% of data). The training set is used to update the network's weights and biases. The validation subset is used to decide when to stop training the model, whilst the testing set is used to select the best model structure. The best model structure is found using a double-loop approach shown in Figure 6.7. The training procedure consists of the following steps:

1. The input signals are processed, and if necessary, the signals are normalised.
2. The optimal number of nodes in the hidden layers, h is chosen by performing a heuristic search [221] of values starting from configuration h_{\min} . In this case, one hidden layer is used, where ten different hidden layer combinations are assessed with $dh = 5$, where the number of hidden nodes range from 15 to 50.
3. In the innermost loop, each neural network is trained using the training set over a certain number of epochs. The number of epochs is established using a method called *early stopping* [222]. In this approach, the validation dataset error is tracked throughout the training process. This error normally decreases during the early training phase, as does the training set error. However, when the network begins to overfit the data, the validation error starts to increase. When the validation error rises for a certain number of iterations, the training is halted, and the weights and biases at the minimum of the validation error are returned.
4. The trained neural network is evaluated using the testing dataset, and the mean squared error is calculated.
5. Every time a model is trained, different weight values are generated due to varying initial weight and bias values. Consequently, different networks trained using the same dataset can give varying outputs for the same input. Each neural network structure is hence trained for several trials, N_{trials} .
6. Once the final hidden layer configuration h_{\max} is trained for N_{trials} , the best performing structure on average is deduced, and the network with the best test performance is chosen.

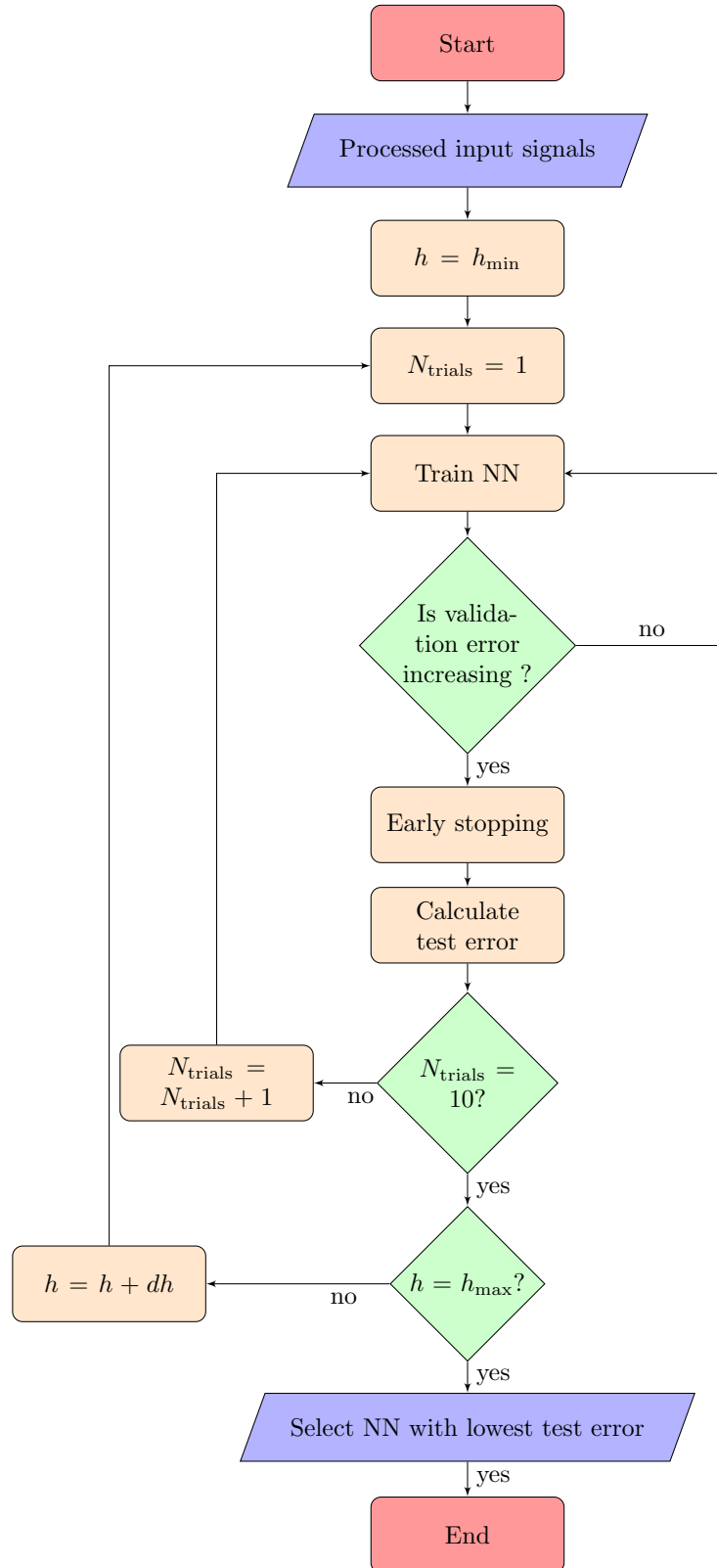


Figure 6.7: Flowchart illustrating the model's training and validation method

Following the training procedure of the ten different structures, the test performances depicted in Figure 6.8 are noted. The ANN with $h = 30$ is hence

selected for this dataset. This means that the model is composed of a total of 121 weights: 90 weights between the input and hidden layer and 31 weights between the hidden and output layer. The details of the trained neural network are provided in Table 6.2.

6.2.3.5 | Transient component, \mathbb{I}_T

Whilst the dynamic component accounts for eddy current effect in different current and ramp rate conditions, this component fails to represent the eddy current transient in static conditions, i.e., when the current is constant and the ramp rate is zero. This behaviour is represented in the time domain, and is derived from an equivalent model circuit of the magnet described in [41]:

$$\mathbb{I}_T = c_9(1 - c_{10} \exp(-c_{11}t_0) - c_{12} \exp(-c_{13}t_0)), \quad (6.11)$$

where the coefficients c_9 to c_{13} are identified as functions of the normalised prior ramp rate \dot{I}_r/I^* and the normalised difference in current between the current and previous plateau $\Delta I/I^*$. Figure 6.9 shows the measured transient component at 500 A/s and the different $\Delta I/I^*$ values (0.14, 0.18, 0.36, 0.54, 0.72, 0.91 and 1). Measurements are limited to two seconds, as independent measurements have shown that the eddy current transients decay fully by this duration.

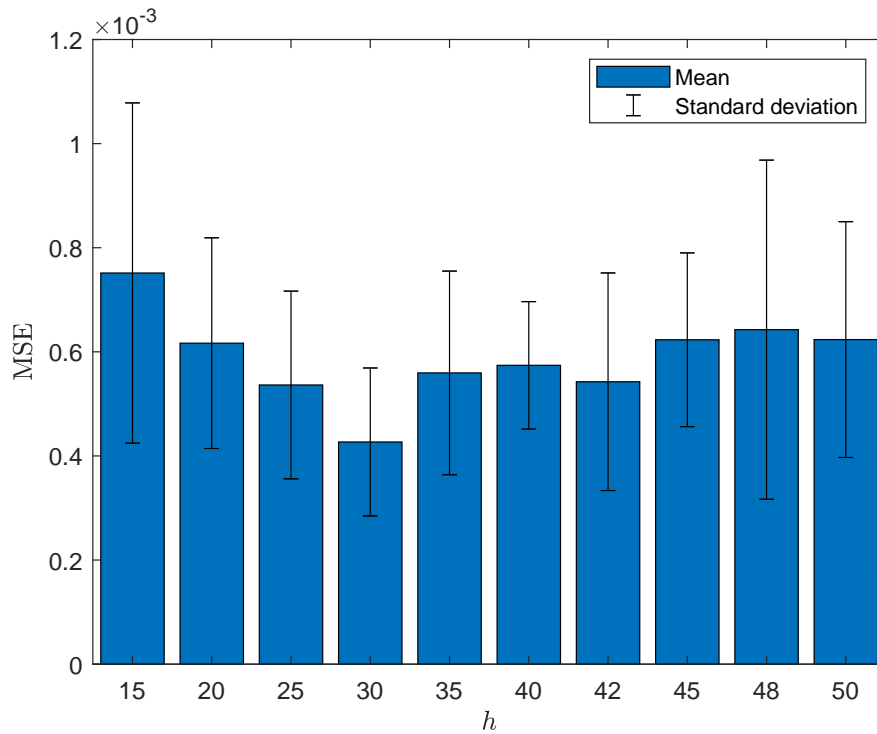


Figure 6.8: Performance of ten different neural network structures

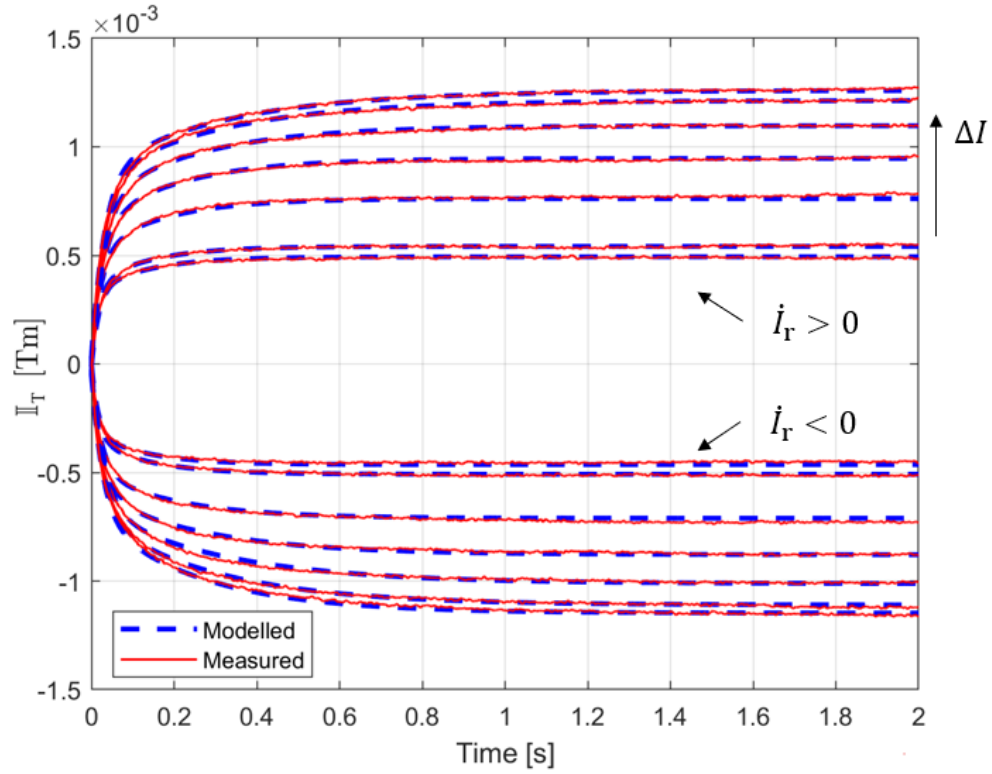


Figure 6.9: Measured and modelled transients at 500 A/s

Equation 6.11 is fitted to each measured signal, and the coefficient values are stored with their respective \dot{I}_r/I^* and $\Delta I/I^*$ labels.

An ANN is used to identify the coefficients based on the values of \dot{I}_r/I^* and $\Delta I/I^*$. After the measurement dataset is complete, measurements are interpolated in order to increase the number of data points in the range required for the application. The ANN in Figure 6.10 is implemented, which in this case is composed of two input nodes, two hidden layers and five output nodes. The same method in Section 6.2.3.4 was carried out to choose and train the ANN. The performance of the ten different neural network structures was evaluated, where a structure with $h = [56, 28]$ was eventually selected. The complete list of parameters of the ANN is recorded in Table 6.2.

6.2.3.6 | Performance indicator

The Normalised Root Mean Square Error (NRMSE) is used in this work to express the error between the estimated output and measurements:

$$\text{NRMSE} = \frac{1}{\max(\mathbb{I}_{\text{meas}}) - \min(\mathbb{I}_{\text{meas}})} \sqrt{\frac{1}{N} \sum_{i=1}^N (\mathbb{I}_{\text{meas},i} - \mathbb{I}_{\text{model},i})^2}, \quad (6.12)$$

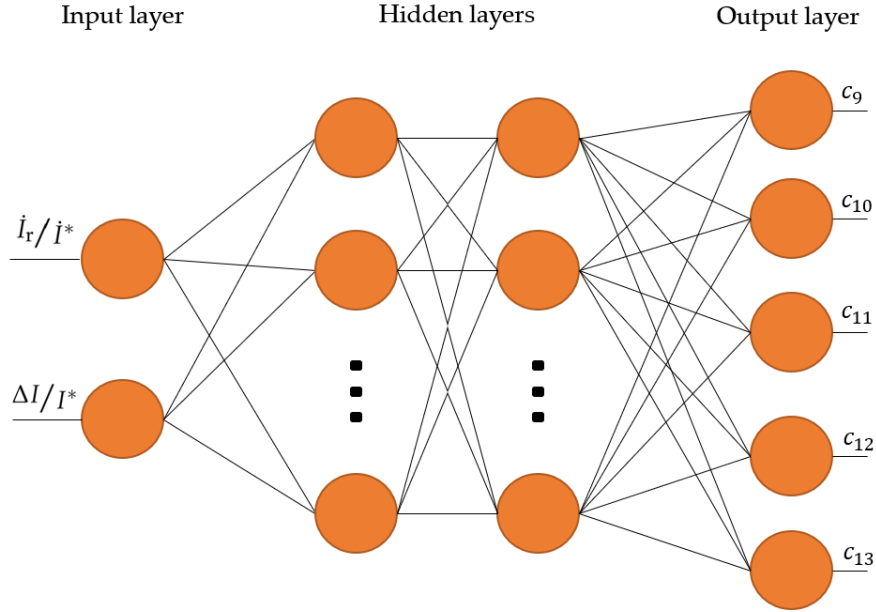


Figure 6.10: Neural network architecture used to identify the transient component coefficients

where \mathbb{I}_{meas} is the measured integral field value, and $\mathbb{I}_{\text{model}}$ is the modelled quantity. By normalising the error, the errors can be scaled to the range of the measurement in a relative manner, hence allowing a suitable comparison across various operating conditions and machines.

6.2.4 | Results

This section presents the experimental results, as well as the comparison of this model with the model presented by Caspers *et al.* [178]. The proposed model in this work is evaluated using the ELENA's acceleration and deceleration cycle data, resulting in a NRMSE of 1 unit. Figure 6.11 shows the residual distribution of the model with respect to time and current. It can be noted that the error is within a relative range of ± 1 unit at all beam injection/extraction times. The highest spiking error values are noted to be at the beginning of plateaus, indicating that the model is not successfully approximating the transient field behaviour at points where the plateau starts. However, the error drops immediately and is at an acceptable level during beam injection/extraction times, which is usually around two seconds after the start of the plateau.

As a comparison between the proposed model and the model by Caspers *et al.* implemented at the PSB and AD [178], the latter model is fitted for the ELENA resulting in a relative error of 10 units. This indicates that the proposed

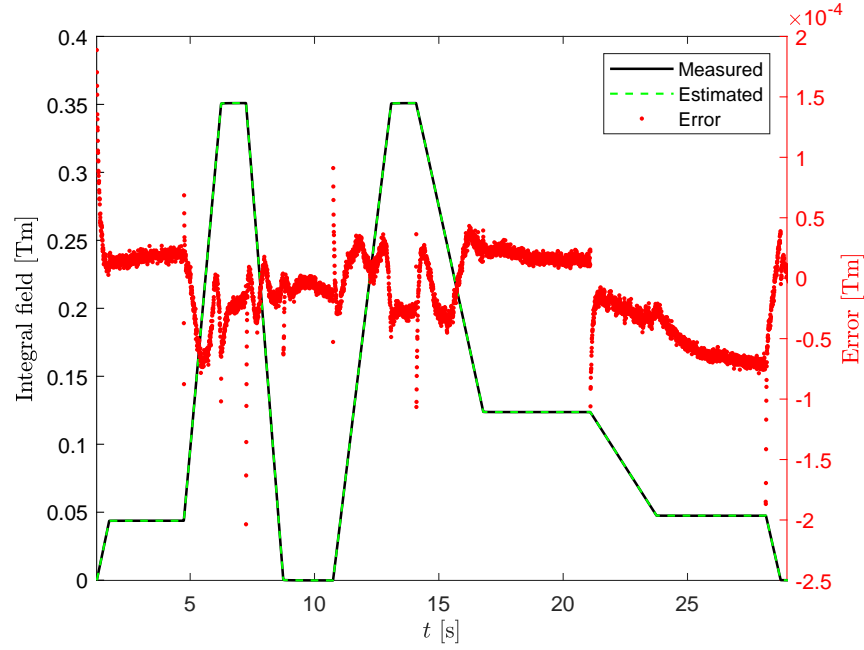
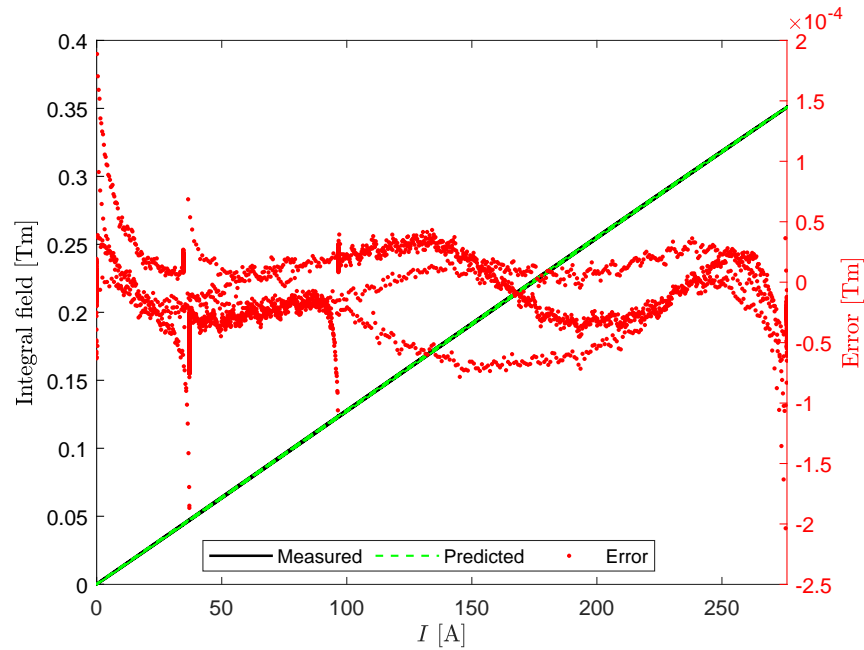
Table 6.2: ANN parameter list

	Parameter	Dynamic ANN	Transient ANN
Model properties	Activation function (hidden layers)	sigmoid	
	Activation function (output layer)	linear	
	number of hidden layers	1	2
	number of hidden nodes, h	30	[56, 28]
	training repetitions, N_{trials}	10	
Input	Nodes	2	
Output	Nodes	1	5
Training set	data	70% of data set	
	epochs	≤ 1000	
	algorithm	Levenberg-Marquadt	
	learning rate	0.1	
	approximate computation time	15 mins	20 hrs
Validation set	data	15% of data set	
Testing set	data	15% of data set	

model performs significantly better than this model. Figure 6.12 shows the excitation current and non-linear field relationship (integral field minus the linear component), for the two ELENA commissioning cycles, as estimated by the two field models. The figure illustrates the extensive non-linear capability of the proposed model, where the model is able to represent the small fraction of non-linearity in a fair manner. Deviations of the model's estimate from the measurement can be attributed to the fact that the model was not trained to represent all ramp rate values, but slower ramp rates behaviours were extrapolated based on the generalisation capabilities of the ANN.

6.2.5 | Discussion and limitations

The developed hysteresis modelling technique is proposed as a suitable choice for magnetic field control systems, presenting an accurate modelling performance. As opposed to currently employed strategies, this method does not require any knowledge of the magnet specifications, except for a measurement campaign at different peak current levels and ramp rates. In real-time operation, the model requires relatively few input data and is not computationally intensive as it only involves addition and multiplication terms. The model also has the advantage that once it is trained over a range of operating conditions, it does not have to be retrained if the changes fall within this range.

(a) Residual distribution with respect to t (b) Residual distribution with respect to I **Figure 6.11:** Residual distribution of the fitted model, with respect to current and time.

This is particularly useful in machines which are undergoing commissioning such as in the ELENA where small changes to the machine cycles are made on a regular basis. Even if the model has to be retrained, the training procedure is partly automatic and lasts a couple of hours at most, depending on the size of the dataset.

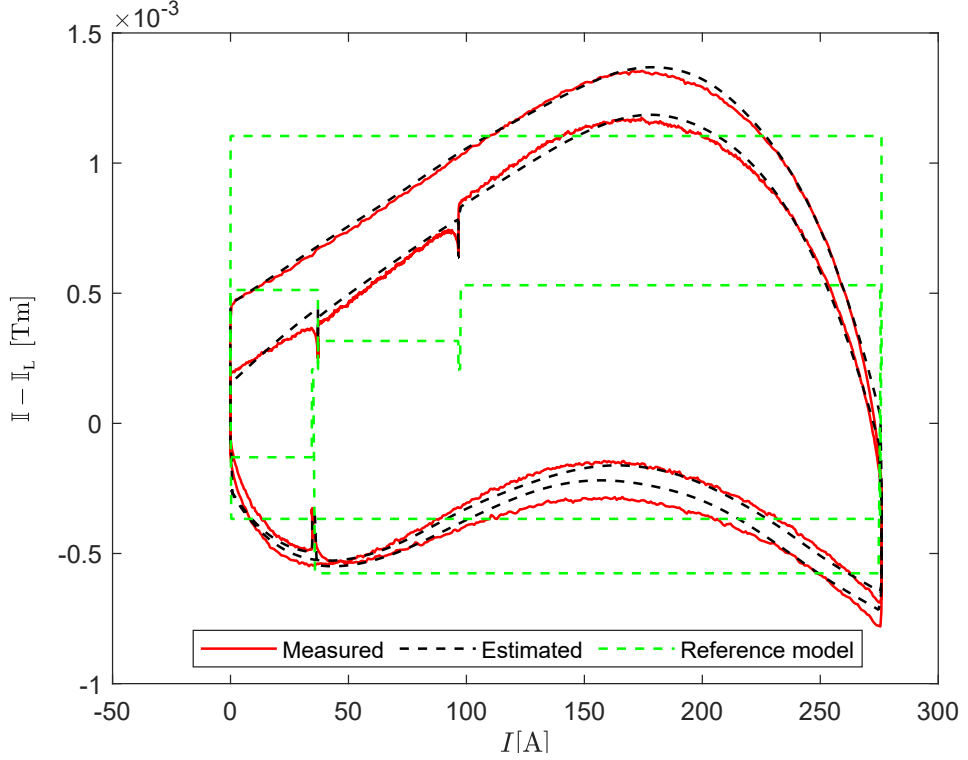


Figure 6.12: Actual and estimated non-linear ELENA field. The estimation using the model by Caspers *et al.* [178] is also depicted.

6.3 | Preisach-RNN model

For the real-time operation of the ELENA B-train, a field model which is not computationally expensive is crucial. This section describes an alternative dynamic ferromagnetic hysteresis model, proposed for simulating the vertical field in different magnetic materials used in manufacturing accelerator magnets. As an example, ARMCO pure iron measurements are modelled, as the material is an important part of the superconducting magnets designed for the High Luminosity upgrade of the LHC. Understanding the dynamic behaviour of this material is important in the design phase of these magnets, and hence an accurate model is required, that can be assembled with a restricted amount of data. The measurement data in this study was acquired by Mariano Pentella, with the complete experimental details provided in [223].

6.3.1 | Method

The Preisach model is a popular method for modelling hysteresis behaviour. However, the classical model is rate-independent, such that the hysteresis output is unaffected by the input ramp rates. The use of neural networks is

proposed to address this issue, by implementing the Preisach model using a RNN. This model is proposed to accurately represent both major and minor hysteresis loops, including saturation regions.

In general, the Preisach model is represented by a double integrator in continuous form as shown in Equation 2.13. Applying a co-ordinate change, $r = (\alpha - \beta)/2$, $v = (\alpha + \beta)$, $\hat{\mu} = \mu(v + r, v - r)$, it is demonstrated that the boundary between the +1 and -1 regions in the Preisach half-plane with coordinates $r > 0$, $v \in \mathbb{R}$ can be expressed by the function $v = P[u](t)$, known as the play operator [224]. This allows Equation 2.13 to be readjusted as:

$$z(t) = \int_0^{+\infty} g(r, P[u](t)) dr, \quad (6.13)$$

which can be discretised to n play operators as follows:

$$z(t) = \sum_{j=1}^n \phi_j P_j[u](t), \quad (6.14)$$

where ϕ_i is the density function of the i th play operator, which needs to be identified. The play operator is illustrated in Figure 2.10(b) and described in Equation 6.15:

$$P_i[u](t) = \max(u(t) - r_i, \min(u(t) + r_i, P_i[u](t - 1))), \quad (6.15)$$

$$P_i[0] = \max(u(0) - r_i, \min(u(0) + r_i, z_0)), \quad (6.16)$$

where z_0 is the play operator's initial condition and r_i expresses the memory depth as follows:

$$r_i = \frac{i-1}{n} [\max(u(t)) - \min(u(t))], \quad (6.17)$$

where $i = 1, 2, 3, \dots, n$.

In this study, a RNN is used as a replacement for the density function ϕ_i of the discrete Preisach model in Equation 6.14, as these structures are recognised for their ability to model any non-linear dynamic system, up to a given degree of accuracy [225]. RNNs are different from feedforward networks as they contain a feedback loop connected to a past node, such that the nodes ingest their own outputs instant after instant as input. This indicates that such networks are a good option to model dynamic behaviours.

In principal, the composition of a RNN is shown in Figure 6.13. Whilst the input and output layers consist of feedforward connections, the hidden layer is composed of recurrent ones. The input vector $\mathbf{v}(t)$ is processed at the input layer at each instant. Subsequently $\mathbf{v}(t)$ is summed with the bias vector ${}^1\mathbf{b}$ and multiplied by the input weight vector ${}^1\mathbf{w}$. Similarly, the internal state $\mathbf{y}(t)$, delayed by a number of time steps d , is multiplied by the gain parameter ${}^h\mathbf{w}$ and summed with the input state as follows:

$$\mathbf{y}(t) = f_h[{}^1\mathbf{w}(\mathbf{v}(t) + {}^1\mathbf{b}) + {}^h\mathbf{w}(\mathbf{y}(t - d))], \quad (6.18)$$

where $f_h(x)$ is the activation function, which is a hyperbolic tangent function in this work, defined as:

$$f_h(x) = \frac{2}{1 + e^{-2x}} - 1. \quad (6.19)$$

The internal state $\mathbf{y}(t)$ is then added with bias ${}^2\mathbf{b}$, multiplied by the weight ${}^2\mathbf{w}$, and the result is passed through a linear activation function $f_o(x)$ as follows:

$$z(t) = f_o[{}^2\mathbf{w}(\mathbf{y}(t) + {}^2\mathbf{b})], \quad (6.20)$$

where $z(t)$ is the predicted output at time t .

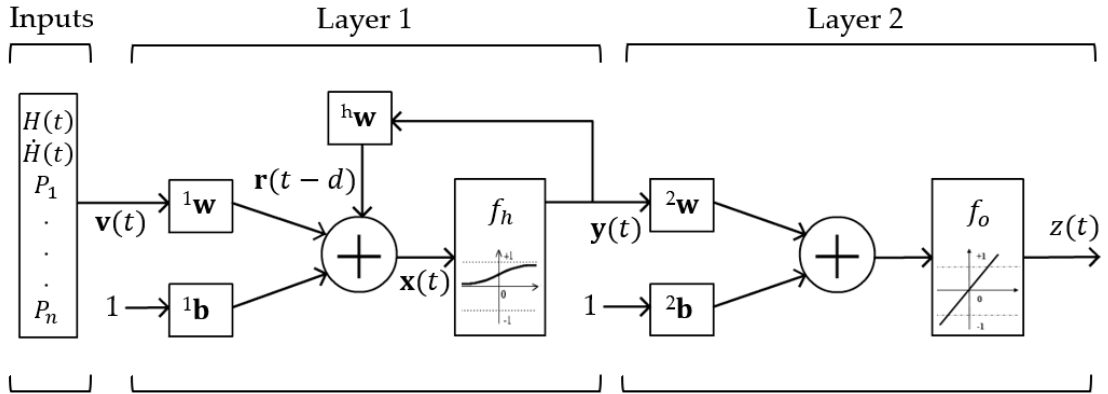


Figure 6.13: Schematic representation of the proposed Preisach-RNN model.

The network's weights are acquired using the *layrecnet* command from the Deep Learning Toolbox [218] by MATLAB. The Levenberg-Marquadt algorithm is implemented to train the network, as described in Section 6.2.3.4. The inputs include the magnetic field $H(t)$, its derivative $\dot{H}(t)$ and a pre-determined amount of play operators $P_i[H](t)$ (chosen according to the complexity of the data). All input and output data is normalised to the range $[-1, 1]$ and the

operators are calculated based on the normalised magnetic field signal.

The training, validation and testing dataset consists of three minor loops and three major loops that ramp at 1025 , 1554 and $6135 \text{ Am}^{-1}\text{s}^{-1}$, as shown in Figure 6.14. This data is divided into three subsets (training, validation and testing) in an interleaved manner, similar to the case in Section 6.2.3.4. When the neural network is trained, and the best model structure is picked, an evaluation signal is used to establish the performance of the model. The evaluation dataset comprises of three major loops that ramp at $3067 \text{ Am}^{-1}\text{s}^{-1}$ and one minor loop that ramps at several random ramp-rates between 1000 and $6200 \text{ Am}^{-1}\text{s}^{-1}$, as depicted in Figure 6.15. The model validation process is identical to the one followed in Section 6.2.3.4 and Figure 6.7. The parameters pertaining to the RNN are listed in Table 6.3. The metric used as the performance indicator is the NRMSE, defined in Section 6.2.3.6.

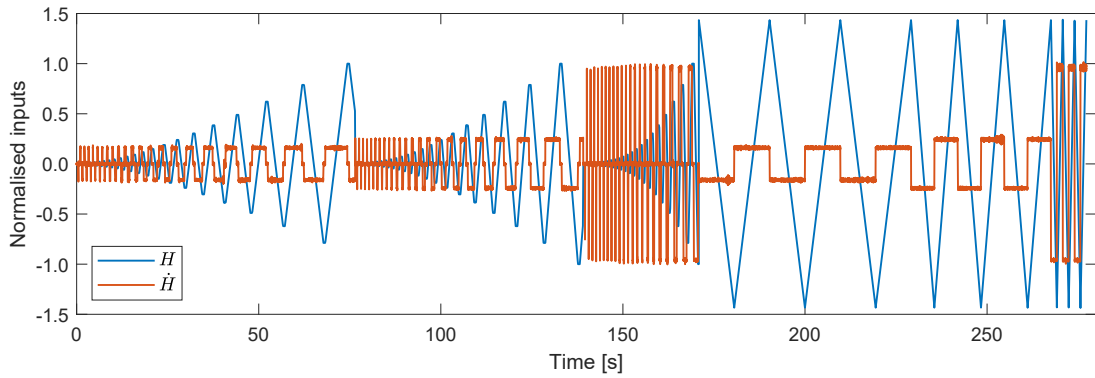


Figure 6.14: The magnetic field signal and its derivative that form the training, validation and testing datasets.

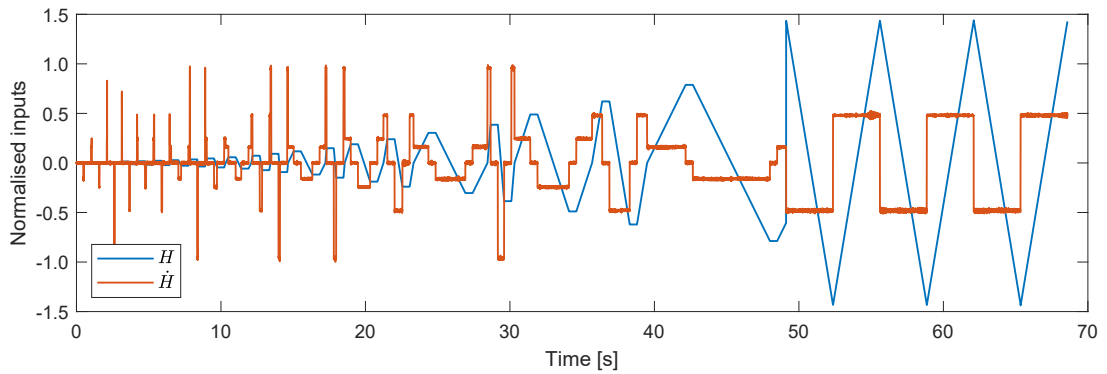


Figure 6.15: The magnetic field signal and its derivative applied for the model's evaluation.

Table 6.3: Recurrent neural network parameters list

	Parameter	Value
Model properties	Activation function (hidden layer)	hyperbolic tangent
	Activation function (output layer)	linear
	Delay, d	2
	Hidden nodes search range, $h_{min} : dh : h_{max}$	4:1:13
	Number of hidden nodes, h	12
	Training repetitions, N	10
Input	Number of play operators	6
Training set	Data	70% of data set
	Epochs	≤ 1000
	Algorithm	Levenberg-Marquadt

6.3.2 | Results

Once the best performing model is trained and tested, it is used for predicting the evaluation dataset in Figure 6.15. The initial few predicted samples in the dataset are ignored to remove the opening transient phase. Considering the major loop, a NRMSE of 0.58% results when predicting a hysteresis loop with an unseen ramp rate not used in the training procedure. Figure 6.16 depicts the major loop data used for training and evaluating the model, along with the predicted data. In the case of the minor loop dataset, a NRMSE of 0.66% is derived with varying random ramp rates, including ramp rates not used for training the model. Figure 6.17 shows the predicted magnetic flux density with respect to time.

The effect of including Preisach operators as inputs to the model is evaluated by repeating the model's training and validation process without the P_j inputs. Putting the two models head-to-head, the addition of the Preisach operators is observed to boost performance by 19% for major hysteresis loops, and 44% for minor hysteresis loops. One must keep in mind that a model without Preisach operators is computationally less expensive, as the optimised structure contains 241 weights as opposed to 409 weights in the original model. Finally, a compromise has to be effected between speed and accuracy depending on the model's application.

A univariate sensitivity analysis is also performed to understand how robust the model is as the input variables change over a specific range [226]. This

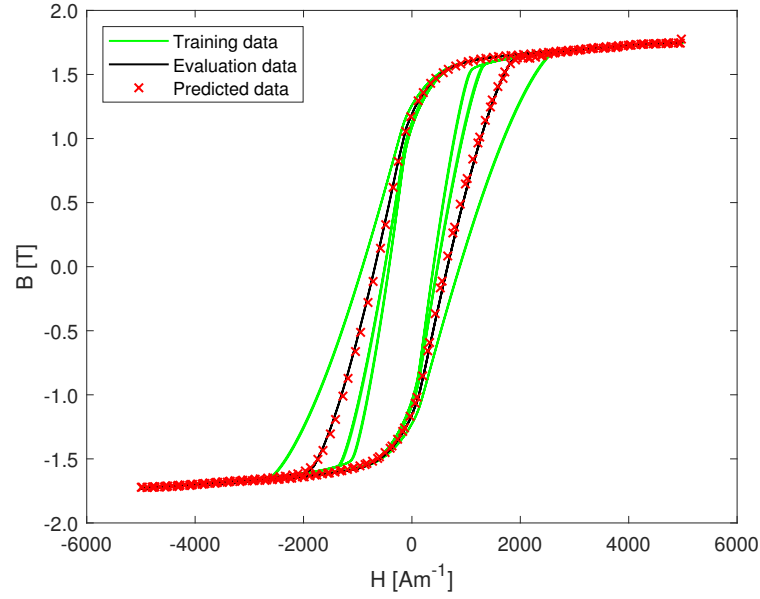


Figure 6.16: Major loop predictions and training data.

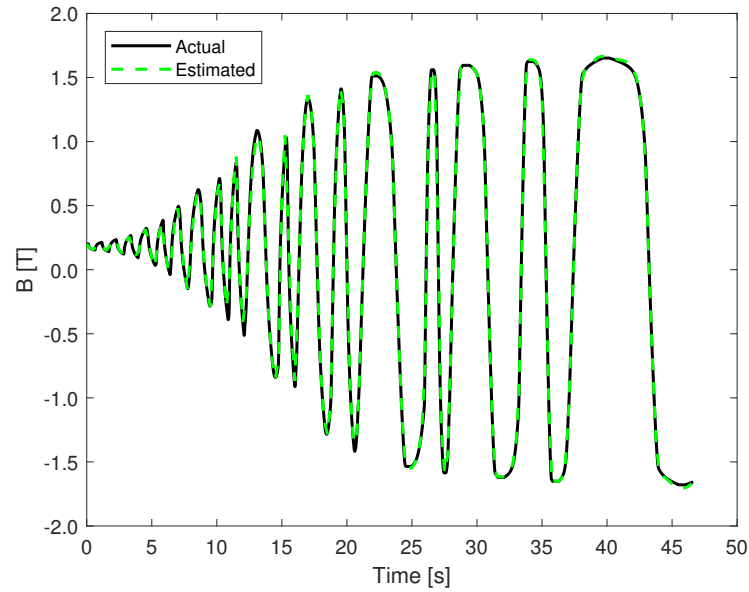


Figure 6.17: Minor loop predictions at random ramp-rates.

exercise indicates which model input parameters notably affect the predicted output, especially due to the fact that the signal, $\dot{H}(t)$ is noisy. An ANN that picks up minor noise throughout the training process can overfit the noise as if it were the signal, resulting in poor accuracy during validation [227]. In the sensitivity analysis, one input variable is fed a varying signal whereas the remaining inputs are kept constant. Simultaneously, the deviation in the output signal is noted. This procedure is repeated for all the model inputs.

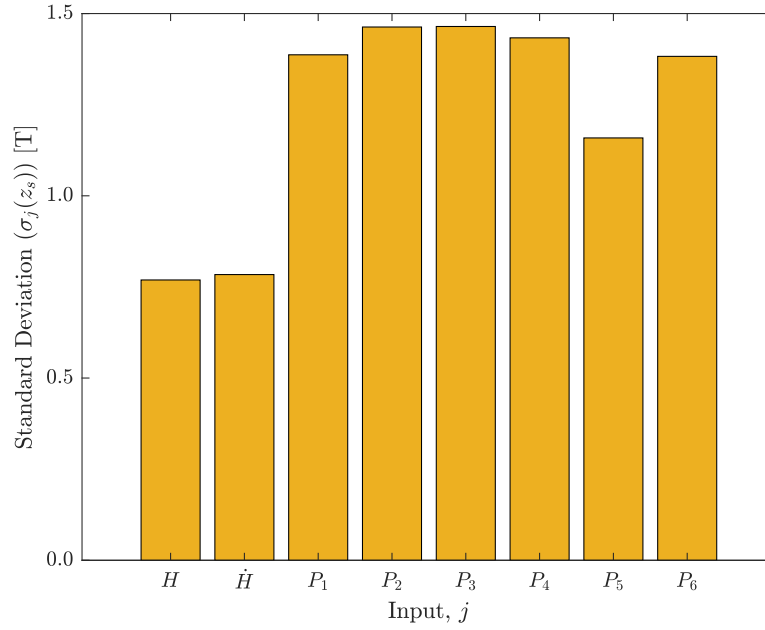


Figure 6.18: The outcome of the sensitivity analysis for each individual input.

In this work, after the model is trained, the input vector is set to 0. Then, for one of the eight variables, a value is selected in the range between $[-1,1]$. This is carried out for 10,000 time instants for each input variable. The standard deviation $\sigma_j(z_s)$ for each variable j is calculated. Figure 6.18 shows a bar chart these results. It can be observed that the output varies much more for operator input variables, hence the model is more sensitive to variations in these parameters. Results also indicate that the output is not significantly sensitive to the noise from the field derivative signal, indicating an aptly trained neural network.

6.4 | Summary

This chapter presented two hysteresis models for two different applications. A model is proposed that predicts the dipole integral magnetic field in low-field synchrotrons based on the excitation current and related parameters related to the magnets' operation. The model decomposes the integral field into five main contributions: the linear, residual, hysteresis, dynamic and transient components. Polynomial equations and ANNs are used to describe the hysteresis curves at different dynamic conditions. The model is constructed using measurements from the ELENA spare magnet, and the neural networks are trained using a novel double-loop approach. Results indicate that the model

can predict the ELENA acceleration and deceleration cycles within a relative error of 1 unit. The proposed model has potential to be used in similar high accuracy situations, where the operating conditions are predictable and do not change very frequently.

A Preisach-RNN model is also presented, which represents the dynamic behaviour of ferromagnetic materials and does not require prior knowledge of the material and its microstructural behaviour. A detailed training and validation method is proposed for the neural network to optimise the weight parameters. A model that can predict both major and minor loop dynamic ferromagnetic hysteresis behaviour is demonstrated, which allows researchers to estimate the dynamic effects of the material having only six different examples at three frequencies.

Chapter 7

Conclusions

7.1 | Summary of achieved aims

The precise knowledge of the dipole magnetic field is crucial to successfully maintain a radially centred beam of particles within synchrotrons. The ELENA ring, a new synchrotron being commissioned in CERN's Antimatter Factory, is one such example. This machine decelerates antiprotons from the AD and extracts the particles to six different antimatter experiments.

As the magnetic field and electric field provided by the RF cavity need to be synchronised so that the radius of the beam remains constant, two methods can be employed to estimate the magnetic field. The first is a magnetic field model, obtained from simulations or previous magnetic field measurements, which due to hysteresis effects can be difficult to formulate. The second method is the use of real-time magnetic measurement systems called B-trains, that are employed to estimate the magnetic field in the ring's dipole magnets. These systems consist of a reference magnet connected in series with the ring magnets, equipped with magnetic field sensors, as well as an electronic acquisition chain which treats and transmits the measured signals. At CERN, a B-train consolidation project is ongoing, presenting a new and improved facility referred to as FIRESTORM. The proposed measurement system includes

modernised electronics and sensors, with an emphasis on uniformity across all machines to improve maintainability. Following several years of developing the electronics and software components of the FIRESTORM system, the ELENA ring is one of the first machines to deploy it as the magnetic field measurement systems, and the first to completely rely on it.

Since the ELENA ring is a particularly different synchrotron from the machines that form part of CERN's LHC injector chain, the B-train system needs to be characterised considering the decelerator's operating conditions, ensuring the correct operation of the sensors and the electronic acquisition chain in this environment. As a result, a measurement model is developed which predicts the average bending magnetic field of the synchrotron, based on the real-time magnetic field measurement using sensors placed within the reference magnet. As measurements of each individual ring magnet and reference magnet are available from the magnets' acceptance campaign, it was possible to upgrade the B-train's measurement model to consider differences in these magnets. Other improvements are the inclusion of errors introduced by offsets in the coil placement and a novel *in-situ* identification procedure for field marker sensors that allows the reliable use of an induction coil to acquire precise absolute measurements, that are repeatable so that they can be adapted to new machine cycles.

This study has developed and applied the upgraded measurement model to the ELENA ring, based on the magnet, sensors and electronic chain characterisation measurements. The measurement accuracy has proven adequate for operation during the first beam commissioning tests. This successful result is a first in the decade-spanning history of B-train systems at CERN. In addition, an uncertainty estimation procedure was carried out to obtain a detailed quantitative estimate of the measurement uncertainty. Delivering the absolute field value, accompanied by a formally derived uncertainty, presents a significant shift of perspective as operators are provided with a clear indicator on whether to first explore the magnetic field, or other subsystems, whenever beam instabilities or other issues come up. In the case of the ELENA, the measurement uncertainty is noted to be dominated by the errors introduced by the difference between the ring and reference magnets, as well as the position of the coil. These factors, however, are expected in this case and are very specific to the ELENA, so a considerably better performance is anticipated for

other systems currently being commissioned. In cases where the uncertainty estimation does not match up to the desired target accuracy, the measurement setup has to be accompanied by a beam calibration method to check and ensure that the accuracy target is met.

Following the identification and characterisation of the B-train system, the performance of the system was evaluated through three main tests: field marker characterisation, a reliability run and a beam calibration procedure. The field marker characterisation tests were performed to test the suitability of using NMR sensors as field markers for the ELENA B-train. The precision of the NMR sensor at the ELENA operating field levels and different ramp rates was measured, so that appropriate ramp rate values could be suggested for the machine operating cycle. In the end, the precision at a field level of 45 mT is noted to be better than 2 units ($\times 10^{-4}$), whilst at 340 mT it is better than 0.09 units. The delay in the trigger signal generation was also calculated, and noticed to be 0.7 units in the worst case at low field, high ramp rate conditions. The novel *in-situ* field marker calibration method accounts for this error, so there is no need to compensate for this systematic offset. Better precision results were noted at lower ramp rates and hence were suggested for the final commissioning cycles.

The second performance evaluation method for the B-train was a reliability run, carried out to validate the performance of sensors, electronics, controls and transmission of the instrument on a statistical basis. The random error sources of the measurement were identified under typical operating conditions: the measurement's drift, noise, and marker repeatability. The high spread of the field at the deceleration cycle's extraction point was noted, signalling the need for an additional mechanism to 'freeze' the field measurement during long plateaus. Overall, the performance of the instrument was found to be acceptable within the desired reproducibility level expected for machine operation.

The systematic offset in the measurement was noted during the third performance evaluation method. A model to estimate the systematic error based on the radial frequency component was proposed in this work. Using the beam's radial position offset, a field error was translated by fitting a first-order polynomial at different field levels where the RF system is on. In the end, a calibration was performed, where the systematic error was reduced by two

orders of magnitude, to less than $\pm 1 \mu\text{T}$.

As the uncertainty estimation procedure identified the field marker measurement as one of the contributors to the combined uncertainty, measurements were carried out to investigate the behaviour of the magnetic length parameter in different positions within the gap of the magnet. Since this parameter is assumed to be constant in all B-trains at CERN, minimal variations of this parameter in different conditions are desired for optimal measurement stability. When measuring the magnetic length of the spare ELENA magnet using the fixed coil and Hall probes, a position was found close to the pole edge, where the magnetic length converges. As the Hall probe was raised vertically, the optimal position was noted to remain constant, whilst the variation of the magnetic length increased proportionally. Moving the sensors in a horizontal manner out of the gap of the magnet, the optimal position shifted proportionally towards the magnet centre, whilst the magnetic length variation remained constant. This is particularly useful information in B-train systems where the field marker sensors are installed within the ring magnets, as no reference magnet is available. In such cases, due to equipment placed in these magnets, field marker placement options are limited to locations out of the central beam path.

In addition, two measurements were carried out to evaluate the feasibility of displacing the field markers in the ELENA B-train to the optimal position. The first test determined the response of magnetic resonance sensors within the magnet gap, confirming operability at the proposed position. In the second test, the proposed setup was installed in the magnet along with the original setup, and the dynamic operation conditions where the proposed setup performs better were determined. Considering the operating conditions during the commissioning period of the ELENA ring, it was concluded that whilst there is no advantage in shifting the low-field marker to the optimal position, shifting the high-field marker presents a relative improvement of 45% in the measurement's repeatability when the two cycles are implemented.

Besides having the ability to transmit the measured magnetic field to the user, the new FIRESTORM system offers the capability of distributing the estimated field based on a model. This is particularly useful for occasions where the power converter is not available, or when an issue arises with the measurement.

A model which can replicate the field within an accuracy level of 2 units is required for precise field control. In Chapter 7, a magnetic field model was proposed based on the decomposition of the integral field in five main terms. A measurement campaign was carried out using the ELENA spare dipole magnet to build a dataset of the integral field at different peak currents and ramp rates. Polynomial equations and ANNs were chosen as the identification methods for the components. A double-loop approach was considered to train the neural networks to an acceptable degree. An important experimental outcome was obtained when the model was tested using the two ELENA cycles. An overall accuracy of 1 unit was noted, which is an improvement over the models used at the PSB and AD at CERN. Furthermore, a Preisach-RNN was proposed for modelling dynamic ferromagnetic hysteresis in accelerator magnets for material science applications. A model which can predict both major and minor loop behaviour was demonstrated.

The next section will now summarise the main contributions of this work to the development of the research field.

7.2 | Personal contributions

This thesis has presented a characterisation procedure, performance evaluation and optimisation of B-train systems at very low fields. A magnetic field model has also been proposed, which can operate in parallel with the real-time measurement. The main contributions of the author towards the research field are listed below:

- A critical review of existing real-time magnetic measurement systems in different synchrotrons as well as an overview of a selection of hysteresis modelling techniques, including the current state-of-the-art models in synchrotrons.
- Development of an absolute measurement model for B-train systems with an associated uncertainty estimation, implemented for the ELENA ring. This includes characterisation procedures for each parameter, including a novel field marker calibration method based on an *in-situ* measurement.
- Development of metrological evaluation methods for B-train systems including magnet, sensor, and electronic chain characterisation tests. A calibration procedure based on beam measurements was also presented.

- Investigating the magnetic length parameter based on measurements performed in different positions along the magnet gap. An optimal position is proposed closer to the magnet edge, where the variation of the magnetic length is minimal and can offer several advantages to synchrotron magnetic field measurement systems. A feasibility analysis of moving field marker sensors in the ELENA was carried out.
- Development of two new hysteresis modelling techniques, one of which can be implemented as part of B-train systems, meeting the accuracy and practical requirements, whilst the second model is able to model major and minor dynamic hysteresis loops.

7.3 | Future Work

Commissioning of the ELENA ring resumes in the second half of 2020, where the testing of equipment such as the electron cooler will continue. Beam extraction to five antimatter experiments is also expected to take place for the first time after the installation of dedicated transfer lines in the first half of 2021. A possible upgrade to the measurement model is the inclusion of the background field as a term in the model. Such a task requires measurement of the background field using a fluxgate close to the ring magnets, as well as in the location of the reference magnet. This would be important to notice and account for any cross-talk between the ring magnets, which is not being picked up by the reference magnet.

On the other hand, to avoid the large uncertainty contribution of α , a different value corresponding to each critical condition can be applied by implementing a software facility which updates the parameter in real-time. This would result in a significant decrease in the measurement combined uncertainty. Other future work on the measurement model involves the integration of this model in other synchrotrons at CERN, starting from the PS and PSB as they are expected to restart operation in the first half of 2021.

With regards to the performance of the instrument, possible improvements include a field marker for correcting the drift on long plateaus, which ‘freezes’ the magnetic field value at these points, as well as the direct use of the measured radial beam position in a feedback loop to calibrate the magnetic field measurement in real-time. In terms of the mathematical modelling of

the magnetic length parameter, further work can be done to model it as a function of excitation current and other parameters. The criterion for optimising the position of field marker sensors can be improved by including weights to different operation conditions such as current, ramp rate and previous excitation history.

This study has explored one option for a reliable and computationally inexpensive magnetic field model for the prediction facility of B-train systems. The research initiative at CERN for developing a magnetic field model for synchrotrons is at its initial stages and this model serves as an appropriate base for future improvements and implementations. Other options which can be explored are different types of neural networks that exhibit temporal dynamic behaviour, such as the NARX model.

Appendix A

Performance Comparison of NMR and FMR sensors

This section discusses a comparative analysis performed to investigate the relative dynamic performances of NMR and FMR sensors when operating at the low field levels and ramp rates experienced in low-energy synchrotrons such as the ELENA ring. Whilst FMR sensors are not planned to be used as part of the ELENA B-train sensor setup, a comparative study is carried out to evaluate the potential of using these sensors alongside, or replacing the standard NMR sensors.

The measurement is executed using the ELENA reference dipole magnet, Metrolab PT2025 teslameter [48] and a National Instruments data acquisition unit NI-USB 6366 [213], with a 1 MHz acquisition rate. Metrolab's NMR Probe 1 (field range of 43 mT to 130 mT) is used for the low field measurements while Probe 3 (field range of 170 mT to 520 mT) is used at the high field mark. The FMR sensor used is a band-pass YIG filter, where the resonating sample is a Gallium-doped YIG sphere of 0.36 mm diameter, with a gyromagnetic ratio $\gamma/2\pi = 28.02495$ GHz/T [54]. The probes are installed in the middle of the magnet gap, and measurements are acquired from both probes simultaneously.

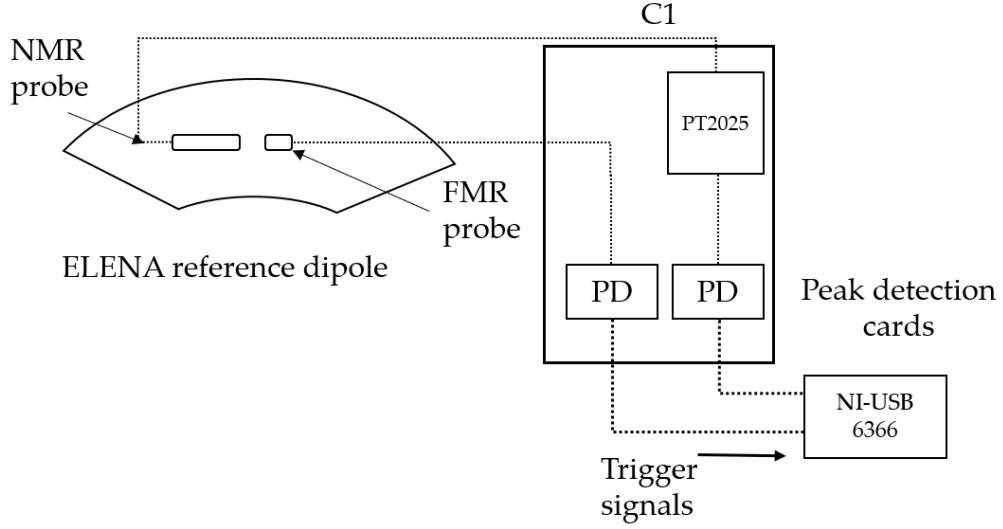


Figure A.1: Reference magnet and electronic experimental setup to compare the precision of two magnetic resonance field markers for the ELENA B-train.

A separate peak detection card is used for each magnetic resonance signal to produce a trigger signal at the minimum peak. The complete experimental setup is illustrated in Figure A.1.

The measurement investigates the performance of these two sensors at five field levels ranging from 43 mT to 200 mT and ramp rates varying from 53 mT/s to 750 mT/s. The cycles applied to the magnet by the ELENA power converters are shown in Figure A.2. Each cycle is applied repeatedly and 100 signals for the each of the 14 different field (B) and ramp rate (\dot{B}) parameters are acquired. Figure A.3 shows an example of the signals acquired at 200 mT and 368 mT/s. The repeatability of one sigma of the trigger signal generation ($\sigma(t_k)$) is calculated by finding the trigger time's standard deviation. Comparing several subsequent cycles assumes that the magnetic history is repeatable as a function of time, and so pre-cycles are ignored in the calculation of this parameter. The equivalent value in Tesla, σ_m is calculated as defined in Section 4.2.1.3, and the reproducibility ($\bar{\sigma}_m$) is found by averaging σ_m to compare the performance of the two magnetic resonance sensors across three different (B, \dot{B}) groups. The delay between the generation of the NMR and FMR trigger signals ($\Delta t_{\text{NMR-FMR}}$) is also noted, in order to characterise the effect of the NMR probe's inbuilt filter in different (B, \dot{B}) scenarios.

The results obtained are listed in Table A.1. The reproducibility is noted to improve at higher field levels and at the lowest ramp rates. The largest difference between the field reproducibility is noted at the lowest field levels.

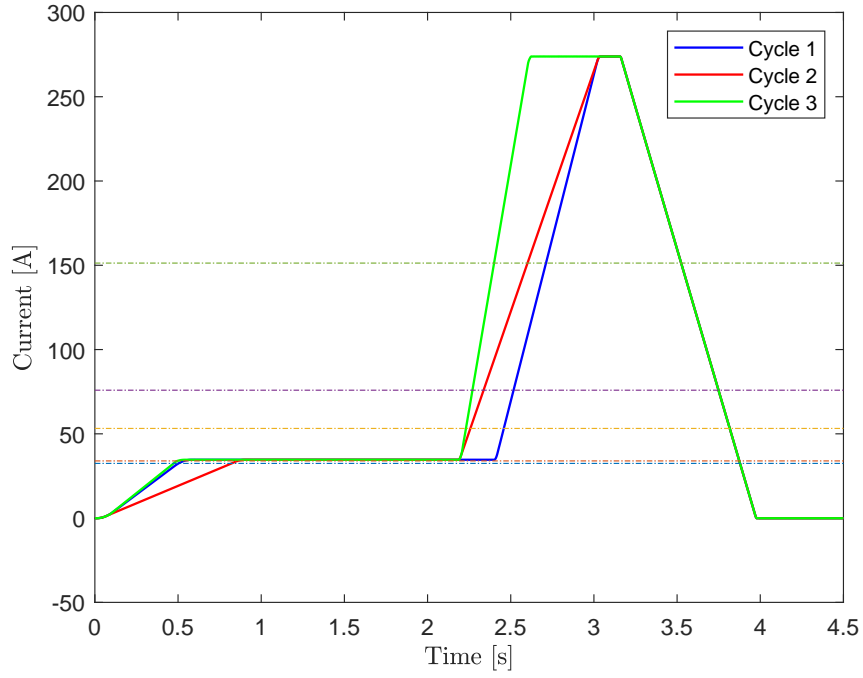


Figure A.2: Cycles applied and corresponding field levels (shown as dotted lines).

This is attributed to the FMR resonant signal's wider shape at lower fields, which leads to imprecise peak detections. To confirm or reject the differences between the two sensors, an independent t-test is carried out, which finds no statistically significant difference between the reproducibility of the two sensors at a level of marginal significance less than 0.05.

In conclusion, under the tested conditions, no sensor is found to outperform the other on a statistical basis. As a result, in the case of the ELENA B-train the choice is hence informed considering the cost and practicality of the sensors. Whilst the commercial NMR instrument is relatively expensive, it can also be used in other DC field measurement applications. With some modifications, the probe can also be adapted to work in stand-alone mode, removing the need for the teslameter unit, which reduces the cost significantly. On the contrary, FMR sensors are developed at CERN and are still undergoing considerable research. An advantage of using FMR sensors is the fact that they operate in the multi-GHz range, resulting in improved noise immunity and cleaner signals as shown in Figure A.3. As the NMR field marker demonstrates slightly better repeatability results across all target field levels and ramp rates, it is chosen as the field marker sensor for the operation of the ELENA ring.

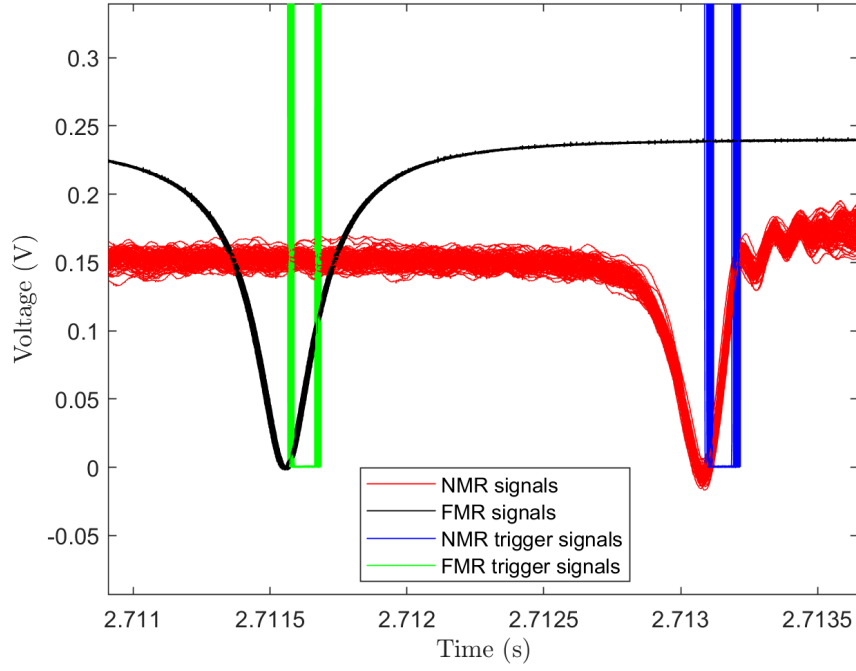


Figure A.3: Generated NMR and FMR signals at 200 mT and 368 mT/s, along with the corresponding trigger signals .

Table A.1: Measured trigger signal repeatability for NMR and FMR sensors

B (mT)	\dot{B} (mT/s)	$\sigma(t_k)$ [μ s]		σ_m [μ T]		$\bar{\sigma}_m$ [μ T]		$\Delta t_{NMR-FMR}$ (ms)
		NMR	FMR	NMR	FMR	NMR	FMR	
43.0	53.3	42.0	63.3	2.2	3.4			0.62
	93.5	37.4	54.1	3.5	5.1			0.72
	53.3	57.8	205	3.1	10.9	4.7 ± 2.6	11.3 ± 8.5	1.00
45.0	93.5	65.9	129	6.2	12.1			0.30
	102	83.0	246	8.4	25.0			1.09
70.0	368	8.3	6.3	3.1	2.3			0.05
	498	6.8	4.7	3.4	2.3			0.01
	748	7.5	3.7	5.6	2.8	3.7 ± 1.0	2.8 ± 0.4	0.10
	368	8.0	7.8	3.0	2.9			0.24
100	498	6.3	6.2	3.1	3.1			0.28
	748	5.5	4.2	4.1	3.2			0.23
200	368	6.8	8.7	2.5	3.2			1.52
	498	6.1	5.2	3.0	2.6	3.3 ± 0.9	2.8 ± 0.3	2.03
	748	5.6	3.6	4.2	2.7			1.05

References

- [1] Institute of Physics, “Particle physics – it matters,” Tech. Rep., 2009. [Online]. Available: http://www.iop.org/publications/iop/2009/page_38211.html
- [2] M. Benedikt, P. Collier, V. Mertens, J. Poole, and K. Schindl, *LHC Design Report*, ser. CERN Yellow Reports: Monographs. Geneva: CERN, 2004. [Online]. Available: <http://cds.cern.ch/record/823808>
- [3] M. Dosanjh, A. Aggarwal, D. Pistenmaa, E. Amakwaa-Frempong, D. Angal-Kalinin, S. Boogert *et al.*, “Developing innovative, robust and affordable medical linear accelerators for challenging environments,” *Clinical Oncology*, 02/2019 2019. [Online]. Available: <https://www.sciencedirect.com/science/article/abs/pii/S093665551930055X?via=ihub>
- [4] E. Cooper, “Accelerators: power cutting-edge research,” *IOP*, 2014. [Online]. Available: https://www.iop.org/publications/iop/2014/file_64291.pdf
- [5] U. Amaldi, “The importance of particle accelerators,” *Europhysics News*, vol. 31, no. 6, pp. 5–9, nov 2000. [Online]. Available: <http://www.europhysicsnews.org/10.1051/epn:2000601>
- [6] H. Wiedemann, “Particle Dynamics in Electromagnetic Fields,” in *Particle Accelerator Physics*. Springer Berlin Heidelberg, 2007.
- [7] S. Baird, “Accelerators for pedestrians,” CERN, Geneva, Tech. Rep. PS-OP-Note-95-17-Rev-1, feb 1997. [Online]. Available: <http://cds.cern.ch/record/1044785>
- [8] B. Holzer, “Beam Dynamics in Synchrotrons,” *CERN Yellow Report CERN-2017-004-SP*, pp. 253–284. 32 p, Apr 2018. [Online]. Available: <http://arxiv.org/abs/1804.08873>
- [9] M. Lamont, J. Wenninger, R. Steinhagen, R. Tomás García, R. Garoby, R. W. Assmann, O. Brüning, M. Hostettler, and H. Damerau, *Accelerator Operations*. Cham: Springer International Publishing, 2020, pp. 519–583. [Online]. Available: https://doi.org/10.1007/978-3-030-34245-6_9

- [10] C. Wyss, *LEP design report, v.3: LEP2*. Geneva: CERN, 1996, vol. 1-2 publ. in 1983-84. [Online]. Available: <http://cds.cern.ch/record/314187>
- [11] N. J. Sammut, L. Bottura, and J. Micallef, "The LHC magnetic field model," *Conf. Proc.*, vol. C0505161, p. 2648, 2005.
- [12] P. Baudrenghien, "Low-level RF: Part I: Longitudinal dynamics and beam-based loops in synchrotrons," in *CAS 2010 - CERN Accelerator School: RF for Accelerators, Proceedings*, Jan 2011, pp. 341–367. [Online]. Available: <http://arxiv.org/abs/1201.2597>
- [13] J. Griggs, "Entering the world's premier antimatter factory," Mar 2012. [Online]. Available: <https://www.newscientist.com/article/mg21328584-000-entering-the-worlds-premier-antimatter-factory/>
- [14] M. Gersabeck, "Why Is There More Matter Than Antimatter?" 2019. [Online]. Available: <https://www.scientificamerican.com/article/why-is-there-more-matter-than-antimatter/>
- [15] S. Pascoli and J. Turner, "Matter–antimatter symmetry violated," *Nature*, vol. 580, no. 7803, pp. 323–324, apr 2020. [Online]. Available: <https://www.nature.com/articles/d41586-020-01000-9>
- [16] S. A. Baird, D. Berlin, J. Boillot, J. Bosser, M. Brouet, J. Buttkus *et al.*, "Design study of the antiproton decelerator: AD," CERN, Tech. Rep. CERN-PS-96-043-AR, Nov 1996. [Online]. Available: <http://cds.cern.ch/record/317704>
- [17] V. Chohan, C. Alanzeau, M. E. Angoletta, J. Baillie, D. Barna, W. Bartmann *et al.*, *Extra Low ENergy Antiproton (ELENA) ring and its Transfer Lines: Design Report*, ser. CERN Yellow Reports: Monographs. Geneva: CERN, 2014. [Online]. Available: <https://cds.cern.ch/record/1694484>
- [18] C. L. Cesar, G. B. Andresen, W. Bertsche, P. D. Bowe, C. C. Bray, E. Butler *et al.*, "Antihydrogen Physics at ALPHA/CERN," in *Canadian Journal of Physics*, 2009.
- [19] C. Malbrunot, C. Amsler, S. A. Cuendis, H. Breuker, P. Dupre, M. Fleck *et al.*, "The ASACUSA antihydrogen and hydrogen program: Results and prospects," in *Philosophical Transactions of the Royal Society A: Mathematical, Physical and Engineering Sciences*, 2018.
- [20] C. Smorra, K. Blaum, L. Bojtar, M. Borchert, K. A. Franke, T. Higuchi *et al.*, "BASE – The Baryon Antibaryon Symmetry Experiment," 2015.
- [21] M. Zieliński, D. Grzonka, W. Oelert, T. Sefzick, G. Gabrielse, J. DiSciaccia *et al.*, "Studies on antihydrogen atoms with the ATRAP experiment at CERN," *Acta Physica Polonica B, Proceedings Supplement*, 2013.

- [22] G. Consolati, S. Aghion, C. Amsler, A. Ariga, T. Ariga, A. Belov *et al.*, “Experiments with low-energy antimatter,” in *EPJ Web of Conferences*, 2015.
- [23] P. Pérez, D. Banerjee, F. Biraben, D. Brook-Roberge, M. Charlton, P. Cladé *et al.*, “The GBAR antimatter gravity experiment,” *Hyperfine Interactions*, 2015.
- [24] W. Oelert, “The ELENA project at CERN,” *Acta Phys. Pol. B*, vol. 46, no. arXiv:1501.05728, p. 181. 10 p, Jan 2015. [Online]. Available: <http://cds.cern.ch/record/1982947>
- [25] M. Hori and J. Walz, “Physics at CERN’s Antiproton Decelerator,” *Prog. Part. Nucl. Phys.*, vol. 72, pp. 206–253, 2013.
- [26] W. Bartmann, P. Belochitskii, H. Breuker, F. Butin, C. Carli, T. Eriksson, W. Oelert, S. Maury, S. Pasinelli, and G. Tranquille, “CERN ELENA project progress report,” in *EPJ Web of Conferences*, vol. 95. EDP Sciences, May 2015.
- [27] T. Eriksson and Others, “ELENA - From Installation to Commissioning,” in *Proc. of International Particle Accelerator Conference (IPAC’17), Copenhagen, Denmark, 14-19 May, 2017*, ser. International Particle Accelerator Conference, no. 8. Geneva, Switzerland: JACoW, May 2017, pp. 3327–3330. [Online]. Available: <http://jacow.org/ipac2017/papers/wepva034.pdf>
- [28] M. Brice, “ELENA ring - start of first beam,” *photograph*, 2016. [Online]. Available: <https://cds.cern.ch/record/2235240>
- [29] M. Buzio, P. Galbraith, G. Golluccio, D. Giloteaux, S. Gilardoni, C. Petrone, L. Walckiers, and A. Beaumont, “Development of upgraded magnetic instrumentation for CERN real-time reference field measurement systems,” in *IPAC 2010 - 1st International Particle Accelerator Conference*, 2010, pp. 310–312.
- [30] D. Perrelet, Y. Brischetto, H. Damerau, D. Oberson, M. Sundal, and A. Villanueva, “White-Rabbit Based Revolution Frequency Program for the Longitudinal Beam Control of the CERN PS,” in *Proceedings, 15th International Conference on Accelerator and Large Experimental Physics Control Systems (ICALEPCS 2015): Melbourne, Australia, October 17-23, 2015*, 2015, p. MOPGF091. [Online]. Available: <http://jacow.org/icalepcs2015/papers/mopgf091.pdf>
- [31] N. A. Spaldin, *Ferromagnetic domains*, 2nd ed. Cambridge University Press, 2010, pp. 79–95.
- [32] F. Decker, “The Physical Way of Standardizing Magnets,” in *Conference Record of the 1991 IEEE Particle Accelerator Conference*, May 1991, pp. 2143–2145 vol.4.
- [33] J. Billan, “Materials,” in *CERN Accelerator School: Measurement and Alignment of Accelerator and Detector magnets*. Anacapri, Italy: CERN, 1997, pp. 107–126.

- [34] P. Bryant and K. Johnsen, *The Principles of Circular Accelerators and Storage Rings*. Cambridge University Press, 2005. [Online]. Available: <https://books.google.ch/books?id=eU7EJkYTiNEC>
- [35] S. E. Zirka, Y. I. Moroz, and E. D. Torre, "Combination hysteresis model for accommodation magnetization," *IEEE Transactions on Magnetics*, vol. 41, no. 9, pp. 2426–2431, Sep 2005.
- [36] E. D. Torre and Y. Jin, "Comparison of the DEMAM and DEAM Accommodation Models," *IEEE Transactions on Magnetics*, vol. 45, no. 3, pp. 1198–1201, Mar 2009.
- [37] L. Bottura, M. Lamont, E. Todesco, W. Venturini Delsolaro, and R. Wolf, "Pre-Cycles of the LHC Magnets during Operation," CERN, Geneva, Tech. Rep. CERN-ATS-2010-174, Aug 2010. [Online]. Available: <https://cds.cern.ch/record/1283477>
- [38] M. Sadiku, *Elements of Electromagnetics*, ser. Oxford series in electrical and computer engineering. Oxford University Press, 2001. [Online]. Available: <https://books.google.com.mt/books?id=w2ITHQAACAAJ>
- [39] G. Moritz, F. Klos, B. Langenbeck, and K. Zweig, "Static and dynamic behaviour of the SIS dipole magnet," *IEEE Transactions on Magnetics*, vol. 32, no. 4, pp. 3065–3068, Jul 1996.
- [40] G. Moritz, "Eddy currents in accelerator magnets," in *CAS 2009 - CERN Accelerator School: Magnets, Proceedings*. CERN, Mar 2010, pp. 103–140.
- [41] P. Arpaia, M. Buzio, G. Golluccio, and G. Montenero, "Eddy current modeling and measuring in fast-pulsed resistive magnets," in *2010 IEEE International Instrumentation and Measurement Technology Conference, I2MTC 2010 - Proceedings*, 2010, pp. 1078–1081.
- [42] S. Igarashi, T. Adachi, H. Someya, N. Tani, and Y. Watanabe, "Eddy current effects of the J-PARC RCS sextupole magnets," in *IEEE Transactions on Applied Superconductivity*, vol. 18, no. 2, Jun 2008, pp. 289–292.
- [43] L. Fiscarelli, private communication, 2016.
- [44] M. Buzio, "Fabrication and calibration of search coils," in *CAS 2009 - CERN Accelerator School: Magnets, Proceedings*, Apr 2010, pp. 387–421. [Online]. Available: <http://arxiv.org/abs/1104.0803>
- [45] C. Petrone and S. Russenschuck, "Wire methods for measuring field harmonics, gradients and magnetic axes in accelerator magnets," 2013. [Online]. Available: <https://cds.cern.ch/record/1601973>

-
- [46] L. Bottura and K. N. Henrichsen, "Field Measurements," *CERN Accelerator School - Superconductivity and Cryogenics for accelerators and detectors*, 2002.
- [47] C. Reymond, "Magnetic Resonance Techniques," in *CERN Accelerator School: Measurement and Alignment of Accelerator and Detector magnets*, S. Turner, Ed. CERN, 1998, pp. 219–232.
- [48] "PT2025 NMR Teslameter User Manual," Sep 2003. [Online]. Available: https://www.metrolab.com/download_files/pt2025_user_manual/
- [49] P. Keller, "NMR Magnetometers." Metrolab, 2011. [Online]. Available: https://www.metrolab.com/wp-content/uploads/2015/07/PT2025_tech_note_NMR-Magnetometers-published-in-Magnetics-Technology-International.pdf
- [50] P. Arpaia, M. Buzio, F. Caspers, G. Golluccio, and C. Petrone, "Static metrological characterization of a ferrimagnetic resonance transducer for real-time magnetic field markers in particle accelerators," in *2011 IEEE International Instrumentation and Measurement Technology Conference*, May 2011, pp. 1–4.
- [51] M. Benedikt, F. Caspers, and M. Lindroos, "Application of magnetic markers for precise measurement of magnetic fields in ramped accelerators," *Particle Accelerators*, no. 63, 1999.
- [52] F. Caspers, "FerriMagnetic Resonance: A method to measure magnetic fields in accelerator environment," CERN, Tech. Rep. CERN-PS-AR-Note-94-21, 1994.
- [53] A. Beaumont, "NMR magnetic field markers of the B-Train for the Proton Synchrotron accelerator," Ph.D. dissertation, University of Technology Belfort-Montbéliard, Belfort, France, Mar 2009. [Online]. Available: <https://edms.cern.ch/document/993482/1>
- [54] A. Beaumont, M. Buzio, and G. Boero, "Ferrimagnetic Resonance Field Sensors for Particle Accelerators," *Review of Scientific Instruments*, vol. 90, no. 6, p. 65005, Jun 2019. [Online]. Available: <https://doi.org/10.1063/1.5097508>
- [55] P. Arpaia, L. Bottura, L. Fiscarelli, and L. Walckiers, "Performance of a fast digital integrator in on-field magnetic measurements for particle accelerators," *Review of Scientific Instruments*, vol. 83, no. 2, p. 24702, Feb 2012.
- [56] A. Beaumont and M. Buzio, "LEIR Reliability Report," CERN, Tech. Rep., 2019.
- [57] K. N. Henrichsen, "Overview of magnet measurement methods," in *CAS - CERN Accelerator School : Measurement and Alignment of Accelerator and Detector Magnets*, Anacapri, Italy. CERN, 1998. [Online]. Available: <https://cds.cern.ch/record/382438>

- [58] C. Germain, "Bibliographical review of the methods of measuring magnetic fields," *Nuclear Instruments and Methods*, vol. 21, no. C, pp. 17–46, 1963.
- [59] J. M. Kelly, "Magnetic Field Measurements with Peaking Strips," *Review of Scientific Instruments*, vol. 22, no. 4, pp. 256–258, 1951. [Online]. Available: <http://dx.doi.org/10.1063/1.1745904>
- [60] M. Buzio, P. Galbraith, G. Golluccio, D. Giloteaux, S. Gilardoni, C. Petrone, L. Walckiers, and A. Beaumont, "Development of Upgraded Magnetic Instrumentation for CERN Real-time Reference Field Measurement Systems," *IPAC*, 2010.
- [61] P. Di Cesare, C. Reymond, H. Rottstock, and P. Sommer, "SPS magnetic field cycle measurement system: Investigation on Nuclear Magnetic Resonance (NMR) system to get a faster reading of field values," CERN, Geneva, techreport CERN-SPS-PCO-Note 89-9, Apr 1989. [Online]. Available: <https://cds.cern.ch/record/2158783>
- [62] F. Velotti, M. Fraser, K. Cornelis, J. Bauche, V. Kain, H. Bartosik, and M. Buzio, "Investigation of the Remanent Field of the SPS Main Dipoles and Possible Solutions for Machine Operation," in *IPAC 2017 - International Particle Accelerator Conference 2017*, 2017.
- [63] M. Benedikt, "B-train systems in the PS-complex," CERN, Tech. Rep. 2133453, 2001.
- [64] R. Vanden Broeck, "LEIR : The Low Energy Ion Ring," Sep 2019. [Online]. Available: <http://cds.cern.ch/record/2692717>
- [65] C. Bovet, R. Gouiran, I. Gumowski, and K. H. Reich, *A selection of formulae and data useful for the design of A.G. synchrotrons*. Geneva: CERN, 1970. [Online]. Available: <https://cds.cern.ch/record/104153>
- [66] A. Peters, E. Feldmeier, C. Schömers, R. Steiner, H. Eickhoff, T. Knapp, and C. Welsch, "Magnetic Field Control in Synchrotrons," in *Joint Accelerator Conferences Website (JACoW), PAC09, 169-171 (2009)*, Vancouver, Canada, 2009, pp. 169–171. [Online]. Available: <https://accelconf.web.cern.ch/accelconf/pac2009/papers/mo6pfp017.pdf>
- [67] E. Feldmeier, T. Haberer, A. Peters, C. Schoemers, and R. Steiner, "Magnetic field correction in normal conducting synchrotrons," in *IPAC 2010 - 1st International Particle Accelerator Conference*, 2010.
- [68] E. Feldmeier and T. Haberer, "Development of a high precision integrator for analog signals to measure magnetic fields in real-time," in *IPAC 2013: Proceedings of the 4th International Particle Accelerator Conference*, 2013.

- [69] E. Feldmeier, T. Haberer, M. Galonska, R. Cee, S. Scheloske, and A. Peters, "The first magnetic field control (B-train) to optimize the duty cycle of a synchrotron in clinical operation," in *IPAC 2012 - International Particle Accelerator Conference 2012*, 2012.
- [70] G. Golluccio, A. Beaumont, M. Buzio, O. Dunkel, M. Stockner, and T. Zickler, "PCB coils array for measuring bent accelerator dipoles. Two case studies on the MedAustron accelerator," in *IMEKO*, Benevento, Italy, 2014.
- [71] P. Fraboulet, K. Ambrosch, I. De Cesaris, and A. Beuret, "The current and field regulation system of the MedAustron Ion-Beam accelerator," in *IECON Proceedings (Industrial Electronics Conference)*, 2013, pp. 7103–7108.
- [72] U. Dorda, A. Fabich, F. Osmic, and M. Benedikt, "Status of the MedAustron Ion Beam Therapy centre," *IPAC 2012 - International Particle Accelerator Conference 2012*, 2012.
- [73] G. Franzini, D. Pellegrini, M. Serio, A. Stella, M. Donetti, M. Pezzetta, and M. Pullia, "Measurements on an A/D interface used in the power supply control system of the main dipoles of CNAO," in *EPAC 2008 - Contributions to the Proceedings*, 2008.
- [74] G. Franzini, O. Coiro, D. Pellegrini, M. Serio, M. Pezzetta, and M. Pullia, "Final Design and Features of the B-train System of CNAO," *IPAC*, 2010.
- [75] M. Pezzetta, G. Bazzano, E. Bressi, L. Falbo, M. Pullia, C. Priano *et al.*, "B-train Performances at CNAO," in *IPAC2011*, San Sebastian, Spain, 2011. [Online]. Available: <https://accelconf.web.cern.ch/accelconf/IPAC2011/papers/mopo039.pdf>
- [76] E. Bressi and Others, "B-train Calibration with RF-master Method," *IPAC*, 2018.
- [77] L. Ahrens and M. Harvey, "Determining the Momentum of a Beam Accelerating in the AGS A Gauss Clock Calibration, and Associated Parameter Determination," University of North Texas Libraries, Tech. Rep., 2002. [Online]. Available: <https://digital.library.unt.edu/ark:/67531/metadc828952/>
- [78] M. Fahmie, "Design of the Advanced Light Source timing system," in *Proceedings of the IEEE Particle Accelerator Conference*, 1993.
- [79] C.-M. Chang, S. Strano, and M. Terzo, "Modelling of Hysteresis in Vibration Control Systems by means of the Bouc-Wen Model," *Shock and Vibration*, vol. 2016, pp. 1–14, 2016.
- [80] P. Duhem, "Die dauernden Aenderungen und die Thermodynamik II," *Zeitschrift für Physikalische Chemie*, vol. 23U, no. 1, Jan 1897.

- [81] W. Xie, J. Fu, H. Yao, and C. Su, "Observer based control of piezoelectric actuators with classical Duhem modeled hysteresis," in *2009 American Control Conference*, Jun 2009, pp. 4221–4226.
- [82] Y. Feng, C. A. Rabbath, T. Chai, and C. Su, "Robust adaptive control of systems with hysteretic nonlinearities: A Duhem hysteresis modelling approach," in *AFRICON 2009*, Sep 2009, pp. 1–6.
- [83] C.-J. Lin and P.-T. Lin, "Tracking control of a biaxial piezo-actuated positioning stage using generalized Duhem model," *Computers & Mathematics with Applications*, vol. 64, no. 5, pp. 766–787, Sep 2012.
- [84] C. Wang, M. Zhou, and R. Xu, "Rate-dependent modeling and tracking control for piezoelectric micro-positioning platform," in *2017 Chinese Automation Congress (CAC)*. IEEE, Oct 2017.
- [85] P. J. van Bree, C. M. M. van Lierop, and P. P. J. van den Bosch, "Control-Oriented Hysteresis Models for Magnetic Electron Lenses," *IEEE Transactions on Magnetics*, vol. 45, no. 11, pp. 5235–5238, Nov 2009.
- [86] C. Hui, T. Yonghong, Z. Xingpeng, D. Ruili, and Z. Yahong, "Identification of Dynamic Hysteresis Based on Duhem Model," in *2011 Fourth International Conference on Intelligent Computation Technology and Automation*, vol. 1, Mar 2011, pp. 810–814.
- [87] J. Oh and D. S. Bernstein, "Semilinear Duhem model for rate-independent and rate-dependent hysteresis," *IEEE Transactions on Automatic Control*, vol. 50, no. 5, pp. 631–645, May 2005.
- [88] B. D. Coleman and M. L. Hodgdon, "On a class of constitutive relations for ferromagnetic hysteresis," *Archive for Rational Mechanics and Analysis*, vol. 99, no. 4, pp. 375–396, Dec 1987. [Online]. Available: <https://doi.org/10.1007/BF00282052>
- [89] J. Voros, "Modeling and Identification of Discrete-Time Nonlinear Dynamic Cascade Systems with Input Hysteresis," *Mathematical Problems in Engineering*, vol. 2015, pp. 1–8, 2015.
- [90] Q. Xu and Y. Li, "Modeling and control of rate-dependent hysteresis for a piezo-driven micropositioning stage," in *2011 IEEE International Conference on Robotics and Automation*. IEEE, May 2011.
- [91] J. Du, Y. Feng, C.-Y. Su, and Y.-M. Hu, "On the robust control of systems preceded by Coleman-Hodgdon hysteresis," *2009 IEEE International Conference on Control and Automation*, pp. 685–689, 2009.

- [92] A. A. Eielsen, J. T. Gravdahl, and K. Y. Pettersen, "Adaptive feed-forward hysteresis compensation for piezoelectric actuators," *Review of Scientific Instruments*, vol. 83, no. 8, p. 85001, 2012. [Online]. Available: <https://doi.org/10.1063/1.4739923>
- [93] K. H. Carpenter and S. Warren, "A wide bandwidth, dynamic hysteresis model for magnetization in soft ferrites," *IEEE Transactions on Magnetics*, vol. 28, no. 5, pp. 2037–2041, Sep 1992.
- [94] R. Ouyang, "Stability Analysis and Controller Design For a System with Hysteresis," Ph.D. dissertation, Dutch Institute of Systems and Control, 2013.
- [95] R. Bouc, "A Mathematical Model for Hysteresis," *Acustica*, vol. 24, no. 1, pp. 16–25, 1971.
- [96] Y. Wen, "Method for Random Vibration of Hysteretic Systems," *Journal of the Engineering Mechanics Division*, vol. 102, no. 2, 1976.
- [97] M. Ismail, F. Ikhoulane, and J. Rodellar, "The Hysteresis Bouc-Wen Model, a Survey," *Archives of Computational Methods in Engineering*, vol. 16, no. 2, pp. 161–188, Jun 2009. [Online]. Available: <https://doi.org/10.1007/s11831-009-9031-8>
- [98] A. Bahar, F. Pozo, L. Acho, J. Rodellar, and A. Barbat, "Parameter identification of large-scale magnetorheological dampers in a benchmark building," *Computers & Structures*, vol. 88, no. 3, pp. 198–206, 2010. [Online]. Available: <http://www.sciencedirect.com/science/article/pii/S0045794909002582>
- [99] A. Rodriguez, N. Iwata, F. Ikhoulane, and J. Rodellar, "Modeling and Identification of a Large-Scale Magnetorheological Fluid Damper," *Advances in Science and Technology*, vol. 56, pp. 374–379, Sep 2008.
- [100] Z. Wang, Z. Zhang, J. Mao, and K. Zhou, "A Hammerstein-based model for rate-dependent hysteresis in piezoelectric actuator," in *2012 24th Chinese Control and Decision Conference (CCDC)*, May 2012, pp. 1391–1396.
- [101] L. Cheng, W. Liu, Z. Hou, J. Yu, and M. Tan, "Neural-Network-Based Nonlinear Model Predictive Control for Piezoelectric Actuators," *IEEE Transactions on Industrial Electronics*, vol. 62, no. 12, pp. 7717–7727, Dec 2015.
- [102] L. Chua and K. Stromsmoe, "Lumped-circuit models for nonlinear inductors exhibiting hysteresis loops," *IEEE Transactions on Circuit Theory*, vol. 17, no. 4, pp. 564–574, 1970.

- [103] A. Iványi, *Hysteresis Models in Electromagnetic Computation*, ser. Scientific review. International Specialized Book Service Incorporated, 1997. [Online]. Available: <https://books.google.ch/books?id=pNXxPAAACAAJ>
- [104] M. A. Krasnosel'skiĭ and A. V. Pokrovskiĭ, *Systems with Hysteresis*. Springer Berlin Heidelberg, 1989.
- [105] P. R. Dahl, "Solid Friction Damping of Mechanical Vibrations," *AIAA Journal*, vol. 14, no. 12, pp. 1675–1682, Dec 1976.
- [106] C. C. de Wit, H. Olsson, K. J. Astrom, and P. Lischinsky, "A new model for control of systems with friction," *IEEE Transactions on Automatic Control*, vol. 40, no. 3, pp. 419–425, Mar 1995.
- [107] J. Swevers, F. Al-Bender, C. G. Ganseman, and T. Projogo, "An integrated friction model structure with improved presliding behavior for accurate friction compensation," *IEEE Transactions on Automatic Control*, vol. 45, no. 4, pp. 675–686, Apr 2000.
- [108] D. M. Rocha, N. F. F. Ebecken, L. P. Calôba, and D. L. Kaiser, "Neural Network Modeling Of The Nonlinear Dynamic Structural Offshore System With Hysteresis," *WIT Transactions on Information and Communication Technologies*, vol. 40, p. 12, 2008.
- [109] C.-L. Hwang, C. Jan, and Y.-H. Chen, "Piezomechanics using intelligent variable-structure control," *IEEE Transactions on Industrial Electronics*, vol. 48, no. 1, pp. 47–59, Feb 2001.
- [110] Y. Wu, Y. Fang, X. Ren, and H. Lu, "Back propagation neural networks based hysteresis modeling and compensation for a piezoelectric scanner," in *2016 IEEE International Conference on Manipulation, Manufacturing and Measurement on the Nanoscale (3M-NANO)*, Jul 2016, pp. 119–124.
- [111] K. S. Narendra and K. Parthasarathy, "Adaptive identification and control of dynamical systems using neural networks," in *Proceedings of the 28th IEEE Conference on Decision and Control*. IEEE, 1989.
- [112] J. L. Elman, "Finding Structure in Time," *Cognitive Science*, vol. 14, no. 2, pp. 179–211, Mar 1990.
- [113] M. Saghafifar, "Magnetic Hysteresis Modelling Using Knowledge Based Engineering Techniques," Master's thesis, University of South Australia, 2004.
- [114] Y. Gao and M. J. Er, "NARMAX time series model prediction: feedforward and recurrent fuzzy neural network approaches," *Fuzzy Sets and Systems*, vol. 150,

- no. 2, pp. 331–350, 2005. [Online]. Available: <http://www.sciencedirect.com/science/article/pii/S0165011404004099>
- [115] W. Zhang, J. Zhu, and D. Gu, “Identification of robotic systems with hysteresis using Nonlinear AutoRegressive eXogenous input models,” *International Journal of Advanced Robotic Systems*, vol. 14, no. 3, p. 1729881417705845, 2017. [Online]. Available: <https://doi.org/10.1177/1729881417705845>
- [116] J.-D. Wei and C.-T. Sun, “Large simulation of hysteresis systems using a piecewise polynomial function,” *IEEE Signal Processing Letters*, vol. 9, no. 7, pp. 207–210, Jul 2002.
- [117] H. Ge, C. Hu, Z. Wei, and D. Hou, “Research on a photovoltaic system of MPPT hysteresis control based on adaptive FIR filter,” in *2014 9th IEEE Conference on Industrial Electronics and Applications*. IEEE, Jun 2014.
- [118] S. Zhang, M. Wang, P. Zheng, G. Qiao, F. Liu, and L. Gan, “An Easy-to-Implement Hysteresis Model Identification Method Based on Support Vector Regression,” *IEEE Transactions on Magnetics*, vol. 53, no. 11, pp. 1–4, Nov 2017.
- [119] I. Mayergoyz, “Chapter 1 - The Classical Preisach Model of Hysteresis,” in *Mathematical Models of Hysteresis and Their Applications*, ser. Electromagnetism, I. D. Mayergoyz, Ed. New York: Elsevier Science, 2003, pp. 1–63. [Online]. Available: <http://www.sciencedirect.com/science/article/pii/B9780124808737500025>
- [120] D. Song and C. J. Li, “Modeling of piezo actuator’s nonlinear and frequency dependent dynamics,” *Mechatronics*, vol. 9, no. 4, pp. 391–410, 1999. [Online]. Available: <http://www.sciencedirect.com/science/article/pii/S0957415899000057>
- [121] A. Adly and S. A. El-Hafiz, “Using neural networks in the identification of Preisach-type hysteresis models,” *IEEE Transactions on Magnetics*, vol. 34, no. 3, pp. 629–635, May 1998.
- [122] B. Zhang, B. Gupta, B. Ducharne, G. Sebald, and T. Uchimoto, “Preisach’s Model Extended With Dynamic Fractional Derivation Contribution,” *IEEE Transactions on Magnetics*, vol. 54, no. 3, pp. 1–4, Mar 2018.
- [123] G. Bertotti, “Dynamic generalization of the scalar Preisach model of hysteresis,” *IEEE Transactions on Magnetics*, vol. 28, no. 5, pp. 2599–2601, Sep 1992.
- [124] E. Eskinat, S. H. Johnson, and W. L. Luyben, “Use of Hammerstein models in identification of nonlinear systems,” *AIChE Journal*, vol. 37, no. 2, pp. 255–268, Feb 1991.

- [125] I. D. Mayergoyz, "Dynamic Preisach models of hysteresis," *IEEE Transactions on Magnetics*, vol. 24, no. 6, pp. 2925–2927, 1988.
- [126] R. B. Mrad and H. Hu, "Dynamic modeling of hysteresis in piezoceramics," in *2001 IEEE/ASME International Conference on Advanced Intelligent Mechatronics. Proceedings (Cat. No.01TH8556)*. IEEE, 2001.
- [127] A. Wilk and M. Michna, "The dynamic model of magnetic hysteresis," in *2015 IEEE International Conference on Industrial Technology (ICIT)*, Mar 2015, pp. 840–843.
- [128] S. Xiao and Y. Li, "Modeling and High Dynamic Compensating the Rate-Dependent Hysteresis of Piezoelectric Actuators via a Novel Modified Inverse Preisach Model," *IEEE Transactions on Control Systems Technology*, vol. 21, no. 5, pp. 1549–1557, Sep 2013.
- [129] J. Füzi, "Computationally efficient rate dependent hysteresis model," *COMPEL - The international journal for computation and mathematics in electrical and electronic engineering*, vol. 18, no. 3, pp. 445–457, Sep 1999.
- [130] M. Kuczmann, "Dynamic Preisach model identification applying FEM and measured BH curve," *COMPEL - The international journal for computation and mathematics in electrical and electronic engineering*, vol. 33, no. 6, pp. 2043–2052, 2014. [Online]. Available: <https://doi.org/10.1108/COMPEL-11-2013-0368>
- [131] D. Makaveev, L. Dupré, M. D. Wulf, and J. Melkebeek, "Dynamic hysteresis modelling using feed-forward neural networks," *Journal of Magnetism and Magnetic Materials*, vol. 254–255, pp. 256–258, 2003. [Online]. Available: <http://www.sciencedirect.com/science/article/pii/S0304885302007850>
- [132] X. Tan and J. S. Baras, "Modeling and control of hysteresis in magnetostrictive actuators," *Automatica*, vol. 40, no. 9, pp. 1469–1480, Sep 2004.
- [133] X. Tan, R. Venkataraman, and P. S. Krishnaprasad, "Control of hysteresis: theory and experimental results," in *Smart Structures and Materials 2001: Modeling, Signal Processing, and Control in Smart Structures*, V. S. Rao, Ed. SPIE, Aug 2001.
- [134] G. Biorci and D. Pescetti, "Analytical theory of the behaviour of ferromagnetic materials," *Il Nuovo Cimento (1955-1965)*, vol. 7, no. 6, pp. 829–842, Mar 1958. [Online]. Available: <https://doi.org/10.1007/BF02745588>
- [135] M. Ruderman and T. Bertram, "Identification of Soft Magnetic B-H Characteristics Using Discrete Dynamic Preisach Model and Single Measured Hysteresis Loop," *IEEE Transactions on Magnetics*, vol. 48, no. 4, pp. 1281–1284, Apr 2012.

- [136] M. Kozek and B. Gross, "Identification and Inversion of Magnetic Hysteresis for Sinusoidal Magnetization," *International Journal of Online and Biomedical Engineering*, 2005.
- [137] L. Rouve, T. Waeckerle, and A. Kedous-Lebouc, "Application of Preisach model to grain oriented steels: comparison of different characterizations for the Preisach function $p(\alpha, \beta)$," *IEEE Transactions on Magnetics*, vol. 31, no. 6, pp. 3557–3559, Nov 1995.
- [138] K. Hergli, H. Marouani, M. Zidi, Y. Fouad, and M. Elshazly, "Identification of Preisach hysteresis model parameters using genetic algorithms," *Journal of King Saud University - Science*, Dec 2017.
- [139] M. Mordjaoui, M. Chabane, and B. Boudjema, "Qualitative modelling for dynamic magnetic hysteresis," *2007 International Aegean Conference on Electrical Machines and Power Electronics*, pp. 226–231, 2007.
- [140] H. Saliah and D. Lowther, "The use of neural networks in magnetic hysteresis identification," *Physica B: Condensed Matter*, vol. 233, no. 4, pp. 318–323, 1997. [Online]. Available: <http://www.sciencedirect.com/science/article/pii/S0921452697003165>
- [141] C. Li and Y. Tan, "A neural networks model for hysteresis nonlinearity," *Sensors and Actuators A: Physical*, vol. 112, no. 1, pp. 49–54, 2004. [Online]. Available: <http://www.sciencedirect.com/science/article/pii/S0924424703006526>
- [142] V. Akbarzadeh, M. Davoudpour, and A. Sadeghian, "Neural network modeling of magnetic hysteresis," *2008 IEEE International Conference on Emerging Technologies and Factory Automation*, pp. 1267–1270, 2008.
- [143] M. R. Zakerzadeh, M. Firouzi, H. Sayyaadi, and S. B. Shouraki, "Hysteresis Nonlinearity Identification Using New Preisach Model-Based Artificial Neural Network Approach," *Journal of Applied Mathematics*, vol. 2011, pp. 1–22, 2011.
- [144] C. Serpico and C. Visone, "Magnetic hysteresis modeling via feed-forward neural networks," *IEEE Transactions on Magnetics*, vol. 34, no. 3, pp. 623–628, May 1998.
- [145] Z. Zhen, C. Qingwei, and M. Jianqin, "Generalized Prandtl-Ishlinskii model for rate-dependent hysteresis: Modeling and its inverse compensation for Giant Magnetostrictive Actuator," in *Proceedings of the 31st Chinese Control Conference*, Jul 2012, pp. 462–466.
- [146] Y. Luo, M. Zhou, and R. Xu, "Modeling of hysteresis nonlinearity in piezoelectric ceramic micro-positioning platform based on generalized rate-dependent

- Prandtl-Ishlinskii model,” in *2017 Chinese Automation Congress (CAC)*, Oct 2017, pp. 574–578.
- [147] G. Zhang, C. Zhang, and J. Gu, “Modeling and control of rate-dependent hysteresis in piezoelectric actuators,” in *Proceedings of the 32nd Chinese Control Conference*, Jul 2013, pp. 1929–1934.
- [148] M. A. Janaideh, S. Rakheja, and C. Y. Su, “A Generalized Prandtl-Ishlinskii Model for Characterizing Rate Dependent Hysteresis,” in *2007 IEEE International Conference on Control Applications*. IEEE, Oct 2007.
- [149] Y. Qin, Y. Tian, D. Zhang, B. Shirinzadeh, and S. Fatikow, “A Novel Direct Inverse Modeling Approach for Hysteresis Compensation of Piezoelectric Actuator in Feedforward Applications,” *IEEE/ASME Transactions on Mechatronics*, vol. 18, no. 3, pp. 981–989, Jun 2013.
- [150] H. Jiang, H. Ji, J. Qiu, and Y. Chen, “A modified Prandtl-Ishlinskii model for modeling asymmetric hysteresis of piezoelectric actuators,” *IEEE Transactions on Ultrasonics, Ferroelectrics and Frequency Control*, vol. 57, no. 5, pp. 1200–1210, May 2010.
- [151] L. Li, G. Gu, and L. Zhu, “Improving the tracking performance of atomic force microscope scanner with the modified rate-dependent Prandtl-Ishlinskii model,” in *2017 International Conference on Advanced Mechatronic Systems (ICAMechS)*, Dec 2017, pp. 456–461.
- [152] L. Riccardi, D. Naso, B. Turchiano, H. Janocha, and D. K. Palagachev, “On PID control of dynamic systems with hysteresis using a Prandtl-Ishlinskii model,” in *2012 American Control Conference (ACC)*. IEEE, Jun 2012.
- [153] X. Chen, C.-Y. Su, and T. Fukuda, “Adaptive Control for the Systems Preceded by Hysteresis,” *IEEE Transactions on Automatic Control*, vol. 53, pp. 1019–1025, 2008.
- [154] Y. Wang, R. Xu, and M. Zhou, “Prandtl-Ishlinskii Modeling for Giant Magnetostrictive Actuator Based on Internal Time-Delay Recurrent Neural Network,” *IEEE Transactions on Magnetics*, vol. 54, no. 11, pp. 1–4, Nov 2018.
- [155] G.-Y. Gu, M.-J. Yang, and L.-M. Zhu, “Real-time inverse hysteresis compensation of piezoelectric actuators with a modified Prandtl-Ishlinskii model,” *Review of Scientific Instruments*, vol. 83, no. 6, p. 65106, Jun 2012.
- [156] H. T. Banks and A. J. Kurdila, “Hysteretic control influence operators representing smart material actuators: identification and approximation,” in *Proceedings of 35th IEEE Conference on Decision and Control*. IEEE, 1996.

- [157] Q. Wang, C.-Y. Su, and Y. Tan, "On the Control of Plants with Hysteresis : Overview and a Prandtl-Ishlinskii Hysteresis Based Control Approach," in *ACTA Automatica Sinica*, 2005.
- [158] H. T. Banks, A. J. Kurdila, and G. Webb, "Identification of hysteretic control influence operators representing smart actuators part I: Formulation," *Mathematical Problems in Engineering*, vol. 3, no. 4, pp. 287–328, 1997.
- [159] Z. Li, C.-Y. Su, and T. Chai, "Compensation of Hysteresis Nonlinearity in Magnetostrictive Actuators With Inverse Multiplicative Structure for Preisach Model," *IEEE Transactions on Automation Science and Engineering*, vol. 11, no. 2, pp. 613–619, Apr 2014.
- [160] E. Cardelli, A. Faba, A. Laudani, M. Pompei, S. Q. Antonio, F. R. Fulginei, and A. Salvini, "A challenging hysteresis operator for the simulation of Goss-textured magnetic materials," *Journal of Magnetism and Magnetic Materials*, vol. 432, pp. 14–23, Jun 2017.
- [161] X. Zhao and Y. Tan, "Neural network based identification of Preisach-type hysteresis in piezoelectric actuator using hysteretic operator," *Sensors and Actuators A: Physical*, vol. 126, no. 2, pp. 306–311, 2006. [Online]. Available: <http://www.sciencedirect.com/science/article/pii/S0924424705006011>
- [162] Z. Tong, Y. Tan, and X. Zeng, "Modeling hysteresis using hybrid method of continuous transformation and neural networks," *Sensors and Actuators A: Physical*, vol. 119, no. 1, pp. 254–262, 2005. [Online]. Available: <http://www.sciencedirect.com/science/article/pii/S0924424704007046>
- [163] Y. Tan, R. Dong, H. Chen, and H. He, "Identification of Hysteresis in Human Meridian Systems Based on NARMAX Model," *Journal of Applied Mathematics*, 2012.
- [164] D. C. Jiles and D. L. Atherton, "Theory of ferromagnetic hysteresis," *Journal of Magnetism and Magnetic Materials*, vol. 61, no. 1-2, pp. 48–60, 1986.
- [165] P. R. Wilson, "Modeling and simulation of magnetic components in electric circuits," Nov 2001. [Online]. Available: <https://eprints.soton.ac.uk/368484/>
- [166] D. C. Jiles, J. B. Thoelke, and M. K. Devine, "Numerical determination of hysteresis parameters for the modeling of magnetic properties using the theory of ferromagnetic hysteresis," *IEEE Transactions on Magnetics*, vol. 28, no. 1, pp. 27–35, Jan 1992.
- [167] L. H. Lewis, J. Gao, D. C. Jiles, and D. O. Welch, "Modeling of permanent magnets: Interpretation of parameters obtained from the Jiles–Atherton hysteresis

- model," *Journal of Applied Physics*, vol. 79, no. 8, pp. 6470–6472, 1996. [Online]. Available: <https://aip.scitation.org/doi/abs/10.1063/1.361975>
- [168] M. F. Jaafar, "Magnetic hysteresis modeling and numerical simulation for ferromagnetic materials," in *2013 International Conference on Control, Decision and Information Technologies (CoDIT)*, May 2013, pp. 516–523.
- [169] K. H. Carpenter, "A differential equation approach to minor loops in the Jiles-Atherton hysteresis model," *IEEE Transactions on Magnetics*, vol. 27, no. 6, pp. 4404–4406, Nov 1991.
- [170] N. Schmidt and H. Guldner, "A simple method to determine dynamic hysteresis loops of soft magnetic materials," *IEEE Transactions on Magnetics*, vol. 32, no. 2, pp. 489–496, Mar 1996.
- [171] D. Lederer, H. Igarashi, A. Kost, and T. Honma, "On the parameter identification and application of the Jiles-Atherton hysteresis model for numerical modelling of measured characteristics," *IEEE Transactions on Magnetics*, vol. 35, no. 3, pp. 1211–1214, May 1999.
- [172] S. Cao, B. Wang, J. Zheng, W. Huang, Y. Sun, and Q. Yang, "Modeling dynamic hysteresis for giant magnetostrictive actuator using hybrid genetic algorithm," *IEEE Transactions on Magnetics*, vol. 42, no. 4, pp. 911–914, Apr 2006.
- [173] S. Hamada, F. Z. Louai, N. Nait-Said, and A. Benabou, "Dynamic hysteresis modeling including skin effect using diffusion equation model," *Journal of Magnetism and Magnetic Materials*, vol. 410, pp. 137–143, Jul 2016.
- [174] E. Sárospataki and M. Kuczmann, "Realization of the Jiles-Atherton Hysteresis Model Applying the Labview and Matlab Software Package," *Journal of Electrical Engineering*, vol. 57, no. 8, 2006.
- [175] R. C. Smith and R. Zrostlik, "Inverse Compensation for Ferromagnetic Hysteresis," in *Proceedings of the 38th IEEE Conference on Decision and Control*, 1999.
- [176] H. Hauser, "Energetic model of ferromagnetic hysteresis: Isotropic magnetization," *Journal of Applied Physics*, vol. 96, no. 5, pp. 2584–2597, Sep 2004.
- [177] P. Fulmek, P. Haumer, H. Wegleiter, and B. Schweighofer, "Energetic model of ferromagnetic hysteresis," *COMPEL - The international journal for computation and mathematics in electrical and electronic engineering*, vol. 29, no. 6, pp. 1504–1513, Nov 2010.

- [178] F. Caspers, W. Heinze, J. Lewis, M. Lindroos, and T. Salvermoser, "An Alternative to classical real time magnetic field measurements using a magnet model," in *International Conference on Accelerator and Large Experimental Physics Control Systems (ICALEPCS 97) Beijing, China, November 3-7, 1997*, 1997.
- [179] E. Bozoki, "Calibration of the Ring Model for the NSLS Rings," *IEEE Transactions on Nuclear Science*, vol. 30, no. 4, pp. 2219–2221, Aug 1983.
- [180] B. C. Brown, "Hysteresis study techniques and results for accelerator magnets with unipolar current excitation," in *Proceedings of the 1999 Particle Accelerator Conference*, vol. 5, Mar 1999, pp. 3315–3317 vol.5.
- [181] R. P. Feynman, R. P. Leighton, and S. Matthew, *The Feynman Lectures on Physics*, M. A. Gottlieb and R. Pfeiffer, Eds. California Institute of Technology, 2011, vol. 2.
- [182] V. Pricop, G. Scutaru, and D. Schoerling, "Hysteresis effects in the cores of particle accelerator magnets," Feb 2016. [Online]. Available: <https://cds.cern.ch/record/2135195>
- [183] CERN, "Simple PCIe FMC Carrier," 2019. [Online]. Available: <https://www.ohwr.org/project/spec/wikis/home>
- [184] Xilinx, "Spartan-6 FPGA," 2011. [Online]. Available: <https://www.xilinx.com/products/silicon-devices/fpga/spartan-6.html>
- [185] G. Kasproicz, "Simple PCIe FMC Carrier Board," 2011. [Online]. Available: <https://edms.cern.ch/item/EDA-02189-V4-0/0>
- [186] K. Richardson and T. Wlostowski, "CTR FMC," 2018. [Online]. Available: <https://edms.cern.ch/item/EDA-03801-V2-0/0>
- [187] P. Alvarez, "CTR User Guide," CERN, Tech. Rep., 2007. [Online]. Available: <https://edms.cern.ch/document/598907/>
- [188] D. Giloteaux, "Peak Position Detector FMC Schematics," 2015. [Online]. Available: <https://edms.cern.ch/document/1513856/1>
- [189] J. Vella Wallbank, M. Amodeo, A. Beaumont, M. Buzio, V. Di Capua, D. Giloteaux, C. Grech, and N. Sammut, "The development of a real-time magnetic measurement system for synchrotrons," *MDPI Electronics*, vol. to be published, 2020.
- [190] D. Giloteaux, "B-Train FMC," 2015. [Online]. Available: <https://edms.cern.ch/item/EDA-02512-V4-1/0>
- [191] D. Giloteaux, "Bsim-Bsynth-WR FMC Assembly Data," 2017. [Online]. Available: <https://edms.cern.ch/document/1745238>

- [192] C. Roderick, R. Billen, and G. Switzerland, "The LSA Database to Drive the Accelerator Settings," CERN, Tech. Rep., 2009.
- [193] P. P. Jansweijer, H. Z. Peek, and E. De Wolf, "White Rabbit: Sub-nanosecond timing over Ethernet," *Nuclear Instruments and Methods in Physics Research, Section A: Accelerators, Spectrometers, Detectors and Associated Equipment*, vol. 725, pp. 187–190, 2013.
- [194] D. Gamba, C. Carli, T. Eriksson, L. Ponce, and G. Tranquille, "ELENA Commissioning," in *Proc. COOL'19*, ser. Workshop on Beam Cooling and Related Topics, no. 12. JACoW Publishing, Geneva, Switzerland, Nov 2019, pp. 52–54. [Online]. Available: <https://jacow.org/cool2019/papers/wex03.pdf>
- [195] O. Dunkel, "Measurement methods and devices for curved dipole and combined function magnets," CERN, Tech. Rep., 2015.
- [196] S. Du, J. Hu, Y. Zhu, and M. Zhang, "A Hall Sensor-Based Position Measurement With On-Line Model Parameters Computation for Permanent Magnet Synchronous Linear Motor," *IEEE Sensors Journal*, vol. 18, no. 13, pp. 5245–5255, Jul 2018.
- [197] S. N. Murnane, R. N. Barnes, S. R. Woodhead, and J. E. Amadi-Echendu, "Electrostatic modelling and measurement of airborne particle concentration," *IEEE Transactions on Instrumentation and Measurement*, vol. 45, no. 2, pp. 488–492, Apr 1996.
- [198] D. Vasic, V. Bilas, and D. Ambrus, "Validation of a Coil Impedance Model for Simultaneous Measurement of Electromagnetic Properties and Inner Diameter of a Conductive Tube," *IEEE Transactions on Instrumentation and Measurement*, vol. 55, no. 1, pp. 337–342, Feb 2006.
- [199] M. Emaami, H. C. Wood, and H. M. Skarsgard, "A controller for plasma motion in a Tokamak based on model estimation," *IEEE Transactions on Industrial Electronics*, vol. 37, no. 4, pp. 317–322, Aug 1990.
- [200] S. T. Spantideas and C. N. Capsalis, "Validation of a source identification method for prediction of low-frequency magnetic fields in space missions," *IEEE Magnetics Letters*, vol. 9, Nov 2017.
- [201] K. Mehlem, "Multiple Magnetic Dipole Modeling and Field Prediction of Satellites," *IEEE Transactions on Magnetics*, vol. 14, no. 5, pp. 1064–1071, 1978.
- [202] M. Amodeo, P. Arpaia, and M. Buzio, "Integrator drift compensation of magnetic flux transducers by feed-forward correction," *Sensors (Switzerland)*, vol. 19, no. 24,

- p. 5455, Dec 2019. [Online]. Available: <https://www.mdpi.com/1424-8220/19/24/5455>
- [203] A. Milanese, "An Introduction to Magnets for Accelerators," in *John Adams Institute Accelerator Course*. Oxford: CERN, 2017. [Online]. Available: <https://indico.cern.ch/event/590390/contributions/2381025/>
- [204] Keysight, *Agilent Technologies 34401A Digital Multimeter Manual*, Keysight Technologies, 2015. [Online]. Available: <https://docs-apac.rs-online.com/webdocs/0b40/0900766b80b40128.pdf>
- [205] L. Bottura, M. Buzio, S. Pauletta, and N. Smirnov, "Measurement of magnetic axis in accelerator magnets: critical comparison of methods and instruments," in *IEEE Instrumentation and Measurement Technology Conference (IMTC 2006)*, 2006, pp. 765–770.
- [206] Hexagon Metrology, "AT402 User Manual," 2013. [Online]. Available: <https://pdf.directindustry.com/pdf/hexagon-manufacturing-intelligence/leica-absolute-tracker-at402-brochure/5623-389495.html>
- [207] "Teslameter FM 3002," 2016. [Online]. Available: <http://www.projekt-elektronik.com/pdf/Teslameter-FM3002-0204-18.pdf>
- [208] "Mag-03 Three-Axis Magnetic Field Sensors," 2010. [Online]. Available: https://www.bartington.com/wp-content/uploads/pdfs/operation_manuals/Mag-03_OM1004.pdf
- [209] Joint Committee for Guides in Metrology, "Evaluation of measurement data: Guide to the expression of uncertainty in measurement," *International Organization for Standardization Geneva ISBN*, vol. 50, no. September, p. 134, 2008.
- [210] B. Taylor and C. Kuyatt, "Guidelines for Evaluating and Expressing the Uncertainty of NIST Measurement Results," NIST, Tech. Rep., 1994.
- [211] Y. Tian, G. S. Nearing, C. D. Peters-Lidard, K. W. Harrison, and L. Tang, "Performance metrics, error modeling, and uncertainty quantification," *Monthly Weather Review*, vol. 144, no. 2, pp. 607–613, Feb 2016. [Online]. Available: <http://journals.ametsoc.org/doi/10.1175/MWR-D-15-0087.1>
- [212] C. Grech, R. Avramidou, A. Beaumont, M. Buzio, N. Sammut, and J. Tinembart, "Metrological characterization of nuclear magnetic resonance markers for real-time field control of the CERN ELENA ring dipoles," *IEEE Sensors Journal*, vol. 18, no. 14, pp. 5826–5833, 2018. [Online]. Available: <https://ieeexplore.ieee.org/document/8370735/>

- [213] *Device Specifications: NI 6366*, National Instruments, 2016. [Online]. Available: <https://www.ni.com/pdf/manuals/374454c.pdf>
- [214] M. E. Angoletta, S. Albright, S. Energico, S. Hancock, M. Jaussi, A. Jones, J. Molendijk, M. Paoluzzi, and J. Sanchez-Quesada, "Initial Beam Results of CERN ELENA's Digital Low-Level RF System," in *IPAC2017*, no. CERN-ACC-2017-264, Copenhagen, Denmark, May 2017, p. THPAB142. 4 p. [Online]. Available: <https://cds.cern.ch/record/2289141>
- [215] R. Marco-Hernández, D. Alves, M. E. Angoletta, O. Marquversen, J. Molendijk, E. Oponowicz, R. Ruffieux, J. Sánchez-Quesada, and L. SØby, "The AD and ELENA orbit, trajectory and intensity measurement systems," *JINST*, vol. 12, no. 07, 2017.
- [216] *Device Specifications: AS-NTM-2*, Projekt Elektronik, 2017. [Online]. Available: <https://www.projekt-elektronik.com/wp-content/uploads/sites/3/2018/03/data-sheet-AS-active-probe-0203-46.pdf#page=15>
- [217] D. Dvir, A. Ben-David, A. Sadeh, and A. J. Shenhar, "Critical managerial factors affecting defense projects success: A comparison between neural network and regression analysis," *Engineering Applications of Artificial Intelligence*, vol. 19, no. 5, pp. 535–543, 2006. [Online]. Available: <http://www.sciencedirect.com/science/article/pii/S0952197606000157>
- [218] *Deep Learning Toolbox*, MATLAB, 2019.
- [219] D. W. Marquardt, "An Algorithm for Least-Squares Estimation of Nonlinear Parameters," *Journal of the Society for Industrial and Applied Mathematics*, 1963.
- [220] M. T. Hagan and M. B. Menhaj, "Training Feedforward Networks with the Marquardt Algorithm," *IEEE Transactions on Neural Networks*, 1994.
- [221] D. Stathakis, "How many hidden layers and nodes?" *International Journal of Remote Sensing*, vol. 30, no. 8, pp. 2133–2147, 2009. [Online]. Available: <https://doi.org/10.1080/01431160802549278>
- [222] L. Prechelt, "Early Stopping — But When?" in *Neural Networks: Tricks of the Trade*, 2012, pp. 53–67.
- [223] C. Grech, M. Buzio, M. Pentella, and N. Sammut, "Dynamic Ferromagnetic Hysteresis Modelling Using a Preisach-Recurrent Neural Network Model," *Materials*, vol. 13, no. 11, p. 2561, jun 2020. [Online]. Available: <https://www.mdpi.com/1996-1944/13/11/2561>
- [224] M. Brokate, "Some mathematical properties of the Preisach model for hysteresis," *IEEE Transactions on Magnetics*, vol. 25, no. 4, pp. 2922–2924, July 1989.

-
- [225] A. M. Schäfer and H. G. Zimmermann, "Recurrent Neural Networks are universal approximators," *International Journal of Neural Systems*, vol. 17, no. 04, pp. 253–263, 2007, pMID: 17696290. [Online]. Available: <https://doi.org/10.1142/S0129065707001111>
- [226] J. D. Saliccioli, Y. Crutain, M. Komorowski, and D. C. Marshall, *Sensitivity Analysis and Model Validation*. Cham: Springer International Publishing, 2016, pp. 263–271. [Online]. Available: https://doi.org/10.1007/978-3-319-43742-2_17
- [227] Z. P. Liu and J. P. Castagna, "Avoiding overfitting caused by noise using a uniform training mode," in *IJCNN'99. International Joint Conference on Neural Networks. Proceedings (Cat. No.99CH36339)*, vol. 3, July 1999, pp. 1788–1793 vol.3.